Imperial College London

Doctoral Thesis

Reservoir modelling and simulation using dynamically optimised meshes

---

Author:
Hossam O.Osman

Supervisor:
Prof Matthew Jackson,
Prof Christopher Pain,
Prof Sebastian Geiger.

A thesis submitted in fulfillment of the requirements for the degree of Doctor of Philosophy

in the

NORMS - Novel Reservoir Modelling and Simulation
Department of Earth Science & Engineering

September 27, 2019

Declaration of Authorship

I, Hossam O.Osman, declare that this thesis titled, "Reservoir modelling and simulation using dynamically optimised meshes" and the work presented in it are my own. I confirm that:

- This work was done wholly or mainly while in candidature for a research degree at this University.
- Where any part of this thesis has previously been submitted for a degree or any other qualification at this University or any other institution, this has been clearly stated.
- Where I have consulted the published work of others, this is always clearly attributed.
- Where I have quoted from the work of others, the source is always given. With the exception of such quotations, this thesis is entirely my own work.
- I have acknowledged all main sources of help.
- Where the thesis is based on work done by myself jointly with others, I have made clear exactly what was done by others and what I have contributed myself.

Signed:

Date:

Copyright Declaration

The copyright of this thesis rests with the author. Unless otherwise indicated, its contents are licensed under a Creative Commons Attribution-Non Commercial 4.0 International Licence (CC BY-NC).

Under this licence, you may copy and redistribute the material in any medium or format. You may also create and distribute modified versions of the work. This is on the condition that: you credit the author and do not use it, or any derivative works, for a commercial purpose.

When reusing or sharing this work, ensure you make the licence terms clear to others by naming the licence and linking to the licence text. Where a work has been adapted, you should indicate that the work has been changed and describe those changes.

Please seek permission from the copyright holder for uses of this work that are not included in this licence or permitted under UK Copyright Law.

IMPERIAL COLLEGE LONDON

Abstract

Reservoirs are inherently heterogeneous. The depositional environment, compaction, deformation and cementation can lead to spatial variability in petrophysical properties, over many orders of magnitude and length-scales, with a profound effect on the flow behaviour of the fluids flowing within it.

Conventional reservoir modelling workflows have adopted k-orthogonal meshes that are fixed in time and space. Due to the complex geometries found in reservoirs and the multi-scale structure of the governing equations, a more flexible approach is needed.

This thesis presents an alternative to conventional grid-based modelling and simulation workflows. Surface-based modelling (SBM) is used to capture geological heterogeneity at all scales that impact flow, without reference to an underlying grid. Petrophysical properties within these domains are modelled as internally homogeneous. We show that cell-to-cell variability in reservoir models is not needed to capture multi-phase flow. Instead one can use a small number of larger, internally homogeneous but geometrically complex geological domains.

For flow simulations, geomodels are discretised using unstructured tetrahedral meshes and the governing equations are solved using a control-volume-finite-element method (CVFEM). The proposed simulator incorporates dynamic adaptive-mesh optimisation (DAMO), designed to tackle the unique challenges of spatially varying petrophysical properties in porous media. Multi-scale features are better captured at lower computational cost by refining the mesh resolution where/when necessary and coarsening elsewhere.

Material discontinuities in porous media strongly influence multi-phase flow. Traditional CVFEMs smear out jump discontinuities of saturation or concentration. The high aspect ratio elements typically required to discretise the heterogeneous domains in subsurface reservoirs are also very challenging on standard CVFEMs. To overcome these issues we develop a new discretisation based on the bubble enriched finite-element method (FEM). This new method is able to accurately represent saturation discontinuities on geologically complex models.

List of Publications

1. H. Osman, G. H. Graham, A. Moncorge, and C. Jacquemyn. "Is cell-to-cell scale variability necessary in reservoir models?. Submitted

2. H.Osman, P. Salinas, C.C. Pain, and M.D. Jackson. "An efficient control volume finite element method for multi-phase flow in heterogeneous porous media on challenging meshes". To be submitted

3. P. Salinas, C. C. Pain, H. Osman, Z. Xie, and M. D. Jackson (2019). "Vanishing artificial diffusion as a mechanism to accelerate convergence for multiphase porous media flow". In: *Computer Methods in Applied Mechanics and Engineering*

4. P. Salinas, D. Pavlidis, Z. Xie, H. Osman, C. C. Pain, and M. D. Jackson (2018a). "A discontinuous control volume finite element method for multi-phase flow in heterogeneous porous media". In: *Journal of Computational Physics* 352, pp. 602–614. ISSN: 00219991. DOI: 10.1016/j.jcp.2017.09.058

5. P Salinas, D Pavlidis, Z Xie, H Osman, C C Pain, and M D Jackson (2018b). "A robust mesh optimisation method for multiphase porous media flows". In: *Computational Geosciences*. ISSN: 1420-0597. DOI: 10.1007/s10596-018-9759-z

6. P. Salinas, C. C. Pain, H. Osman, C. Heaney, D. Pavlidis, and M. D. Jackson (2018c). "Vanishing Artificial Capillary Pressure For Improved Real-Size Reservoir Simulations". In: *ECMOR XVI-16th European Conference on the Mathematics of Oil Recovery.*

7. H. Osman, G. H. Graham, A. Moncorge, and M. D. Jackson (2018). "Impact Of Cell-To-Cell Scale Variability On Flow In Reservoir Models". In: *15th European Conference on the Mathematics of Oil Recovery (ECMOR XV)* September 2018

8. Y. Melnikova, C. Jacquemyn, H. Osman, P. Salinas, G. Gorman, G. J. Hampson, and M. D. Jackson (2016). "Reservoir Modelling Using Parametric Surfaces and Dynamically Adaptive Fully Unstructured Grids". In: *ECMOR XV - 15th European Conference on the Mathematics of Oil Recovery*. DOI: 10.3997/2214-4609.201601887

Acknowledgements

None of this work would have been possible without the generous time and support of my supervisors and colleagues. First of all, I would like to thank my supervisor Matthew Jackson. I express my sincere gratitude for allowing me the chance to work with you and for sharing your expertise and perspectives. You've helped me be more concise and deliberate in my thinking and writing for which I am eternally grateful. Thank you for making the NORMS research group such a fun and stimulating environment to work in.

I would also like to thank my co-supervisors Christopher Pain and Sebastian Geiger for insightful comments and suggestions. I especially want to thank Christopher Pain for his boundless enthusiasm for numerical methods and his original development of IC-FERST.

No one works in isolation and I have had the pleasure to work alongside some amazing people in the research group and wider at the Earth Science and Engineering Department. NORMS has been like a little family, thank you all for making social events so much fun and being a great sounding board for my ideas. I particularly appreciate the help and generosity of Pablo Salinas and Carl Jacquemyn who have gone above and beyond the call of duty. This project would not have been possible without their combined input and support.

I would also like to extend my thanks to the NERC Centre for Doctoral Training in Oil and Gas for sponsoring and funding this project under the framework of Extending the Life of Mature Basins.

Last but not least to my family. Thank you for your endless love and support. You have always encouraged me to achieve my goals and have put up with my rants about work without complaint.

Contents

Declaration of Authorship **iii**

Copyright Declaration **v**

Abstract **vii**

List of Publications **ix**

Acknowledgements **xi**

List of Figures **xvii**

List of Tables **xxix**

1 Introduction **1**

1.1 Motivation 1

1.2 Thesis outline 6

2 Background and Literature review **9**

2.1 Modelling multi-phase flow through porous media 10

2.1.1 Pore scale modelling 10

2.1.2 Continuum scale modelling 11

2.2 Numerical schemes 15

2.2.1 Finite-difference method 16

2.2.2 Finite-volume method 18

2.2.3 Finite-element method 20

2.2.4 Multi-scale methods 23

2.2.5 Temporal discretisation 23

2.3 Building geological models 25

2.3.1 Conventional modelling methods 27

2.3.2 Gridding 29

2.3.3 Surface-based modelling 32

2.3.4 Unstructured adaptive meshes 38

2.4 Summary 45

3 Numerical Method **47**
3.1 Introduction 47
3.2 Modified governing equations 48
3.3 Weak formulation 50
3.4 Discrete formulation 52
3.4.1 Force-balance 52
3.4.2 Rock and fluid properties 54
3.4.3 Global continuity 54
3.4.4 Time stepping approach 55
3.4.5 Pressure projection 56
3.4.6 Mass balance for the fluid phases 57

4 Investigating the effect of cell-to-cell variability in reservoir models **61**
4.1 Introduction 62
4.2 Test cases 64
4.2.1 Lower SPE 10: Fluvial Model 65
4.2.2 Upper SPE 10: Shallow Marine Model 65
4.2.3 H-Field: North Sea Reservoir 66
4.2.4 Rock and fluid properties 66
4.2.5 Well placements and controls 70
4.3 Methodology 72
4.3.1 Goodness of fit 72
4.3.2 Removal of cell-by-cell variability 73
4.4 Results 75
4.4.1 Lower SPE 10 model: Segmentation and Clustering . . . 75
4.4.2 Upper SPE 10 model: Summary of Goodness of Fit results 81
4.4.3 H-Field Model: Summary of Goodness of Fit results . . . 83
4.5 Discussion 83
4.6 Conclusions 87

5 Dynamic adaptive-mesh optimisation for multi-phase flow in geological formations **91**
5.1 Introduction 92
5.2 Dynamic adaptive-mesh optimisation 93
5.2.1 Metric formation 93
5.2.2 Mesh optimisation 95

5.2.3 Mesh to mesh interpolation . . . 97
5.2.4 Accounting for high Courant numbers . . . 98
5.3 Test cases . . . 100
5.3.1 Counter-current Spontaneous Imbibition . . . 102
5.3.2 DNAPL infiltration . . . 104
5.3.3 Surface-based models . . . 106
5.4 Results . . . 113
5.4.1 Spontaneous imbibition . . . 113
5.4.2 DNAPL infiltration . . . 114
5.4.3 Fracture model (SBM 1) . . . 116
5.4.4 Channel model (SBM 2) . . . 116
5.4.5 Fault model (SBM 3) . . . 118
5.5 Cost of adaptivity . . . 122
5.6 Discussion . . . 126
5.7 Conclusions . . . 128

6 Modelling material and property discontinuities 131
6.1 Introduction . . . 132
6.2 Stability . . . 133
6.3 Discretisation with bubble functions . . . 136
6.3.1 Force-balance equation . . . 136
6.3.2 Global and local continuity equation . . . 138
6.3.3 Inter-element fluxes . . . 138
6.3.4 Special considerations for the mass matrix . . . 139
6.3.5 Solution mechanism . . . 140
6.4 Numerical Experiments . . . 140
6.5 Results . . . 143
6.5.1 Model 1 . . . 143
6.5.2 Model 2 . . . 143
6.5.3 Model 3 . . . 147
6.6 Conclusions . . . 149

7 Conclusions and Future Work 155
7.1 Conclusions . . . 155
7.2 Future Work . . . 156

Bibliography 159

A Analytical solution for Spontaneous Imbibition 187
A.1 Analytical solution for Spontaneous Imbibition . . . 187

List of Figures

1.1 Conventional modelling and simulation workflow (Jackson et al., 2013). 5

2.1 (A) The representative elementary volume (REV) concept after Bear (1972)), (B) porous media at the micro-scale, large fluctuations in property averages occur as the volume samples more grain or void space (pores), (B) at macro-scale volumes spanning several grains where average property becomes independent from the averaging volume, (C) heterogeneous layered systems can introduce further fluctuations due to spatial variability in flow properties. 13

2.2 Conceptual sketch illustrating multi-scales ($n = 1, 2, 3$) of REV related to geological heterogeneities and scales of measurement, from Nordahl and Ringrose (2008) 14

2.3 (A) Deviated grid for a sloping fault. Warmer colours indicate greater deviations from orthogonality; (B) Error in total vertical flux vs fault angle for the vertical-flow problem (Wu and Parashkevov, 2009) 18

2.4 (A) two-point-flux approximation (TPFA) in one dimension (1D); (B) multi-point-flux approximation (MPFA) in 2D; the interaction region is depicted by the dashed lines and centred around vertices to form a dual grid. Modified from Juanes et al. (2005). 19

2.5 A control volume in the triangular finite element mesh. Filled circles represent element vertices, empty circles are the centroids. 21

2.6 Traditional CVFEM, here for a $P0_{DG}P1$ element pair. The exact solution $p(x)$ is approximated by $\hat{p}(x)$ using the piecewise linear interpolation functions N_i and N_j of each finite element. The piecewise constant derivative of this solution $\frac{d\hat{p}}{dx}$ is proportional to the Darcy velocity but discontinuous across two neighbouring finite elements. Flux continuity is achieved across boundaries of adjacent control-volume (CV) built around the nodes of the finite element. Integration of the fluxes over the surface of the CVs ensures mass conservation. Adapted from Paluszny et al. (2007). 22

2.7 Heterogeneity at various scales within a generic shoreface-shelf sandstone reservoir (Sech et al., 2009). 26

2.8 Various modelling methodologies on a continuum from the conventional geostatistical models (far left) which are able to incorporate data directly to the unconditional (no data integration) process-based models (far right), from Pyrcz et al. (2015). 29

2.9 Loss of fidelity in grid-based models, adapted from Jackson et al., 2015 31

2.10 Modelling of a faulted domain using (A) Cartesian grid; (B) Corner-point grid; (C) 2.5-D perpendicular-bisector grid (PEBI) (Jackson et al., 2015). In (A), the grid is orthogonal, the dipping-fault has to be approximated by staircase-like steps. In (B), the fault geometry is better captured but is non-orthogonal both in plan view and cross section. In (C), the grid is approximately k-orthogonal in plan view but still non-orthogonal in cross section. 32

2.11 A generic example of the rule-based surface-hierarchy. Structural surfaces (1-2) are at the top of the hierarchy as they truncate all other surfaces. Stratigraphic surfaces (3-5) are at the next in the hierarchy, truncated by structural surfaces but truncate facies boundaries. Sedimentological surfaces (6-11) are the base of the hierarchy (Jackson et al., 2015). 33

2.12 Overview of the surface-based modelling approach adopted by Bertoncello et al. (2013). (A) Basal surface, representing the sea floor; (B) thickness events extracted from process-based model (Michael et al., 2010); (C) Top view of final model; (D) Cross section of final geological model. Colours represent different domains enclosed by surfaces. 34

2.13 Surfaces govern the architecture of the grid using stratigraphic corner point gridding. Where geological zones pinch out, degenerate quadrilateral cells are generated. To avoid no flow barriers and to maintain vertical continuity non-neighbour connections are used. Adapted from White and Barton (1999). 35
2.14 2D section through surface-based models showing the corner gridding scheme used to preserve geological architecture of the dipping surfaces. (A) from Sech et al. (2009), here clinoform dips were $< 1°$, (B) from Graham et al. (2015a) where clinoform dips were up to $5°$ 36
2.15 a) Cross-bedded sandstones model used to investigate the sensitivity of effective permeability to sample volume, b) effective permeability in the dip and strike directions as a function of sample volume, normalised by the permeability of equivalent sandstone only sample. The error bars indicate the numerical artefacts introduced by cornerpoint gridding. From Massart et al. (2016). 37
2.16 Common structural heterogeneities represented using non-uniform b-spline curves and surfaces (NURBS). (A) Faulted recumbent fold, (B) Conjugate normal fault sets, C) Listric growth fault. Adapted from Jacquemyn et al. (2018). 39
2.17 Multiple surfaces representing internal heterogeneity within a channelised body (Jacquemyn et al., 2018). 40
2.18 Geological complexity of an outcrop of Liassic limestone on the southern Bristol Channel coast, UK. (A) Photograph of a small-scale fold structure intersected by carbonate veins crosscut by later Alpine joints; (B) NURBS computer aided design (CAD) model of the same structure with the numerous intersection curves and acute intersection angles between fractures. (Paluszny et al., 2007) 41
2.19 Common procedures for adapting a mesh. (A) to (B) local refinement or coarsening of the mesh is known as *h-adaptivity*, (C) to (D) relocating or moving mesh points is known as *r-adaptivity* and (E) to (F) locally varying the polynomial basis functions is known as *p-adaptivity*. 42

2.20 Scalar field with a sharp interface represented on different meshes with the same minimum edge length. (A)-(B) Structured mesh. Capturing the interface requires 56,320 elements. (C)-(D) Isotropic unstructured mesh. The use of unstructured meshes leads to a significant reduction in the number of elements, 5,667 elements. (E)-(F) Anisotropic unstructured mesh. A further reduction can be seen with the use of anisotropic meshes to only 2,805 elements. 44

3.1 (A) Rock properties permeability and porosity are piecewise constant in the finite element, (B) Fluid properties such as viscosity and saturation are constant within the sub-control volume. . . . 55

3.2 Finite element representation of the force density ($\boldsymbol{\nu}_\alpha$) and Darcy velocity ($\mathbf{u}_\alpha$) on a two dimensions (2D) element. (A) discontinuous P0 finite element representation of the force density; (B) as $\boldsymbol{\sigma}_\alpha$ is made up of finite-element (FE)- and CV-wise terms, the Darcy velocity is discontinuous across sub-control volumes. 59

3.3 Flow chart of the non-linear solver algorithm. The algorithm consists of three main loops, thick solid line denotes the outer time loop, dotted line denotes the fixed point iteration method used to solve the non-linear system of equations. The dashed lines denote the saturation fixed point iteration (SFPI) used to accelerate the Anderson-fixed point method (Salinas et al., 2017a). 60

4.1 (A) Reservoir models typically contain cell-to-cell variations in petrophysical properties; (B) The geological concept captures the architecture of key heterogeneities. 62

4.2 Petrophysical properties within the Lower SPE 10 Model. Plots (A-C) show the spatial distribution of horizontal permeability in (A) three dimensions (3D); (B) vertical cross section (X-X') and (C) horizontal cross section (Y-Y'). Dimensions in metres. Plots (D-F) show the frequency distribution of (D) horizontal permeability; (E) vertical permeability and (F) porosity. Plots (D-F) also show the frequency distribution after division into three segments; see Method section for more details. 67

4.3 Petrophysical properties within the Upper SPE 10 Model. Plots (A-C) show the spatial distribution of horizontal permeability in (A) 3D; (B) vertical cross section (X-X') and (C) horizontal cross section (Y-Y'). Dimensions in metres. Plots (D-F) show the frequency distribution of (D) horizontal permeability; (E) vertical permeability and (F) porosity. 68

4.4 The H-Field Model. Plot (A) shows the 3D spatial distribution of horizontal permeability; plot (B) shows the fault blocks, where red indicates the fault plane; plot (C) shows the location of production wells in green and water injection wells in blue. Dimensions in metres. Plots (D-F) show the frequency distribution of (D) horizontal permeability; (E) vertical permeability and (F) porosity. 69

4.5 Segmentation and clustering of the Lower SPE 10 Model. (A) Segmented model with three segments. (B) 3x3x3 cube around an input cell during clustering. The central cell's value is then replaced with the modal value of the neighbouring cells; here a green permeability value is replaced by a blue one. (C) Clustered model. The cell-to-cell variability is removed, creating more geologically meaningful *domains*. 76

4.6 Goodness of Fit (GOF) as a function of segment number. (A) Lower SPE 10 Model with the inverted five spot well configuration; (B) Lower SPE 10 model with the line drive well configuration; (C) Upper SPE 10 Model with the inverted five spot well configuration; (D) Upper SPE 10 Model with the line drive well configuration; (E) H-Field model. Points with lines denote the segmented models without clustering. The different line markers denote the different fluid viscosity ratios. Dashed and solid lines denote the GOF including and excluding water breakthrough, respectively. Unfilled and filled triangles denote the GOF with and without water breakthrough for the clustered models. 77

4.7 Well and reservoir responses of the base, segmented and clustered models of the Lower SPE 10 Model and the inverted five spot well configuration with uniform oil and water viscosities. Plots (A-D) show oil production rate as a function of time for each producer well. Plots (E-H) show water production rate as a function of time for each producer well. Plot (I) shows the bottom hole pressure for the water injection well. Plots (J-L) show, respectively, the total reservoir oil production rate, water production rate and cumulative oil production as a function of time. 78
4.8 Horizontal cross sections through the Lower SPE 10 Model showing horizontal permeability and water saturation at a given time step during production via the inverted five spot well configuration with uniform oil and water viscosities. Plots (A) and (B) show, respectively, the permeability at a horizontal section through the base and 10-segment and clustered models. Plots (C) and (D) show the water saturation at a given timestep on the same horizontal section. 79
4.9 Vertical cross sections through the Lower SPE 10 Model showing horizontal permeability and water saturation at a given time step during production via the inverted five spot well configuration with uniform oil and water viscosities. Plots (A) and (B) show the vertical section through the base and 10-segment and clustered models, respectively. Plots (C) and (D) show the water saturation at the same vertical section. 79
4.10 Horizontal sections through the Upper SPE 10 Model showing horizontal permeability. Plot (A) shows the base Upper SPE 10 model; plot (B) shows the Upper SPE 10 model with 10 segments after clustering. 82
4.11 Horizontal sections through the H-Field Model showing horizontal permeability. Plot (A) shows the base H-Field model; plot (B) shows the H-Field model with 20 segments after clustering. . . . 82
4.12 Goodness of Fit of segmented models without clustering, as a function of segment number for 10 realisations of the H-Field. (A) Goodness of Fit excluding water breakthrough; (B) Goodness of Fit including water breakthrough. 84
4.13 Surface-based model inspired by SPE 10 model 2. (A) Full model; (B) Lower, fluvial section; from below (Jacquemyn et al., 2018). 88

5.1 Work flow to generate and adapt unstructured meshes on surface-based models. (A) Original surface-based model depicting two domains; (B) a 2D surface mesh is built to capture the bounding surfaces; (C) an initial coarse 3D tetrahedral mesh is built within the domains; during flow simulation the volume meshes can be refined, (D), or coarsened, (E) using hr adaptivity but the geology remains intact. From Jackson et al. (2015). 94
5.2 Topological operations performed on elements in order to optimise a mesh (Pain et al., 2001; Piggott et al., 2009). 96
5.3 (A) and (B) Two triangular meshes with some finite element solution depicted by different colours. (C) and (D) show the same triangular supermesh with the FE solutions mapped from mesh (A) and (B), respectively. Adapted from Farrell and Maddison (2011). 98
5.4 Standard mesh adaptivity algorithm. The mesh is adapated to user-specified field(s) after a user-defined number of time-steps. 99
5.5 Non-linear mesh adaptivity. The mesh is adapted as part of the non-linear solver with an addition loop (dashed line). 101
5.6 (A) Domain split into two regions. A large porosity is set for the left-hand domain to ensure insignificant change in saturation. The right-hand domain's porosity is kept at 0.20 and homogeneous permeability of $1 \times 10^{-13}\mathrm{m}^2$, (B) the right-hand side domain is initially saturated with the oil phase and no external forces are applied i.e. all boundaries are no flow boundaries. The wetting phase invades the domain purely by capillary forces. 104
5.7 Geometry and boundary conditions of DNAPL infiltration test case (Helmig, 1997) 106
5.8 1.5×1.5m sample of the Kilve model (Figure 5.9c) extruded 0.1 m . Fracture width are uniform at 3 mm. 108
5.9 (A) Structural map of Lilstock on the southern margin of the Bristol Channel coast, showing the Lilstock anticline and regional map showing the location of the Kilve model; (B) The gently folded alternating limestone and shale beds of the Kilve anticline. Early joints were formed parallel to the fold axis around the hinge zone of the anticline; (C) Kilve sketch, Area = 6×6m. From Belayneh et al. (2006). 109

5.10 SBM 2. Channelised sandstone reservoir with three channel groups; 1,000 mD (Domain 1), 200 md (Domain 2) and 100 mD (Domain 3). Non-reservoir mudstone is not modelled. Vertical exaggeration 4×. 110
5.11 Cross section of SBM 2, discretised using Cartesian grids at decreasing resolution (vertical exaggeration 5×). (A) model made up of 400,000 cells (109,585 active cells); (B) model made up of 100,000 cells (26,735 active cells); (C) model made up of 25,000 cells (6,477 active cells). The connectivity of the smallest channels is lost as the mesh is coarsened. We also encounter some artificial connectivity. 111
5.12 Surface-based channel model (SBM 2) made up (A) approximately 8,000 elements (mesh D1); (B) mesh D2, 13,000 elements . . . 112
5.13 SBM 3. Conjugate normal faults offsetting stratigraphic layers of contrasting permeability; 1,000 mD (Domain 1) and 1 mD (Domain 2); (A) side view; (B) top view; (C) example of unstructured tetrahedral mesh. 113
5.14 Saturation snap shots after 10,000 seconds. (A) with a fixed mesh (mesh A3, 8,000 elements); (B) adapted mesh AA3 with < 100 elements. 114
5.15 (A) Comparison of numerical results for counter-current spontaneous imbibition against the analytical solution for fixed mesh simulations. The dashed line denotes the analytical solution; (B) The L1 error norm of the fixed and adaptive mesh solutions after 10,000 seconds; the dashed line denotes linear convergence. The adaptive mesh simulations yields similar solution quality to the fixed mesh results using approximately two orders of magnitude fewer elements when comparing the highest resolution adaptive and fixed models. 115
5.16 Infiltration results after 2,360 seconds. (A) Fixed mesh B1 (202 elements) simulation; (B) fixed mesh B2 (666 elements) simulation; (C) fixed mesh B3 (2,604 elements); (D) fixed mesh B4 (17,082) (B) DAMO simulation with an average of 1380 elements (mesh BA3); (C) experimental results (Helmig and Huber, 1998). . . . 117
5.17 Normalised mass leakage into the capillary barrier corresponding to the time step in Figure 5.16 118

5.18 Water saturation after approximately 0.1 pore volumes injected. (A) fixed mesh C1, with 33,606 elements; (B) fixed mesh C2, with 477,759 elements; (C) DAMO simulation an average of 41,653 elements (mesh CA1). 119
5.19 Oil recovery and water cut plots as a function of the pore volume injected (dimensionless time), (A) Oil recovery as a proportion of the volume originally in place; (B) watercut (ratio of produced water to total volume produced) 120
5.20 The geometry of SBM 2 is maintained at all levels of refinement. This ensures that the connectivity of the channels are preserved during DAMO. 121
5.21 Oil recovery and water cut plots as a function of the pore volume injected (dimensionless time), (A) Oil recovery as a proportion of the volume originally in place; (B) zoomed in section of oil recovery; (C) watercut (ratio of produced water to total volume produced); (D) zoomed in section of watercut 121
5.22 Production plots as a function of time for simulations of the fault model. (A) oil recovery; (B) water cut. 123
5.23 Water saturation after 0.2 pore volumes injected. (A) Mesh A; (B) Mesh D; (C) DAMO simulation. 124
5.24 Comparison of CPU times (normalised to the coarsest fixed mesh time) between one time step without adaptivity (blue bars) and one time step followed by one adaptive step (red bar). (A) SI model; (B) Fault model (SBM 3). 125
5.25 Total CPU time for the Fault model (SBM 3) normalised to CPU time for mesh E1. Blue bars denote fixed meshes, red bar denotes the DAMO simulation. 126

6.1 Four CVFEM schemes in their lowest order variants (A) *Continuous double control-volume-finite-element method (DCVFEM)*, where CVs span multiple elements. Sharp saturation/component interfaces can not be preserved without significant grid refinement. (B) interface control-volume-finite-element method (ICVFEM) from Abushaikha et al. (2015), where pressure nodes are placed on the element-element interfaces. CVs are therefore shared by, at most, two elements. CV smearing is reduced but not eliminated. (C) *Discontinuous CVFEM* from Salinas et al. (2018a), where pressure nodes are allowed to be discontinuous between elements. CVs are therefore discontinuous and sharp saturation/component interfaces can be honoured. However this discretisation is based on a $P2_{DG}-P1_{DG}$ element pair making it an expensive method in terms of the DOFs needed and is not robust on distorted meshes. (D) The new *discontinuous DCVFEM* uses a linear element pair $P1_{DG}-P1_{DG}$ with a bubble function augmented velocity space i.e. $P1_{BLDG}-P1_{DG}$. 134

6.2 1D illustration of an unstable equal order discretisation. The pressure field is piecewise linear; the pressure gradient is therefore piecewise constant. The discrete gradient operator $\mathbf{M}^{-1}\mathbf{C}p$ evaluates the gradient onto the velocity nodes, in this case at the same locations as it is equal order. This results in the gradient being evaluated as zero everywhere. Adapted from Wilson (2009). 135

6.3 Intra-element fluxes (sold lines) between sub-control volumes inside the element are calculated for both the continuous and discontinuous formulations. With the discontinuous formulation, sub-control volumes are discontinuous between elements as well, where inter-element flux (dashed lines) are calculated. 139

6.4 Numerical experiments to obtain the optimal β scaling parameters in 2D and 3D. Error evolution for the 2D Buckley Leverett a) and 3D b) solution as a function of β. 141

6.5 (A) The coarsest 2D mesh used in the Buckley-Leverett model, (B) saturation maps of the water phase after 0.6 pore volumes injected (PVI) with the continuous DCVFEM and the new discontinuous DCVFEM, respectively. Water is injected at the left-hand boundary displacing oil of equal viscosity in a homogeneous domain. 144

6.6 Comparison of the analytical Bucklet-Leverett solution at distance 0.5 dimensionless units from the inlet boundary to the numerical solution of the new method (discontinuous DCVFEM) using three meshes. Number of elements are in the flow direction, meshes are refined by edge splitting. 144
6.7 a) Convergence of the L_1 error of the water saturation as a function of the mesh element length for the numerical solution of the Buckley-Leverett problem using the continuous DCVFEM, the discontinuous DCVFEM and the new element pair reported discontinuous DCVFEM; b) Convergence of the L_1 error as a function of number of degrees of freedom. 145
6.8 (A) Permeability map and dimensions (dimensionless units) of the embedded fracture model (Salinas et al., 2018a). Permeability contrast of 1×10^4 between the high permeability fracture and surrounding low permeability domain, (B) an example of the unstructured tetrahedral mesh used. 146
6.9 2D slice of the embedded fracture model using the classical CVFEM (left) and the new formulation (right). (A),(B) The control volume dual mesh for each method. The embedded fracture is depicted by the red rectangle. The CVs around the fracture are highlighted in green. In the classical CVFEM discretisation they span the fracture boundary while in the new formulation the sharp interface is retained. Both meshes have the same number of degrees of freedom. (C),(B) saturation maps of the water phase after 0.08 PVI and (E),(F) saturation maps of the water phase after 0.15 PVI. 147
6.10 Normalised mass leakage into the low permeability domain in the embedded fracture model at (A) after 0.08 PVI; (B) after 0.15 PVI. The ratio of velocity:pressure nodes is shown in (A) for the three discretisations. 148
6.11 Channel model meshed using unstructured tetrahedral elements. Three groups of channels are shown with large contrast in permeability (top). High aspect ratio elements are needed to capture the geometry. Examples of distorted elements are highlighted in red (bottom). 150
6.12 Reduction in residual error as a function of the number of iterations for the initial time-step. Solid lines, dashed lines and dotted lines are, respectively, the results on Mesh A, B and C. 151

6.13 Water saturation distribution at various time steps of the channel model using the continuous DCVFEM (left) and the discontinuous DCVFEM (right); vertical exaggeration $\times 4$. Water injection is at the right boundary, production at the left boundary. 152

7.1 Semi-structured meshing. Starting from a coarse mesh represented by a single element in (A), a hierarchy of meshes can be obtained by refine-by-splitting (B) and (C). 157

List of Tables

4.1 Model data 71

5.1 Fixed and DAMO simulations 103
5.2 Material and fluid properties for SI test case 105
5.3 Material and fluid properties for DNAPL test case (Helmig, 1997) 107
5.4 Rock and fluid properties for surface-based models 108

6.1 Model set up. 143

Chapter 1

Introduction

Contents

1.1 Motivation **1**

1.2 Thesis outline **6**

1.1 Motivation

The modelling of multi-phase fluid flow through subsurface reservoirs is of great interest in a wide range of engineering applications, including the exploitation of natural resources (groundwater, hydrocarbons, geothermal), storage of CO_2 and disposal of nuclear waste.

Geological modelling and flow simulation have become instrumental in the understanding and management of these reservoirs. In the petroleum industry, for example, the high cost of field development requires accurate prediction of oil recovery and oil production rates. The volume of unrecovered oil (and to a lesser extent, gas) is strongly correlated to the geological heterogeneity of reservoirs (Fisher, 1991). This inverse correlation between reservoir heterogeneity and final recovery highlights the need for improved reservoir modelling and simulation workflows (Matthäi et al., 2007).

Geological modelling and flow simulation are the basic components of most reservoir evaluation workflows. During the modelling stage, field data (e.g. seismic, well logs and core measurements) and geological analogues are used to build a model of the reservoir. Flow is then simulated, providing the user with a means to understand the complex interactions of the chemical, physical and fluid flow processes occurring in the subsurface. Sufficient understanding of these processes is key if we are to optimise the recovery or storage mechanism.

The major challenge in understanding and predicting reservoir performance is therefore two-fold: realistically modelling the reservoir geology, and accurately simulating the chemical, physical and flow processes. This is far from a trivial problem as the highly heterogeneous nature of geological formations tend to create very complex reservoir architectures and hydraulic conductivities. These heterogeneities exist over a wide range of scales.

The conventional modelling workflow applied throughout the petroleum industry, and incorporated within commercial software packages (e.g. Petrel^{TM}) is described by, amongst others, Bryant and Flint (1993) and Jackson et al. (2013). This workflow has remained essentially static for over two decades (Figure 1.1).

The reservoir volume is first delineated by surfaces that represent the top, base and key bounding faults of the reservoir. This volume is then partitioned into geologically defined zones (e.g. different depositional environments or lithological contrasts), using surfaces that are interpreted from seismic data or correlated between wells. A *fixed, (close to) k-orthogonal* grid is then defined within each reservoir zone, discretising the reservoir volume into a large number (currently up to 1×10^9) of grid cells (Jackson et al., 2015). Facies codes are then assigned to each grid cell using one of a number of geostatistical methods: typically pixel-based methods such as sequential indicator simulation (SIS) or object-based methods such as boolean simulation (Seifert and Jensen, 2000). The aim is to replicate the conceptual geological model developed for each reservoir zone. Once the geomodel is built, the next step is to distribute the petrophysical properties within these reservoir zones.

Models of flow and transport in porous media are based on the continuum theory through the notion of a representative elementary volume (REV). The REV is based on the idea that petrophysical properties, such as porosity and permeability, are constant within a small but representative volume, constituting a natural length scale for modelling porous media. However, multi-phase flow in porous media does not show a clear separation of scale (Moyner and Lie, 2016). Instead, the petrophysical properties and governing equations exhibit multi-scale behaviour.

Petrophysical properties are measured at the scale of a few centimetres, using core experiments or wireline tools (McCarthy, 1995). In contrast, geomodel grid block sizes are typically of the order of 10s of metres. Traditionally, upscaling techniques are used to overcome this issue of scale. To quantify the macroscopic behaviour of flow, upscaling procedures are used to generate *effective* properties at the scale of a grid block (Haldorsen and Damsleth, 1990; Jackson et al., 2003).

Property models are then built, again typically using pixel-based geostatistics to populate the grid blocks.

The availability of vast amounts of seismic, geological and reservoir data have resulted in very large, high resolution geomodels, which can be simulated directly (e.g. GigaPOWERS^{TM}, Dogru et al., 2002; Dogru et al., 2009). However, it is often unfeasible to simulate such models (within a reasonable turnaround time), as the computational cost for simulation are much greater than that to model geological properties. The final step in conventional modelling workflows typically upscales the fine-scale model onto a *coarser-scale* grid ready for conventional reservoir simulation, where the finite-difference-finite-volume method (FDFVM) with the two-point-flux approximation (TPFA) are typically used to solve the governing equations. However, it is recognised that this second upscaling step can lead to a loss in smaller-scale heterogeneities that may have a significant impact on flow (Aarnes et al., 2008; Kippe et al., 2008; Jackson and Muggeridge, 2000).

Despite the ubiquity and longevity of this workflow, the use of k-orthogonal grids limits the complexity of the geometries that can be represented in geological models. Further loss of fidelity occurs during the upscaling step, where the resulting simulation model often fails to honour the original geological concepts or capture key heterogeneities. The geometry of the grid is restricted to be k-orthogonal in most commercial simulators, in order to be consistent with the TPFA. This leads to the use of (close to) k-orthogonal grids such as Cartesian, corner point or 2.5D Voronoi grids which often provide a poor representation of geological heterogeneities (Berge et al., 2019). It is well known that conforming pillar grids to complex geological features such as inclined faults can give large grid-orientation errors (Wu and Parashkevov, 2009). To tackle this, several authors have developed 3D Voronoi grids able to conform to geological and well boundaries (Berge et al., 2019; Klemetsdal et al., 2017; Manzoor et al., 2018). However, for these methods additional care should be taken for more complex structural features (e.g. intersecting faults) where post-processing may be needed (Merland et al., 2014).

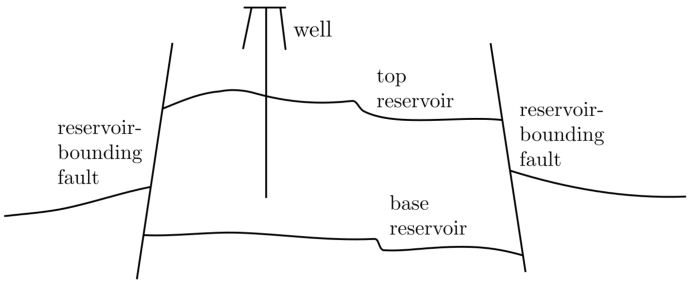
In real engineering applications, engineers often compromise between strictly Cartesian-type grids and representing geological realism. A promising modelling approach is the Cartesian cut cell where solid bodies are cut out of a background Cartesian mesh (Ingram et al., 2003; Mallison et al., 2014) and the related Cut Finite Element methods (CutFEM) (Burman et al., 2015), where the boundary of the domain is represented using, for instance, a level set function.

Another limitation of conventional simulation models is that grid resolution is fixed throughout a given reservoir zone. Multi-phase flow through porous media results in complex interfaces, such as sharp saturation fronts, which move through the domain. Accurate representation of these localised phenomena requires small grid block sizes. This can lead to very large models with superfluous resolution in areas where large grid sizes would suffice.

Adaptive gridding offers a more efficient use of computational effort where the grid is adapted in time and space to provide sufficient spatial resolution where needed. The idea of using adaptive gridding for reservoir simulation is not new, dating back to the early 1980s. One of the first applications was by Heinemann and Von Hantelmann (1983) who described a 2D implementation of dynamic local grid refinement of Cartesian grids using finite-difference methods (FDMs). Later Schmidt and Jacobs (1988) presented an adaptive gridding method with mixed finite elements. However, most early applications created isotropic adapted meshes, primarily through edge splitting. Adaptive gridding/meshing techniques have seen significant advances in the last few years (Alauzet and Loseille, 2016). However, these have been almost exclusively for free flow problems. One of the biggest obstacles to adaptive meshing for porous media flows is how to represent the spatially varying petrophysical properties and how to interpolate those values (especially permeability) from the old to the new mesh. This will be discussed further in Chapter 5, where we describe the dynamic adaptive-mesh optimisation (DAMO) algorithm used in this work.

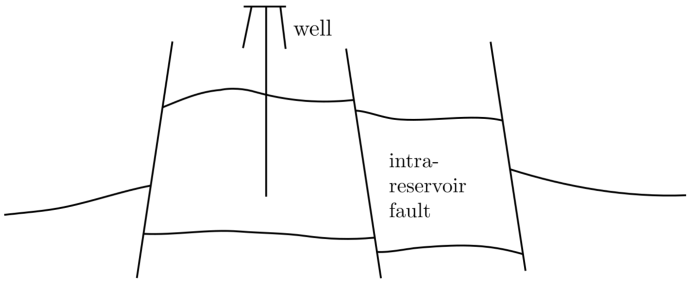
An alternative geological modelling approach, termed surface-based modelling (SBM) (e.g. Denver and Phillips, 1990; Xie et al., 2001; Caumon et al., 2009; Sech et al., 2009; Jackson et al., 2013) uses surfaces to capture all geological heterogeneities, whether structural, stratigraphic, sedimentological or diagenetic, that impact fluid flow. The discrete volumes are bounded by surfaces without reference to a fixed grid.

Control-volume-finite-element methods (CVFEMs) that use non k-orthogonal unstructured meshes (e.g. Huyakorn and Pinder, 1978; Fung et al., 1992; Edwards, 2002; Jackson et al., 2013) can greatly increase the utility of the SBM approach, by enabling the representation of more complex geometries. The method proposed here also integrates a DAMO algorithm (Pain et al., 2001) that optimises the mesh resolution to resolve areas of dynamic interest. DAMO has the potential to greatly increase the computational efficiency of the simulation by focusing resources where they are needed most to increase the solution accuracy.



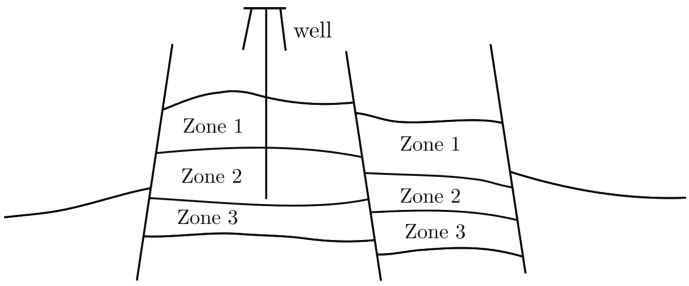
(A)

Step 1. The reservoir volume is defined by surfaces representing the top and base of the reservoir, and surfaces representing key bounding faults. These surfaces are typically interpreted from seismic data.



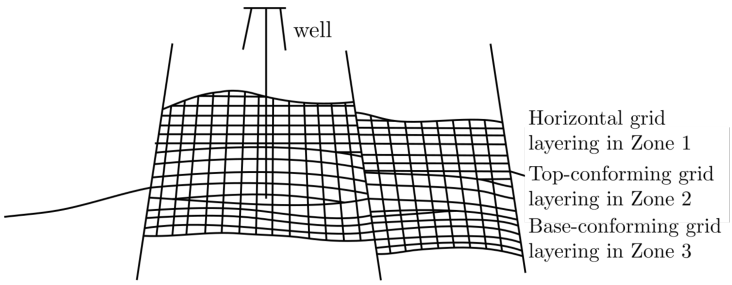
(B)

Step 2. Additional faults within the reservoir are represented by additional surfaces, across which the top and base surfaces may be offset. These surfaces are typically interpreted from seismic data.



(C)

Step 3. The reservoir is subdivided into geologically defined zones by one or more surfaces, which may be offset across the fault surfaces. These surfaces may be interpreted from seismic data, or correlated between wells, and represent key stratigraphic surfaces, facies boundaries, or lithologic contrasts.

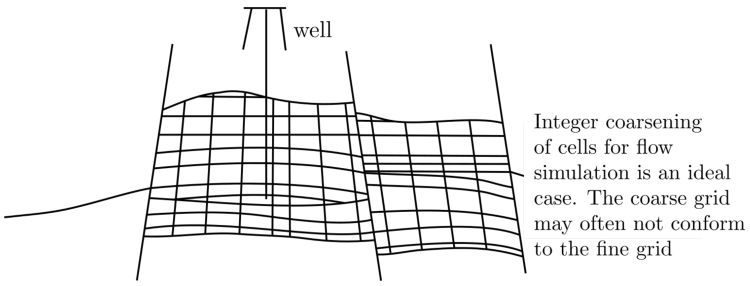


(D)

Step 4. A grid is defined within each reservoir zone. The areal (x-y) resolution of the grid is uniform but the layering (z) resolution and style may vary between zones.

Step 5. Each grid cell is assigned a facies code, typically using a geostatistical method.

Step 6. Each grid cell is assigned a value of porosity and permeability, typically using a geostatistical method within each facies type.



(E)

Step 7. The grid is coarsened for flow simulation, and porosity and permeability values are scaled up from the fine-scale grid cells so each coarse-scale cell is assigned a single value.

FIGURE 1.1: Conventional modelling and simulation workflow (Jackson et al., 2013).

The shortcomings of the conventional modelling and simulation methodologies are widely recognised (Heinemann et al., 1991; Verma and Aziz, 1997; Wu and Parashkevov, 2009; Sech et al., 2009; Jackson et al., 2013; Lie et al., 2018). Substantial developments have been made to tackle these issues, however, more research work is required. The work in this thesis builds upon decades of work by previous authors in order to develop an integrated geological modelling and reservoir simulation methodology.

SBM was first considered in the 90's by Denver and Phillips (1990) and Hu et al. (1994). However, conventional pillar gridding and FDFVM simulation methodologies dependent on the TPFA limited the complexity of geological architectures that could be captured due to the requirement of k-orthogonality. Alternatively, advanced discretisations such as the multi-point-flux approximation (MPFA) (Aavatsmark, 2002; Edwards, 2002; Aavatsmark et al., 2008; Lie et al., 2012) can be used when the grid is distorted away from k-orthogonality.

A large body of work exists on the use of CVFEM in flow simulations, as far back as the late 1970's (e.g Huyakorn and Pinder, 1978; Dalen, 1979; Fung et al., 1992; Edwards, 2002; Geiger et al., 2004; Helmig et al., 2006; Matthäi et al., 2007; Aarnes et al., 2005), and as mentioned earlier, the use of dynamic mesh optimisation is also not new (e.g Schmidt and Jacobs, 1988; Dahle et al., 1990).

1.2 Thesis outline

For improved representation of multi-scale geological heterogeneity and prediction of subsurface flows, modelling workflows must have three important features: (1) accurately capture important multi-scale geological architectures, (2) discretise the flow equations with compatible numerical schemes and (3) allocate computational resources in an efficient manner. Most published contributions have focused on at most two of these features. As a result, there is a lack of a holistic workflow for the meshing and simulation of reservoir models. These contributions are summarised in Chapter 2.

In this work, use a surface-based approach for modelling and simulation that replaces conventional grid-based workflows (Jackson et al., 2013; Jackson et al., 2015). Geological models are constructed using grid-free parametric surfaces (non-uniform b-spline curves and surfaces (NURBS)) that can efficiently and accurately capture geological heterogeneity at multiple scales. Petrophysical properties are modelled as constant within geologically defined domains bounded by surfaces. Models are then discretised using unstructured, non-k-orthogonal

meshes to simulate flow. The mesh is dynamically refined or coarsened within the geological domains, while preserving geological architectures. In Chapter 3 we set out the numerical framework which makes use of a hybrid node-centred CVFEM for simulating multi-phase flow on surface-based models within the Imperial College Finite Element Reservoir SimulaTor (IC-FERST).

In Chapter 4 we test the hypothesis underpinning our application of SBM: that surface bounded volumes can be used to model all heterogeneities of interest. While conventional modelling workflows use surfaces to delineate large scale features such as bounding faults and geological zones (Figure 1.1), with SBM, surfaces are used to bound all heterogeneities of interest. Petrophysical properties are modelled as being uniform within each of these volumes. While the allocation of property values in these volumes may be stochastic in nature, the volumes are homogeneous and remove the cell-to-cell variation in petrophysical properties common with conventional approaches. In Chapter 4 we investigate whether these cell-to-cell heterogeneities are needed to capture important flow characteristics.

The DAMO algorithm used in this work is detailed in Chapter 5. We explore the benefits and difficulties encountered with our approach using both capillary dominated and advection dominated porous media flows. The cost of adapting the mesh is also assessed.

Large variations in material properties such as permeability have profound effects on fluid flow (Dawe et al., 1992; Debbabi et al., 2017a; Debbabi et al., 2017b). These boundaries are well represented using finite element methods; however, when the transport is modelled using node-centred control-volume (CV), jump discontinuities are smeared out across these material interfaces (Salinas et al., 2018a). This is a well known issue of CVFEM and often requires a very fine mesh at material interfaces. To address this issue, a new numerical method is developed in Chapter 6. The new discretisation has a minimal computational overhead over the traditional CVFEM and is simultaneously stable in very challenging meshes.

The thesis closes with the conclusion chapter summarising the contributions and scope for future work.

Chapter 2

Background and Literature review

In geological formations, fluids flow through tiny interconnected pores ranging from the sub-millimetre down to the nanometre scale. In this chapter we review the different approaches used to model multi-phase flows through geological reservoirs. While most of the examples in this thesis come from the petroleum industry, the methods and applications can readily be applied to other disciplines due to the generality of the underlying physics.

We then describe the various approaches to geological modelling used to capture subsurface architectures and numerical schemes used to discretise and solve the governing equations. Conventional modelling workflows ubiquitous in the petroleum industry are shown and their limitations explored. Surface-based modelling, which forms the basis for our new modelling workflow, is introduced.

We finish with adaptive unstructured meshing of subsurface models. Significant advances in mesh adaptivity have been made in the last few decades; however they have focused almost exclusively on free flow problems. The idea of adaptive meshes for flows in geological formations is relevantly new, a novelty that we will to exploit later in this thesis.

Contents

2.1 Modelling multi-phase flow through porous media 10
2.1.1 Pore scale modelling 10
2.1.2 Continuum scale modelling 11
2.2 Numerical schemes 15
2.2.1 Finite-difference method 16
2.2.2 Finite-volume method 18
2.2.3 Finite-element method 20

2.2.4 Multi-scale methods 23
2.2.5 Temporal discretisation 23
2.3 Building geological models 25
2.3.1 Conventional modelling methods 27
2.3.2 Gridding 29
2.3.3 Surface-based modelling 32
2.3.4 Unstructured adaptive meshes 38
2.4 Summary 45

2.1 Modelling multi-phase flow through porous media

The flow of multi-phase fluids through geological formations is of fundamental importance in a wide range of engineering applications. These include, enhanced hydrocarbon recovery, storage of CO_2, remediation of contaminants in groundwater aquifers, enhanced hydrocarbon recovery, nuclear waste storage and heat production from high-enthalpy geothermal systems.

2.1.1 Pore scale modelling

Fluids in subsurface reservoirs flow through tiny interconnected pores from the micron to sub-micron scale (Nelson, 2009). The simultaneous flow of multiple phases in the pore space is a complex process. Rock wettability, geometry and the balance of viscous/capillary/gravity forces all play a role in controlling how fluids are arranged in the pore space. Understanding how fluids move at this scale is crucial to building representative continuum-scale models to describe flow at the reservoir scale. The macroscopic averaged properties can either be measured experimentally or computed via pore-scale models. Using modern computer tomographic methods it is possible to image and distinguish between rock, pore space and fluid phases under static and transient conditions (Blunt, 2017). Assessing the variability in flow properties would require a number of representative samples. However, with specialised and expensive equipment, typically requiring a long time to complete, it is often unfeasible to assess this variability experimentally. Recent work by Mosser et al. (2017) has proposed the use of machine learning algorithms to efficiently reconstruct the solid-void structures of porous media. This is currently an active area of research that

utilises trained neural networks to produce synthetic images that capture the key statistical and morphological characteristics of the parent porous media (Mosser et al., 2017; Mosser et al., 2018; Wang et al., 2018).

At the pore scale, flow is governed by the Navier-Stokes momentum equations, which for an incompressible Newtonian fluid with constant viscosity μ can be written as (Blunt, 2017)

$$\mu\nabla^2\mathbf{v} - \rho\left(\frac{\partial\mathbf{v}}{\partial t} + \mathbf{v}\cdot\nabla\mathbf{v}\right) - \nabla p_\mu + \rho\mathbf{g} = \mathbf{0} \tag{2.1}$$

where $\mathbf{v}$ is the velocity field vector, p_μ is the microscopic fluid pressure, $\mathbf{g}$ is the acceleration due to gravity and ∇ is the divergence operator.

The momentum equation is combined with the continuity equation enforcing conservation of mass

$$\nabla\cdot\mathbf{v} = 0 \tag{2.2}$$

The Navier-Stokes equation, Equation 2.1, combined with the continuity equation, Equation 2.2, form a system of equations. With appropriate boundary conditions these equations can describe the flow of single-phase fluids in the pore space.

2.1.2 Continuum scale modelling

While pore-scale models are practically used in the millimetre to centimetre scale, the problems of interest such as oil recovery, contaminant flows and CO_2 migration must be simulated at the metre to kilometre scale (Aghaei and Piri, 2015). Computational limitations makes the use of pore-scale methods for these problems impossible.

In order to describe the flow at larger scales, an averaged description of the flow is needed. The representative elementary volume (REV) concept forms the basis for macroscopic modelling of flow in porous media. The REV is defined as the minimum volume at which pore-scale fluctuations in flow properties, such as porosity, approach a constant value (Bear, 1972, Figure 2.1a). The behaviour of these property averages are a function of length scale. At the micro- (pore-) scale, flow properties exhibit sharp fluctuations. If the averaging volume is very

small then the property can oscillate depending on whether a greater number of grains or pores are sampled. Taking porosity (ϕ) as an example, the averaging volume can either be within a single grain, in which case $\phi = 0$, or within a void (pore) where $\phi = 1$. Neither value is representative of the whole domain. As the length scale is increased these fluctuations begin to dampen. A a certain length scale, the averaged property is independent of the averaging volume. It is at this length scale that REV is defined.

In homogeneous systems, further increases in length scale do not impact the average value. However, in heterogeneous systems this is not the case: flow properties are a function of location as well as scale. This complicates the simple definition of the REV. Geological porous media in fact have several scales where a REV can be defined. A number of authors have shown how REVs can be established at the lithofacies scale i.e. decimetre scale (Jackson et al., 2013; Nordahl and Ringrose, 2008). Lithofacies are by definition a recognisable subdivision of a stratigraphic unit. It follows that larger REV scales could be defined that capture larger geological features such as parasequences and facies association. To this end, Nordahl and Ringrose (2008) show that the size of the REV is dependent on both the property itself and the correlation length scale of the lithological element. Based on this they proposed a multi-scale REV framework (Figure 2.2), where the natural averaging length scale and measurement length scales can be compared. We will return to this idea in Chapter 4 where we look at how conventional approaches model the spatial discretisation of these flow properties.

Continuity equation

At the micro-scale the continuity equation is derived in the REV where relevant flow parameters are averaged (Bear, 1972). Defining the Darcy velocity, $\mathbf{q} = \phi\mathbf{v}$, as a volume averaged velocity over many pores, and for multi-phase flow the saturation, $S_\alpha = \phi_\alpha/\phi$, as the fraction of the pore space filled by phase α, the multi-phase continuity equation, in differential form reads

$$\phi\frac{\partial S_\alpha}{\partial t} + \nabla \cdot \mathbf{q}_\alpha - \Psi_\alpha = \mathbf{0} \tag{2.3}$$

where Ψ_α is the mass flux due to sources ($\Psi_\alpha > 0$) or sinks ($\Psi_\alpha < 0$).

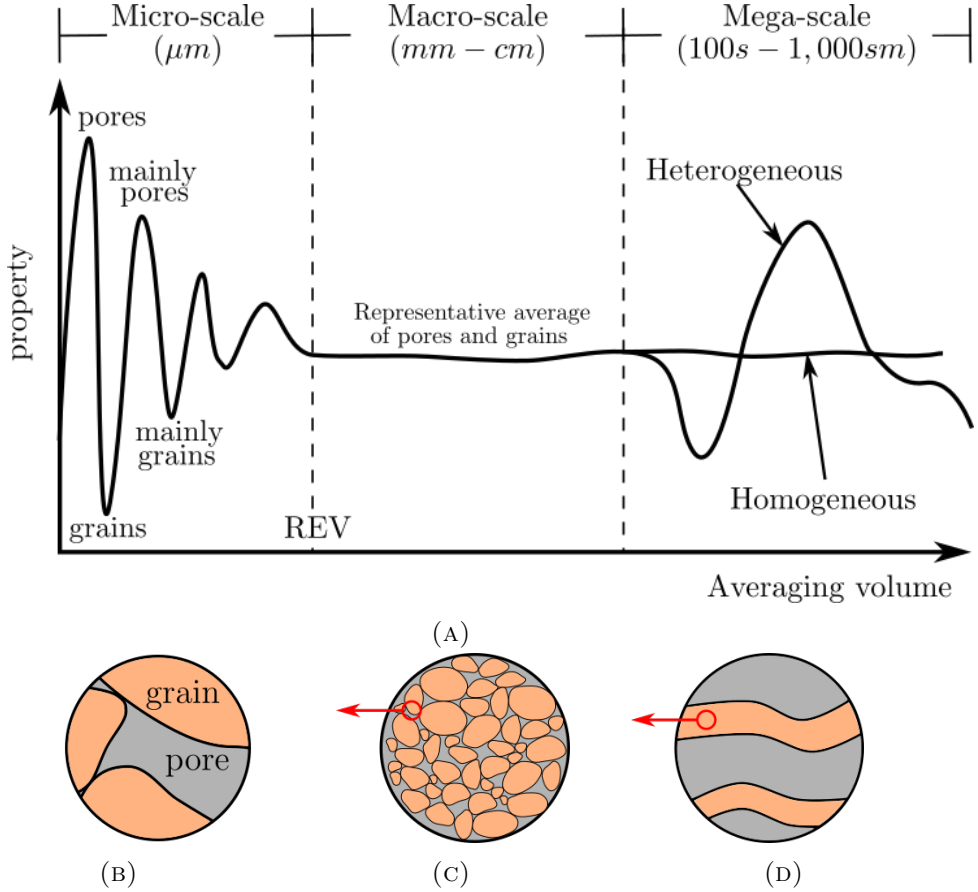


FIGURE 2.1: (A) The REV concept after Bear (1972)), (B) porous media at the micro-scale, large fluctuations in property averages occur as the volume samples more grain or void space (pores), (B) at macro-scale volumes spanning several grains where average property becomes independent from the averaging volume, (C) heterogeneous layered systems can introduce further fluctuations due to spatial variability in flow properties.

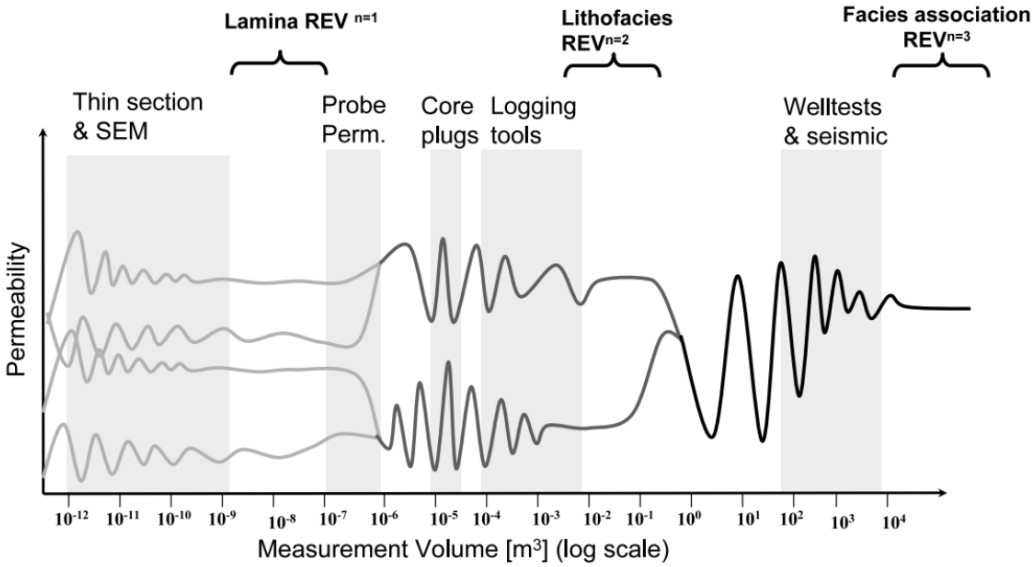


FIGURE 2.2: Conceptual sketch illustrating multi-scales ($n = 1, 2, 3$) of REV related to geological heterogeneities and scales of measurement, from Nordahl and Ringrose (2008)

Darcy's law

The transition from the microscopic to macroscopic scale also creates a new momentum equation. This leads to the introduction of Darcy's law (Nutting, 1930; Wyckoff et al., 1933), which describes the macroscopic flow of a single fluid phase through an ensemble of pores

$$\mathbf{q} = -\frac{\mathbf{K}}{\mu}(\nabla p - \rho \mathbf{g}) \tag{2.4}$$

where $\mathbf{q}$ is the Darcy velocity, p is the *macroscopic* pressure and $\mathbf{K}$ is the permeability tensor.

The permeability ($\mathbf{K}$) is an intrinsic property that is a measure of the resistance provided by the porous medium to fluid flow. It therefore indicates the level of tortuosity and connectivity of the pore space. One of the greatest impacts on permeability is the pore size (or grain size). Different rock types, from sandstone to mudstones have a range of permeability that can span many orders of magnitude.

For multi-phase flow this becomes (Muskat, 1949)

$$\mathbf{q}_\alpha = -\frac{\mathbf{K} k_{r_\alpha}}{\mu_\alpha} \left(\nabla p_\alpha - \rho_\alpha \mathbf{g}\right) \tag{2.5}$$

where k_{r_α} is the relative permeability, a dimensionless quantity that indicates the additional resistance to flow of fluid phase α in the presence of other phases.

2.2 Numerical schemes

Analytical solutions to the coupled system of equations above are available under simplified assumptions and can play a crucial role in validating numerical methods. Analytical solutions can also help interpret experimental results as well as make sense of the complex non-linear interactions of the governing equations. However, the complex geological geometries and time varying boundary conditions cannot be resolved by analytical solutions. For most systems of practical interest the governing equations must be solved numerically. To this end, the equations, computational domain, boundary and initial conditions must be discretised.

The spatial discretisation of the domain and of the governing equations must be coordinated in a way that ensures accurate approximation of the physical processes. Unfortunately, developments of the geological modelling (Section 2.3) and reservoir simulation technologies have often been conducted separately. Conventional modelling approaches typically discretise both the petrophysical properties and flow equations on the same grid, an accidental outcome of the gradual evolution of modelling workflows. Attempting to better represent complex geometries invariably leads to deformed grids unsuitable for conventional simulators. Stair stepping grids have the opposite problem; they fail to accurately capture complex geometries while being suitable for conventional simulators.

In the following section we will summarise the numerical schemes used to solve the governing equations. The continuous functions in the governing equations are approximated by a finite number of discrete values which may be distributed arbitrarily in space. A number of numerical schemes exist for the discretisation of partial differential equations, the most popular of which are

- finite-difference method (FDM), which approximate derivatives by Taylor series expansions;

- finite-volume method (FVM), which are based on the underlying integral conservation law and consider fluxes between control-volumes (CVs); and
- finite-element method (FEM), which reduce the integral equations into a number of simple patches with limited overlapping support.

2.2.1 Finite-difference method

The most predominant numerical method among theoretical/practical applications is based on the finite-difference method (Firoozabadi and Hoteit, 2015). This is largely due to their easy implementation, low computational cost and mass conservative formulations.

Starting with the conservation equation in differential form, the solution domain is partitioned by a grid and the approximate solution of a continuous function $g(x,t)$ at node i is a pointwise approximation

$$g_i(t) \approx g(\mathbf{x}_i, t) \tag{2.6}$$

The differential operators that appear in the governing equations are then approximated by differences, as functions of the pointwise approximations g_i, using the Taylor series expansion. Considering a uniform mesh, a first-order approximation (global error norm of $\mathcal{O}(\Delta x)$) of the first derivative of g in the x direction at node i is given by

$$\left(\frac{\partial g}{\partial x}\right)_i \approx \frac{g_{i+1}(t) - g_i(t)}{\Delta x} \tag{2.7}$$

The mass flux f_{ij} between grid cells $i-j$ involves a number of cells defining a stencil. The simplest scheme generates a 5-point stencil in 2D (or 7-point in 3D), which can be written using the well known concept of transmissibility (Maliska et al., 2007)

$$\begin{aligned} f_{ij} &= \sum_{\alpha} (\lambda_\alpha \mathbf{K})_{ij} \frac{A_{ij}}{h_{ij}} (\Phi_j - \Phi_i)_\alpha \\ &= T_{ij} \sum_{\alpha} \lambda_\alpha (\Phi_j - \Phi_i)_\alpha \end{aligned} \tag{2.8}$$

where $f_{ij} = \mathbf{u}_{ij} \cdot A_{ij}$ is the mass flux between adjacent grid cells i and j in the discretised solution. λ_α represents the phase mobility $\left(\frac{k_{r,\alpha}}{\mu_\alpha}\right)$ and $\Phi_\alpha = p_\alpha - g\rho_\alpha z$

is the phase potential. A_{ij} and h_{ij} are the flow area and grid spacing between points i and j. T_{ij} is transmissibility, defined as

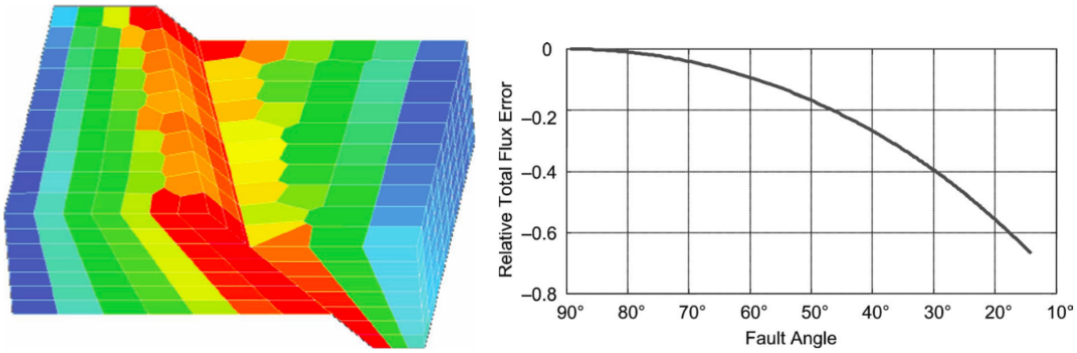
$$T_{ij} = \mathbf{K}_{ij} \frac{A_{ij}}{h_{ij}} \tag{2.9}$$

An important characteristic of the Equation 2.8 is that the flux across the grid cell face between i and j depends solely on the potential gradient in the $i - j$ direction; hence, it is named the two-point-flux approximation (TPFA). The permeability tensor ($\mathbf{K}_{ij}$) is assumed diagonal in this scheme; use of the TPFA with full tensors will result in errors (e.g. Aavatsmark et al., 1994).

This scheme requires that the grid be *k-orthogonal*, where the principal elements of the permeability tensor are aligned with the local coordinate system. On such grids, the flux across a boundary can be well approximated by a factor of the fluid-potential difference between two neighbouring cells. However, for non-orthogonal grids, the flux calculation across a boundary depends on all components of the potential gradient on the boundary (Aziz, 1993). Applying transmissibility, in the current form (Equation 2.9), on non-orthogonal grids therefore leads to errors in the flux evaluation. It is well known that the TPFA is inconsistent with the Darcy flow equation when k-orthogonality is not satisfied (e.g. Jones et al., 1997; Chen et al., 2007; Wu and Parashkevov, 2009; Jackson et al., 2015), i.e. the solution will not converge to the exact answer even with infinite grid refinement.

The dependency of simulation results on the type of grid is called the *grid orientation* effect. Since it was first demonstrated for the 5-point finite difference scheme by Todd et al. (1972), many works have been published on this phenomenon (e.g. Coats et al., 1974; Potempa, 1985; Wu and Parashkevov, 2009). In their paper, Wu and Parashkevov (2009) conducted a detailed analysis of the simulation errors associated with deviated grids. Figure 2.3a shows an example of a 2.5D Voronoi grid representing a fault-block geometry. In generating this grid, non-orthogonality is introduced in vertical cross section. Wu and Parashkevov (2009) concluded that for most practical cases, while errors in horizontal flow are relatively small, the adverse effect of non-orthogonality on vertical flow can be quite significant (Figure 2.3b).

There exists a large body of work devoted to techniques for reducing the grid orientation effect (e.g. Yanosik and McCracken, 1979; Ko and Au, 1979; Quandalle and Besset, 1985; Hurtado et al., 2007; Bagheri and Settari, 2007; Pruess and Bodvarsson, 1983). However there is still no universally accepted remedy.



(A) (B)

FIGURE 2.3: (A) Deviated grid for a sloping fault. Warmer colours indicate greater deviations from orthogonality; (B) Error in total vertical flux vs fault angle for the vertical-flow problem (Wu and Parashkevov, 2009)

Despite the inconsistency of the TPFA method (for non k-orthogonal grids), it is still widely used in most commercial reservoirs. On structured grids these methods are unmatched in efficiency and robustness (Wu and Parashkevov, 2009). However, one of the major disadvantages of the FDM is that they are restricted to simple geometries (Ferziger and Perić, 2002).

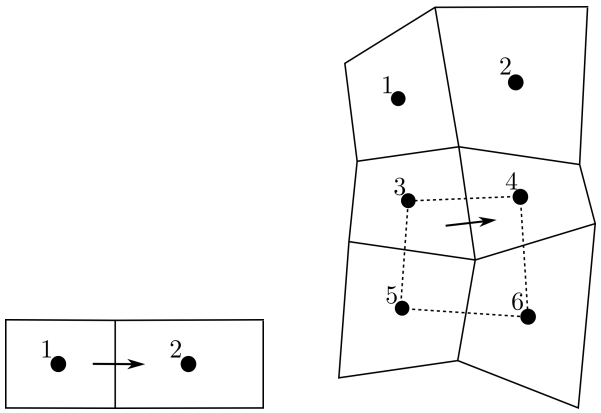
2.2.2 Finite-volume method

In the FVM, the solution domain is subdivided into a finite number of non-overlapping CVs. Mass conservation is then established over the CV by approximating the flux across control volume boundaries. Using the integral form of the conservation equation, the flux through a CV surface (Γ) is given by

$$f_\alpha = -\int_\Gamma (\lambda_\alpha \mathbf{K} \nabla \Phi_\alpha) \cdot \mathbf{n} ds \tag{2.10}$$

where $\mathbf{n}$ is the unit outward normal vector to the control boundary surface (Γ).

Traditionally, the TPFA was used to approximate the flux across each face of the CVs but, as explained above, this scheme is inconsistent with the Darcy equation for non-k-orthogonal grids. To obtain a more consistent scheme, a more advanced discretisation is needed, termed the multi-point-flux approximation (MPFA) (e.g. Aavatsmark et al., 1994; Edwards and Rogers, 1998; Verma and Aziz, 1997; Lie et al., 2012). These methods are based on an extended stencil that uses more than two grid cells to approximate the interface fluxes. Following the pioneering work by the early authors, a whole class of MPFA methods now exist (Aavatsmark, 2002).



(A) (B)

FIGURE 2.4: (A) TPFA in one dimension (1D); (B) MPFA in 2D; the interaction region is depicted by the dashed lines and centred around vertices to form a dual grid. Modified from Juanes et al. (2005).

In the MPFA method, the fluxes are computed across half-edges inside an interaction region (Figure 2.4b). The flux across an interface i can be approximated by

$$f_{i,\alpha} = \sum_{j \in J} T_{ij} \Phi_j \tag{2.11}$$

where J is the set of grid cells that surround interface i. This naturally leads to a 9-point stencil in 2D, and 27-point stencil in 3D (Verma and Aziz, 1997).

MPFA methods have received a lot of attention due to their easy incorporation into legacy reservoir simulation codes and is undergoing further development as a result (e.g. Eigestad et al., 2002; Mlacnik et al., 2006; Njifenjou and Nguena, 2008; Chen et al., 2007; Friis and Edwards, 2011; Ahmed et al., 2015; Lie et al., 2012). However the MPFA comes with a large computational cost due to the larger stencil employed. MPFA schemes are also not guaranteed to produce symmetric and positive-definite discrete systems.

While in principle the FVM can accommodate any type of grid, most commercial simulators using FVM employ the TPFA (Manchuk and Deutsch, 2009) and are therefore limited to using k-orthogonal grids. Although corner point grids do offer greater flexibility over Cartesian grids they are not guaranteed to be k-orthogonal. It is also difficult to align corner point grids with complex well trajectories, overturned surfaces and intersecting faults (Farmer, 2005).

2.2.3 Finite-element method

Similar to the FVM, FEM discretise the domain into a number of discrete volumes (or finite elements). These elements are generally unstructured and usually triangles or quadrilaterals in 2D, while tetrahedral and hexahedral elements are most often employed in 3D (Zienkiewicz et al., 2013). Unlike finite-difference-finite-volume method (FDFVM) with the TPFA, FEM in general do not suffer from the k-orthogonal grid restriction. Unknown variables and gradients are approximated using known element interpolation functions. This allows variables such as saturation and concentration to vary within a given element which helps to reduce numerical dispersion. A key step in the implementation of FEMs is the use of reference elements on which a set of interpolation functions is constructed once and mapped to each element in a mesh (Elman et al., 2006). FEMs are therefore only suitable when mapping between physical and reference elements are well-defined.

Standard finite element methods are based on the Galerkin formulation of weighted residuals (Donea and Huerta, 2003) and have gained wide popularity in several branches of engineering science, especially in civil and aeronautical engineering (Zienkiewicz et al., 2013). The success of the standard Galerkin finite-element (SG) methods in these fields drew many researchers to apply these techniques in fluid dynamics. However, for multi-phase flow in porous media, it was quickly apparent that the solution was unstable, producing oscillations near sharp fronts and converging to the wrong solution (Spivak et al., 1975).

One variant developed to avoid this issue is the fully coupled upwind-weighted finite-element method (FUG) (Huyakorn and Pinder, 1978; Dalen, 1979; Forsyth, 1991; Helmig and Huber, 1998; Bastian and Helmig, 1999). A comparative study by Helmig and Huber (1998) showed that the SG method failed to produce accurate results due to non-physical mobility terms which leads to incorrect fluxes. Accurate results were obtained using the FUG method where the mobility is fully upstream weighted, equal to the value of the mobility at the upstream node.

A drawback of FUG methods is that the algebraic solution matrices are often poorly conditioned and not diagonally dominant, making the use of fast matrix solvers difficult (Geiger et al., 2004). Another draw back is that, in general, the SG and FUG methods are not locally mass conservative.

A need for local mass conservative formulations lead to the development of hybrid control-volume-finite-element method (CVFEM). The CVFEM were first

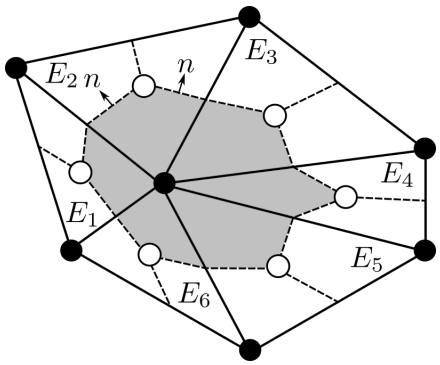


FIGURE 2.5: A control volume in the triangular finite element mesh. Filled circles represent element vertices, empty circles are the centroids.

proposed by Baliga and Patankar (1980) and Prakash (1987) for Navier-Stokes equations. The CVFEM are similar in some respects to FVM with MPFA, in that the integral conservation equations are applied to polygonal CVs, built around each node of the triangular mesh. The dual control volume mesh is formed from the finite element mesh by joining the centroids of the elements and the element edge midpoints (Figure 2.5).

The geometric flexibility of the finite element method is therefore retained and combined with the local mass conservation property of the finite volume method. In the CVFEM, the pressure field is solved for using the standard Galerkin method and the saturation is solved on the CV. For traditional CVFEM the fluid velocity is obtained by element-wise differentiation of the pressure field and Darcy's law.

A 1D representation is shown in Figure 2.6 for a $P0_{DG}P1$ element pair, where pressure varies linearly across each element (P1) and velocity is constant within each element and is discontinuous between elements ($P0_{DG}$). The piecewise constant derivative of the pressure field across each finite-element (FE) leads to a discontinuous velocity field across two adjacent elements. The dual CV mesh is then used to provide a flux continuity across the boundaries of adjacent CVs (Geiger et al., 2004).

Material properties such as porosity and permeability are defined FE-wise. While this ensures accurate representation of the complex geological heterogeneities, the node-centred CVs smear out saturation solutions across material boundaries (Edwards, 2006; Nick and Matthäi, 2011; Abushaikha et al., 2015; Salinas et al., 2018a).

It is well known, although rarely reported in the literature that solving the

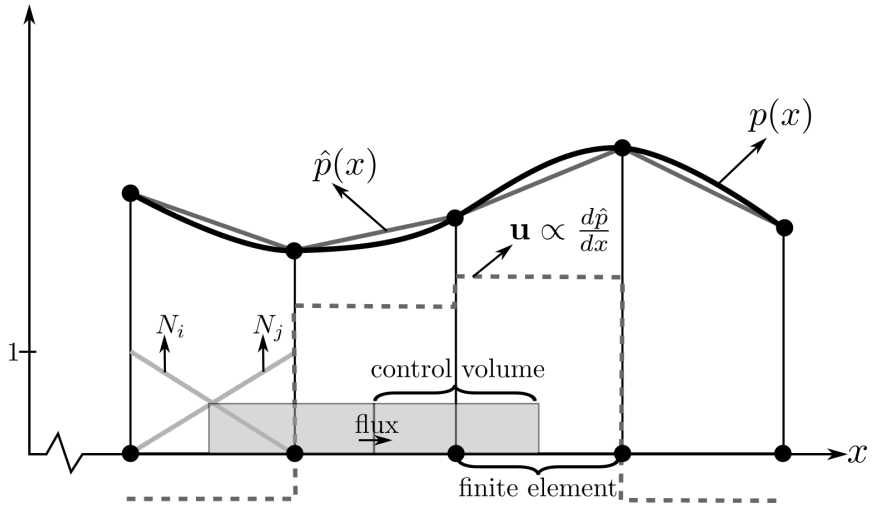


FIGURE 2.6: Traditional CVFEM, here for a P0$_{DG}$P1 element pair. The exact solution $p(x)$ is approximated by $\hat{p}(x)$ using the piecewise linear interpolation functions N_i and N_j of each finite element. The piecewise constant derivative of this solution $\frac{d\hat{p}}{dx}$ is proportional to the Darcy velocity but discontinuous across two neighbouring finite elements. Flux continuity is achieved across boundaries of adjacent CV built around the nodes of the finite element. Integration of the fluxes over the surface of the CVs ensures mass conservation. Adapted from Paluszny et al. (2007).

pressure equation with the CVFEM presents difficulties in poor quality meshes. Pressure solutions may fail to converge, or be physically unrealistic (Salinas et al., 2017b). The derivative of the pressure solution is approximated by derivatives of the interpolation functions. However, when element angles are large, determining accurate derivatives of these interpolation functions can be challenging. This can lead to the pressure solution failing to converge (Salinas et al., 2017b). In this work, we will introduce a variant of the CVFEM termed the double control-volume-finite-element method (DCVFEM) in Chapter 3 and later extend it to address the issue of saturation smearing in Chapter 6.

It is clear, therefore, that in the standard CVFEM, the velocity representation is one order less accurate than the pressure representation. In contrast to this the mixed FEM (Chen and Hou, 2002; Hoteit and Firoozabadi, 2006; Durlofsky and Chien, 1993; Aarnes et al., 2006) allow for the simultaneous computation of the pressure and its gradient. The pressure and velocity are therefore of the same order of accuracy. Moreover, mixed FEMs yield continuous velocities across element edges and are thus locally conservative, similar to the FVMs (Durlofsky and Chien, 1993; Wheeler and Yotov, 2006). A computational drawback of standard mixed methods is the need to solve an algebraic system of saddle point type (Helmig, 1997). However, hybridisation of the mixed finite element

formulation was demonstrated to overcome this deficiency. In the mixed-hybrid FEM Lagrangian multipliers are used to obtain a linear system of equations with more favourable properties (Huber and Helmig, 1999; Moortgat and Firoozabadi, 2016; Farhloul and Fortin, 2002; Arnold and Brezzi, 1985; Aarnes et al., 2008; Farthing et al., 2003).

The approach used in this thesis and described in Chapter 3 achieves the same objective of higher order velocities using an alternative method. In essence, we use a FE interpolation of the CV solutions to provide, potentially, very high order velocity approximations (Gomes et al., 2017).

2.2.4 Multi-scale methods

As discussed earlier, typically an upscaling approach is used to develop effective flow properties such as permeability from an underlying fine-scale 'geo-model' to a 'simulation model', where any of the above discretisation schemes can be used. However, upscaling techniques are generally process dependent and limited to certain boundary conditions (Durlofsky et al., 1997). As an alternative to traditional upscaling techniques, so-called multi-scale discretisation methods were developed (Hou and Wu, 1997; Klemetsdal et al., 2018; Aarnes et al., 2008; Tchelepi et al., 2007). These methods are based on hierarchical grids with basis functions used to map between associated cells of the fine-scale and coarse-scale grids. Similar to traditional upscaling techniques, these basis functions are found by solving a localised flow problem (Moyner and Lie, 2016). However, unlike the effective properties of traditional upscaling methods, these basis functions are able to account for the local fine-scale variations.

Multi-scale methods therefore have the potential to capture small-scale effects on large-scale models and accelerate flow simulations. However, most multi-scale methods have been implemented on simple grid geometries (e.g. Lunati and Jenny, 2006; Wang et al., 2014). Significant developments have been made over the past decade, the methods are now applicable to grids with general polyhedral geometry and unstructured topology (e.g. tetrahedral, prismatic, hexahedral elements) (Moyner and Lie, 2016; Lie et al., 2017a).

2.2.5 Temporal discretisation

As well as the spatial discretisation, the governing equations require temporal discretisation. As unsteady flows are parabolic in time, the solution at a particular time step depends solely on previous time steps. The semi-discrete

method is the most commonly used technique; where the time derivatives are replaced by finite-differences. Various time stepping schemes exist to advance the solution depending on the time at which the equation is discretised.

The simplest scheme is the explicit forward Euler where the solution at t^{n+1} is obtained directly from known values at time t^n. The explicit scheme is easy to implement and parallelise. However, for stability reasons, explicit methods can impose severe restrictions on the time step size, especially for strongly varying velocity and/or mesh size, i.e. the Courant–Friedrichs–Lewy (CFL) condition (Courant et al., 1967).

Alternatively, the implicit backward Euler scheme involves iteratively solving a system of equations to obtain the solution at t^{n+1}. Although more expensive to implement, the implicit method is stable for large Courant numbers (Donea and Huerta, 2003).

The level of 'implicitness' can be tuned with the implicitness parameter θ ($0 \leq \theta \leq 1$). The forward Euler is obtained for $\theta = 0$ and the backward Euler is returned when $\theta = 1$. Both explicit and implicit methods are first-order; an alternative is the second-order Crank-Nicolson method, where $\theta = 0.5$, often used due to its simple two-level time stepping approach and unconditional stability (Donea and Huerta, 2003).

Implicit schemes include the fully implicit (FI) method and sequential implicit methods. In the FI method the coupled system is solved simultaneously and is unconditionally stable, allowing for large time steps. However, FI methods can be more expensive and more dissipative than explicit methods. On the other hand sequential methods decouple pressure and saturation equations which adds flexibility in the discretisation and solution methodology.

A classical sequential method is the implicit pressure explicit saturation (IMPES) scheme, such as the streamline methods (e.g. Blunt et al., 1996), where the pressure equation is solved implicitly while the saturation equations are treated explicitly. However, for highly heterogeneous models, the CFL stability condition, of the explicit update, may lead to severe time step restrictions in smooth regions away from sharp fronts that make it less efficient than implicit methods (Blunt and Rubin, 1992). This can be further exacerbated when non-linearity is introduced; when, for example, high capillary effects are included.

To improve stability of sequential implicit methods Watts (1986) proposed an approach treating both pressure and saturation implicitly, allowing much larger time steps than those achieved with IMPES. However, the semi-implicit

treatment of velocity still caused stability and mass conservation issues (Aziz and Settari, 1979; Watts, 1986). Recently the sequential fully implicit (SFI) method was proposed by Jenny et al. (2006) to address these issues. The SFI method implicitly solves the pressure and saturation equations iteratively before advancing to the next time step. The method provides a consistent, mass conservative solution (Jiang and Tchelepi, 2019).

Another approach is an adaptively implicit scheme, which smoothly switches from Crank-Nicolson ($\theta = 0.5$) to backward Euler (Blunt and Rubin, 1992; Gomes et al., 2008), which we use in this thesis. The level of implicitness is controlled by a local stability criterion based on a total variation diminishing scheme (Kuzmin, 2010). This ensures that the scheme is able to resolve shock fronts with a first-order, non-oscillatory method while higher-order time accuracy are used in smooth regions (Gomes et al., 2017).

2.3 Building geological models

The mathematical formulation describing flow through porous media requires adequate boundary and initial conditions and a description of the subsurface geometry. Creating the representative geological architecture and the attributable properties such as rock and fluid properties is known as *geological modelling*.

Many of the geological heterogeneities of interest, have complex geometries that occur over a broad range of length scales, from the scale of the pore to the depositional system (Figure 2.7). These heterogeneities can be attributed to the complex sedimentary, diagenetic and tectonic events that created them. Accurate prediction of reservoir performance depends on the accurate estimation of the subsurface material properties and fluid distribution.

Understanding of reservoir architectures has improved considerably with the advent of advanced imaging techniques and characterisation of reservoir analogues (Jia et al., 2012). The combination of higher resolution reservoir data and computing power has lead to a step change in reservoir characterisation capabilities. The most significant advances have been in seismic acquisition and processing. The introduction of 3D seismic, increasingly high resolution data and improved processing capabilities have allowed geoscientists to interpret seismic data faster and more accurately.

Unfortunately, many of the important geological heterogeneities are below seismic resolution, and detailed core and well-log data typically sample less than 0.1% of

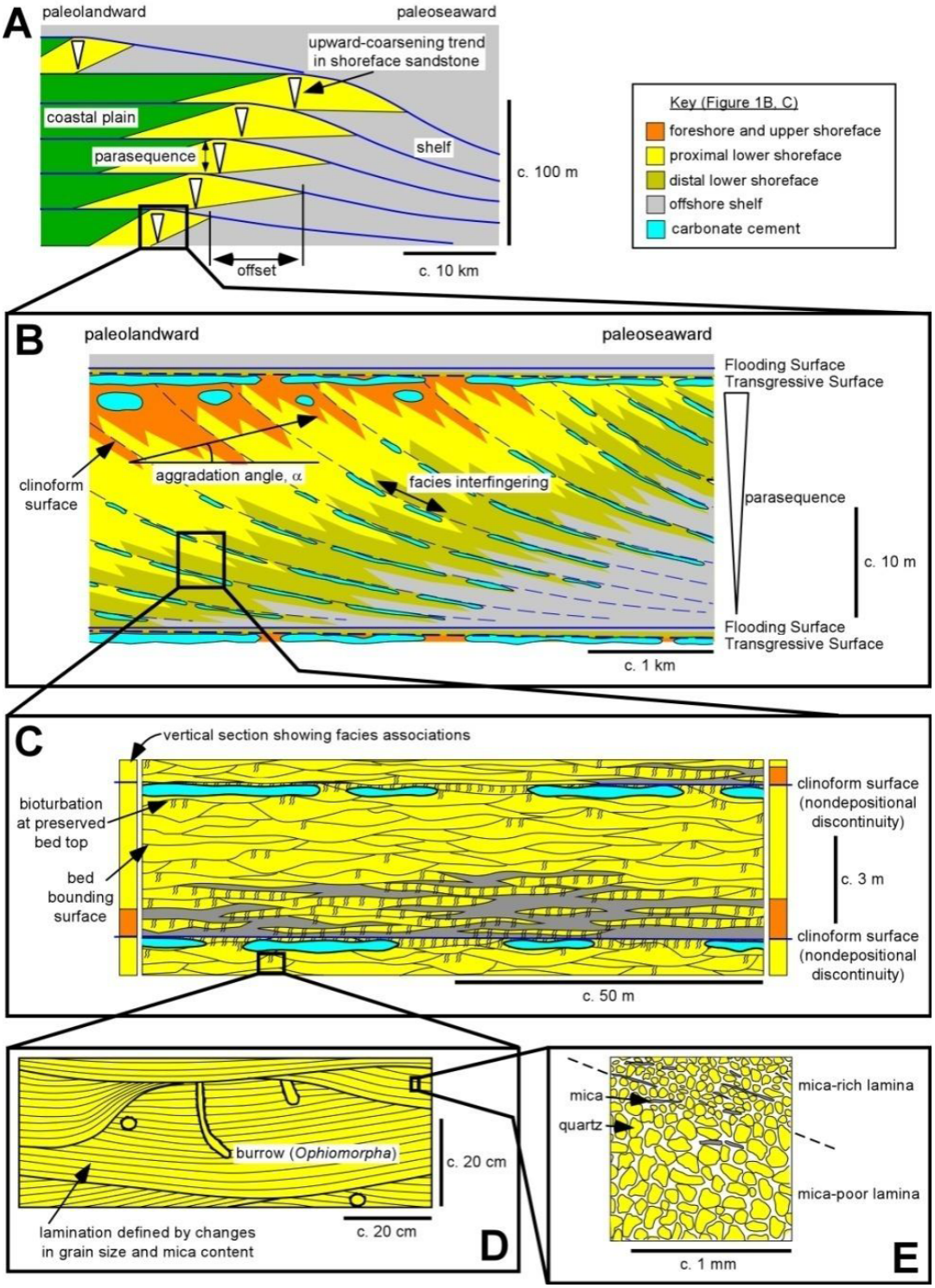


FIGURE 2.7: Heterogeneity at various scales within a generic shoreface-shelf sandstone reservoir (Sech et al., 2009).

the reservoir volume (Carlson, 2003). With the limited resolution and extent of field data, the major challenge in subsurface modelling is how to utilise geological analogues, seismic and sparse well data, to develop a conceptual description of the subsurface. Stochastic models provide a means to represent the spatial uncertainty through the construction of multiple realisations, constrained to data (Haldorsen and Damsleth, 1990; Damsleth et al., 1992; Pyrcz and Deutsch, 2014). A wide variety of geostatistical methodologies have been developed to achieve this dual goal.

2.3.1 Conventional modelling methods

Conventional modelling workflows generally follow the steps outlined in Figure 1.1. Reservoir volumes and large scale reservoir zones are typically delineated using surfaces. Once these large scale structures have been defined, 3D reservoir grids are typically built on which facies and petrophysical properties are assigned.

Facies are one of the most important features that determine the quality of the reservoir, capturing the depositional setting, lithofacies and architecture (Pyrcz and Deutsch, 2014). Facies modelling techniques can be categorised into four main groups: (1) Pixel-based models (variogram-based and multi-point statistics), (2) object-based models, (3) rule-based methods and 4) process-based models. These methods can be placed in a continuum of modelling techniques (Pyrcz et al., 2015; Figure 2.8). Pixel-based methods are typically easier to condition but lack the ability to honour sedimentological concepts such as connectivity and ordering relations, while process-based models can produce highly realistic heterogeneity but are unconditional to local observations.

Variogram-based approaches describe the spatial correlation of two points in space as a function of the distance between them. These methods have gained popularity due to their simplicity, stability and unlimited ability to condition to well data and trends (Pyrcz et al., 2015). Variogram-based models include, among others, sequential indicator simulations (SISIM; Journel and Huijbregts, 1978) and truncated Gaussian simulations (TGSIM; MacDonald et al., 1998). However, variogram methods are limited to two-point statistics (Deutsch and Journel, 1998) and cannot look at spatial continuity with more than two locations; as a result, complex geological structures are not well modelled (Pyrcz et al., 2005).

More recently Strebelle (2002) extended pixel-based methods to use multiple-point statistics (MPS), which is capable of capturing more complex spatial

features as well as ordering relations. With MPS, the spatial heterogeneity is inferred from a training image depicting the geometric features expected in the subsurface. The statistics inferred from the training images (TIs) are used to build models conditioned to well data. The TI is a conceptual image of the expected spatial structure, often built using measured data. Current MPS methods are designed for stationary TIs; however reservoir properties typically exhibit non-stationary features such as trends. It is therefore difficult to create realistic TIs with no trend or the trends removed, although some progress has been made to address the problem of non-stationarity (e.g. Hu and Chugunova, 2008).

Object-based or boolean techniques were pioneered by Haldorsen and Lake (1984), Stoyan et al. (1987), and Haldorsen and Damsleth (1990) with the aim of constructing more geologically realistic stochastic models. Unlike the pixel-based method, object-based algorithms assign whole objects or sets of cells, each having a well defined geometry, to groups of cells or points in space. Object models have been shown to be very efficient at reproducing repetitive geological structures, such as fluvial channels and deltaic lobes (e.g. Shmaryan and Deutsch, 1999; Seifert and Jensen, 2000; Damsleth et al., 1992; Deutsch and Wang, 1996). However, difficulty in parameterisation of these object shapes means that these methods lack flexibility and must often be done by trial and error (Allard et al., 2004). This is particularly true when conditioning to dense data or when exhaustive information such as seismic data needs to be integrated.

A first principles approach to geological modelling is the process-based method. In this approach models are built by simulating the fundamental physics of the sedimentation and depositional processes (Tetzlaff and Harbaugh, 1989; Martinez and Harbaugh, 1993). An understanding of the physics of surface water flow and sediment transport as well as basin formation and filling mechanisms allows process-based models to produce realistic geometries not limited by prior assumptions of spatial structure (Michael et al., 2010). However, initial and boundary conditions for these models are highly uncertain. The high computational costs of process-based models also limit the consideration of multiple realisations. Despite the promise of more realistic model realisations process, models are rarely used for flow prediction models, due to their limited ability to condition to seismic and well data (Reza et al., 2006; Michael et al., 2010).

Alternative *rule-based* approaches such as surface-based methods play an important role in expanding the capability of geostatistical modelling approaches.

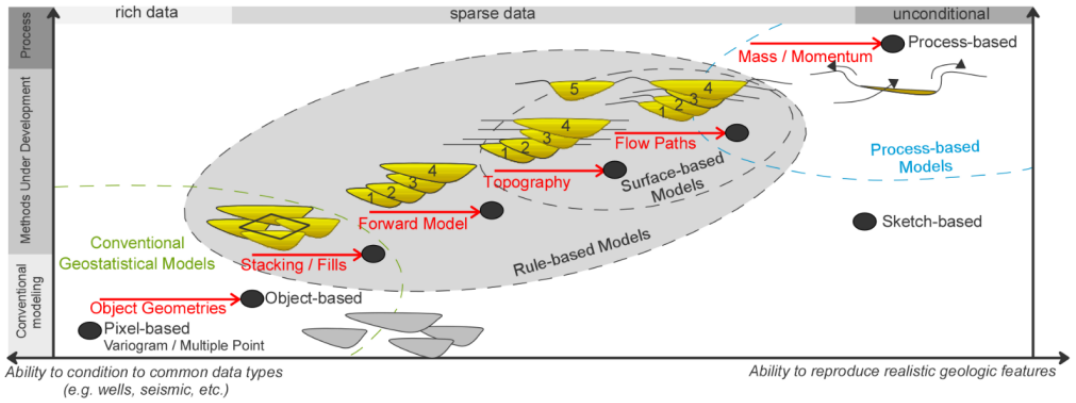


FIGURE 2.8: Various modelling methodologies on a continuum from the conventional geostatistical models (far left) which are able to incorporate data directly to the unconditional (no data integration) process-based models (far right), from Pyrcz et al. (2015).

Unlike process-based models, rule-based models do not aim to simulate sediment transport, deposition and erosion; rather, they mimic the geometries created by the geological process at varying scale and detail (Pyrcz et al., 2015). Surface-based models are intuitive and able to accurately reproduce idealised geometries, honouring facies continuity with relative ease. Our modelling approach make use of this approach, which is explained in more detail later in this thesis.

2.3.2 Gridding

Regardless of the method used to guide the representation of heterogeneity, and the data used to constrain the uncertainties in geometry or property distribution, discretised models are needed for numerical calculations. Pixel- and object-based approaches are built upon predefined grids. With a predefined grid, the spatial resolution and structural complexity of the model is limited by the resolution of the underlying grid. One approach to handling fine-scale heterogeneity is to simply use a very large number of k-orthogonal grid blocks. With increased computational capabilities, there has been an effort to develop massively parallel simulators that allow simulations on models that contain 100s millions to billions of grids cells (e.g. GigaPowers^{TM}; Dogru et al., 2002; Dogru et al., 2009). There are several issues with this approach. First, intensive computational resources are required to populate such large grid-based models with petrophysical properties. Second, significant memory requirements are needed to store, visualise and manipulate these models. Third, flow simulating these large models requires substantial computational overhead. All these issues reduce the flexibility of

modellers to test various geological concepts and reservoir engineers to explore production/storage strategies.

Various gridding approaches have been developed which attempt to produce discretised geomodels that retain the geometry of the geology, while suppressing the number of distorted, non-k-orthogonal cells which are harmful to conventional flow simulations or require multi-point flux approximation for flow computation.

The simplest gridding type is the Cartesian grid or *regular grid* which subdivides the reservoir into *sugar-cube* cells. Such grids fulfil the orthogonality constraint of conventional numerical schemes but typically provide a very poor representation of geological features without the use of a large number of grid cells. For structurally complex environments, it is important to take into account discontinuities such as faults, which are not aligned with the principle axis. On Cartesian grids this can only be achieved by approximating inclined faults using staircase-like steps (Figure 2.10a). This ensures the resulting grid is k-orthogonal and therefore compatible with conventional flow simulators.

Corner point grids are the most common grid type in commercial workflows (e.g. RMS^{TM}, PETREL^{TM}). They are sometimes referred to as *pillar grids* (Ponting, 1992). Corner point grids offer greater flexibility to describe more complex geometries (structural or stratigraphic) than Cartesian grids. Grid cells are defined by their corner nodes enabling the model to conform to the geometry of the reservoir, but at the expense of grid orthogonality, both in plan view and cross section (Figure 2.10b). Pillars form a skeletal framework which runs through the full thickness of the domain and the same resolution (i.e. number of pillars) is imposed across all layers. Areal grid resolution is therefore fixed, leading to large features being over-resolved while small features are under-resolved or even omitted (Jacquemyn et al., 2018). When modelling non-vertical faults, pillar gridding can cause large volume distortions and non-orthogonality problems. Structurally complex interpretations can be difficult or impossible to represent, such as vertically intersecting and listric faults, where modifications of the fault geometries, simplifications and/or removal from the model are often required. Pillar grids also make many common geological features impossible to represent, such as non-monotonic surfaces associated with recumbent folds and injected bodies (Jacquemyn et al., 2018).

Semi-unstructured grids such as perpendicular bisector (PEBI) grids or 2.5D Voronoi grids are a more flexible gridding approach than corner point grids and are commonly applied in commercial reservoir simulators. First introduced to petroleum engineering by Heinemann et al. (1991), PEBI grids make it possible

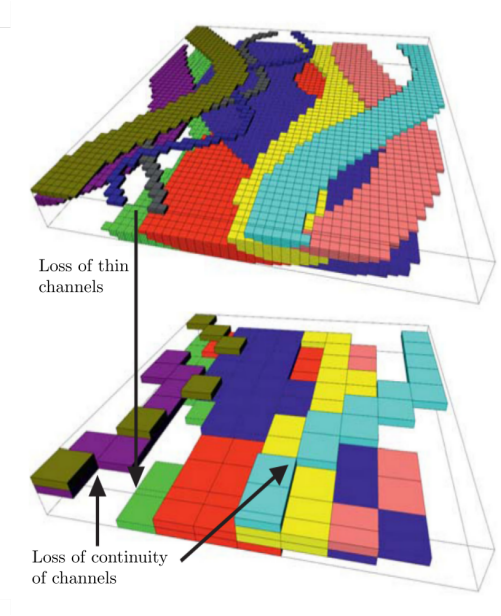
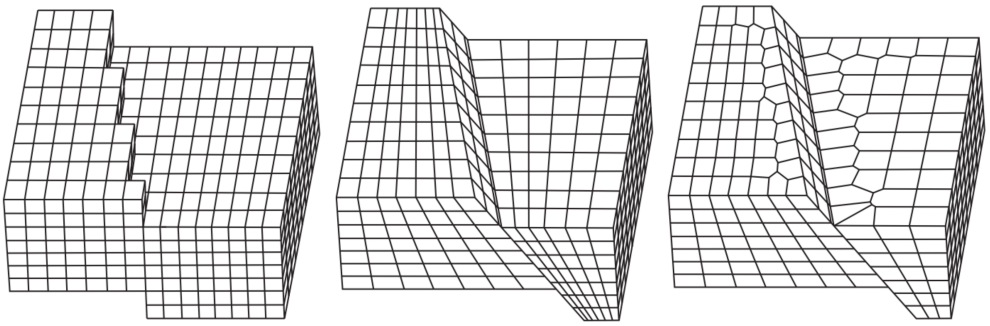


FIGURE 2.9: Loss of fidelity in grid-based models, adapted from Jackson et al., 2015

to capture complex boundaries such as faults with a grid which is (approximately) k-orthogonal in plan view, helping to reduce grid orientation errors (Verma and Aziz, 1997). However, non-orthogonality is still present in cross section (Figure 2.10c). Although less problematic than corner point grids, generating 2.5D Voronoi grids remains a challenge, especially for complex geology and sharp material interfaces. Another major drawback is that Voronoi cells cannot be represented in parametric space (Paluszny et al., 2007), which reduces its utility in an integrated FE code.

Some modern modelling tools (SKUA-GOCAD^{TM}, JewelSuite^{TM}) have attempted to bridge the gap between geomodels and flow simulation models, without simplifying the structural interpretation. With SKUA models, a paramterisation of the subsurface is built which provides a representation for both geo- and flow simulation models. For flow simulations SKUA geomodels are typically mapped onto Cartesian grids, where stratigraphic and structural features are captured in a stair-stepped fashion (Gringarten et al., 2009). This allows flow simulation to be done using conventional finite-difference (FD) TPFA simulators. However, as these methods still rely on k-orthogonal grids, they suffer from the same drawbacks discussed earlier.



(A) (B) (C)

FIGURE 2.10: Modelling of a faulted domain using (A) Cartesian grid; (B) Corner-point grid; (C) 2.5-D perpendicular-bisector grid (PEBI) (Jackson et al., 2015). In (A), the grid is orthogonal, the dipping-fault has to be approximated by staircase-like steps. In (B), the fault geometry is better captured but is non-orthogonal both in plan view and cross section. In (C), the grid is approximately k-orthogonal in plan view but still non-orthogonal in cross section.

2.3.3 Surface-based modelling

Surface-based geological modelling (SBM) is an alternative modelling approach to grid-based methods, where all geological heterogeneity that impacts flow is represented explicitly by their bounding surfaces (Xie et al., 2001; Pyrcz et al., 2005; Zhang et al., 2009; Sech et al., 2009; Caumon et al., 2009; Graham et al., 2015a; Graham et al., 2015b; Jacquemyn et al., 2018). A key difference to other modelling approaches is that all heterogeneities of interest are built without reference to an underlying grid.

Xie et al. (2001) suggested modelling the reservoir as a collection of separate sedimentary units, where each unit is stochastically generated. Sech et al. (2009) showed how surfaces can be deterministically interpolated between control lines or points. These individual units are later assembled, maintaining the realistic heterogeneity patterns. Any structural, stratigraphic, sedimentological and diagenetic heterogeneities can be incorporated into the reservoir model using a hierarchy of surfaces. The resulting facies and property models are able to reproduce realistic geological architectures. Surfaces can be ranked into a hierarchy of surfaces based on their interactions. Surfaces representing erosion, for example, can be created by one surface truncating another (Figure 2.11; Jackson et al., 2013).

Bertoncello et al. (2013) considered deposition of lobes in a turbidite reservoir (Figure 2.12). A set of parametrised lobe templates (Figure 2.12b) are stacked

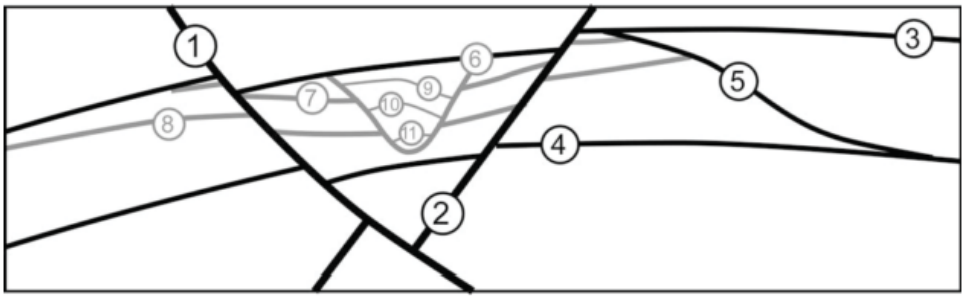


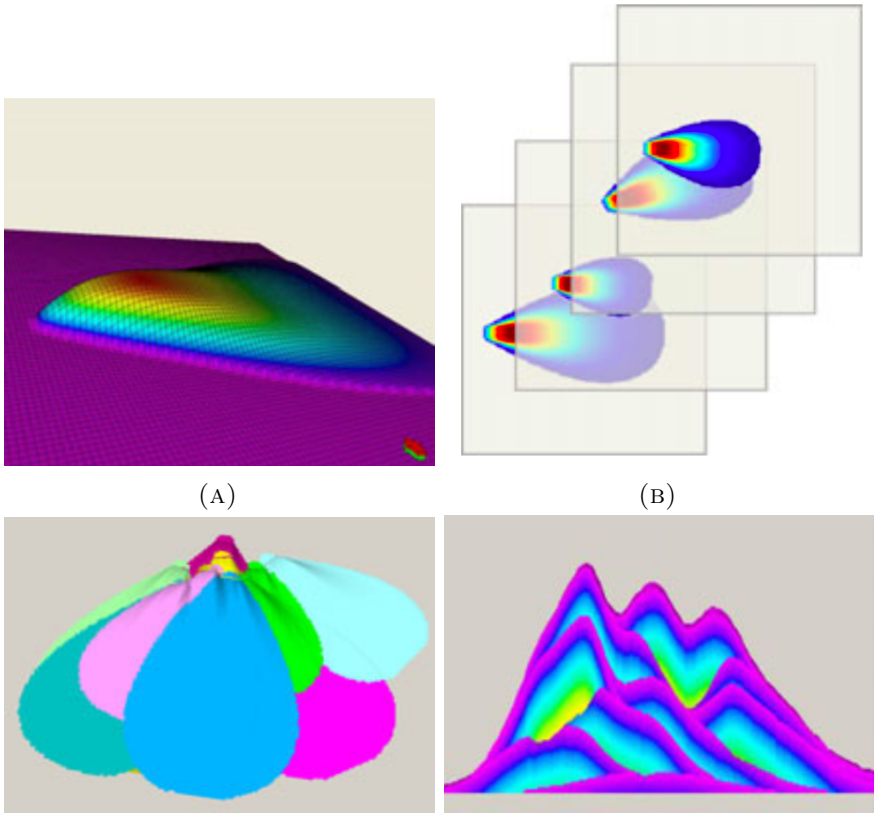
FIGURE 2.11: A generic example of the rule-based surface-hierarchy. Structural surfaces (1-2) are at the top of the hierarchy as they truncate all other surfaces. Stratigraphic surfaces (3-5) are at the next in the hierarchy, truncated by structural surfaces but truncate facies boundaries. Sedimentological surfaces (6-11) are the base of the hierarchy (Jackson et al., 2015).

sequentially upon a basal surface representing the sea-floor topography (Figure 2.12a). The final model, Figures 2.12c - 2.12d accounts for the series of complex depositional and erosional events.

There are a number of surface-based modelling (SBM) methods and codes that have been developed in the past few years although, so far, no single, integrated software package is available. While previous studies have shown that SBMs are able to accurately reproduce realistic geological geometries, most only developed static models. For the study of dynamic effects, the geometry needs to be discretised and one of a variety of numerical methods can be used for flow simulation.

White and coworkers (White and Barton, 1999; Willis and White, 2000; White et al., 2004) developed a surface-based approach to modelling 2D outcrop exposures. Similar works by Sech et al. (2009) and Graham et al. (2015a) extended the SBM approach to 3D models of shallow marine reservoirs. Surfaces were traced over photomontages of the outcrop exposures and later used to constrain corner grids for flow simulations, i.e. *stratigraphic corner point* gridding. Grid blocks at pinch outs (where two surfaces coincide) generate degenerate quadrilateral cells with one edge having negligible thickness (Figure 2.13). The adjacent grid cells with negligible thickness are marked as inactive and vertical continuity is preserved using non-neighbour connections (Figure 2.13).

The modelling approach described above proved to be successful for the shallow dipping stratigraphic surfaces, termed clinoforms ($< 1°$) modelled by Sech et al. (2009) and White et al. (2004) (Figure 2.14a), where grid deviations from k-orthogonality were small. However, the steeper dipping clinoforms modelled



(A) (B)

(C) (D)

FIGURE 2.12: Overview of the surface-based modelling approach adopted by Bertoncello et al. (2013). (A) Basal surface, representing the sea floor; (B) thickness events extracted from process-based model (Michael et al., 2010); (C) Top view of final model; (D) Cross section of final geological model. Colours represent different domains enclosed by surfaces.

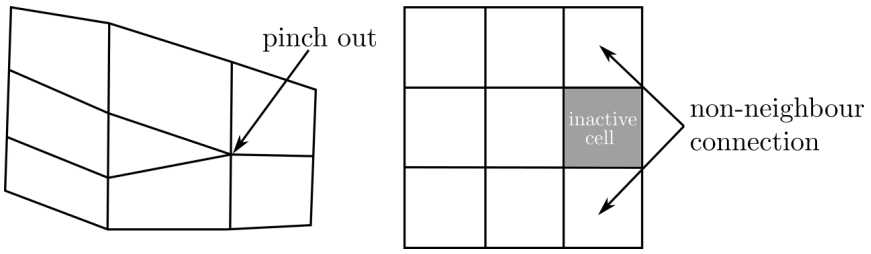


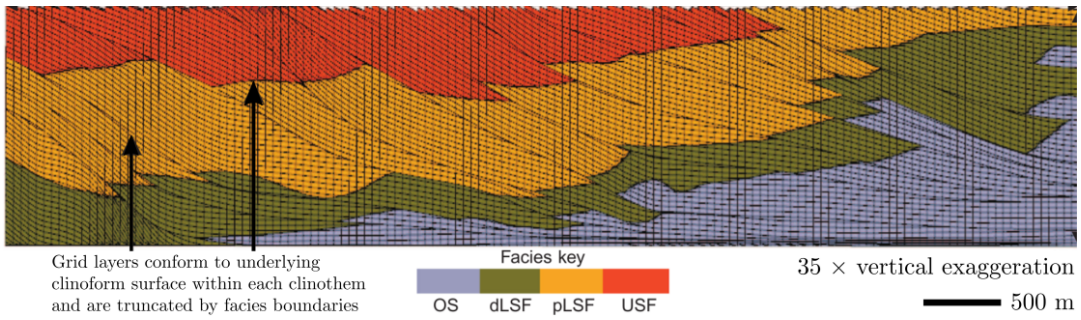
FIGURE 2.13: Surfaces govern the architecture of the grid using stratigraphic corner point gridding. Where geological zones pinch out, degenerate quadrilateral cells are generated. To avoid no flow barriers and to maintain vertical continuity non-neighbour connections are used. Adapted from White and Barton (1999).

by Graham et al. (2015a) (up to 5°; Figure 2.14b) caused severe deviations and manual editing, including the addition of a dummy grid layer to reduce bypass in degenerate cells, was needed to avoid large numerical errors compromising the accuracy of the flow simulations.

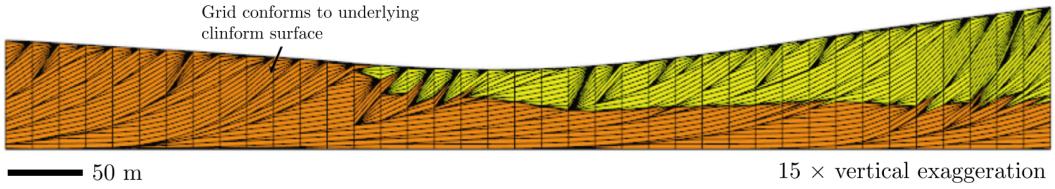
These numerical artefacts were illustrated in the work by Massart et al. (2016). A surface-based modelling approach was developed to determine the effective flow properties of heterolithic, cross-bedded tidal sandstones (Figure 2.15a). A corner point gridding scheme was used to discretise the model. The computed permeability is shown in Figure 2.15b. The variations in effective permeability are obscured by the large errors due to numerical artefacts caused by non-k-orthogonality, introduced by stratigraphic corner point gridding.

The previous studies, and others have shown that the use of stratigraphic corner point grids is not ideal for complex geometries. Next generation flow simulators have started moving away from TPFA numerical schemes (Edwards, 2002; Paluszny et al., 2007; Jackson et al., 2015), which have, hitherto, restricted simulation models to (close to) k-orthogonal grids. The next stage should be to find a robust way of building 3D surface-based geological models suitable for next generation flow simulations.

Jackson et al. (2015) proposed a surface-based modelling and reservoir simulation workflow that replaces conventional grid-based methods. All geological heterogeneity of interest that affects the spatial distribution of petrophysical properties is represented by surface-bounded volumes. These discrete volumes (geological domains) are modelled as internally homogeneous. The petrophysical properties within these domains are determined from core- or log-derived data, or alternatively upscaled from fine-scale models that capture smaller-scale heterogeneities below that of the modelled surfaces.



(A)

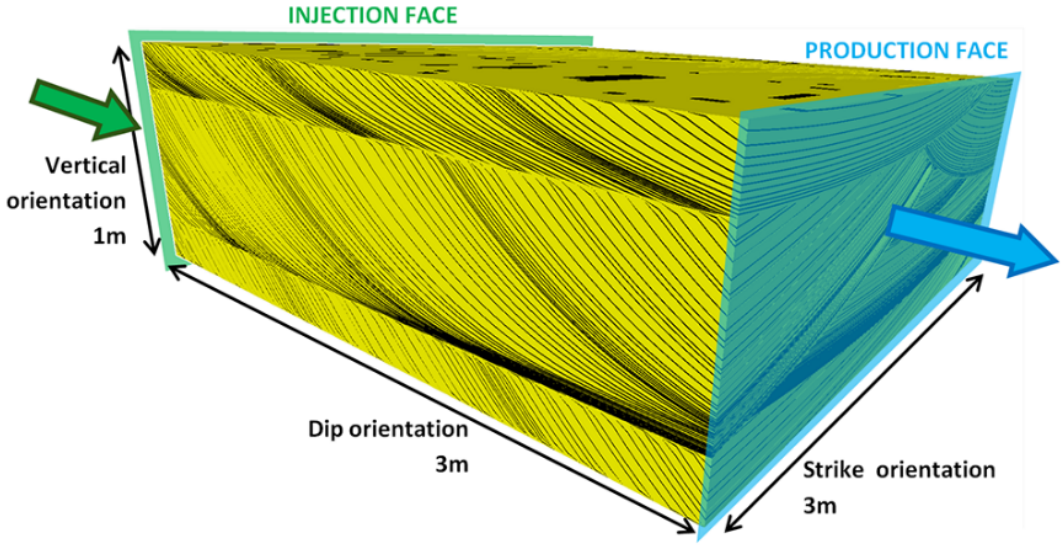


(B)

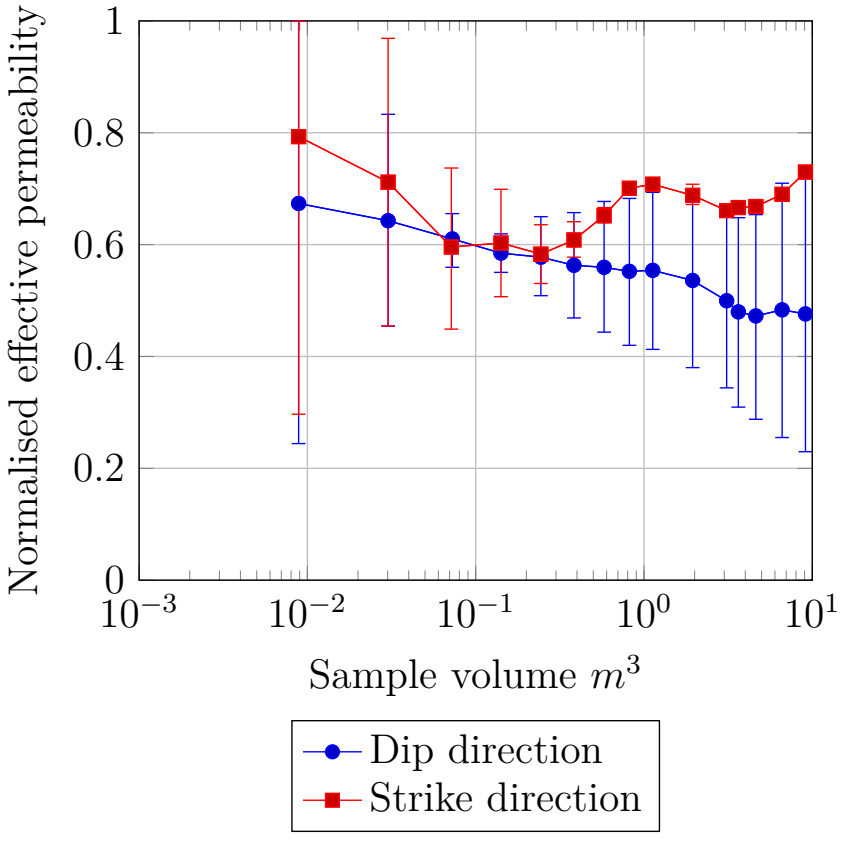
FIGURE 2.14: 2D section through surface-based models showing the corner gridding scheme used to preserve geological architecture of the dipping surfaces. (A) from Sech et al. (2009), here clinoform dips were $< 1°$, (B) from Graham et al. (2015a) where clinoform dips were up to $5°$

The SBM approach is grid-free, synonymous with the Boundary REPresentation format (BREP) frequently used in computer aided design (CAD) for engineering applications (Farin, 2002). With BREP, volume shapes are approximated by their outer boundary, delineated by bounding surfaces. Several methods exist to represent these bounding surfaces including non-smooth polyhedral (triangulated) surfaces and smooth non-uniform b-spline curves and surfaces (NURBS). While triangulated surfaces are easier to condition to well data, they are scale dependent and it is often difficult to construct complex intersecting geometries in 3D (Matthäi et al., 2005b). Alternatively, NURBS are an efficient and flexible way to represent curves and surfaces using local control (Farin, 2002). With local control points i.e. control points that only affect their immediate neighbours, multiple boundaries can be matched. This allows complex, non-monotonic shapes to be represented (e.g. Figure 2.16).

Another major advantage of this approach is that it is grid-free i.e. individual elements are modelled as volumes bounded by parametric surfaces without employing an underlying grid. This allows a flow simulation grid to be defined only when needed; the geological model resolution is therefore not limited by the grid resolution.



(A)



(B)

FIGURE 2.15: a) Cross-bedded sandstones model used to investigate the sensitivity of effective permeability to sample volume, b) effective permeability in the dip and strike directions as a function of sample volume, normalised by the permeability of equivalent sandstone only sample. The error bars indicate the numerical artefacts introduced by cornerpoint gridding. From Massart et al. (2016).

However, a disadvantage of NURBS is that they are based on a tensor-product structure leading to unavoidable gaps when expressing the intersection of two NURBS surfaces (Sederberg et al., 2008). In the workflow adopted in this thesis the 'watertightness' of the model is therefore only guaranteed at the meshing stage. Significant research effort has recently been placed to solve the inconsistencies in geometric and simulation models, known as design and analysis models in the CAD literature. This has lead to the concept of isogeometric analysis (IGA), to more closely integrate design and analysis models (Johannessen, 2014). Several authors have proposed spline technologies for this purpose including locally refined (LR) B-splines by Dokken et al. (2013). However, their discussion is out of the scope of this thesis.p

As alluded to earlier, in their methodology, Jackson et al. (2015) incorporate the property model directly into their geometrical model. When surfaces generated are insufficient to represent all the heterogeneity of interest, additional surfaces can be added. The combination of surfaces at lower hierarchical levels allows the model to incorporate heterogeneity at multiple scales. Figure 2.17 demonstrates this concept on a channelised sand body. The base of the channel represents the highest hierarchical level and a further five surfaces are inserted that terminate against the base surface, representing a channel lag and lateral accretion surfaces.

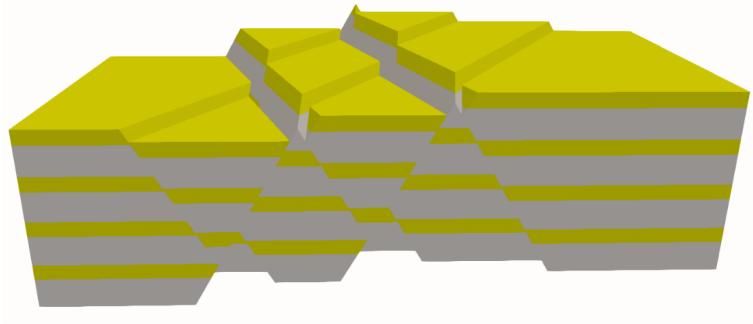
While NURBS surface-based models representing complex, geological geometries may be discretised using conventional k-orthogonal grids, the refinement required to track boundaries not aligned with the principle axis might be prohibitive. The workflow advocated by Jacquemyn et al. (2018) and used in this thesis will be to use unstructured tetrahedral meshes (Melnikova et al., 2016) to discretise the surfaces and the volumes defined by the surfaces.

2.3.4 Unstructured adaptive meshes

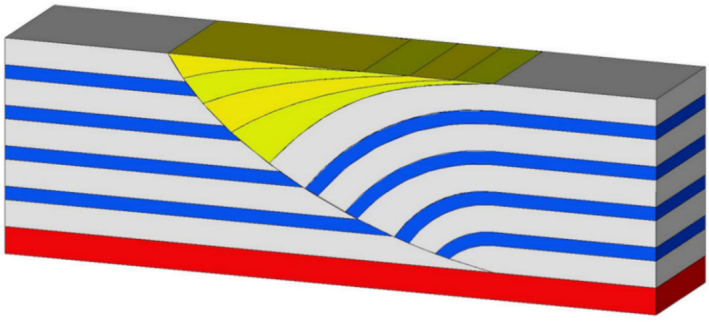
One of the major challenges in flow simulating surface-based models is how to discretise the model, while maintaining important geological features. Unstructured, non-k-orthogonal meshes offer several advantages: one of the most important is the accurate representation of complex geometries, both in plan view and cross-section. These grids can be designed to align with fault surfaces, stratigraphic layers, facies boundaries and other important interfaces such as impermeable shale boundaries or 'super k' (very high permeability) zones. Faults and fractures are especially challenging to model as they exhibit large aspect ratios, layer displacement and complex cross-cutting relationships (Paluszny et al., 2007). Figure 2.18 is an example of a complex fractured fold, observed at



(A)



(B)



(C)

FIGURE 2.16: Common structural heterogeneities represented using NURBS. (A) Faulted recumbent fold, (B) Conjugate normal fault sets, C) Listric growth fault. Adapted from Jacquemyn et al. (2018).

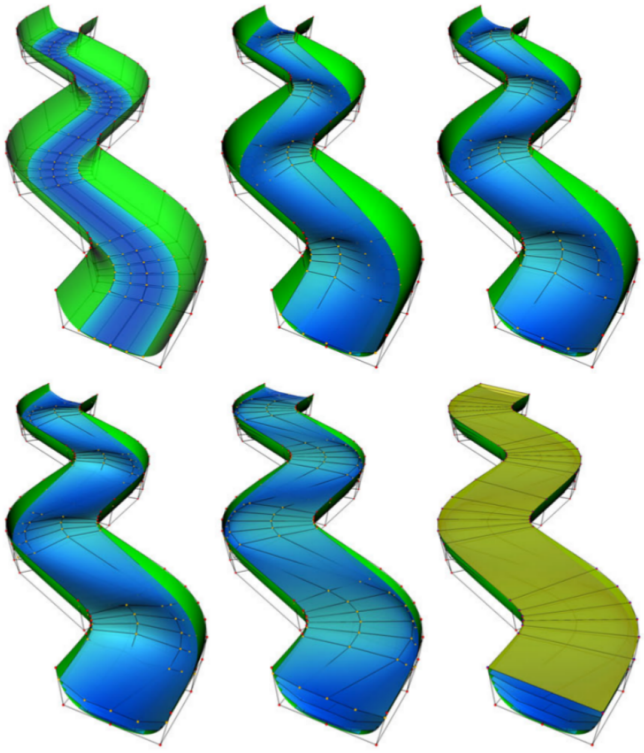
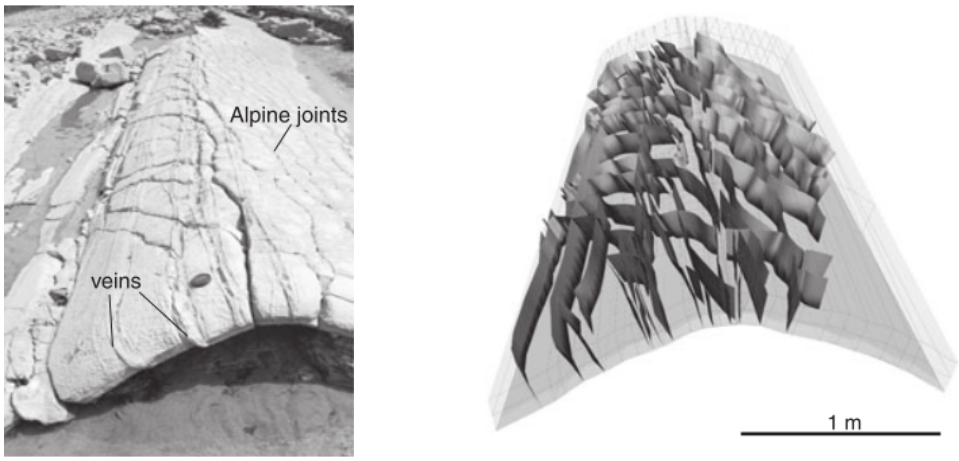


FIGURE 2.17: Multiple surfaces representing internal heterogeneity within a channelised body (Jacquemyn et al., 2018).

an outcrop on the southern margin of the Bristol Channel coast. The fractures have variable apertures and range in size over many orders of magnitude. This would be impossible to represent using conventional (close to) k-orthogonal grids without using a prohibitively large number of grid cells.

While unstructured, non-k-orthogonal meshes offer greater flexibility in preserving complex geometries, they do come at an additional computational cost. Unlike structured meshes, grid points on an unstructured mesh can be arbitrarily connected to their neighbours; determining the location of neighbour cells is no longer trivial. However, this does also allow the resolution of the mesh to vary arbitrarily from one region to another.

Conventional reservoir simulation models employ the same *fixed*, coarse grid resolution throughout a given reservoir zone. In many production scenarios, higher grid resolution may be needed in zones of dynamic interest, based on the curvature of the solution fields of interest such as pressure or saturation (Schmidt and Jacobs, 1988; Trangenstein, 2002; Mostaghimi et al., 2015; Jackson et al., 2015). For example, during waterflooding in an oil reservoir, i.e. the displacement of oil by the injection of water, a large saturation gradient exists at the water front (shock front), which can be resolved more accurately with a



(A) (B)

FIGURE 2.18: Geological complexity of an outcrop of Liassic limestone on the southern Bristol Channel coast, UK. (A) Photograph of a small-scale fold structure intersected by carbonate veins crosscut by later Alpine joints; (B) NURBS CAD model of the same structure with the numerous intersection curves and acute intersection angles between fractures. (Paluszny et al., 2007)

higher resolution grid. Behind the front (rarefaction) the change in saturation is gradual and a lower resolution grid may be sufficient.

Computational memory and run time limit the maximum number of elements that can be used in flow simulations. It is therefore impractical to simulate high resolution models. Previous work in other areas of computational fluid dynamics (CFD) have shown that a more efficient use of computational resources, without losing the accuracy of the numerical solution, is to employ adaptive meshing techniques to refine the grid where necessary (Alauzet and Loseille, 2016).

Several ways of modifying a mesh exist (Figure 2.19):

1. splitting or amalgamating existing elements and changing the connectivity of the nodes – called h-adaptivity (Berger and Colella, 1989),

2. removing vertices to make new elements while retaining the same connectivity – r-adaptivity (Budd et al., 2009), and

3. varying the polynomial order of the approximation – called p-adaptivity (Babuska and Suri, 1994)

Mesh adaptivity is not a new idea. Significant progress has been made on automatic mesh generation, error estimates and anisotropic meshes over the

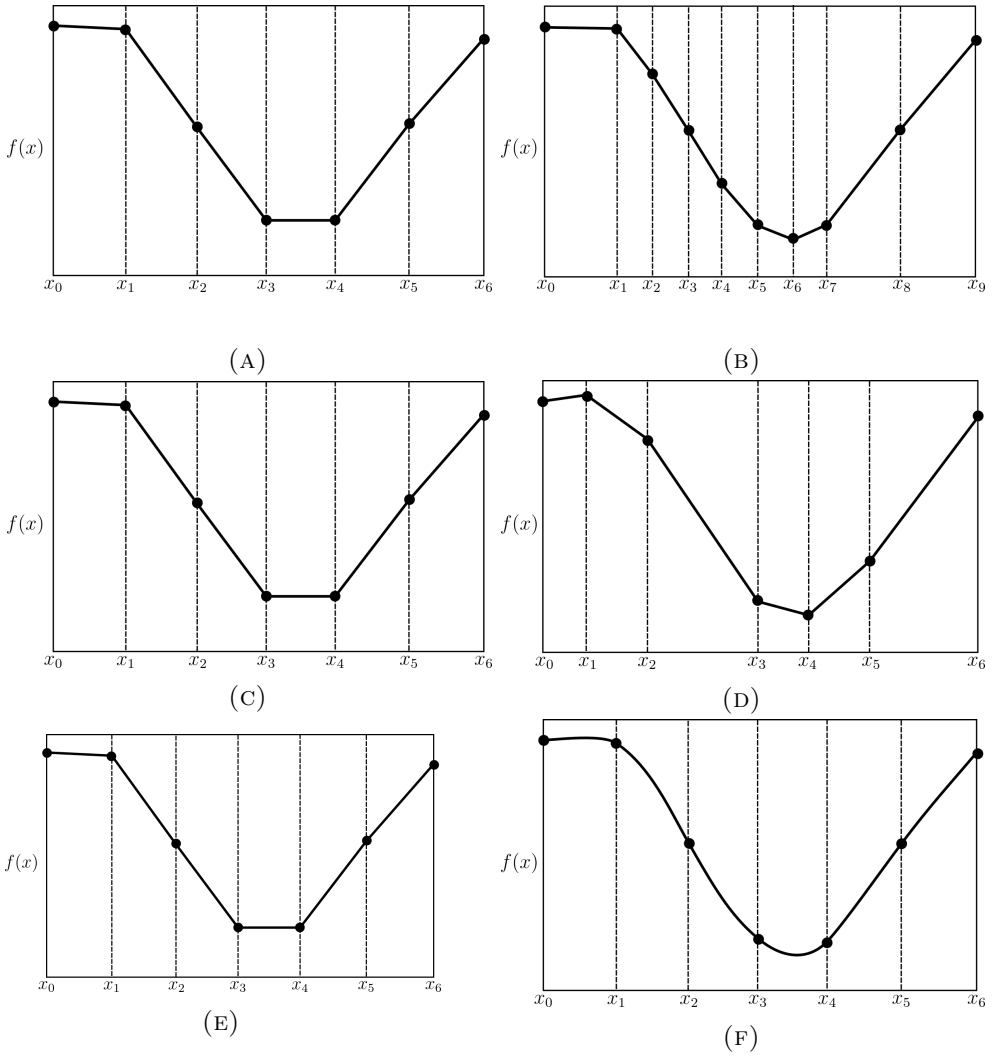


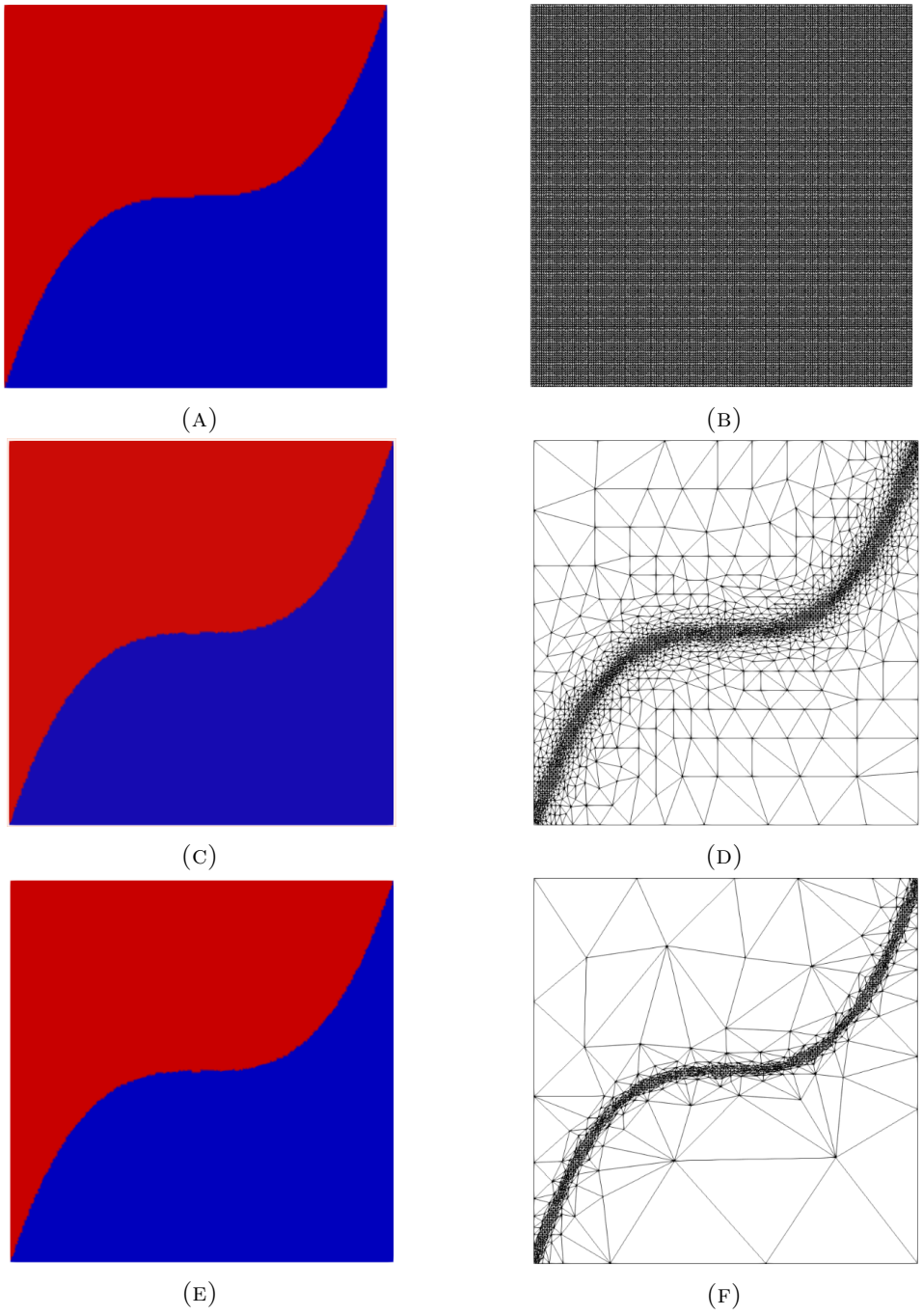
FIGURE 2.19: Common procedures for adapting a mesh. (A) to (B) local refinement or coarsening of the mesh is known as *h-adaptivity*, (C) to (D) relocating or moving mesh points is known as *r-adaptivity* and (E) to (F) locally varying the polynomial basis functions is known as *p-adaptivity*.

past two decades (Alauzet and Loseille, 2016). However, these have been almost exclusively for free flow problems.

Two basic strategies exist for mesh adaptivity in porous media flows: adaptive mesh refinement (AMR) and dynamic mesh optimisation (DMO). AMR methods are based on the ideas of Berger and Oliger (1984) using a sequence of nested, logically rectangular meshes, adding or removing cells to achieve the desired level of accuracy (Quandalle and Besset, 1985; Ewing et al., 1989; Heinemann and Von Hantelmann, 1983). These methods have been shown to be particularly effective on focusing resolution around fixed singular points such as wells. However, early applications ignored geological heterogeneities, limiting the utility of such techniques (e.g. Schmidt and Jacobs, 1988; Dahle et al., 1990; Dahle et al., 1992). Recent applications have used only h-adaptive methods and Cartesian or corner point grids (e.g. Batenburg and Bosch, 2011; Hoang and Kleppe, 2006; Pau et al., 2012).

In dynamic mesh optimisation, the mesh evolves in order to cluster grid points where high resolution is needed (Hiester et al., 2011; Jackson et al., 2015; Mostaghimi et al., 2015). This requires a mapping of material properties from old to new meshes. However, on conventional cell-based grids, material properties need to be re-scaled (up-, down- or cross-scaled) to the adapted mesh. Wolff et al. (2013) started with a fine-scale geological model and upscaled material properties to a range of predefined coarse grid cells prior to flow simulation. However, this a-priori approach compromises the flexibility of adaptivity; it is impossible to know what the mesh geometry should be at each time step before simulating the model.

Efficiency of mesh adaptivity can be further enhanced by identifying anisotropy in the material or fluid interfaces that are to be captured. Sand-shale sequences, for example, may contain a large number of thin, high aspect ratio layers. The petrophysical properties vary by orders of magnitude but primarily in one direction. In an efficient mesh, grid spacing would be smallest normal to the interface and largest along the length of the interface. Isotropic meshes, however, place the same spacing throughout. This leads to a superfluous number of elements and thus increases the computational cost of the simulation. Figure 2.20 shows an example of unstructured meshes used to capture a sharp interface in a non-geological application. A significant reduction in the number of elements used to capture the interface is achieved by use of anisotropic meshes.



(A) (B) (C) (D) (E) (F)

FIGURE 2.20: Scalar field with a sharp interface represented on different meshes with the same minimum edge length. (A)-(B) Structured mesh. Capturing the interface requires 56,320 elements. (C)-(D) Isotropic unstructured mesh. The use of unstructured meshes leads to a significant reduction in the number of elements, 5,667 elements. (E)-(F) Anisotropic unstructured mesh. A further reduction can be seen with the use of anisotropic meshes to only 2,805 elements.

2.4 Summary

The REV is a key concept that allows a porous medium to be treated as a continuum. In heterogeneous porous media, there exist multiple REVs at various length scales, forming recognisable subdivisions (domains) of the stratigraphic units such as lithofacies and parasequences. Geological porous media typically comprise high aspect ratio geometries and non-parallel, non-orthogonal boundaries over a broad range of length scales.

In conventional modelling workflows, the reservoir volume is subdivided early in the workflow into a grid or mesh that contains a large number of discrete volumes (grid blocks) and geostatistical methods are used to populate these cells with petrophysical properties (Janssen et al., 2006; Feyen and Caers, 2006). The equations governing fluid flow are then discretised and solved numerically (e.g. Helmig and Huber, 1998; Jackson et al., 2015; Lie et al., 2012).

In many numerical simulation approaches, geological domain boundaries are aligned with grid-block boundaries and the governing equations are solved using FDFVM and the TPFA (Aziz and Settari, 1979). However, the TPFA yields accurate solutions only when the grid is k-orthogonal, so non-parallel, non-orthogonal domain boundaries must be represented in 'stair-step' fashion on the grid. More sophisticated numerical methods, such as the MPFA, are required if the grid is distorted to follow non-parallel, non-orthogonal domain boundaries (Aavatsmark, 2002; Edwards, 2002; Aavatsmark et al., 2008). However, MPFA is computationally expensive and rarely used in current commercial workflows. It is more common to simplify the geometry of the grid, requiring grids which are k-orthogonal (rectangular or Voronoi) or close to k-orthogonal (corner point) to avoid introducing significant discretisation errors in the resulting solutions (e.g. Helmig and Huber, 1998; Miller et al., 1998; Li et al., 2003; Gerritsen and Durlofsky, 2005; Wu and Parashkevov, 2009; Jackson et al., 2015).

In most real applications engineers compromise between strictly k-orthogonal grids and representing geological realism, where numerical errors are not catastrophic. However, this may not always be possible for complex subsurface structures (Jacquemyn et al., 2018; Graham et al., 2015a). An alternative modelling and simulation workflow proposed by Jackson et al. (2013) and Jackson et al. (2015) can replace conventional grid-based methods. In the approach presented here we have chosen to use NURBS surfaces as a flexible and computationally efficient way of capturing these heterogeneities. There are several potential advantages to surface-based modelling: surfaces can accurately and

realistically capture complex geological features at low computational cost; the model geometry can be created without reference to a grid or mesh defined early in the workflow, so the grid resolution does not place restrictions on model resolution, and the surfaces can be used to constrain the geometry of a grid or mesh that is optimally designed for the numerical solution of interest.

When ready for flow simulation, the geomodel can be discretised using unstructured tetrahedral meshes. The governing equations are then solved using FE methods, with space discretised using unstructured hexehedral or tetrahedral meshes and mass conservation enforced using CV in a CVFEM (Dalen, 1979; Fung et al., 1992; Geiger et al., 2004; Matthäi et al., 2007; Schmid et al., 2013; Mostaghimi et al., 2015; Jackson et al., 2015). The proposed simulator incorporates dynamic adaptive-mesh optimisation (DAMO), refining the mesh resolution where/when necessary and coarsening elsewhere.

Chapter 3

Numerical Method

In this chapter we present the computational framework, Imperial College Finite Element Reservoir SimulaTor (IC-FERST) used in this work. The approach applies a variant of the standard CVFEM on unstructured meshes termed the DCVFEM.

Contents

3.1 Introduction 47

3.2 Modified governing equations 48

3.3 Weak formulation 50

3.4 Discrete formulation 52

3.4.1 Force-balance 52

3.4.2 Rock and fluid properties 54

3.4.3 Global continuity 54

3.4.4 Time stepping approach 55

3.4.5 Pressure projection 56

3.4.6 Mass balance for the fluid phases 57

3.1 Introduction

Although control-volume-finite-element methods (CVFEMs) can provide accurate solutions to the multi-phase flow equations on unstructured meshes that preserve the complex geometries of geologic domains (e.g. Forsyth, 1991; Fung et al., 1992; Durlofsky, 1994; Geiger et al., 2004; Jackson et al., 2015; Salinas et al., 2017a), their use is still not widespread. As discussed in Chapter 2, a key issue of the standard CVFEMs is that accurate solutions to the pressure equation can be challenging to obtain on the high aspect ratio elements, typically required

to discretise the heterogeneous domains in geological porous media (Salinas et al., 2017b; Schneider et al., 2018). If element angles are large, discretisation errors in the solution becomes unacceptably large (Batdorf et al., 1997) while if element angles are small, the condition number of the pressure matrix becomes unacceptably large (Fried, 1972). Thus, numerical solutions on high aspect ratio elements are both less accurate and harder to compute. A large body of work has been devoted to methods for creation of good quality meshes (Shewchuk, 1996; Erten and Üngör, 2009; Erten and Ungor, 2009; Shewchuck, 2002), but poor quality meshes may be unavoidable when discretising geological domains with complex, high aspect ratio geometries.

Few studies have reported methods to improve the robustness of the CVFEM on high aspect ratio elements. Salinas et al. (2017b) proposed a variation of the standard CVFEM, termed the double control-volume-finite-element method (DCVFEM). In this approach, pressure is discretised control-volume (CV)-wise rather then finite-element (FE)-wise; all other variables are discretised following the classical CVFEM. Salinas et al. (2017b) demonstrated that the DCVFEM produced good quality pressure matrices even with very poor quality meshes. Moreover, the DCVFEM is able to produce a solution where the classical CVFEM cannot.

The formulation presented in this thesis was implemented in the open-source modelling framework, Fluidity for multi-phase flow called the Imperial College Finite Element Reservoir SimulaTor (IC-FERST). The code is actively being developed with recent advancements in multi-component/ interface-capturing flows (Pavlidis et al., 2015; Xie et al., 2016, compressible flows (Xiao et al., 2017; Yang et al., 2019), porous media flows (Jackson et al., 2015; Mostaghimi et al., 2015; Salinas et al., 2015; Gomes et al., 2017) and parallelisation (Piggott et al., 2008; Gorman et al., 2012). In this thesis, simulations are performed using the DCVFEM with mesh adaptivity within IC-FERST. The modelling framework is outlined below, with particular focus on the spatial and temporal discretisations used. The adaptive mesh algorithm termed dynamic adaptive-mesh optimisation (DAMO) will be introduced later in Chapter 5.

3.2 Modified governing equations

In our formulation the governing equations derived in Chapter 2 are slightly modified. We introduce a saturation-weighted Darcy velocity, $\mathbf{u}_\alpha = \mathbf{q}_\alpha / S_\alpha$.

Darcy's law can then be written as (Gomes et al., 2017)

$$S_\alpha \left(\frac{\mu_\alpha}{k_{r,\alpha}} \right) \mathbf{K}^{-1} \mathbf{u}_\alpha = -\nabla p_w + \mathbf{\Lambda}_\alpha, \tag{3.1a}$$

$$\boldsymbol{\sigma}_\alpha \mathbf{u}_\alpha = -\nabla p_w + \mathbf{\Lambda}_\alpha, \tag{3.1b}$$

$$\boldsymbol{\nu}_\alpha = -\nabla p_w + \mathbf{\Lambda}_\alpha \tag{3.1c}$$

where $\boldsymbol{\nu}_\alpha$ is the force density, $\boldsymbol{\sigma}_\alpha$ represents the implicit linearisation of the viscous frictional forces and $\mathbf{\Lambda}_\alpha$ is a source term, which may include gravity and capillary pressure.

Defining Darcy's law as in Equation 3.1c helps to reduce the non-linearity of the equation: relative permeability is often a power-law function of saturation (or similar), dividing through by saturation has the effect of reducing the non-linearity (Gomes et al., 2017). In this form, Equation 3.1c exactly enforces the force balance represented by multi-phase Darcy's Law, and will hereinafter be referred to as the *force balance equation.*

The material properties, relative permeability ($k_{r\alpha}$) and capillary pressure (p_c) are typically given as functions of saturation

$$k_{r\alpha} = k_{r\alpha}(S_\alpha), \tag{3.2a}$$

$$p_c = p_c(S_\alpha) \tag{3.2b}$$

Fluid viscosities are, in general, functions of temperature and pressure and described using viscosity models. Here, we assume immiscible fluids of constant viscosity. Moreover, in certain circumstances, reservoir fluids filling the pore space must be treated as compressible, where changes in density are related to changes in pressure and temperature. For non-isothermal reservoirs an energy equation is added to the system of governing equations. Compressibility is especially important for gaseous fluids. For gases, changes in density are captured through an equation of state, which relates density to pressure and temperature (e.g. Peng-Robinson; Peng and Robinson, 1976). For liquids, density is typically related to pressure through a *compressibility* parameter ($(N/m^2)^{-1}$). Moreover, if the porous medium is also considered to be compressible, the porosity is no longer constant. The compressibility can then be seen as a combined compressibility of the medium and the fluid within.

In this work we consider the flow of incompressible, immiscible, isothermal fluids through a rigid porous medium. The continuity equation for each phase states

$$\phi \frac{\partial S_\alpha}{\partial t} + \nabla \cdot \mathbf{q}_\alpha = \Psi_\alpha \tag{3.3}$$

which can be written as a scalar transport equation

$$\phi \frac{\partial S_\alpha}{\partial t} + \nabla \cdot (\mathbf{u}_\alpha S_\alpha) = \Psi_\alpha \tag{3.4}$$

which is equivalent to

$$\phi \frac{\partial S_\alpha}{\partial t} + \nabla \cdot \left(\boldsymbol{\sigma}_\alpha^{-1} \boldsymbol{\nu}_\alpha S_\alpha \right) = \Psi_\alpha \tag{3.5}$$

A global continuity equation is then formed by summing Equation 3.5 for all phases and using the saturation constraint $\sum_{\alpha=1}^{n_\alpha} S_\alpha = 1$

$$\nabla \cdot \left(\sum_{\alpha=1}^{n_\alpha} \left(\boldsymbol{\sigma}_\alpha^{-1} \boldsymbol{\nu}_\alpha S_\alpha \right) \right) = \sum_{\alpha=1}^{n_\alpha} \Psi_\alpha, \tag{3.6}$$

where n_α is the total number of phases.

The numerical method that will be used in this project is the DCVFEM formulation developed by Salinas et al. (2017b). Here the continuity equations are embedded into the pressure equation which enforces mass conservation and the exact force balance. The velocity, permeability, porosity and viscosity are represented FE-wise while the pressure, saturation and relative permeabilities are defined CV-wise.

3.3 Weak formulation

The FE method is based upon the discretisation of a variational form of the partial differential equations. The finite-element method (FEM) is well established; further details can be found elsewhere (e.g. Zienkiewicz et al., 2013; Donea and Huerta, 2003). The variational form requires the introduction of two classes of functions: test (or weighting) functions and trial (or admissible) solutions.

Test functions ($\mathcal{V}$) are defined such that

$$\mathcal{V} = \left\{\omega \in \mathcal{H}^1(\Omega)\right\} \tag{3.7}$$

where $\mathcal{H}^1(\Omega)$ is the first Hilbertian Sobolev, consisting of vectors of which all components and their derivatives are square integrable ($\mathrm{L}^2(\Omega)$).

Traditionally, Dirichlet boundary conditions are enforced at this stage. The test functions vanish on the Dirichlet portion (Γ_D) of the boundary of the domain ($\partial\Omega$) and the trial function for $\boldsymbol{\nu}$ must satisfy the Dirichlet boundary condition on Γ_D. This is known as the *strong satisfaction* of the boundary condition. However, in this formulation, we implement a *weak satisfaction* of the boundary conditions (Bazilevs and Hughes, 2007). The discrete solutions are not required to satisfy the Dirichlet conditions and are instead added to the variational formulation. The trial solution of $\boldsymbol{\nu}(\mathbf{x}, t)$ therefore coincides with the test function ($\mathcal{V}$) above.

Finally we introduce a space of square integrable functions $\mathcal{Q}$ for $p_w(\mathbf{x}, t)$

$$\mathcal{Q} = \left\{L^2\right\} \tag{3.8}$$

We are now able to construct the weak form of Equations 3.1c and 3.6. We multiply Equation 3.1c by test function $\omega \in \mathcal{V}$ and Equation 3.6 by $q \in \mathcal{Q}$. Integrating over the computational domain Ω we obtain

$$\int_\Omega \omega \left(\boldsymbol{\nu}_\alpha - \boldsymbol{\Lambda}_\alpha\right) dV + \int_\Omega \omega \nabla p_w dV + \int_{\Gamma_D} \omega \left(p_w - p_{w,bc}\right) \cdot \mathbf{n} ds = \mathbf{0} \tag{3.9}$$

$$\int_\Omega q \nabla \cdot \left(\sum_{\alpha=1}^{n_\alpha} \left(\boldsymbol{\sigma}_\alpha^{-1} \boldsymbol{\nu}_\alpha S_\alpha\right)\right) dV - \int_\Omega q \sum_{\alpha=1}^{n_\alpha} \Psi_\alpha dV = \mathbf{0} \tag{3.10}$$

The last term of Equation 3.9 is used to weakly enforce the pressure level to p_{bc} on the Dirichlet portion of the computational domain boundary. Equations 3.9 and 3.10 are jointly used to determine the velocity and pressure distribution in the porous media. The calculated velocities are then used to compute the mass balance for the fluid phases using the weak form of the transport equation (Equation 3.4)

$$\int_\Omega q\phi \frac{\partial S_\alpha}{\partial t} dV + \int_\Omega q \nabla \cdot \left(\mathbf{u}_\alpha S_\alpha\right) dV - \int_\Omega q \Psi_\alpha dV = \mathbf{0} \tag{3.11}$$

3.4 Discrete formulation

To form the discrete system we first partition the computational domain Ω into a family of triangular or tetrahedral finite elements. The finite element model is obtained by restricting the weak form (Equations 3.9, 3.10 and 3.11) to the finite dimensional spaces $\mathcal{V}^h \subset \mathcal{V}$ and $\mathcal{Q}^h \subset \mathcal{Q}$.

We can then write any test function $\omega^h \in \mathcal{V}^h$ and $q^h \in \mathcal{Q}^h$ as

$$\omega^h(\mathbf{x}) = \sum_j^{n_\nu} N_j(\mathbf{x}) \tag{3.12}$$

$$q^h(\mathbf{x}) = \sum_j^{n_p} M_j(\mathbf{x}) \tag{3.13}$$

where n_v and n_p are the number of degrees of freedom of the force density and pressure respectively.

Similarly the approximate solutions $\boldsymbol{\nu}_\alpha^h$ and p^h can be represented as a linear combination of piecewise-polynomial basis functions N_j (discontinuous between elements) and CV basis function M_j, respectively spanning a finite-dimensional space

$$\begin{aligned} \boldsymbol{\nu}_\alpha(\mathbf{x},t) \approx \boldsymbol{\nu}_\alpha^h(\mathbf{x},t) &= \sum_j^{n_\nu} N_j(\mathbf{x})\boldsymbol{\nu}_{\alpha,j}(t) \\ p_w(\mathbf{x},t) \approx p_w^h(\mathbf{x},t) &= \sum_j^{n_p} M_j(\mathbf{x}) p_{w,j}(t) \end{aligned} \tag{3.14}$$

Notice that with the above definition the temporal and spatial variations of the approximate solutions are separated, associated with basis functions (e.g. $M_j(\mathbf{x})$) and nodal values (e.g. $p_{w,j}(t)$) respectively. This allows for time derivatives to be applied to the nodal values and gradient and divergence operators to be applied to the basis functions separately.

3.4.1 Force-balance

The discretised version of Equation 3.9 becomes

$$\sum_E \int_{\Omega_E} N_i \left(N_j \boldsymbol{\nu}_{\alpha,j} - \boldsymbol{\Lambda}_\alpha\right) dV + \sum_{CV} \int_{\Gamma_{CV_j}} N_i p_{w,j} \cdot \mathbf{n} ds + \int_{\Gamma_D} N_i M_j \left(p_{w,j} - p_{w,bc}\right) \cdot \mathbf{n} ds = \mathbf{0} \tag{3.15}$$

where the divergence theorem was used to convert the second volume integral in Equation 3.9 to a surface integral. Ω_E and Γ_E are the volume and boundary of the element E, respectively, and Γ_D is the Dirichlet boundary of the computational domain. As $M_j = 1$ on the CV around node j and zero elsewhere, it does not appear in the second term above.

In matrix form Equation 3.15 can be written as

$$\mathbf{M}\underline{\boldsymbol{\nu}} = -\mathbf{C}\underline{\mathbf{p}} + \underline{\boldsymbol{R}} \tag{3.16}$$

where $\underline{\boldsymbol{\nu}}$ and $\underline{\mathbf{p}}$ solution vectors are defined as

$$\begin{aligned} \underline{\boldsymbol{\nu}} &= \left((\nu_x, \nu_y, \nu_z)_{1,1}, \ldots, (\nu_x, \nu_y, \nu_z)_{2,1}, \ldots, (\nu_x, \nu_y, \nu_z)_{n_\alpha, n_v}\right)^T \\ \underline{\mathbf{p}} &= \left(p_{w,1}, p_{w,2}, \ldots, p_{w,n_p}\right)^T \end{aligned} \tag{3.17}$$

where (ν_x, ν_y, ν_z) are the components associated with the x, y and z dimensions, respectively of the force density $\boldsymbol{\nu}$.

The elemental matrix and vector contributions of phase α, of the mass matrix $\mathbf{M}$, gradient matrix $\mathbf{C}$ and right hand side vector $\underline{\boldsymbol{R}}$ are defined respectively as

$$\begin{aligned} \mathbf{m}_{i,j} &= \int_{\Omega_E} N_i N_j dV, \\ \mathbf{c}_{i,j} &= \sum_{CV \ni E} \int_{\Gamma_{CV}} N_i M_j \cdot \mathbf{n} ds + \int_{\Gamma_E \ni \Gamma_D} N_i M_j \cdot \mathbf{n} ds \\ \boldsymbol{r}_i &= \int_{\Omega_E} N_i \boldsymbol{\Lambda}_i dV - \int_{\Gamma_E \ni \Gamma_D} N_i M_j p_{w,bc} \cdot \mathbf{n} ds, \end{aligned} \tag{3.18}$$

where i and j are the degrees of freedom of element E. Here, $\mathbf{n} = (n_1, n_2, n_3)^T$ are the outward-pointing normal vectors of the domain Ω.

Note that the $\mathbf{c}$ matrix does not contain derivatives of shape functions. This is one of the fundamental differences between the DCVFEM and the traditional

CVFEM and is key in improving the quality of the pressure matrix, as well as the consistency and accuracy of flux calculations on highly distorted meshes (Salinas et al., 2017b).

The matrix **m** is known as the element mass matrix. Since the velocity field in our formulation is discontinuous between elements, the assembled system mass matrix **M** is block-diagonal (with one block per element) and thus more easily invertible and cheaper to store.

3.4.2 Rock and fluid properties

In this formulation rock properties (permeability and porosity) are assigned homogeneously to the FE. This formulation is therefore well-suited to surface-based models where geological heterogeneities are represented by their bounding surfaces (Section 2.3) and can be accurately preserved once discretised using FEs. Fluid properties such as saturation and relative permeability and capillary pressure are assigned to the CV. Thus, the viscous-friction damping tensor, $\boldsymbol{\sigma}_\alpha$, is piecewise constant within the sub-control-volumes defined through intersections between the elements and CVs (Figure 3.1)

However, a well known issue of CVFEM is that node-centred CVs (where sub-control volumes sharing a node are combined) lead to jump discontinuities being smeared out across material boundaries. Relative permeability and capillary heterogeneity (assumed to be functions of saturation) are therefore not accurately captured. Later in the thesis we show how DAMO can reduce this smearing while optimising computational effort (Chapter 5). We also present a new numerical discretisation (Chapter 6) that does not require CVs to span material boundaries, thereby capturing both discontinuities in rock and saturation dependent properties (i.e. saturation, relative permeability and capillary pressure).

3.4.3 Global continuity

The global continuity equation (Equation 3.10) is now discretised in space using the finite-volume method (FVM) by multiplying by CV test functions M_j and integrating over the domain (Ω).

$$\int_\Omega M_j \nabla \cdot \left(\sum_{\alpha=1}^{n_\alpha} \left(\boldsymbol{\sigma}_\alpha^{-1} \boldsymbol{\nu}_\alpha S_\alpha \right) \right) dV = \int_\Omega M_j \Psi_\alpha dV, \tag{3.19}$$

Applying the divergence theorem and recalling that M_j is 1 over CV j and zero elsewhere we obtain the following integral over each CV

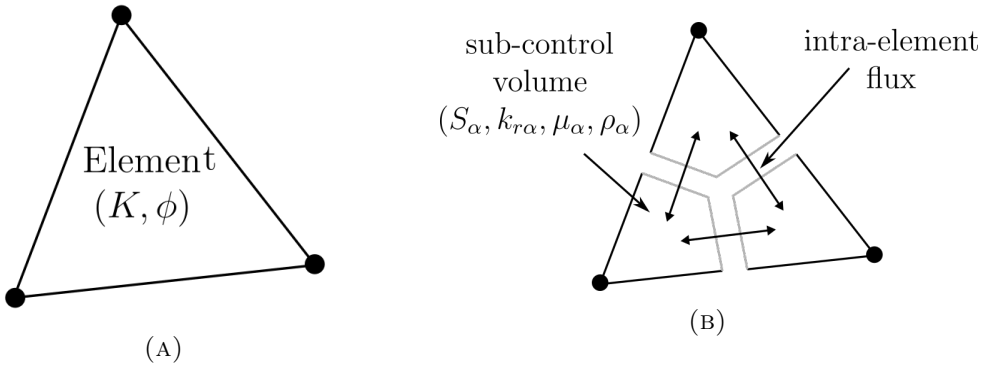


FIGURE 3.1: (A) Rock properties permeability and porosity are piecewise constant in the finite element, (B) Fluid properties such as viscosity and saturation are constant within the sub-control volume.

$$\int_{\Gamma_{CV_j}} \mathbf{n} \cdot \left(\sum_{\alpha=1}^{n_\alpha} \left(\boldsymbol{\sigma}_\alpha^{-1} \boldsymbol{\nu}_\alpha S_\alpha \right) \right) ds = \int_{CV} \Psi_\alpha dV, \tag{3.20}$$

where Γ_{CV_j} is the surface bounding CV j and $\mathbf{n}$ is the outward point normal.

In matrix form Equation 3.20 reads

$$\mathbf{C}^T \underline{\boldsymbol{\nu}} = \underline{\mathbf{G}} \tag{3.21}$$

3.4.4 Time stepping approach

The non-linear algebraic system of equations (Equation 3.16 and 3.21) which requires an iterative approach. Two strategies typically employed are the Newton's method and Fixed-point (Picard) iteration. Within these iterations a linearized system of equations is developed. While it is well known that Newton's methods are typically quadratically convergent, this requires the initial iterate to be 'close enough' to the solution otherwise convergence is not guaranteed (Elman et al., 2006). Moreover, while the linearized system of equations arising from Newton's methods show faster convergence they are more difficult to solve (higher cost per iteration), than a Fixed-point iteration.

Fixed-point approach is typically used because of its simplicity, where the discretized equations are directly solved. Moreover, Fixed-point iterations have a much larger ball of convergence, requiring fewer conditions to achieve convergence (Elman et al., 2006). In this work a modified Fixed-point method of Anderson (Salinas et al., 2017a) with acceleration is used. Within these iterations there is also a pressure correction step to ensure a divergence free velocity field (see

next section). The new method developed by Salinas et al. (2017a) is able to admit much larger Courant numbers with an efficient backtracking parameter. Computational effort is reduced with the use of acceleration techniques based on Anderson's method (Anderson, 1965) and artificial diffusion (Salinas et al., 2017a and later improved in Salinas et al. (2019)).

3.4.5 Pressure projection

In general, the force density solution and subsequent Darcy velocity will not satisfy the continuity equation, i.e. the Darcy velocity will not be divergence free. To project to a divergence free space, a pressure correction is calculated (Davies et al., 2011). The algorithm starts by solving for an intermediate force density $\underline{\boldsymbol{\nu}}_*^{n+1}$ from an initial guess for pressure $\underline{\mathbf{p}}_*^{n+1}$ using Equation 3.16

$$\mathbf{M}\underline{\boldsymbol{\nu}}_*^{n+1} = -\mathbf{C}\underline{\mathbf{p}}_*^{n+1} + \underline{\boldsymbol{R}}^{n+1} \tag{3.22}$$

Subtracting Equation 3.22 from Equation 3.16 we obtain the force density correction equation

$$\mathbf{M}\left(\underline{\boldsymbol{\nu}}^{n+1} - \underline{\boldsymbol{\nu}}_*^{n+1}\right) = -\mathbf{C}\left(\underline{\mathbf{p}}^{n+1} - \underline{\mathbf{p}}_*^{n+1}\right) \tag{3.23}$$

Multiplying this equation by $\mathbf{C}^T\mathbf{M}^{-1}$, and using Equation 3.21, $\underline{\boldsymbol{\nu}}^{n+1}$ can be eliminated leaving the pressure correction equation

$$\mathbf{C}^T\mathbf{M}^{-1}\mathbf{C}\left(\underline{\mathbf{p}}_*^{n+1} - \underline{\mathbf{p}}^{n+1}\right) = -\mathbf{C}^T\underline{\boldsymbol{\nu}}_*^{n+1} + \underline{\mathbf{G}}^{n+1} \tag{3.24}$$

where the matrix $\mathbf{C}^T\mathbf{M}^{-1}\mathbf{C}$ is the projection matrix.

In the next section we describe how the saturation, S_α and viscous-friction damping tensor, $\boldsymbol{\sigma}_\alpha$ used in $\mathbf{C}^T$ are determined. The linear system of equations above (Equation 3.24) are then solved for $\underline{\mathbf{p}}^{n+1}$ using the generalised minimal residual (GMRES) Krylov subspace solver (Saad and Schultz, 1986) with a multi-grid preconditioner of the PETSc framework (Balay et al., 1997). The corrected pressure is then used to calculate $\underline{\boldsymbol{\nu}}^{n+1}$.

3.4.6 Mass balance for the fluid phases

Once $\underline{\boldsymbol{\nu}}^{n+1}$ is determined, the saturation is then transported between CVs using interface fluxes, which we refer to here as *intra-element fluxes* to differentiate them from *inter-element fluxes* which we will encounter in Chapter 6.

The transport equation (Equation 3.11) is discretised in space by testing with CV basis functions M_j and invoking Gauss' theorem on the divergence term. For temporal discretisation we apply the adaptive implicit $\theta-$method, which is locally selected based on a total variational diminishing (TVD) criterion.

$$\begin{aligned} \int_{CV} \frac{\phi\left(S_\alpha^{n+1}-S_\alpha^n\right)}{\Delta t} dV + \\ \int_{\Gamma_{CV}} \left[\theta^{n+\frac{1}{2}} \mathbf{n}\cdot\mathbf{u}_\alpha^{n+1} S_\alpha^{n+1} + \left(1-\theta^{n+\frac{1}{2}}\right)\mathbf{n}\cdot\mathbf{u}_\alpha^n S_\alpha^n\right] ds - \\ \int_{CV} \Psi_\alpha^{n+\theta} dV = \mathbf{0} \end{aligned} \tag{3.25}$$

TVD schemes aim to ensure an advected scalar field, e.g. saturation, remains uniformly bounded. The bounding procedures use an 'indicator' function that follows the local shape of the solution to determine where and when to intervene, to ensure non-oscillatory solutions. These indicator functions require the calculation of a 'far upwind' value; while simple to determine on structured meshes, extension to unstructured meshes is more challenging. In this work we apply a normalised variable diagram (NVD) approach (Darwish and Moukalled, 1994; Jasak et al., 1999; Pavlidis et al., 2015) to smoothly transition from first-order to higher-order schemes. The 'far upwind' value is found by projecting a line through the CV nodes from the downwind node to the upwind node and extending the line upstream by the same distance. The solution at this point is then found by linear interpolation of the FEM solution in the upwind element (see Pavlidis et al. (2015) for a detailed explanation).

To solve equation 3.25, the fluxes, $\mathbf{n}\cdot\mathbf{u}_\alpha$, and saturation, S_α, at the CV faces need to be determined. The (saturation-weighted) Darcy velocity, $\mathbf{u}_\alpha$, depends on the absolute permeability, which in this formulation is stored FE-wise, and the relative permeability which is stored CV-wise (Figure 3.1). As a result, $\mathbf{u}_\alpha$ is discontinuous across the sub-control volume. However, the force density, $\boldsymbol{\nu}_\alpha$ is continuous within an element and can therefore be stored FE-wise. Figure 3.2 shows an example of a P0 element. Within an element $\mathbf{u}_\alpha$ and $\boldsymbol{\nu}_\alpha$ have the same direction but differ only in magnitude, so an upwind direction is not ambiguous.

For a first-order accurate scheme in space, Equation 3.25 can be solved using upwind approximations for $\mathbf{u}_\alpha$ and S_α. However, this can lead to highly diffusive solutions, which can make the distinction between numerical and physical dispersion difficult. This can be particularly detrimental where mixing due to dispersion and spatial heterogeneity, such as compositional modelling, are important (Matthäi et al., 2005a; Schmid et al., 2013; Lie et al., 2018; Moortgat and Firoozabadi, 2010). High-order accurate schemes are therefore needed. Moreover, high-order schemes not only provide better precision but in our case reductions in numerical diffusion allow for much larger computational elements. This can be especially useful during mesh adaptivity where smooth regions can be discretised with a small number of larger elements.

We obtain a second-order accurate solution of saturation, $\tilde{S}_\alpha$ via a FE reconstruction, by solving the following equation

$$\int_\Omega N_i \left(S_\alpha^{FE} - S_\alpha^{CV}\right) dV = 0 \tag{3.26}$$

where S_α^{FE} and S_α^{CV} are the FE-wise and CV-wise representations of the saturation given by

$$S_\alpha^{FE} = \sum_j N_j S_{\alpha,j}^{FE} \tag{3.27}$$

$$S_\alpha^{CV} = \sum_j M_j S_{\alpha,j}^{CV} \tag{3.28}$$

where N_j and M_j are the FE test function associated with node j and the CV test function associated with node j, respectively.

A higher-order representation for the viscous-friction damping tensor, $\tilde{\boldsymbol{\sigma}}_\alpha$, can then be calculated using the second-order Taylor series expansion

$$\tilde{\boldsymbol{\sigma}}_\alpha = \boldsymbol{\sigma}_{\alpha,k} + \left(\tilde{S}_\alpha - S_{\alpha,k}\right)\left(\frac{\partial \boldsymbol{\sigma}_\alpha}{\partial S_\alpha}\right)_k + \frac{1}{2}\left(\tilde{S}_\alpha - S_{\alpha,k}\right)^2 \left[\frac{\left(\frac{\partial \boldsymbol{\sigma}_\alpha}{\partial S_\alpha}\right)_k - \left(\frac{\partial \boldsymbol{\sigma}_\alpha}{\partial S_\alpha}\right)_l}{\left(\tilde{S}_{\alpha,k} - S_{\alpha,l}\right)}\right] \tag{3.29}$$

where

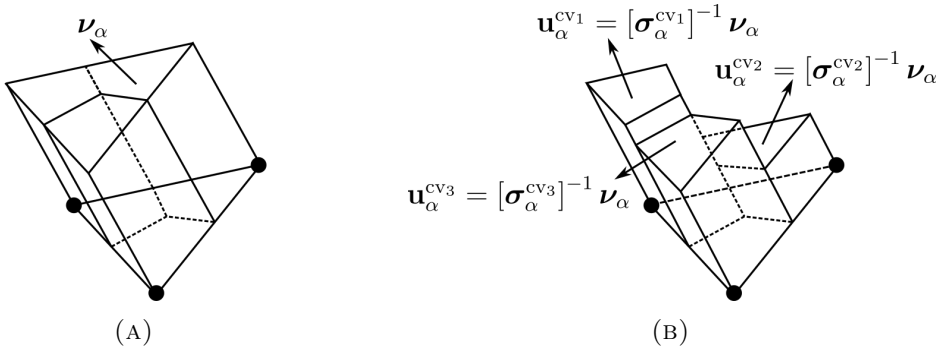


FIGURE 3.2: Finite element representation of the force density ($\boldsymbol{\nu}_\alpha$) and Darcy velocity ($\mathbf{u}_\alpha$) on a two dimensions (2D) element. (A) discontinuous P0 finite element representation of the force density; (B) as $\boldsymbol{\sigma}_\alpha$ is made up of FE- and CV-wise terms, the Darcy velocity is discontinuous across sub-control volumes.

$$\begin{aligned} k = i \text{ and } l = j \quad &\text{if } \mathbf{n} \cdot \mathbf{u}_\alpha > 0 \\ k = j \text{ and } l = i \quad &\text{if } \mathbf{n} \cdot \mathbf{u}_\alpha < 0 \end{aligned} \tag{3.30}$$

Therefore the high-order interface flux across the CV interface between CV i and j is given by

$$\mathbf{u}_\alpha = \tilde{\boldsymbol{\sigma}}_{\alpha,k}^{-1} \boldsymbol{\nu}_\alpha, \quad k = \{i, j\} \tag{3.31}$$

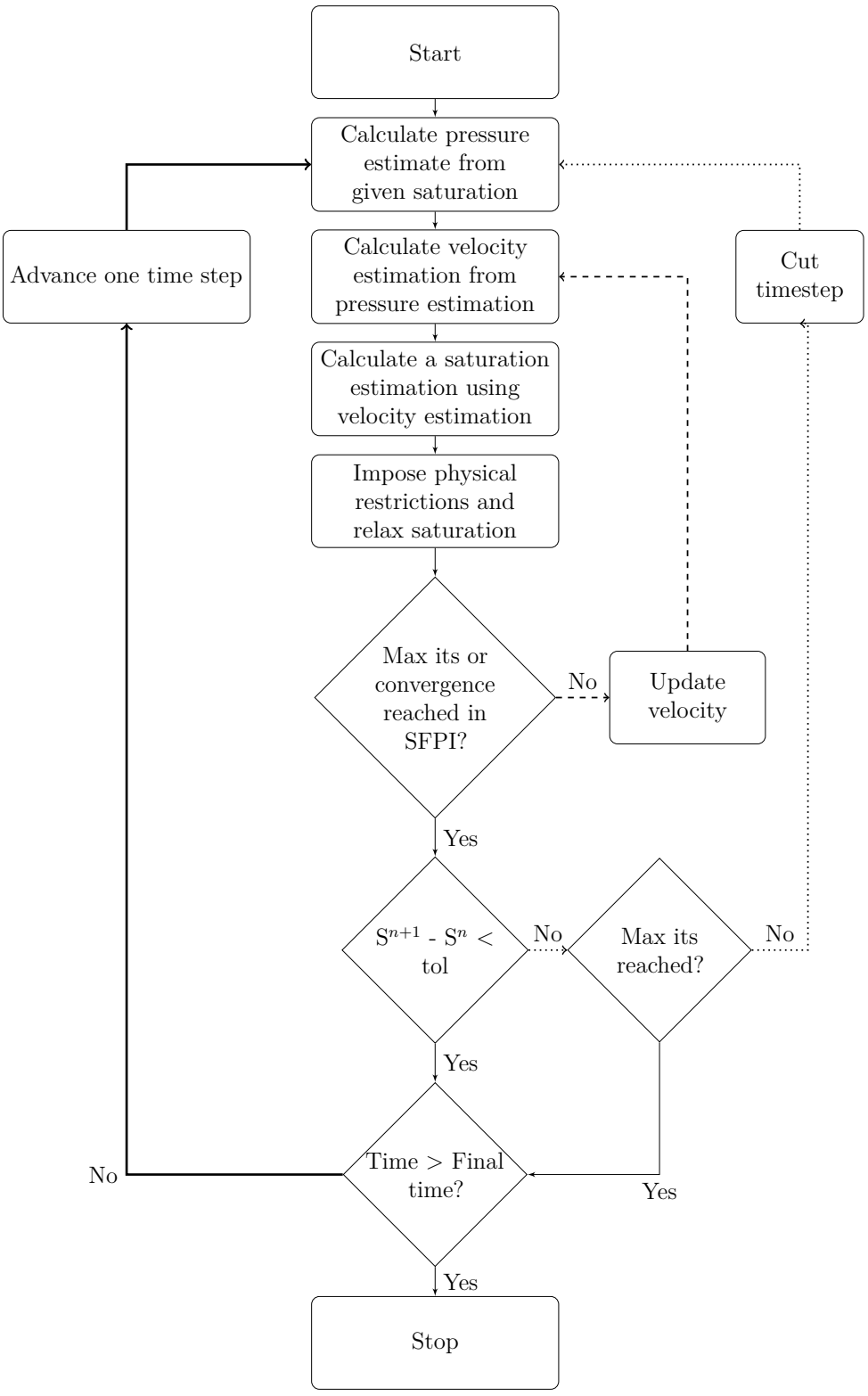


FIGURE 3.3: Flow chart of the non-linear solver algorithm. The algorithm consists of three main loops, thick solid line denotes the outer time loop, dotted line denotes the fixed point iteration method used to solve the non-linear system of equations. The dashed lines denote the saturation fixed point iteration (SFPI) used to accelerate the Anderson-fixed point method (Salinas et al., 2017a).

Chapter 4

Investigating the effect of cell-to-cell variability in reservoir models

Reservoir models typically contain hundreds-of-thousands to millions of grid cells in which petrophysical properties such as porosity and permeability vary on a cell-to-cell basis. However, although the petrophysical properties of rocks do vary on a point-to-point basis, this variability is not equivalent to the cell-to-cell variations in models. We investigate the impact of removing cell-to-cell variability on predictions of fluid flow in reservoir models. We remove cell-to-cell variability from models containing hundreds of thousands of unique porosity and permeability values to yield models containing just a few tens of unique porosity and permeability values grouped into a few internally homogeneous domains. The flow behaviour of the original model is used as a reference. We find that the impact of cell-to-cell variability on predicted flow is small. Cell-to-cell variability is not necessary to capture flow in reservoir models; rather, it is the spatially correlated variability in petrophysical properties that is important. Reservoir modelling effort should focus on capturing correlated geological domains in the most realistic and computationally efficient manner.

Contents

4.1 Introduction 62

4.2 Test cases 64

4.2.1 Lower SPE 10: Fluvial Model 65

4.2.2 Upper SPE 10: Shallow Marine Model 65

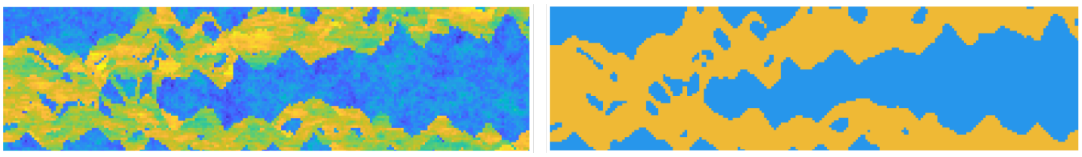
4.2.3 H-Field: North Sea Reservoir 66

4.2.4 Rock and fluid properties 66

4.2.5 Well placements and controls 70
4.3 Methodology 72
4.3.1 Goodness of fit 72
4.3.2 Removal of cell-by-cell variability 73
4.4 Results 75
4.4.1 Lower SPE 10 model: Segmentation and Clustering 75
4.4.2 Upper SPE 10 model: Summary of Goodness of Fit results 81
4.4.3 H-Field Model: Summary of Goodness of Fit results 83
4.5 Discussion 83
4.6 Conclusions 87

4.1 Introduction

In most modelling workflows, the model volume is subdivided early in the workflow into a grid or mesh that contains a large number (typically hundreds-of-thousands to millions) of discrete volumes (grid blocks/cells/elements or similar, heretoforward termed cells) and geostatistical methods are used to populate these cells with petrophysical properties (Janssen et al., 2006; Feyen and Caers, 2006). In some studies, the same grid is used to model the petrophysical properties and solve the flow equations; more typically, the flow equations are solved using a coarser grid and petrophysical properties upscaled from the finer grid. In either case, the grid used to simulate flow contains petrophysical properties that vary on a cell-to-cell basis (e.g. Figure 4.1a).



(A) (B)

FIGURE 4.1: (A) Reservoir models typically contain cell-to-cell variations in petrophysical properties; (B) The geological concept captures the architecture of key heterogeneities.

While petrophysical properties of rocks do vary on a point-by-point basis (where a point here corresponds to a representative elementary volume (REV) (e.g. Nordahl and Ringrose, 2008), this variability is at a different (and usually much finer) scale than the cell-to-cell variability captured in reservoir models. That

petrophysical properties and flow equations are discretised on the same grid appears to be an accidental outcome of the gradual evolution of modelling workflows. Discretisation of the petrophysical properties should be designed to preserve those features that are most important to flow; discretisation of the flow equations should be designed to yield the most accurate solutions for the lowest computational cost. It is highly improbable that a single grid will meet both of these requirements. There are many publications devoted to the problem of upscaling. Many techniques have been developed to better identify the heterogeneity in the upscaling process, such as the ones proposed in Dagan et al., 2013; Chen et al., 2003; Christie and Blunt, 2001; Durlofsky et al., 1997 amongst others.

The alternative to grid-based workflows advocated in this thesis is the surface-based modelling (SBM) (Xie et al., 2001; Pyrcz et al., 2005; Jackson et al., 2005; Sech et al., 2009; Zhang et al., 2009; Jackson et al., 2009; Caumon et al., 2009; Jackson et al., 2015; Graham et al., 2015a; Graham et al., 2015b; Massart et al., 2016; Jacquemyn et al., 2018). All geological heterogeneity that impacts flow is modelled as discrete volumes, or 'geological domains', bounded by surfaces. A nested hierarchy of surfaces can represent multi-scale heterogeneity

In SBM the surfaces are modelled without reference to an underlying grid; a grid or mesh is created only when required for numerical calculations. The grid cells inherit the petrophysical properties of the parent geological domain. The cell-to-cell variability in petrophysical properties observed in grid-based models is omitted (e.g. Figure 4.1b). It is not yet clear whether this cell-by-cell variability is required to properly capture flow. If short length-scale, cell-to-cell variability can be omitted from reservoir models while still correctly predicting fluid flow, then the route is open to focus modelling effort on capturing geologically defined, surface-bounded domains in models that are 'fit for purpose' (Ringrose and Bentley, 2015; Bentley and Ringrose, 2017).

No previous studies have specifically investigated the importance of cell-to-cell scale variability on predicted fluid flow, although some have tested the relative importance of modelling petrophysical property variations within, and between, geologically defined domains that correspond to lithofacies or lithofacies assemblages. Bianchi and Zheng (2016) found that a key control on contaminant flow was the connectivity of different lithofacies types, which were associated with significant contrasts in petrophysical properties. Similarly, Feyen and Caers (2006) found that lithofacies geometry (and the related permeability variation) was more important to solute migration than the distribution of

permeability within lithofacies. However, in both studies, cell-to-cell variability in petrophysical properties within lithofacies was retained, so the hypothesis that cell-to-cell variability is not important to flow was not tested. White and co-workers (White and Barton, 1999; Willis and White, 2000; White et al., 2004) examined a number of petrophysical modelling approaches including homogenised lithofacies, assigning lithofacies-specific geometric mean values of permeability. Other approaches tested used geostatistical methods following Deutsch and Journel (1998) to populate petrophysical properties within lithofacies, yielding cell-to-cell variability. Comparison of the models using flow-based measures showed that if the length scale of petrophysical variability was small with respect to the length scale of the problem of interest, the impact on flow was small.

In this chapter, we test the hypothesis that cell-to-cell variability can be omitted in reservoir models. We test whether it is necessary to model cell-to-cell scale variability in petrophysical properties in the first place. Cell-to-cell variability is removed from grid-based models, each of which initially contain several hundred thousand unique values of porosity and permeability. This results in models containing just a few tens of unique porosity and permeability values grouped into a few hundred to a few thousand domains. The same initial grid is used to solve the flow equations and the flow behaviour of the original model is used as a reference.

The resulting domains which represent spatially correlated variability in petrophysical properties can be defined using surface-based modelling workflows as mentioned earlier. Alternatively, aggregation-based coarsening can be used to upscale cells within these captured domains. The application of aggregation-based coarsening has seen increasing use in upscaling (e.g. Thomas et al., 2019; Guion et al., 2019) and multi-scale methods (e.g. Lie et al., 2017b; Klemetsdal et al., 2019). With this method one often tries to identify and recreate underlying geological objects in order to homogenise (upscale methods) or compute basis functions (multi-scale methods) on the coarse grid cells. With surface-based modelling geological objects that represent important geological heterogeneities are preserved throughout the modelling workflow to simulation. There is therefore more room to develop reduced order models to reduce computational effort.

4.2 Test cases

Three reservoir-scale models were used as test cases. The first two models are synthetic and represent unfaulted reservoirs deposited in fluvial and shallow

marine environments. The third is a real reservoir comprising fluvial, deltaic and shallow marine deposits divided into several different fault blocks. The synthetic models were taken from the SPE 10 Model 2, a classic benchmark model (Christie and Blunt, 2001), the 'SPE 10 Model'. This model has been widely used to represent a challenging problem for reservoir simulation with a highly heterogeneous distribution of petrophysical properties. All three models simulated multi-phase flow where oil is displaced by water, although we suggest that the key findings of the study generalise to other types of flow relevant to aquifers and CO_2 storage. The impact of heterogeneity on flow in the synthetic models was tested using two different injector/producer well configurations and three sets of oil/water fluid properties. The real reservoir case used the properties of the fluids in place and the well configuration applied in the field development.

4.2.1 Lower SPE 10: Fluvial Model

The first synthetic model comprised the lower 50 layers of the SPE 10 Model, which was originally constructed to represent reservoirs in the Upper Ness formation, part of the Middle Jurassic Upper Brent Group in the Northern North Sea (Mitchener et al., 1992). The Upper Ness formation was largely deposited in a non-marine, fluvial environment and reservoirs are typically characterised by high permeability channelised sandbodies surrounded by low permeability mudstone (Mitchener et al., 1992). The synthetic model with dimensions of $365 \times 670 \times 30$ m is described on a regular $60 \times 220 \times 50$ Cartesian grid (Figures 4.2a - 4.2c). The model contains high permeability channelised sandbodies surrounded by low permeability mudstone and the modelling of these different lithofacies types yields bimodal porosity and permeability distributions (Figure 4.2d-4.2f). The model has a variable permeability anisotropy (K_V/K_H) ratio of 0.3 in the sandstone and 10^{-3} in the mudstone.

4.2.2 Upper SPE 10: Shallow Marine Model

The second synthetic model comprised the upper 35 layers of the SPE 10 Model with dimensions of $365 \times 670 \times 21$ m, described on a regular $60 \times 220 \times 35$ Cartesian grid. This model was originally constructed to represent reservoirs in the Tarbert formation, which directly overlies the Upper Ness formation. The Tarbert formation was largely deposited in a shallow marine environment and reservoirs are typically characterised by an overall upwards coarsening and general distal to proximal coarsening succession (Mitchener et al., 1992). However, there is no strongly correlated heterogeneity present in the model and

no clear evidence of upwards coarsening or distal to proximal coarsening trends (Figure 4.3a - 4.3c). The porosity and horizontal permeability show uni-modal distributions; however, the vertical permeability exhibits a bi-modal distribution. Although not clear from Christie and Blunt, 2001, it appears that two different K_V/K_H ratios of 0.3 and 10^{-3} were applied in the upper SPE 10 model (Figure 4.3d - 4.3f).

4.2.3 H-Field: North Sea Reservoir

The real field example is located in the East Shetland Basin. The field comprises a number of N-S trending, westerly dipping, Mesozoic fault blocks. The reservoir is provided by fluvial, deltaic and shallow marine sandstones of the Brent Group, Lower Jurassic Statfjord Formation and Upper Triassic Upper Lunde Formation (Ritchie, 2003). Bitumen horizons observed at specific levels suggest a staged filling of the reservoir, protecting up-dip regions from continued diagenesis (Baillie et al., 1996). The reservoir therefore exhibits significant permeability contrasts between layers due to this complex diagenetic phenomenon (Figure 4.4a - 4.4c), with marked improvement in reservoir quality above the paleo-oil-water contact (Baillie et al., 1996). However, the petrophysical properties exhibit a uni-modal frequency distribution (Figure 4.4d- 4.4f). The structure of the reservoir model is complex, comprising a number of fault-bounded blocks, described on a $58 \times 145 \times 40$ corner point grid with stair-stepped faults (Figure 4.4a - 4.4c).

4.2.4 Rock and fluid properties

The rock properties used in the SPE 10 models were the same as Christie and Blunt (2001). The relative permeability model is based on the Brooks-Corey correlation, defined by

$$k_{rw}(S_w) = \left(\frac{S_w - S_{wirr}}{1 - S_{wirr} - S_{or}} \right)^{n_w} \tag{4.1a}$$

$$k_{ro}(S_o) = \left(\frac{S_o - S_{nwr}}{1 - S_{wirr} - S_{or}} \right)^{n_o} \tag{4.1b}$$

where $k_{rw}(S_w)$ and $k_{ro}(S_o)$ are, respectively, the water and oil relative permeabilities, S_{wirr} and S_{or} are the irreducible water and oil phase saturations, and

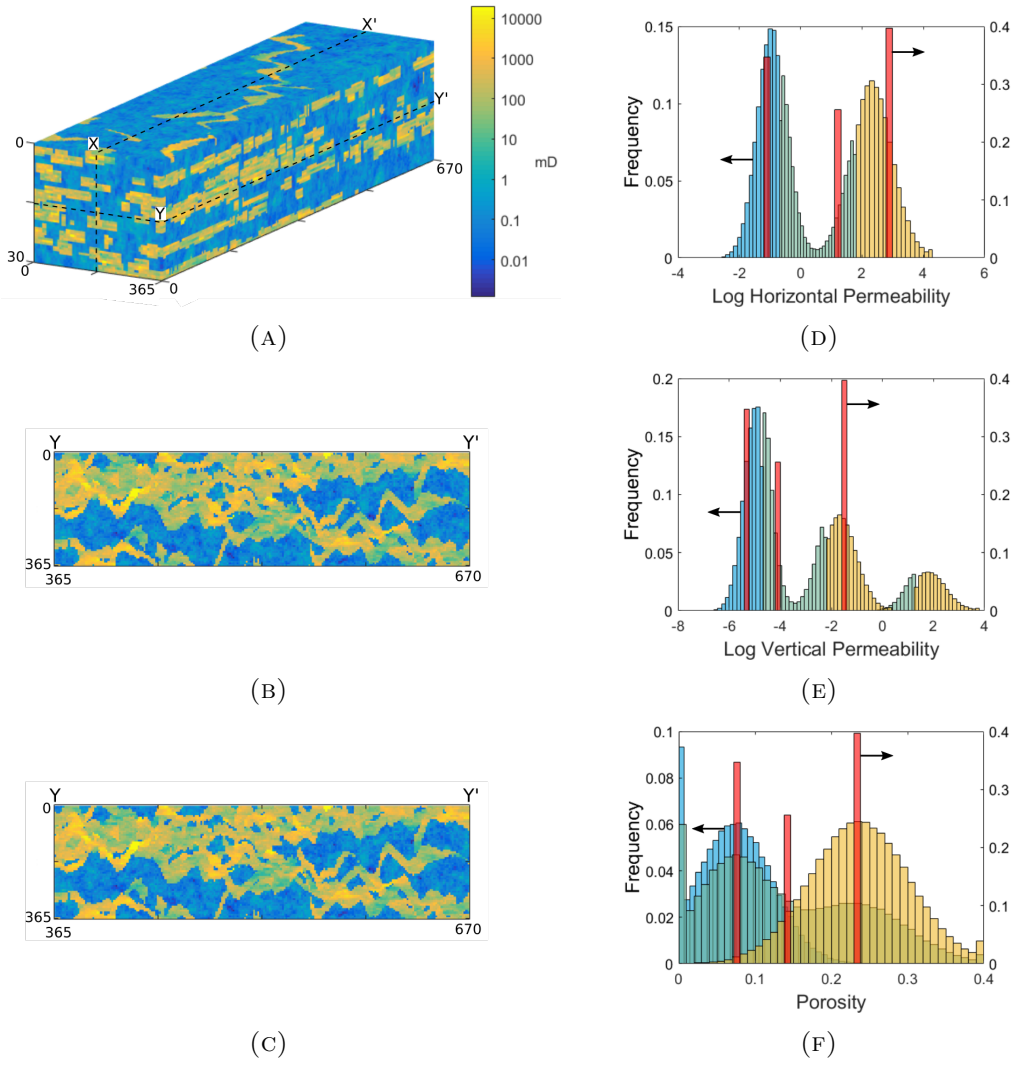


FIGURE 4.2: Petrophysical properties within the Lower SPE 10 Model. Plots (A-C) show the spatial distribution of horizontal permeability in (A) three dimensions (3D); (B) vertical cross section (X-X') and (C) horizontal cross section (Y-Y'). Dimensions in metres. Plots (D-F) show the frequency distribution of (D) horizontal permeability; (E) vertical permeability and (F) porosity. Plots (D-F) also show the frequency distribution after division into three segments; see Method section for more details.

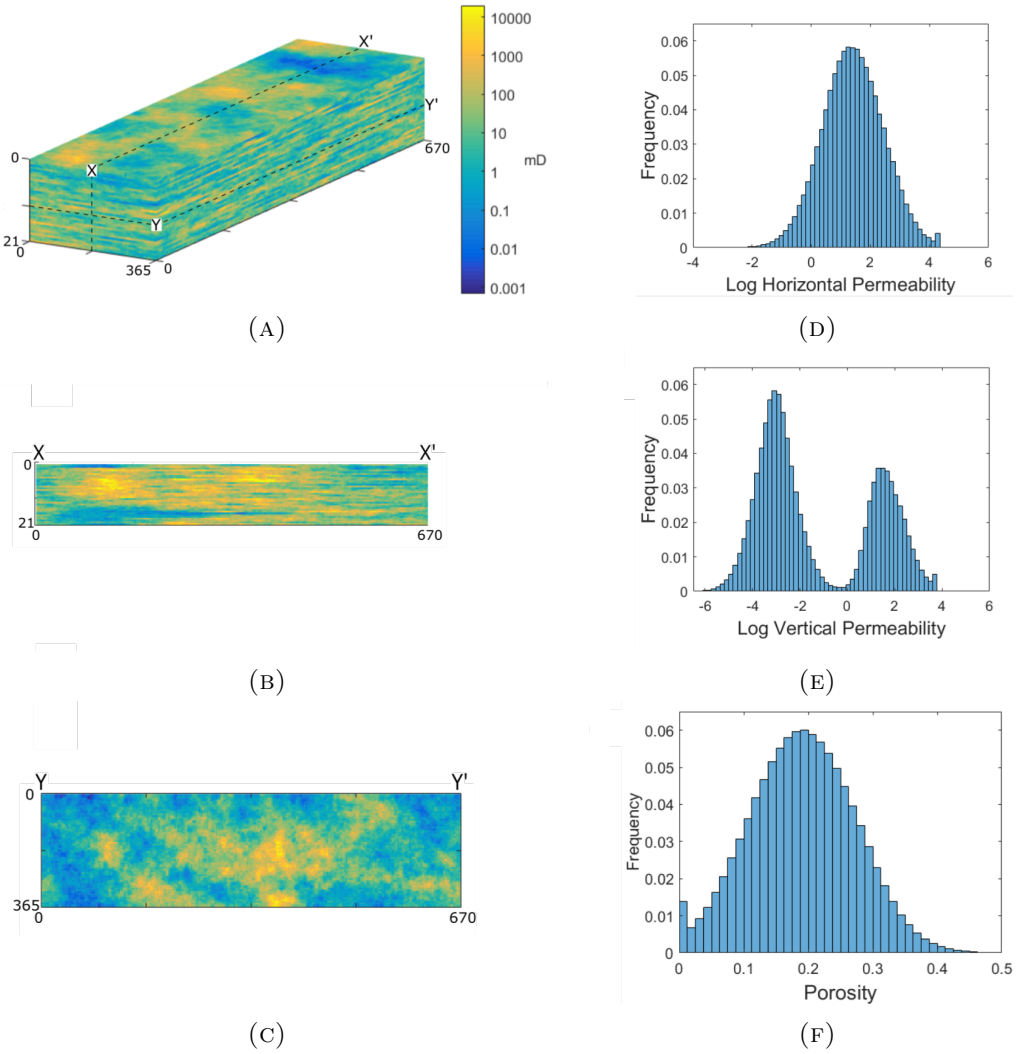


FIGURE 4.3: Petrophysical properties within the Upper SPE 10 Model. Plots (A-C) show the spatial distribution of horizontal permeability in (A) 3D; (B) vertical cross section (X-X') and (C) horizontal cross section (Y-Y'). Dimensions in metres. Plots (D-F) show the frequency distribution of (D) horizontal permeability; (E) vertical permeability and (F) porosity.

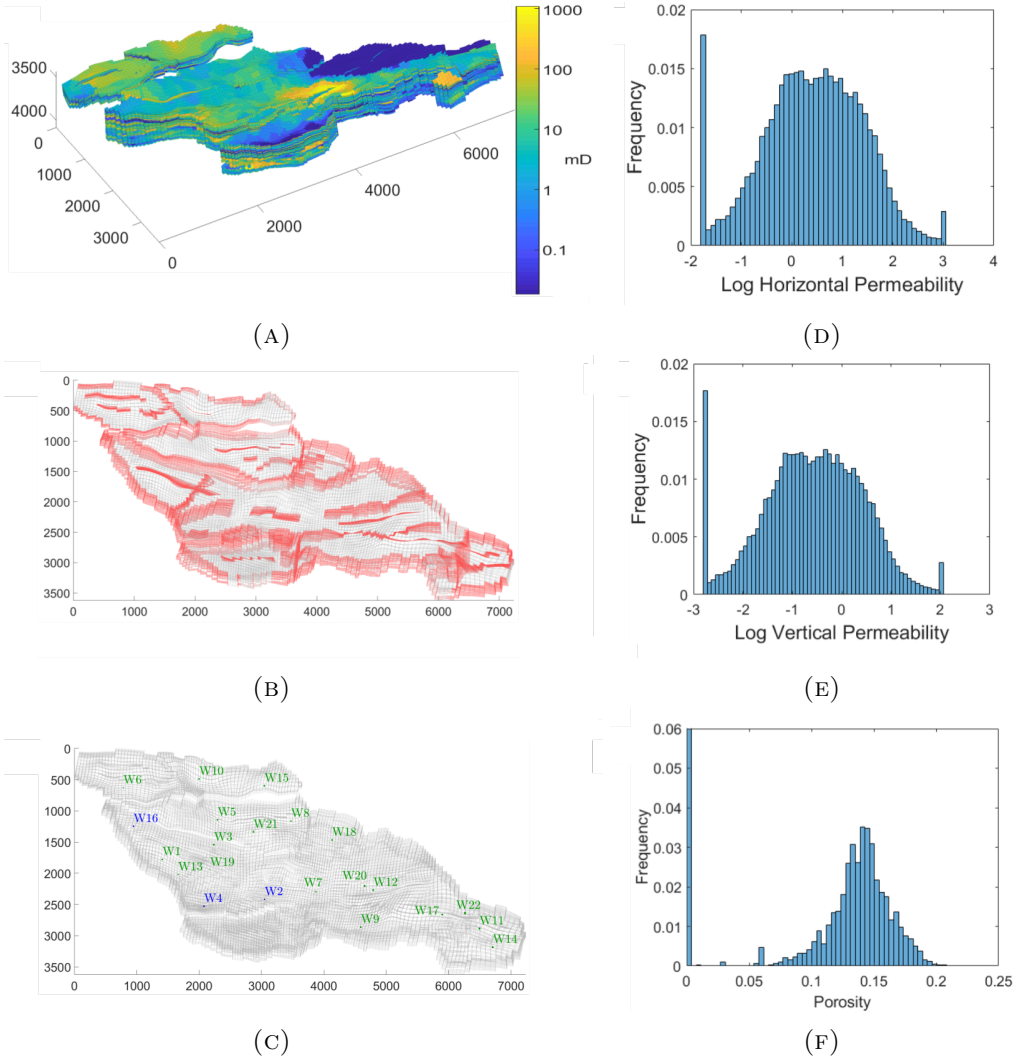


FIGURE 4.4: The H-Field Model. Plot (A) shows the 3D spatial distribution of horizontal permeability; plot (B) shows the fault blocks, where red indicates the fault plane; plot (C) shows the location of production wells in green and water injection wells in blue. Dimensions in metres. Plots (D-F) show the frequency distribution of (D) horizontal permeability; (E) vertical permeability and (F) porosity.

n_w and n_o are the exponents for the water and oil phases. The irreducible saturations used are $S_{wirr} = S_{or} = 0.2$ and the exponents are $n_w = n_o = 2$.

Gravity and capillary pressure were neglected for the SPE 10 models, following Christie and Blunt (2001). The modelled water viscosity was 1×10^{-3} Pa.s and displacements were simulated using three different modelled oil viscosities of 1×10^{-3}, 3×10^{-3} and 10×10^{-3} Pa.s respectively. This allowed the effect of mobility ratio to be tested.

The oil composition in the H-Field varies with depth, with volatile oil at the base of the hydrocarbon column evolving to gas condensate at the top of the column with no sharp change in composition. Consequently, three phase relative permeability and capillary pressure curves were required in the model. The model consists of two regions in which the oil-water capillary pressure curves are markedly different. The water-oil and gas-oil relative permeability curves are uniform in the model across both regions

The Leverett J-Function was used to scale the water-oil and gas-oil capillary functions to the rock porosity and permeability. The modelled water viscosity is 0.35×10^{-3} Pa.s while the hydrocarbon viscosity is modelled using the compositional viscosity correlation of Lorenz, Bray, and Clark (Lohrenz et al., 1964) ranging from $0.07 - 1.91 \times 10^{-3}$ Pa.s. The remaining model parameters are summarised in Table 4.1. The water/oil displacement process in all models was simulated using commercial software.

4.2.5 Well placements and controls

Two different injector/producer well configurations were used in the synthetic models to investigate whether the hypothesis tested here holds regardless of the dominant flow direction relative to the modelled heterogeneity. The first induced predominantly radial flow, using an inverted five spot pattern, with a central injector and four producers at the corners of the model. The second induced predominantly linear flow, using a line drive pattern, with a row of injectors on one face and a row of producers on the other face of the model. The production wells flowed at a fixed bottom hole pressure and the injection well(s) flowed at a fixed injection rate. For the H-Field case, the flow directions were dictated by the well placements chosen for the field development. The production and injection wells were set to flow at the historic (measured) rates.

TABLE 4.1: Model data

Data	Lower SPE 10	Upper SPE 10	H-Field
Grid	$60 \times 220 \times 50$	$60 \times 220 \times 35$	$58 \times 145 \times 40$
Grid dimensions (m)	$365 \times 670 \times 30$	$365 \times 670 \times 21$	$3500 \times 7000 \times 500$
Initial Pressure (Pa)	414×10^5	414×10^5	568×10^5
Surface densities (kg/m^3)	$\rho_n = 850$ $\rho_w = 1025$	$\rho_n = 850$ $\rho_w = 1025$	$\rho_n = 600$ $\rho_w = 1100$
Rock compressibility (Pa^{-1})	1.00×10^{-11}	1.00×10^{-11}	5.20×10^{-10}
Water formation volume factor	1.01	1.01	1.02
Water viscosity (Pa.s)	1.00×10^{-3}	1.00×10^{-3}	0.35×10^{-3}
Water compressibility (Pa^{-1})	4.35×10^{-10}	4.35×10^{-10}	0
Oil viscosity (Pa.s)	1.0×10^{-3} 3.0×10^{-3} 10.0×10^{-3}	1.0×10^{-3} 3.0×10^{-3} 10.0×10^{-3}	Lorentz-Bray-Clark viscosity correlation Range: $0.07 - 1.91 \times 10^{-3}$

4.3 Methodology

The methodology used in this chapter removed the cell-to-cell variability in petrophysical properties while keeping the grid resolution fixed. The flow behaviour was then measured using a 'Goodness of Fit' between the well responses of the refined models and the corresponding base model. The following well responses were chosen for the synthetic models: (i) oil rate, (ii) water cut (the fraction of the produced fluid that is water) and (iii) the bottom hole pressure of the injection well(s). For the H-Field model, the well responses used for the Goodness of Fit were (i) gas rate; (ii) water cut and (iii) the bottom hole pressure of the injection wells. In addition to these 'global' parameters, the first arrival time of water (i.e. the time of water breakthrough) at the production wells was also tested in all models. Water breakthrough time is sensitive to the 'local' flow around the production wells.

4.3.1 Goodness of fit

The normalised root-mean square deviation was used to determine the Goodness of Fit of an individual well response for each well

$$E_{r,w} = 1 - \sqrt{\frac{\sum_{t=1}^{T}(y^*_{r,w,t} - y_{r,w,t})^2}{\sum_{t=1}^{T}(y^*_{r,w,t})^2}} \tag{4.2}$$

where $E_{r,w}$ is the Goodness of Fit for a given response (r) in a given well (w), $y^*_{r,w,t}$ is the well response on the base model and $y_{r,w,t}$ is the well response on the refined model. The Goodness of Fit ranges between -inf (bad fit) and 1 (perfect fit). The averaged Goodness of Fit, for a given response over all the wells, is then given by E_r

$$E_r = \frac{\sum_{w=1}^{W} E_{r,w}}{W} \tag{4.3}$$

Finally, $\overline{E}$ is the Goodness of Fit for the whole reservoir, averaged over all of the wells and all of the well responses

$$\overline{E} = \frac{\sum_{r=1}^{N} E_r}{N} \tag{4.4}$$

4.3.2 Removal of cell-by-cell variability

The workflow removed cell-by-cell variability in petrophysical properties in a two-step process. First, the base model was segmented into a number of discrete domains with internally homogeneous petrophysical properties. Uniform petrophysical values were assigned to each segment, calculated using the arithmetic average of the cell-based values within that segment. A series of simulations were then run on each segmented model. Flow behaviour was compared using the Goodness of Fit described in the previous section (Equation 4.4). The optimal number of segments was defined as the number of segments above which the Goodness of Fit between segmented and base models did not significantly increase. Second, the number of discrete domains in the optimum segmented model was reduced by using a clustering algorithm based on neighbourhood filtering. The Goodness of Fit of the subsequent clustered model is then determined. The optimal window size (in terms of Goodness of Fit) depends on the connectivity of the domains and was determined by trial and error. The neighbourhood algorithm is most suited to a Cartesian grid as it assumes simple neighbourhood connections. Consequently, the clustering of the H-Field model (built on a corner point grid) was not optimal, but, as will be shown later, proved sufficient.

The workflow implemented the following steps:

Step 1.1: The log-space distribution of the horizontal permeability was used to divide the data into Z discrete *segments*. This was done by dividing the range $[\min(log_{10}(K_H)),\ \max(log_{10}(K_H))]$, where K_H is the horizontal permeability field, into Z non-overlapping, equal (in range) segments.

Step 1.2: An indicator function $I(x)$ was introduced, such that $I(x) = 1$ if the horizontal permeability at grid-block x is a member of Segment 1, $I(x) = 2$ if the horizontal permeability is a member of Segment 2, and so on, i.e

$$I : X \rightarrow \{1, 2, ...Z\}$$

$$I(x) = \left\{ \begin{array}{ll} 1, & \text{if } K_H(x) \in \text{Segment 1} \\ 2, & \text{if } K_H(x) \in \text{Segment 2} \\ \vdots & \\ \text{Z}, & \text{if } K_h(x) \in \text{Segment Z} \end{array} \right\} \tag{4.5}$$

where x is the grid cell number and Z is the total number of segments. The same indicator function was used to segment the vertical permeability and porosity.

Step 1.3: The property values within each segment were homogenised to yield a single value for each. Porosity was averaged using the volume-weighted arithmetic mean. Horizontal permeability was averaged using an arithmetic average and vertical permeability using a geometric average.

Step 1.4: The indicator function was used to distribute the averaged properties on the original grid. The resulting model is now called a 'segmented' model. Figure 4.5a shows an example segmentation of the horizontal permeability in the Lower SPE 10 Model using $Z = 3$, i.e. three segments.

Step 1.5: The Goodness of Fit ($\bar{E}$) of the flow performance between the segmented and base models was then calculated based on the results of numerical simulations of flow in each model. Steps 1-4 were repeated, increasing the number of segments (Z) after each iteration, until no significant improvement in $\bar{E}$ was seen. At this stage, this 'optimal' segmented model will contain fewer and larger domains than were present in the base model. However, various isolated domains comprising just one or a few cells remained in the model.

Step 2.1: A sliding neighbourhood algorithm (Thompson and Shure, 1995) was applied on the segmented model (Figure 4.5). The algorithm scans the model, cell-by-cell, creating a 'window' containing a chosen number of cells around each input cell (in this example, the window size is $3 \times 3 \times 3$). The input cell is then replaced by the modal value of all cell values in the cube. This was repeated for each cell of the model. Figure 4.5c shows an example of a clustered model. The homogeneous regions are now referred to as *domains*. This step reduces the total number of domains by removing isolated groups of grid cells that can be a few cells wide.

Step 2.2: The flow performance of the clustered model was compared to that of the parent segmented model. The optimal window size was defined as the one which gave the closest fit (based on Goodness of Fit) to the optimal segmented model.

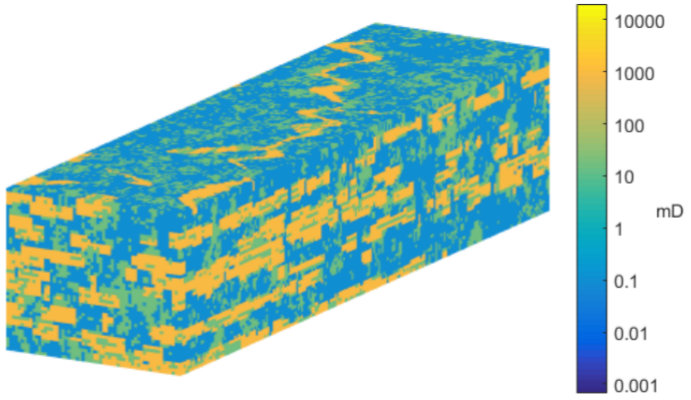
Step 2.3: The final Goodness of Fit ($\bar{E}$) of the flow performance between the optimal clustered and base models was then calculated based on the results of numerical simulations of flow in each model.

4.4 Results

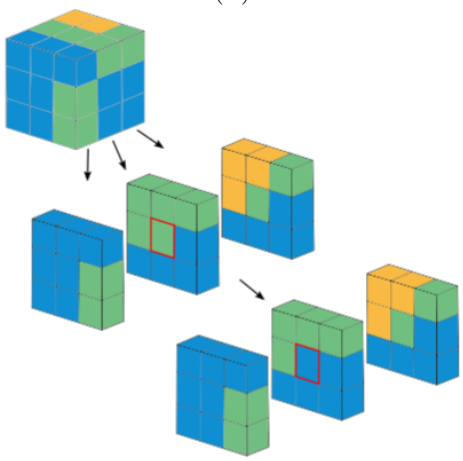
Results from the Lower SPE 10 Model at each step of the workflow are first reported to illustrate application of the workflow and show how the final Goodness of Fit results were obtained. For the other test cases, only the final Goodness of Fit results are reported, as they show similar behaviour to the Lower SPE 10 Model and the individual workflow steps were the same.

4.4.1 Lower SPE 10 model: Segmentation and Clustering

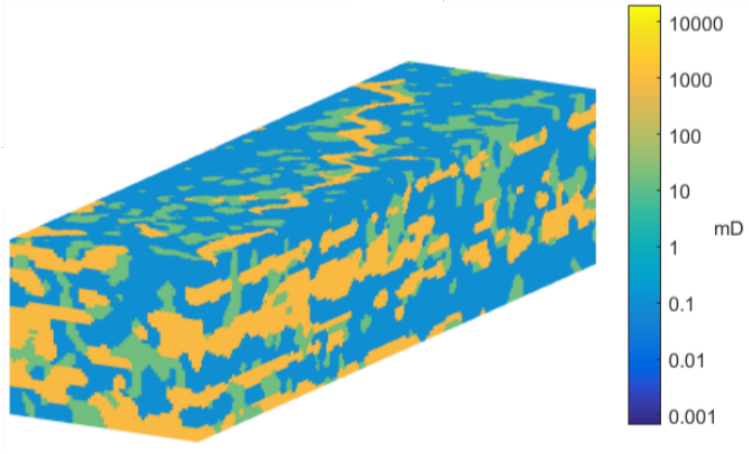
We first consider the Goodness of Fit for the segmented (but not clustered) Lower SPE 10 Model for the various fluid properties tested and the inverted five spot well pattern (inducing primarily radial flow) (Figure 4.6A). The solid lines denote the Goodness of Fit including only 'global' measures of well response i.e. production rates and pressures. The dashed lines denote the Goodness of Fit with both 'global' and 'local' well responses (water breakthrough time) included. Even with only two segments, the Goodness of Fit for the segmented model calculated without water breakthrough is greater than 88%, except for the case with the highest oil viscosity. A two segment model captures the contrast between high permeability, channelised sandstones and low permeability mudstones. However, increasing the number of segments beyond two further improves the fit and, at 10 segments or more, the Goodness of Fit for the segmented model is greater than 93% and insensitive to the oil and water viscosity contrast. Further increasing the number of segments beyond 10 yields a very slow rate of increase in the fit, tending towards one as the number of segments approaches the number of cells in the model. Note that 10 segments corresponds to a very small number of unique values of porosity and permeability compared to the $660,000$ cells in the base model. The inclusion of water breakthrough in the Goodness of Fit measure causes a large increase in the mismatch with a small number of segments. The increase in mismatch with few segments is due to the loss of connectivity of facies in the near-well regions. However, these connected flow paths are recovered by increasing the number of segments, mismatch decreases plateauing at only 10 segments..



(A)



(B)



(C)

FIGURE 4.5: Segmentation and clustering of the Lower SPE 10 Model. (A) Segmented model with three segments. (B) 3x3x3 cube around an input cell during clustering. The central cell's value is then replaced with the modal value of the neighbouring cells; here a green permeability value is replaced by a blue one. (C) Clustered model. The cell-to-cell variability is removed, creating more geologically meaningful *domains*.

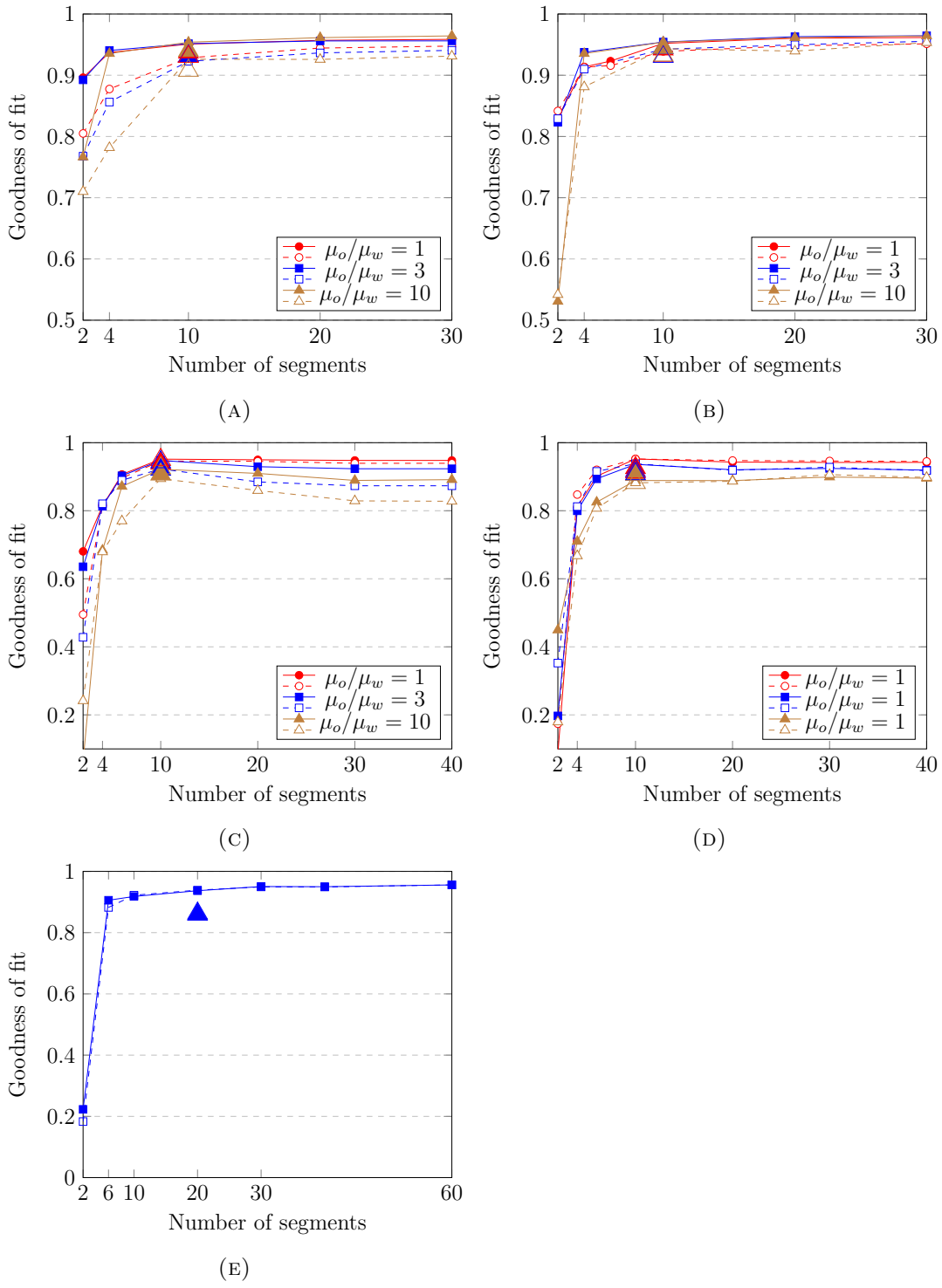


FIGURE 4.6: Goodness of Fit (GOF) as a function of segment number. (A) Lower SPE 10 Model with the inverted five spot well configuration; (B) Lower SPE 10 model with the line drive well configuration; (C) Upper SPE 10 Model with the inverted five spot well configuration; (D) Upper SPE 10 Model with the line drive well configuration; (E) H-Field model. Points with lines denote the segmented models without clustering. The different line markers denote the different fluid viscosity ratios. Dashed and solid lines denote the GOF including and excluding water breakthrough, respectively. Unfilled and filled triangles denote the GOF with and without water breakthrough for the clustered models.

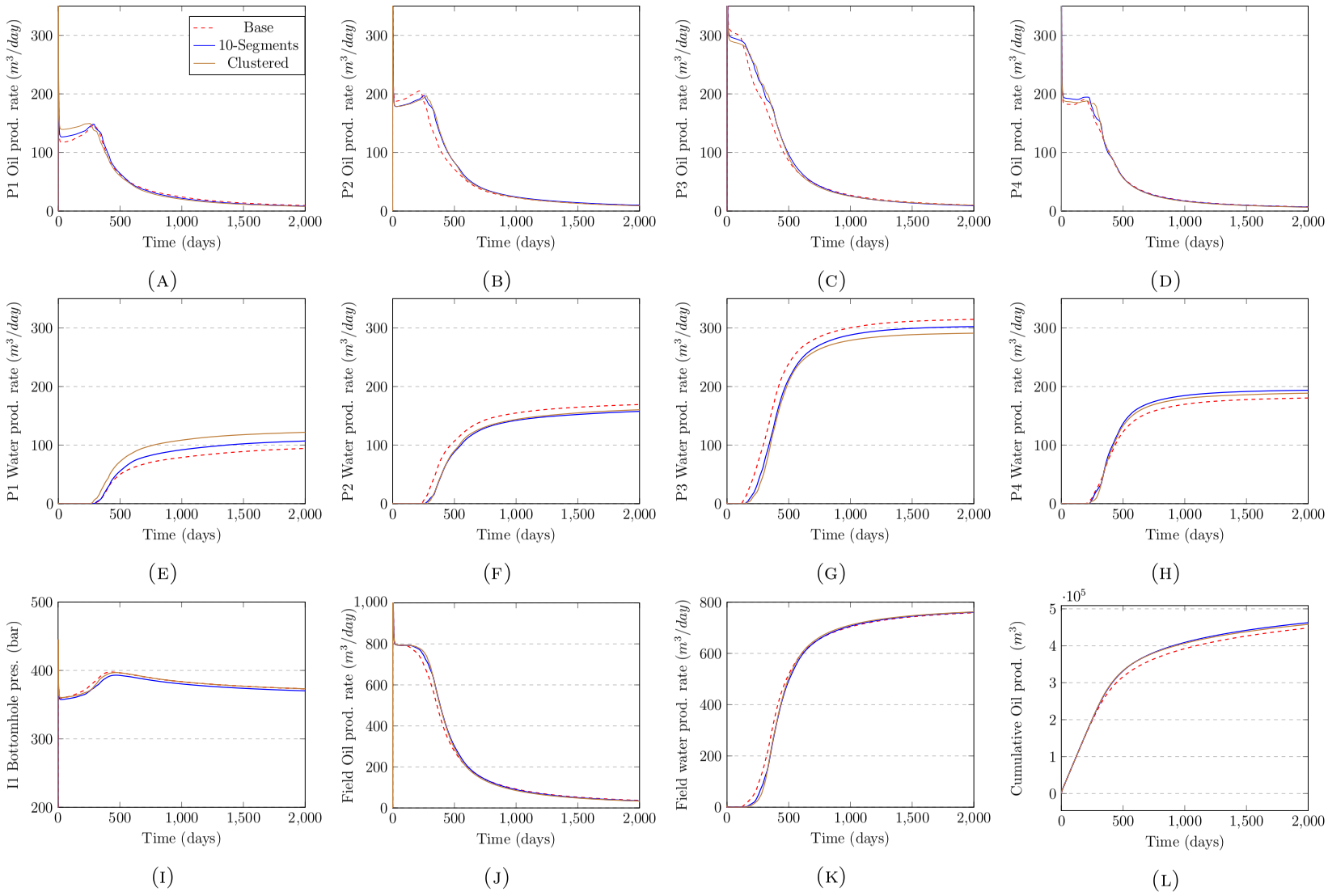


FIGURE 4.7: Well and reservoir responses of the base, segmented and clustered models of the Lower SPE 10 Model and the inverted five spot well configuration with uniform oil and water viscosities. Plots (A-D) show oil production rate as a function of time for each producer well. Plots (E-H) show water production rate as a function of time for each producer well. Plot (I) shows the bottom hole pressure for the water injection well. Plots (J-L) show, respectively, the total reservoir oil production rate, water production rate and cumulative oil production as a function of time.

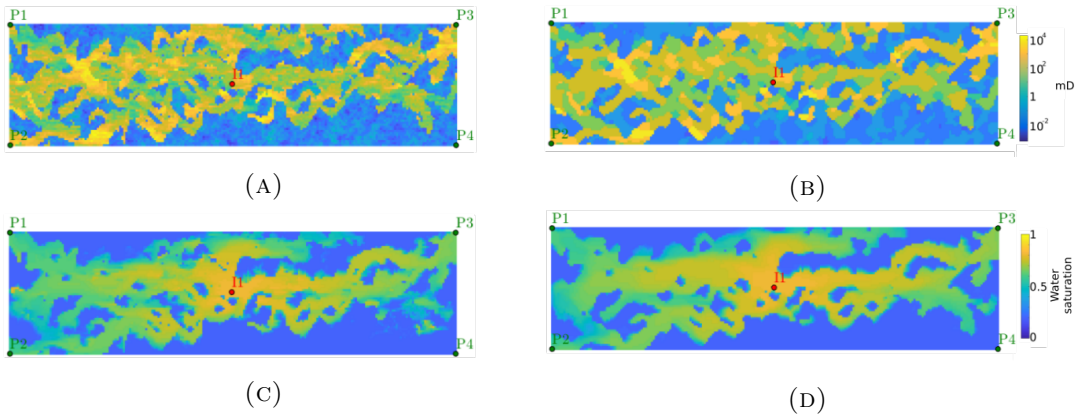


FIGURE 4.8: Horizontal cross sections through the Lower SPE 10 Model showing horizontal permeability and water saturation at a given time step during production via the inverted five spot well configuration with uniform oil and water viscosities. Plots (A) and (B) show, respectively, the permeability at a horizontal section through the base and 10-segment and clustered models. Plots (C) and (D) show the water saturation at a given timestep on the same horizontal section.

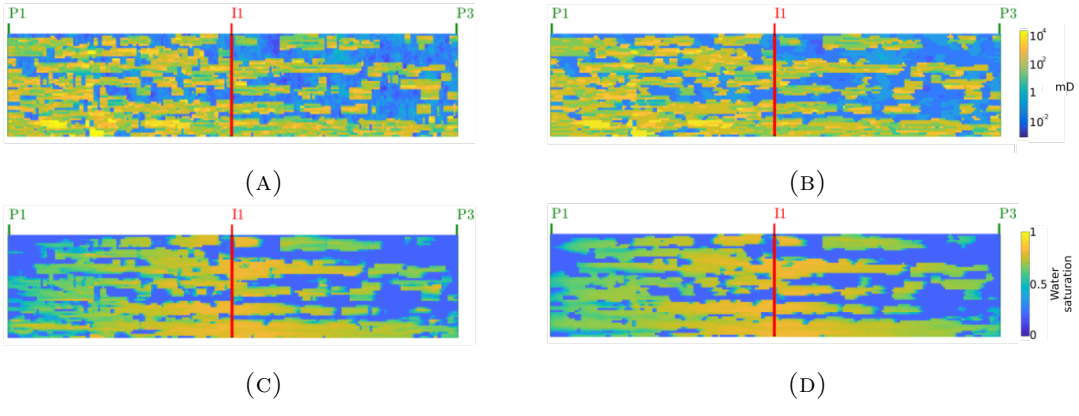


FIGURE 4.9: Vertical cross sections through the Lower SPE 10 Model showing horizontal permeability and water saturation at a given time step during production via the inverted five spot well configuration with uniform oil and water viscosities. Plots (A) and (B) show the vertical section through the base and 10-segment and clustered models, respectively. Plots (C) and (D) show the water saturation at the same vertical section.

The Goodness of Fit for the same test case with the line drive well pattern (inducing primarily linear flow) shows similar behaviour, except that the fit for the two segment model is lower, especially with the higher oil viscosity (Figure 4.6b). Including water breakthrough has a more limited effect on the Goodness of Fit in this case with linear flow than it did with primarily radial flow. However, at 10 segments or more, the Goodness of Fit for the segmented model is again high and identical irrespective of the oil and water viscosity contrast. Further increasing the number of segments beyond 10 yields a very slow rate of increase in the fit. The 10-segment model was therefore considered optimal for the Lower SPE 10 Model and was taken into the clustering step.

The clustering algorithm was applied using a window size of $3 \times 3 \times 1$ twice sequentially, yielding approximately 2,000 individual domains. The Goodness of Fit of the clustered models is shown by the triangles in Figure 4.6. Clustering causes the Goodness of Fit to decrease by a few percent (up to 4%), as confirmed by examination of the individual well and reservoir responses (Figure 4.7). The model with just 10 segments (and, in Figure 4.7, equal oil and water viscosities and the inverted five spot well pattern) provides a close match to the oil and water rates in each production well (Figures 4.7A-H). Not only were the production rates closely matched, but the water breakthrough time was also captured in each well. The bottom hole pressure in the injection well (Figure 4.7I) shows very good agreement with the base model. Most of the discrepancy in a given response occurs at relatively early time (first 400 days, or 20% of simulated production). The 10-segment model also provides a good match to the reservoir responses of oil and water production rate, and cumulative oil produced (Figure 4.7J-L).

The key geological heterogeneity that the Lower SPE 10 Model needed to capture was the connectivity of the high permeability channelised sandbodies (Figures 4.8 and 4.9; see also Figure 4.1). The two segment model did reasonably well in this respect, capturing the high permeability channelised sandstones and low permeability mudstones. However, the geostatistical method used in the original model to populate permeability within lithofacies created some connections between channelised sandstones via one or a few cells in the mudstone with intermediate permeability values. Increasing the number of segments to 10 preserved these intermediate permeability connections, yielding very similar connectivity and, therefore, sweep patterns in the base and 10-segment models (Figure 4.8-4.9). The clustering step did not significantly modify the permeability distribution. Thus a model with just 10 unique values of porosity

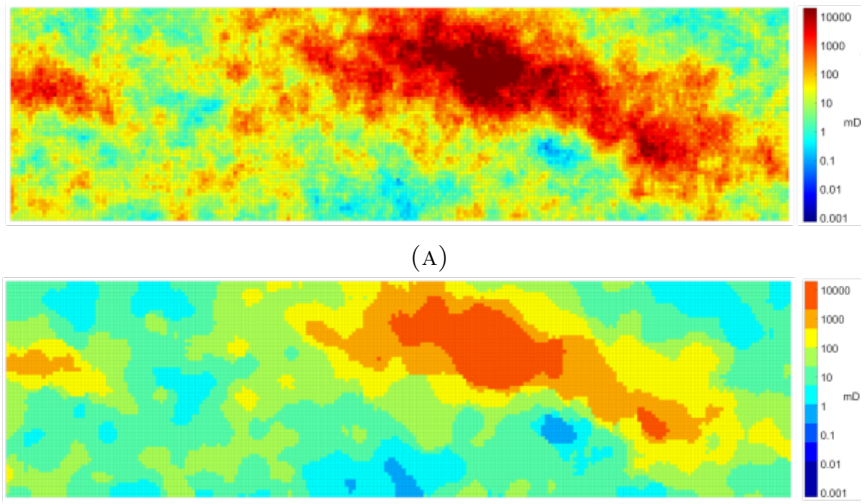
and permeability, grouped into a few thousand domains, was able to replicate the two-phase flow behaviour of a model with 660,000 cells, each of which contains a different value of porosity and permeability to its neighbour, irrespective of the well configuration or fluid properties tested.

4.4.2 Upper SPE 10 model: Summary of Goodness of Fit results

The Goodness of Fit results for the same study on the Upper SPE 10 Model show similar behaviour to those of the Lower SPE 10 Model (Figure 4.6c - 4.6d). The Goodness of Fit for two segments is lower than for the Lower SPE 10 Model, but increases as the number of segments increases. At 10 segments or more, the Goodness of Fit for the segmented model is high (90%) irrespective of the oil and water viscosity contrast or well configuration. Further increasing the number of segments beyond 10 yields a very slow rate of increase in the fit. Including water breakthrough in the Goodness of Fit in this case had a larger effect for the highest viscosity ratio and the inverted 5 spot well pattern. The Goodness of Fit at 20 or more segments was lower. This was found to be due to a few cells very close to the wells. The effect for the line drive well configuration was negligible. Overall, for both well patterns, the 10-segment model was considered optimal for the Upper SPE 10 Model and was taken into the clustering step.

The clustering algorithm was run with a window size of $6 \times 6 \times 1$ yielding approximately 850 individual domains. The base and final clustered models are shown in Figure 4.10. The Goodness of Fit of the clustered models is shown by the triangles in Figure 4.6. Clustering reduced the Goodness of Fit by a few percent but, similar to the Lower SPE 10 Model, the decrease was small.

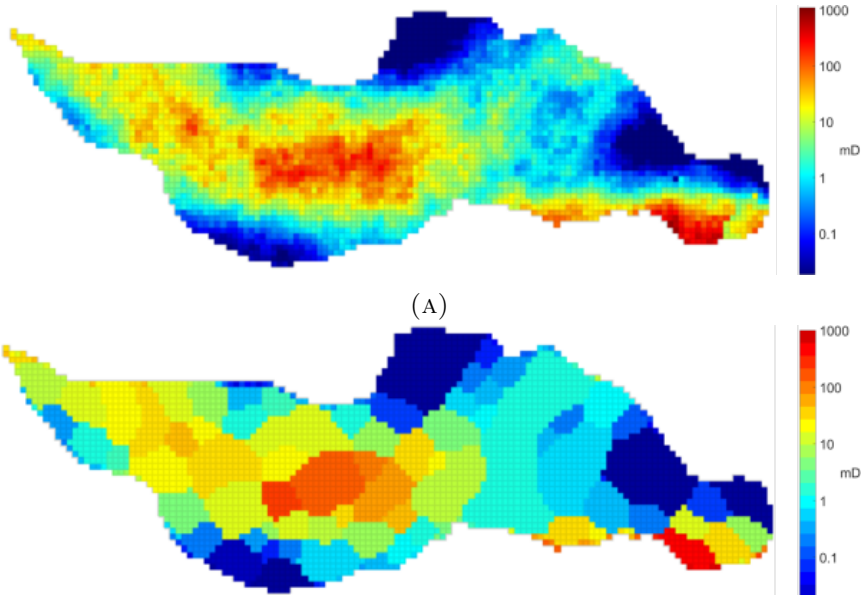
Unlike the Lower SPE Model, the Upper SPE 10 shows no strongly correlated permeability distribution and there are no clear geological heterogeneities that should be captured in the model. Thus the two segment model yields a significantly lower Goodness of Fit for the Upper SPE 10 Model as compared to the Lower SPE 10 Model. However, at 10 segments, the segmented and clustered models again yield a close match to the base model. A model with just 10 unique values of porosity and permeability, grouped into hundreds of domains, was able to replicate the two-phase flow behaviour of a model with 462,000 cells, each of which contains a different value of porosity and permeability to its neighbour, irrespective of the well configuration or fluid properties tested.



(A)

(B)

FIGURE 4.10: Horizontal sections through the Upper SPE 10 Model showing horizontal permeability. Plot (A) shows the base Upper SPE 10 model; plot (B) shows the Upper SPE 10 model with 10 segments after clustering.



(A)

(B)

FIGURE 4.11: Horizontal sections through the H-Field Model showing horizontal permeability. Plot (A) shows the base H-Field model; plot (B) shows the H-Field model with 20 segments after clustering.

4.4.3 H-Field Model: Summary of Goodness of Fit results

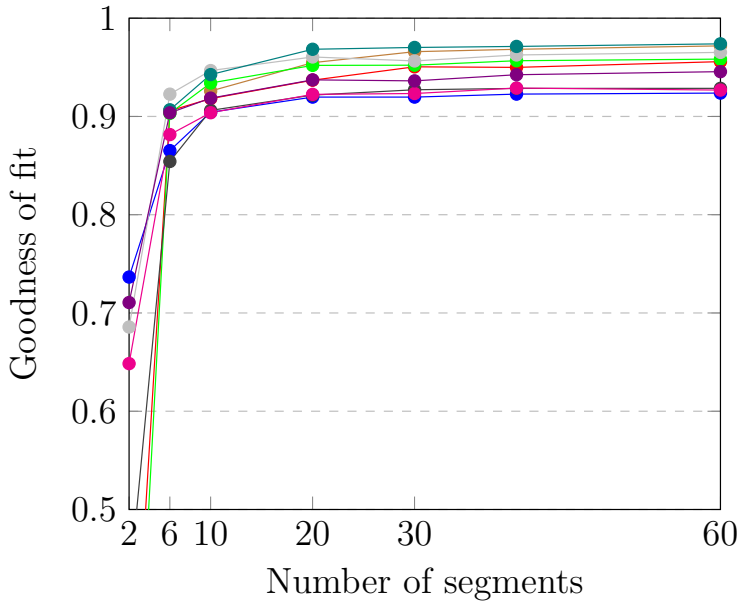
We finish by reporting the Goodness of Fit results for the same study on the H-Field Model (Figure 4.6e). Despite the significantly higher complexity of the H-Field, in terms of geological heterogeneity, number of wells, and multi-phase flow, the results are similar to the synthetic SPE 10 test cases. The Goodness of Fit for two segments is low, but increases as the number of segments increases. At 20 segments or more, the Goodness of Fit for the segmented model is high. Further increasing the number of segments beyond 20 yields a very slow rate of increase in the fit. The 20-segment model was therefore considered optimal for the H-Field Model and was taken into the clustering step. The model was clustered using three iterations of the algorithm, with a window size of $5 \times 5 \times 5$, then two with $5 \times 5 \times 1$, yielding approximately 850 individual domains. The H-Field model was more sensitive to clustering than the synthetic SPE 10 test cases; however, the mismatch was still small.

The H-Field model shown in Figure 4.4 is only one geological realisation. Applying the same statistical description of the petrophysical properties, many more realisations are possible. Figure 4.12 shows the Goodness of Fit for 10 realisations of the H-Field model. While there is significant sensitivity with < 20 segments, the increase in Goodness of Fit is very slow with 20 or more segments. Thus the observed behaviour is not specific to a single model realisation.

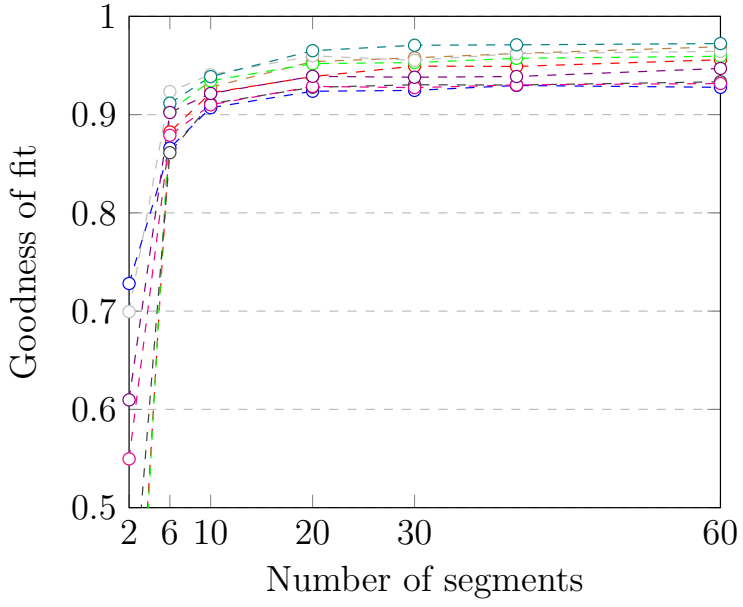
The H-Field model captures many geological heterogeneities, including complex structure with several fault blocks, and diagenetically modified permeability values controlled by a multi-stage filling history during initial charging with oil. Perhaps because of this, more segments and domains were required to reproduce the base model behaviour. Nevertheless, a model with just 20 unique values of porosity and permeability, grouped into a few hundred domains, was able to replicate the multi-phase, multi-component flow behaviour of a model with $146,000$ cells, each of which contains a different value of porosity and permeability, to its neighbour.

4.5 Discussion

The results presented here indicate that grid-based reservoir models containing many unique values of petrophysical properties (of order hundreds-of-thousands in the examples tested) varying on a cell-to-cell basis can be collapsed into a much smaller number of larger but more geometrically complex domains which



(A)



(B)

FIGURE 4.12: Goodness of Fit of segmented models without clustering, as a function of segment number for 10 realisations of the H-Field. (A) Goodness of Fit excluding water breakthrough; (B) Goodness of Fit including water breakthrough.

are internally homogeneous, irrespective of the reservoir geology, fluid properties or well configuration. Thus, while it is always possible that testing of further cases may contradict this, the evidence presented here suggests that cell-to-cell scale variability is not necessary in reservoir models. Modelling workflows should instead focus on capturing the domains that represent spatially correlated variability in petrophysical properties (particularly permeability) in the most realistic and computationally efficient manner. The correlated variability reflects the underlying geological heterogeneity that is important to flow.

In the approach adopted here, 'domain-based' models were created by segmenting and clustering existing grid-based models. However, we adopted this approach only to test the effect of removing cell-to-cell scale variability from grid-based models, and we do not recommend this workflow for model construction. The important finding here is that capturing domains that represent spatially correlated variability in petrophysical properties is key. This finding offers the prospect of alternative modelling workflows to the grid-based methods used ubiquitously to date.

One approach to capture these domains is to model the surfaces that bound them. Surface-based modelling (or boundary representation) has been suggested as an alternative to grid-based modelling to capture a wide variety of different geological heterogeneity types, including faults (Julio et al., 2015), stratigraphy (Sylvester et al., 2015), facies and lithological boundaries (Hassanpour et al., 2013; Ruiu et al., 2016), and fractures (Belayneh et al., 2006; Geiger et al., 2012; Paluszny et al., 2007). Indeed, all geological heterogeneity that impacts the spatial distribution of petrophysical properties can be modelled using surfaces (Jackson et al., 2013). Moreover, the surfaces can be modelled using a parametrised description without reference to a predefined grid or mesh (Graham et al., 2015b; Jacquemyn et al., 2018), significantly increasing computational efficiency. A mesh is created only when required for numerical calculations and preserves the surface-based representation of geological heterogeneity (Jackson et al., 2015). Petrophysical properties in each element of the mesh are inherited from the parent domain i.e. no further property modelling is required. If significant heterogeneity is expected within a domain, additional surfaces can be introduced. Therefore such models omit cell-to-cell scale variability. The models are not less complex or less realistic than grid-based models; as we show here, they simply omit variability that is not important to flow. Indeed, surface-based models can much better capture correlated heterogeneities with complex geometries that are important to flow (Jackson et al., 2009; Deveugle et al., 2014; Graham et al.,

2015b).

In the approach adopted here, we assumed that each base model yields the 'correct' flow behaviour for the corresponding reservoir, and the removal of cell-to-cell scale variability was tested by comparison against the flow behaviour of the base model. Yet the base models may not have captured important geological heterogeneities present in the reservoir. For example, the Upper SPE 10 Model was originally constructed to represent reservoirs deposited in a shallow-marine environment. Numerous studies have shown that facies architecture is a key control on flow in such reservoirs, with facies types corresponding to order-of-magnitude contrasts in horizontal and vertical permeability (Ringrose et al., 2008; Deveugle et al., 2014). The thickness and relative proportion of each facies type strongly controls flow, along with interfingering of facies along inclined surfaces termed clinoforms. Calcite cements are also a common feature of such reservoirs and are often associated with clinoform surfaces (Sech et al., 2009; Jackson et al., 2009). Yet, despite the importance of clinoform surfaces in controlling the spatial arrangement of key geological heterogeneities, they are typically neglected in reservoir models because their inclined geometry relative to reservoir bounding surfaces means they are difficult to represent using grid-based approaches.

There is no evidence that the key heterogeneities described above are captured in the Upper SPE 10 Model (Figure 4.3) and, despite its ubiquitous use in later studies, it likely provides a poor representation of flow in shallow-marine reservoirs (White and Barton, 1999; Sech et al., 2009; Jackson et al., 2009; Enge and Howell, 2010; Deveugle et al., 2014; Graham et al., 2015b amongst many others). Figure 4.13a shows a surface-based model of the SPE 10 geology (Jacquemyn et al., 2018). The upper part of the model represents a reservoir deposited in a shallow-marine environment and corresponds to the Upper SPE 10 Model; the lower part of the model represents a fluvial reservoir and corresponds to the Lower SPE 10 Model. The surface-based model was constructed entirely using parametrised surfaces (in this case, Non Uniform Rational Basis Splines or NURBS) without reference to a predefined grid or mesh. The surfaces have been assembled to create volumes that correspond to geological domains. Domains of different facies/lithologies are shown by the different colours. In the upper part of the model, the domains correspond to different shallow-marine sandstone facies types; in the lower part of the model, domains corresponding to channelised sandstones. Domains representing non-reservoir mudstones have not been visualised, but are present in the model.

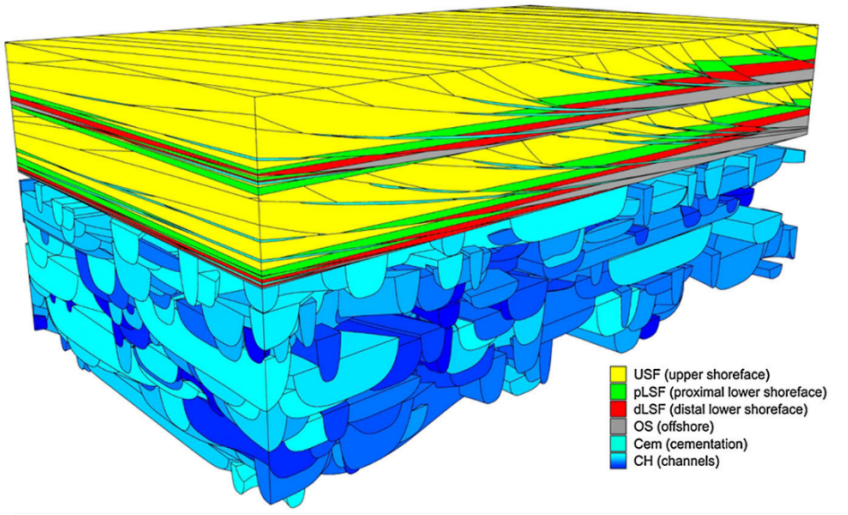
A further test case, left for future work, could be to discretise this surface-based of the lower SPE 10 model using conventional grids and run it through the same algorithm (Section 4.3). With a better representation of the geological heterogeneities we would expect a better performance than the original lower SPE 10 model.

The surface-based representation of the Upper SPE 10 geology includes clinoforms and the shallow marine facies interfinger along these surfaces; the model also includes patches of calcite cement along clinoform surfaces. Thus, although the model does not include cell-to-cell variability in petrophysical properties, it includes the key correlated heterogeneities observed to impact flow (Jackson et al., 2009; Graham et al., 2015b). Similarly, the surface-based representation of the Lower SPE 10 geology includes channelised sandbodies of varying width and sinuosity and, although the model does not include cell-to-cell scale variability, it captures the spatial distribution and connectivity of the sandbodies, which is the key heterogeneity observed to impact flow. Such a model can be used as the initial input to new generation simulators where the model domain is discretised using adaptive watertight unstructured meshes. to optimise computational effort when solving the governing flow equations (Mostaghimi et al., 2015; Jackson et al., 2015; Gomes et al., 2017; Salinas et al., 2018a).

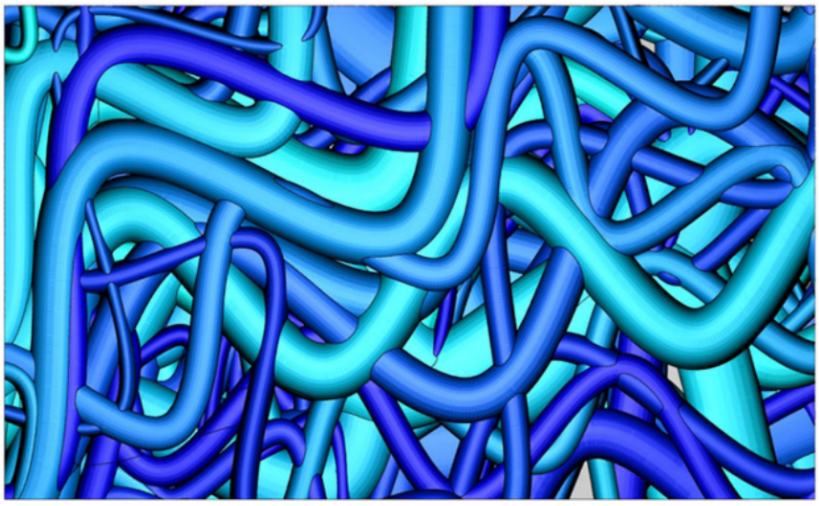
There are a few outstanding issues for surface-based modelling methods. While it is possible to accurately represent the complex geometries of geology, conditioning these models to control data, such as well or seismic data, remains a challenge (Bertoncello et al., 2013). Another challenge is to update surface-based models to better match observed behaviour (history match). These challenges are by no means insurmountable (e.g. Trani and Graham, 2016); however, further work is needed to develop workflows to condition and history match surface-based models.

4.6 Conclusions

We show that grid-based reservoir models containing a large number of petrophysical property values that vary on a cell-to-cell basis can be collapsed into a much smaller number of larger and internally homogeneous but more geometrically complex geological domains, irrespective of the reservoir geology, fluid properties or well configurations tested. We argue that cell-to-cell scale variability is not necessary in reservoir models to capture multi-phase flow. Although the geometrically complex domains can be represented in standard grid-based



(A)



(B)

FIGURE 4.13: Surface-based model inspired by SPE 10 model 2. (A) Full model; (B) Lower, fluvial section; from below (Jacquemyn et al., 2018).

models, surface-based reservoir modelling methods are more flexible and better able to capture the complex geometries of geological domains in a realistic and computationally efficient manner. Numerical solutions to the governing flow equations can be obtained in such models using adaptive unstructured meshes.

Chapter 5

Dynamic adaptive-mesh optimisation for multi-phase flow in geological formations

The existence of localised phenomena such as steep saturation, concentration and pressure gradients in multi-phase flow motivates the need for temporally and spatially adaptive meshes. Dynamic adaptive meshes have the potential to increase the accuracy of numerical simulations of flow through geological formations, in a computationally efficient manner. In this chapter, we describe the dynamic adaptive-mesh optimisation (DAMO) algorithm utilised in the Imperial College Finite Element Reservoir SimulaTor (IC-FERST).

Contents

5.1 Introduction 92

5.2 Dynamic adaptive-mesh optimisation 93

5.2.1 Metric formation 93

5.2.2 Mesh optimisation 95

5.2.3 Mesh to mesh interpolation 97

5.2.4 Accounting for high Courant numbers 98

5.3 Test cases 100

5.3.1 Counter-current Spontaneous Imbibition 102

5.3.2 DNAPL infiltration 104

5.3.3 Surface-based models 106

5.4 Results 113

5.4.1 Spontaneous imbibition 113

5.4.2 DNAPL infiltration 114

5.4.3 Fracture model (SBM 1) 116
5.4.4 Channel model (SBM 2) 116
5.4.5 Fault model (SBM 3) 118
5.5 Cost of adaptivity 122
5.6 Discussion 126
5.7 Conclusions 128

5.1 Introduction

As discussed in earlier chapters, conventional simulations are run on fixed meshes where a single resolution is used throughout a given reservoir zone. However, in multi-phase flow in porous media, steep local gradients that are spatially and temporally variable often need to be captured at scales much lower than typical grid block sizes. With fixed meshes, this requires a fine resolution throughout the domain. High performance computing and massively parallel codes, have made it possible to simulate very large models (Dogru et al., 2009; Dogru et al., 2002). However, this can be computationally inefficient and in some cases prohibitive. One solution is to place high resolution only in regions where solution variables (e.g. pressure, saturation, concentration) are varying rapidly and low resolution elsewhere. This allows for an improved representation of transient, local flow features in a computationally efficient manner.

There are two classes of local grid refinement: Adaptive mesh refinement (AMR) and Dynamic msh optimisation (DMO). AMR is commonly used for problems with fixed wells, faults and pinchouts. DMO allows the mesh to follow fluid interfaces as it moves across the reservoir domain. However, the use of local grid refinement can limit the time steps of the non-linear solver by the Courant–Friedrichs–Lewy (CFL) condition. Local time stepping (LTS) is a promising approach which uses small time steps in nearwell regions (and other high Courant number regions) and large time steps elsewhere. Several authors have studied different approaches combining AMR and LTS (e.g. Quandalle and Besset, 1985; Mlacnik and Heinemann, 2001). However, unlike adaptive mesh refinements, local time stepping techniques are far less mature (Gander and Halpern, 2013).

Although common in free-flow problems, dynamic adaptive meshes are seldom used for multi-phase flow simulations in geological reservoirs. The biggest obstacle is the need to represent the spatially varying material properties (especially

permeability) of the reservoir. Up-, cross- or down-scaling permeability is non-trivial and would make existing dynamic adaptive-mesh optimisation (DAMO) algorithms prohibitively expensive. In this chapter, we outline a method to adapt the mesh of surface-based models during flow simulations that admits the significant advantages of DAMO observed in other computational fluid dynamics (CFD) applications (Alauzet and Loseille, 2016).

5.2 Dynamic adaptive-mesh optimisation

Mesh optimisation is used to generate the mesh to represent the geological and (evolving) fluid structures and reduce discretisation errors. Our approach retains the original complex geological structures of the surface-based models.

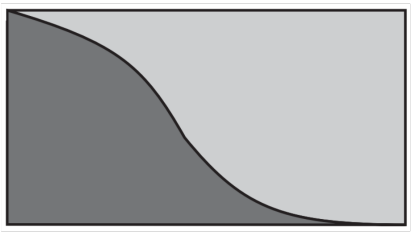
Figure 5.1 illustrates the methodology. As described earlier, surface-based models are built without reference to an underlying grid. Using unstructured triangular elements, an initial 2D mesh is built that accurately captures the complex geometries of the surface bounded domains with the minimum number of elements, within a specified error. Next, a 3D tetrahedral mesh is built within each geological domain to form an initial coarse volume mesh. This initial volume mesh is only created to ensure that the 2D mesh is capable of producing a suitable volume mesh. Nodes of the 2D mesh form a series of *master nodes*. During the adaptivity routine, master nodes are not removed or modified. This ensures that once the surface-based model is discretised the geometric integrity of that model is preserved throughout the mesh adaptivity routine and throughout the flow simulation.

Each domain is associated with certain material properties (such as permeability and porosity), which are assigned to each element in that domain. During flow simulation, the mesh is adapted to better represent the evolving structures using the series of topological operations outlined in Figure 5.2.

5.2.1 Metric formation

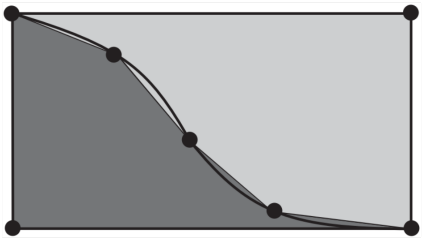
For most problems of interest, predicting the location of areas of interest that require high resolution is not possible *a-priori* and therefore an *a-posteriori* method needs to be found. The approach adopted here employs a metric based formulation which is used to guide the mesh optimisation step.

The metric is built upon the Hessian matrix, a solution dependent error measure which varies both in space and time (Pain et al., 2001). The Hessian gives



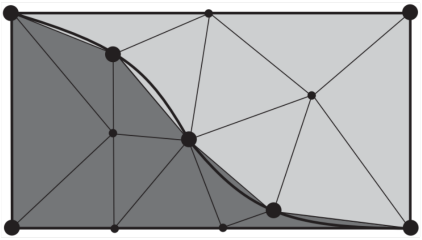
Surface-based representation of two different geologic domains of contrasting petrophysical properties (denoted by shading).

(A)



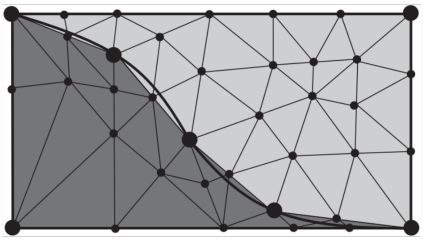
Meshing of surfaces using a 2D Delaunay triangulation that captures surface intersections and is iteratively optimized to preserve complex surface topology within a user-defined error margin. The surface nodes defined here (large points) are preserved throughout dynamic AMO.

(B)



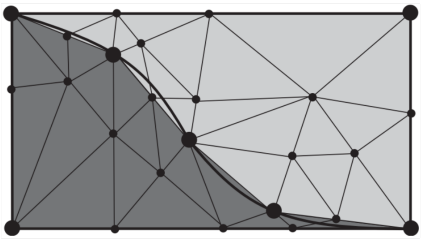
Generation of initial 3D tetrahedral mesh within each geologic domain through repeat application of the mesh adaptivity library, constrained to generate the desired number of degrees of freedom. The tetrahedral elements within each domain are assigned the values of petrophysical properties associated with that domain. The volume nodes (small points) can be moved, removed or added to during dynamic AMO.

(C)



During simulation the adaptivity routine allows dynamic AMO to flow-based fields; here the mesh has locally refined. The surface nodes remain fixed so the 2D mesh representing the surface-based geologic model is preserved. New elements created by AMO are assigned the petrophysical properties for the domain so there is no need to scale up, cross-scale or downscale f elements change size or shape, or new elements are created.

(D)



Dynamic AMO drives a previously refined mesh to coarsen again if allowed by flow-based error metrics. The surface nodes remain fixed, so the surface-based geologic model is preserved when the volume mesh coarsens. There is no need to scale up if elements change size or shape.

(E)

FIGURE 5.1: Work flow to generate and adapt unstructured meshes on surface-based models. (A) Original surface-based model depicting two domains; (B) a 2D surface mesh is built to capture the bounding surfaces; (C) an initial coarse 3D tetrahedral mesh is built within the domains; during flow simulation the volume meshes can be refined, (D), or coarsened, (E) using hr adaptivity but the geology remains intact. From Jackson et al. (2015).

information about the concavity of the solution fields at each point in every direction. This allows the adaptivity algorithm to identify anisotropies in the solution structures resulting in anisotropic and inhomogeneous mesh resolutions (Pain et al., 2001; Piggott et al., 2008; Davies et al., 2011).

The metric ($\mathcal{M}$) is calculated using the following expression (Pain et al., 2001)

$$\mathcal{M}(\mathbf{x}) = \det\left(|\mathbf{H}(\mathbf{x})|\right)^{\frac{1}{2\mathrm{p}+\mathrm{n}}} \frac{|\mathbf{H}(\mathbf{x})|}{\epsilon(\mathbf{x})} \tag{5.1}$$

where p is the degree of the polynomial of the norm, n is the number of dimensions of the problem, ϵ is a user-defined desired error and $|\mathbf{H}|$ is a modified Hessian matrix given by

$$|\mathbf{H}(\mathbf{x})| = \mathbf{Q}(\mathbf{x})^T |\Lambda(\mathbf{x})| \mathbf{Q}(\mathbf{x}), \quad |\Lambda(\mathbf{x})|_{i,j} = \begin{cases} |\lambda_i(\mathbf{x})|, & i = j \\ 0, & i \neq j \end{cases} \tag{5.2}$$

where $\{\lambda_i\}$ are the eigenvalues of the Hessian and $\mathbf{Q}$ are the ortho-normal matrix of eigenvectors.

The user can specify a minimum and maximum edge length via restrictions on the eigenvalues of the modified Hessian matrix (Equation 5.2). Additional bounds such as the desired number of degrees of freedom and the local metric change between neighbouring elements allows the user to specify the preferred anisotropic mesh resolution.

It is often necessary to adapt to multiple solution fields. In this formulation a metric is formed for each solution field. A final metric is then obtained via superimposition of the metrics for individual fields. This ensures that only one metric is needed at the mesh optimisation step.

5.2.2 Mesh optimisation

Given the target metric ($\mathcal{M}$), a new computational mesh with edges, $\mathbf{e}$, is generated such that

$$||\mathbf{e}||_{\mathcal{M}} = \sqrt{\mathbf{e}^T \mathcal{M} \mathbf{e}} = 1 \tag{5.3}$$

i.e. all the edges in the mesh have unit length with respect to the metric $\mathcal{M}$.

A functional defining the quality of the mesh is then used to guide the mesh optimisation towards Equation 5.3

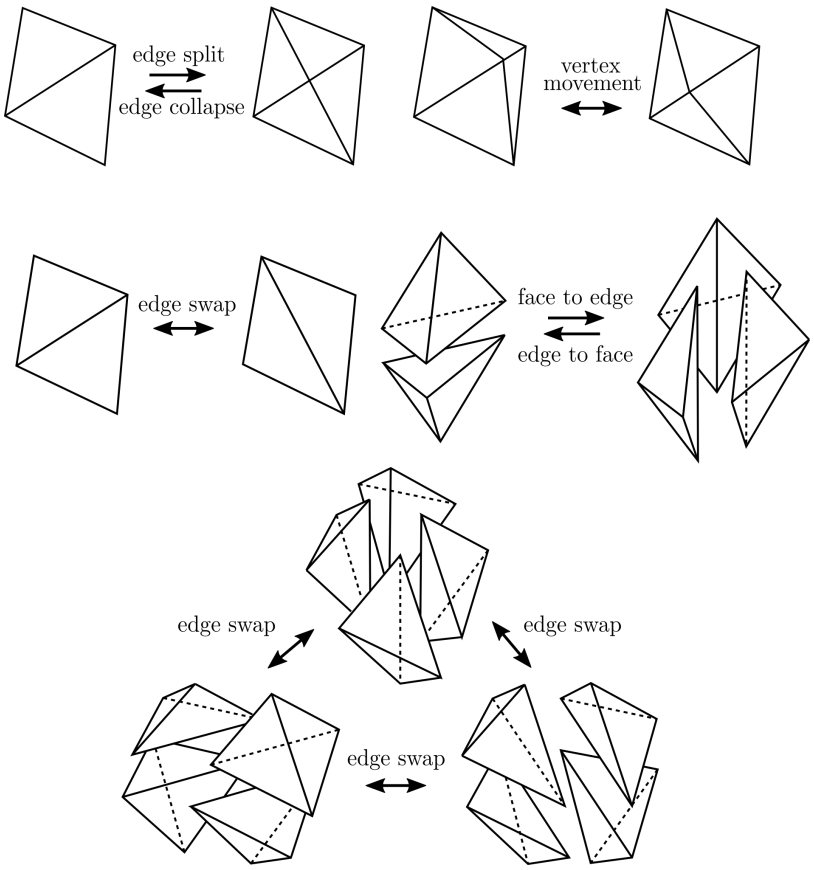


FIGURE 5.2: Topological operations performed on elements in order to optimise a mesh (Pain et al., 2001; Piggott et al., 2009).

$$F_{e|\mathcal{M}} = \frac{1}{2} \sum_{e \in \text{edges}} \left(d_{e|\mathcal{M}}\right)^2 + \left(q_{e|\mathcal{M}}\right)^2 \tag{5.4}$$

where $d_{e|\mathcal{M}}$ and $q_{e|\mathcal{M}}$ gauge the size and shape of an element measured with respect to the metric $\mathcal{M}$. These are defined such that $d_{e|\mathcal{M}} = q_{e|\mathcal{M}} = 0$ for an ideal element (i.e. with edge lengths and aspect ratios of unity with respect to $\mathcal{M}$). The minimisation of the functional $F_{e|\mathcal{M}}$ therefore ensures a mesh with the optimal size and shape is created.

The new mesh is generated from the existing mesh via the sequential application of remeshing operations on local clusters of elements where needed, while preserving the old mesh in other regions. The mesh structure is modified using node or vertex repositioning, element refinement/splitting, coarsening by edge collapse, and face-edge/edge-face swapping (Figure 5.2).

5.2.3 Mesh to mesh interpolation

When the mesh adaptivity algorithm has terminated, two meshes exist: the donor mesh (old mesh) and a target mesh (new mesh). These two meshes will in general be different and yet it is necessary to transfer the solution fields such as saturation, pressure and velocity from the donor to the target mesh. The transfer between the two meshes is known as interpolation. Several options exist. The simplest approach is called consistent interpolation whereby the value of the field at the target mesh is set to the value at those physical positions on the donor mesh (Lohner et al., 1985). This method is sometimes referred to as collocation interpolation. However, consistent interpolation is not conservative in that the integral of a field over the whole domain on the donor mesh will not be preserved on the target mesh. The method is also unsuitable for discontinuous meshes as co-located nodes will share the same value therefore discontinuous fields will be smoothed as they are transferred to the target mesh.

The other option, which we use, is the Galerkin projection (Farrell and Maddison, 2011). The method proceeds by constructing a supermesh which is the intersection between donor and target meshes. The integral of the field over the domains of the donor and target mesh are then equated. As the supermesh contains the nodes and edges of both the donor and target meshes, Galerkin projection allows an accurate solution to this integral (Figure 5.3).

The computational overhead of Galerkin projection interpolation is low as there is no need to recalculate values of material properties such as porosity and permeability. Permeability is particularly difficult as simple volume-weighted averages cannot be used. Up-scaled permeability values are strongly dependent on the underlying fine scale spatial correlation, evaluating a representative value at a coarser scale is therefore non-trivial. A large number of methods exist for permeability up-scaling. Flow based upscaling involves performing flow simulations, sampling a fine mesh distribution of permeability, and evaluating the average properties that reproduce the behaviour on a coarser mesh (Renard and De Marsily, 1997). Up-, cross- or down-scaling permeability would therefore make DAMO prohibitively expensive. However, in our approach, the permeability (and other material properties) are constant within each geological domain. They are therefore simply assigned to mesh elements within a domain after each mesh adapt, regardless of their size (Jackson et al., 2015). No up-, cross- or down-scaling of material properties is required and saturation-dependent material properties such as relative permeability and capillary pressure can simply be recalculated using the local saturation.

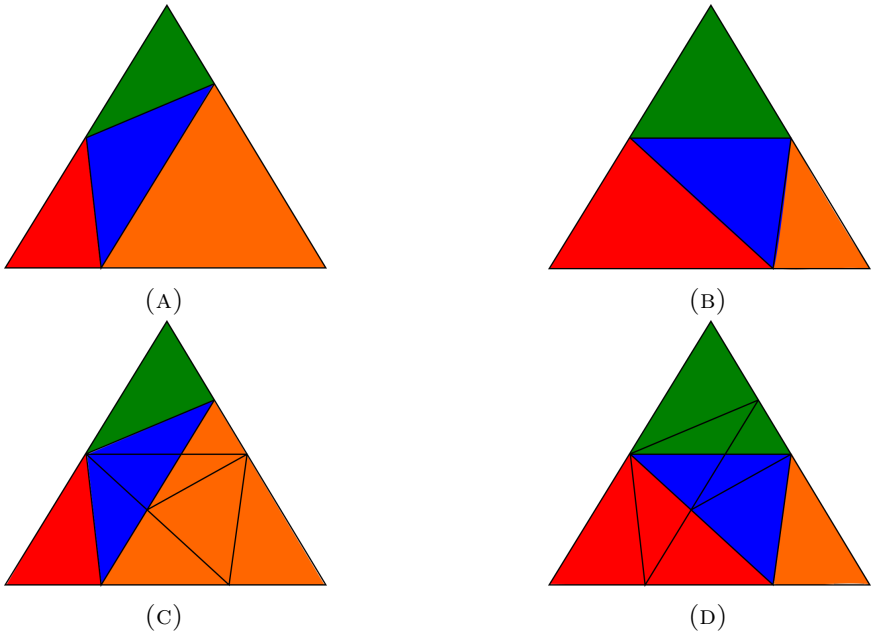


FIGURE 5.3: (A) and (B) Two triangular meshes with some finite element solution depicted by different colours. (C) and (D) show the same triangular supermesh with the finite-element (FE) solutions mapped from mesh (A) and (B), respectively. Adapted from Farrell and Maddison (2011).

5.2.4 Accounting for high Courant numbers

The complex, high aspect ratio geometries encountered in porous media flows can lead to large variations in element size (Graham et al., 2015a). Moreover, the order of magnitude variations in petrophysical properties and large pressure drops in nearwell regions can lead to large variations in Darcy velocities. Courant numbers can therefore vary significantly throughout space and time.

While the non-linear solvers used in Imperial College Finite Element Reservoir SimulaTor (IC-FERST) and other multi-phase porous media flow simulators can handle large Courant numbers (Anderson, 1965; Jenny et al., 2009; Salinas et al., 2017a), this can be a challenge for mesh adaptivity algorithms. *A-posteriori* mesh adaptivity for time-dependent problems will, by definition, trail the solution. This is not a problem for low Courant number flows (< 1) as the solution will not have moved past the refined region (Salinas et al., 2018b). However, solutions of high Courant number flows may be compromised when the solution enters coarse regions. Numerical diffusion is therefore increased and high resolution features can be irrevocably lost.

Several methods have been proposed to address this issue. One, is the use of mesh gradation control to limit the size variation of neighbouring mesh elements,

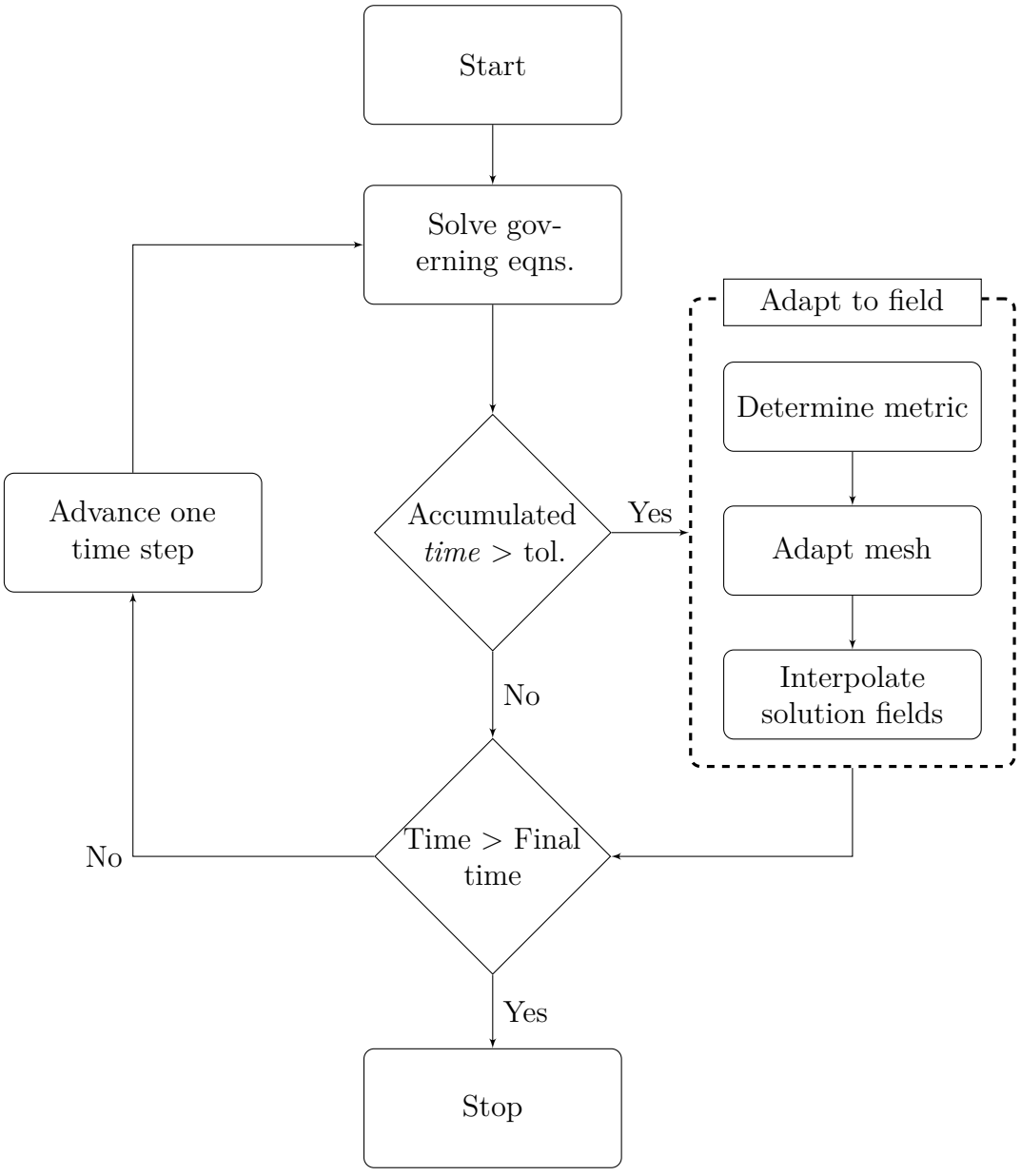


FIGURE 5.4: Standard mesh adaptivity algorithm. The mesh is adapated to user-specified field(s) after a user-defined number of time-steps.

thereby expanding the refined region. Two, is metric advection where the mesh is pushed ahead of the flow using flow velocities at the current time level (Hiester et al., 2011). This reduces the likelihood of the dynamics of interest moving out of the higher resolution regions. Three, involves adapting the mesh as part of the non-linear solver, first presented by Alauzet et al. (2007) for Navier-Stokes flows and later modified by Salinas et al. (2018b) for porous media flows (Figure 5.5). Rather than adapting the mesh after a specified number of time steps, the adaptivity is triggered after a defined accumulated Courant number is reached (dashed loop; Figure 5.5).

In the numerical examples that follow, we use both the standard adaptivity algorithm, (Figure 5.4), if Courant numbers are expected to be low (< 1) and use the non-linear adaptivity algorithm, (Figure 5.5), when Courant numbers are high.

5.3 Test cases

We demonstrate the methodology outlined above using 2D and 3D models that capture typical subsurface reservoir processes and architectures. We test the implementation of this method in IC-FERST using the double control-volume-finite-element method (DCVFEM) in which the pressure is discretised CV-wise rather then FE-wise and all other variables are discretised following the classical CVFEM. Previous studies have shown benchmarking of IC-FERST using the DCVFEM against viscous dominated flow (Salinas et al., 2017b), and using conventional codes, ECLIPSE (Jackson et al., 2015), which we will not repeat here.

Instead we present two test cases of capillary dominated flows compared against analytical and experimental results. The capillary pressure curve for the first test case, simulating spontaneous imbibition is generated using a power-law model

$$p_c = \bar{p}_c \left(1 - S_{wr}\right)^a \tag{5.5}$$

where $\bar{p}_c$ is maximum capillary pressure at the irreducible water saturation (S_{wr}), and a is the capillary pressure exponent.

The capillary pressure function for the second test case, simulating the infiltration of dense non-aqueous liquids is given by the following Brooks-Corey model

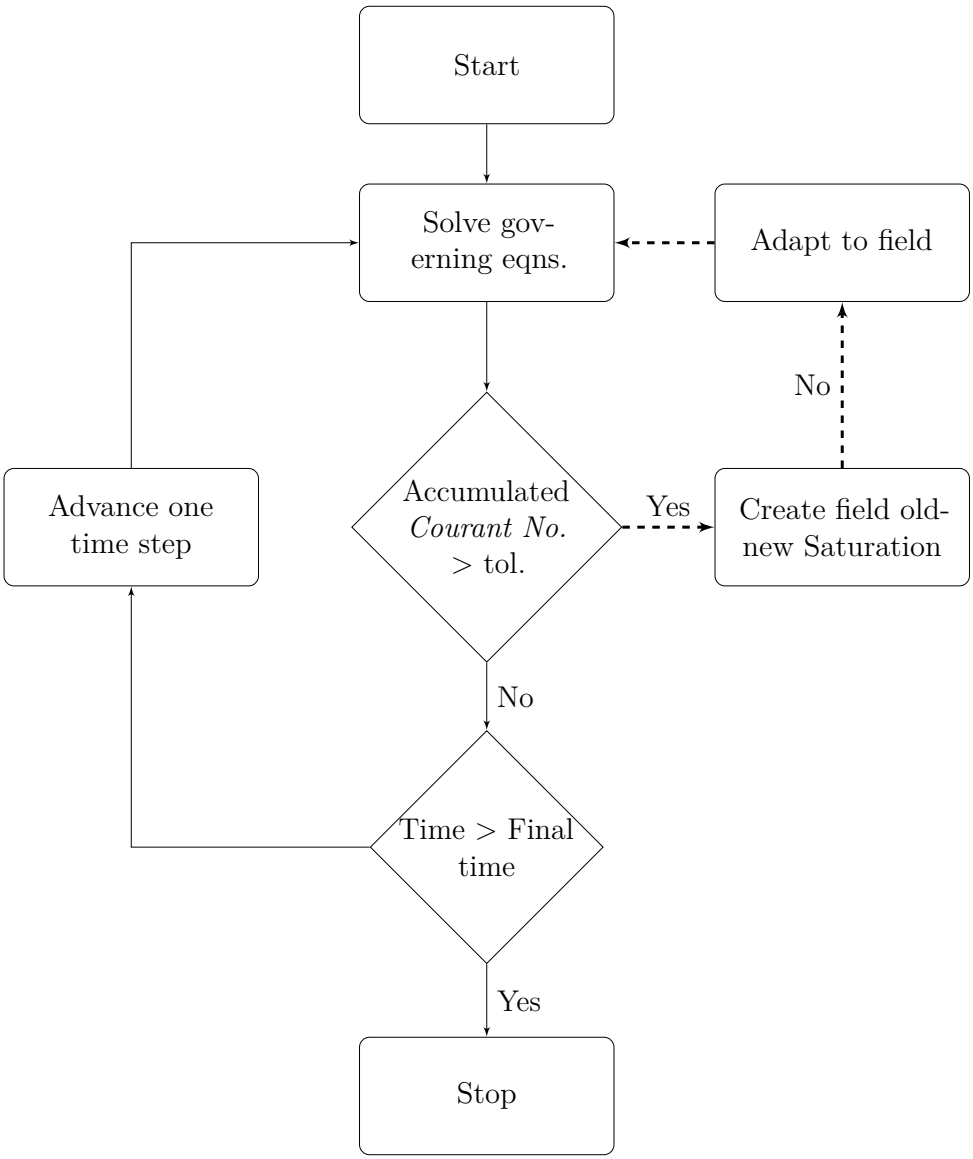


FIGURE 5.5: Non-linear mesh adaptivity. The mesh is adapted as part of the non-linear solver with an addition loop (dashed line).

$$p_c = p_d \left(\frac{S_w - S_{wr}}{1 - S_{wr} - S_{nr}} \right)^a \tag{5.6}$$

where p_d is the entry pressure, i.e. the capillary pressure which must be exceeded before the non-wetting phase (e.g. oil) is able to displace the wetting phase (e.g. water) from a porous medium, and a is the pore size distribution index.

We then use three surface-based models to illustrate several advantages and highlight some issues with DAMO. For these surface-based models we simulate the displacement of oil by water with negligible gravitational and capillary forces.

For all the simulations the relative permeabilities are given by the Brooks-Corey model

$$\begin{aligned} k_{rw}(S_w) &= k_{rw}^{max} \left(\frac{S_w - S_{wr}}{1 - S_{wr} - S_{nr}} \right)^{n_w} \\ k_{rn}(S_n) &= k_{rn}^{max} \left(\frac{S_n - S_{nwr}}{1 - S_{wr} - S_{nr}} \right)^{n_n} \end{aligned} \tag{5.7}$$

where $k_{rw}(S_w)$ and $k_{rn}(S_n)$ are, respectively, the water and oil relative permeabilities, $k_{rw}^{max}(S_w)$ and $k_{rn}^{max}(S_n)$, are the water and oil end-point relative permeabilities, S_{wr} and S_{nr} are the irreducible water and oil phase saturations, and n_w and n_n are the exponents for the water and oil phases.

All the following models are simulated using both fixed and dynamically adaptive meshes. The model dimensions, number of elements and adaptivity criteria are summarised in Table 5.1.

5.3.1 Counter-current Spontaneous Imbibition

We begin with a validation test case of a capillary dominated flow by simulating counter-current spontaneous imbibition (SI). We compared our results against the analytical solution, derived in Appendix A (McWhorter and Sunada, 1990; Schmid and Geiger, 2012; Nooruddin and Blunt, 2016; Nourdeen, 2018). SI occurs when a wetting (e.g. water) phase enters a porous medium, displacing a non-wetting (e.g. oil) phase by capillary forces alone. We set this model up as a closed rectangular domain, with two regions (Figure 5.6a). Counter-current flow is imposed by setting the water saturation of the left region to a maximum value of $(1 - S_{nr})$, where S_{nr} is the residual oil phase saturation and setting a large porosity. The large porosity ensures that changes to the saturation in

TABLE 5.1: Fixed and DAMO simulations

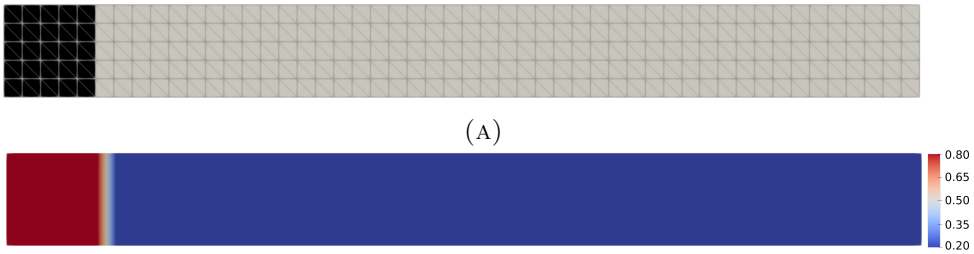
		Fixed mesh			Adaptive mesh			
Model	Dimensions (m)	Mesh	Min. edge len. (m)[a]	No. elements	Mesh	Field[b]	Algorithm[c]	No. elements[d]
SI	1×0.1	A1	0.02	500	AA1	S_w	Standard	124
		A2	0.01	2000	AA2			132
		A3	0.005	8000	AA3			170
DNAPL	0.90×0.65	B1	0.05	666	BA1	S_w	Standard	345
		B2	0.025	2604	BA2			800
		B3	0.01	17082	BA3			1380
		B4	0.005	65769	BA4	–	–	–
SBM 1	$1.5 \times 1.5 \times 0.1$	C1	0.03	33606	CA	S_w	Non-linear	41653
		C2	0.015	477759	–	–	–	–
SBM 2	$900 \times 1000 \times 20$	D1	27	7795	DA	S_w	Non-linear	10200
		D2	22	12854	–	–	–	–
		D3	18	102832	–	–	–	–
		D4	6.7	879040	–	–	–	–
SBM 3	$220 \times 100 \times 82$	E1	10	11300	EA	S_w & p	Non-linear	60518
		E2	6	45425	–	–	–	–
		E3	3.5	227051	–	–	–	–
		E4	2.5	621998	–	–	–	–

[a] Minimum edge of triangle/tetrahedron of fixed mesh

[b] The field that the DAMO algorithm adapts to

[c] Standard algorithm: Figure 5.4; Non-linear algorithm: Figure 5.5

[d] Denotes the average value



(A)

(B)

FIGURE 5.6: (A) Domain split into two regions. A large porosity is set for the left-hand domain to ensure insignificant change in saturation. The right-hand domain's porosity is kept at 0.20 and homogeneous permeability of $1 \times 10^{-13}\text{m}^2$, (B) the right-hand side domain is initially saturated with the oil phase and no external forces are applied i.e. all boundaries are no flow boundaries. The wetting phase invades the domain purely by capillary forces.

the left-hand region remains insignificant. The right-hand region is initially saturated with the oil phase. Material and fluid properties are summarised in Table 5.2.

For the adaptive mesh simulations, the mesh is adapted to minimise the error of the saturation field only, with a tolerance of 1%. The standard algorithm is used as the Courant number is low.

5.3.2 DNAPL infiltration

The second test case concerns the migration of dense non-aqueous liquids (DNAPL) through porous media, which involves the computation of two-phase flow in heterogeneous porous media with gravity and capillary effects. DNAPLs are widespread throughout industrialised areas; common examples are chlorinated solvents which can be 50-60% denser than groundwater. This allows them to migrate deep below the water table and risk long term contamination due to their limited solubility (Hofstee et al., 2003). No analytical solution exists for the infiltration of DNAPL in heterogeneous porous media; here, we test the numerical formulation against laboratory experiments conducted by Barczewski and Koschitzky (1996). Contrasts in capillary pressure (in particular entry pressures) result in saturation discontinuities at the interface between the two mediums. Figure 5.7 shows the configuration of the test case. Trichloroethylene (TCE) is infiltrated (at a rate of 5.12×10^{-5} m/s) and under gravity, into a small container measuring 90 cm by 65 cm filled with two different, relatively homogeneous quartz sands. The properties of the sands are given in Table 5.3.

TABLE 5.2: Material and fluid properties for SI test case

Parameter	Unit	Left-hand domain	Right-hand domain
Permeability (K)	$[m^2]$	1×10^{-13}	1×10^{-13}
Porosity	[-]	1000	0.20
Initial water saturation (S_{wr})	$[-]$	0.80	0.20
Initial oil saturation (S_{nr})	$[-]$	0.20	0.80
Capillary pressure exponent (a)	[-]	2	2
Max. capillary pressure ($\bar{p}_c$)	$[Pa]$	1×10^5	1×10^5
Residual water saturation (S_{wr})	$[-]$	0.20	0.20
Residual oil saturation (S_{nr})	$[-]$	0.20	0.20
Parameter	Unit	Water phase	Oil phase
Density (ρ)	$[kg/m^3]$	1000	1000
Viscosity (μ)	$[Pa.s]$	0.001	0.001
Endpoint rel. permeability (k_r^{max})	$[-]$	1	1
Corey exponent	$[-]$	2	2

The capillary pressure resistance at the first horizontal interface between the coarse and fine sands stops the DNAPL penetrating the fine sand lens.

As traditional control-volume-finite-element methods (CVFEMs) consist of control-volumes (CVs) that span element boundaries, saturation will be smeared across the capillary barrier leading to a premature penetration of the DNAPL into the find sand lens. While it will not eliminate it completely, mesh adaptation will reduce this saturation smearing by reducing the size of elements (and the CVs) at the interface between the coarse and fine sands.

Similar to the SI simulation, the mesh is adapted to minimise the error of the saturation field only, with a tolerance of 1%. The standard algorithm is used as the Courant number is low.

A normalised measure of non-physical leakage into the fine sand lens is used to compare the fixed and DAMO simulations.

$$\eta = \sum_{i}^{n_{cv}^{k_f}} S_{i,nw} \phi^{k_f} V^{k_f} \tag{5.8}$$

where $S_{i,nw}$ is the DNAPL saturation, $n_{cv}^{k_f}, \phi^{k_f}$ and V^{k_f} are the number of control volumes within the fine sand lens, the porosity and volume of fine sand,

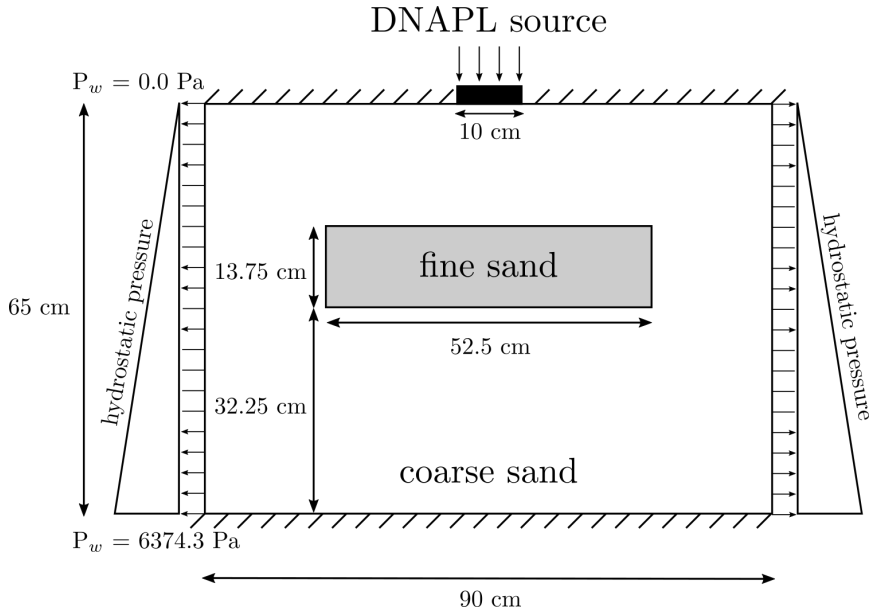


FIGURE 5.7: Geometry and boundary conditions of DNAPL infiltration test case (Helmig, 1997)

respectively. The mass leakage is normalised against the error calculated for the coarsest mesh.

5.3.3 Surface-based models

We then consider three surface-based models describing typical geological heterogeneities (Table 5.4).

Fracture model (SBM 1)

SBM 1 is a 2.5D (pseudo 3D) model of a fractured carbonate (Figure 5.8). The model is a 1.5×1.5 m sample of the 6×6 m mapped Kilve section, on the southern margin of the Bristol Channel coast (Figure 5.9; Belayneh et al., 2006; Belayneh et al., 2009). The Kilve section is an anticline with a prominent joint set parallel to its axis and a second set terminating against the long joints. Fracture apertures (Domain 1) are set to a uniform width of 3 mm with a permeability of $10,000$ mD within a matrix (Domain 2) of 1 mD. The model is initially saturated with oil and residual water. Water is injected at the left-hand boundary and oil and water is produced from the right-hand boundary, with all other boundaries closed. SBM 1 is used to highlight some issues with adaptive mesh simulations of fractures which are explicitly resolved.

For adaptive mesh simulations, the mesh is adapted for saturation only at a tolerance of 1%. Due to the large variations in Darcy velocity at the fracture

TABLE 5.3: Material and fluid properties for DNAPL test case (Helmig, 1997)

Parameter	Unit	Coarse sand	Fine sand
Permeability	$[m^2]$	6.64×10^{-11}	7.15×10^{-12}
Porosity	[-]	0.4	0.39
Capillary pressure exponent (a)	[-]	-0.37	-0.50
Entry pressure (p_d)	$[Pa]$	755	2060
Residual water saturation (S_{wr})	$[-]$	0.09	0.12
Residual DNAPL saturation (S_{nr})	$[-]$	0	0
Parameter	Unit	Water phase	DNAPL phase
Density (ρ)	$[kg/m^3]$	1000	1460
Viscosity (μ)	$[Pa.s]$	0.001	0.0009

tips and fracture intersections (and the large variations in element size), the standard adaptivity algorithm will not be sufficient (Salinas et al., 2018b). For this simulation we use the non-linear adaptivity algorithm.

Channel model (SBM 2)

SBM 2 is of a typical subsurface sandstone reservoir (Salinas et al., 2017b; Figure 5.10). A surface-based model is used to capture channelised sandbodies in a non-reservoir mudstone background. Channelised sandstone reservoirs are among the most common geological architectures and yet representing them using conventional k-orthogonal grids remains a challenge as discussed earlier. Typically, non-reservoir facies are set to be inactive. In this example, SBM 2 is made up of three groups of channels (Domains 1, 2 and 3; Table 5.4) with large contrasts in permeability.

In conventional modelling approaches a large number of grids blocks are required to capture complex, features that are not aligned with grid-block boundaries, in a stair-stepping fashion. Figure 5.11 shows a cross-section of SBM 2 discretised using conventional Cartesian grids at decreasing resolution. Over 100,000 active grid blocks (400,000 in total) are needed to capture the channel geometry (Figure 5.11a). As the resolution is decreased there is a loss in connectivity between the small channels, and with a further decrease in resolution we start to see connectivity where there should not be. This can result in significantly different flow behaviours in conventional grid-based simulations. At higher resolutions

TABLE 5.4: Rock and fluid properties for surface-based models

Property	Unit	SBM 1	SBM 2	SBM 3
Domain 1 permeability	$[mD]$	10000	1000	1000
Domain 2 permeability	$[mD]$	1	200	1
Domain 3 permeability	$[mD]$	N/A	100	N/A
Domain 1 porosity	$[-]$	1	0.2	0.2
Domain 2 porosity	$[-]$	0.2	0.2	0.1
Domain 3 porosity	$[-]$	N/A	0.2	N/A
Water/oil phase density	$[kg/m^3]$	1000	1000	1000
Water/oil phase viscosity	$[Pa.s]$	0.001	0.001	0.001
Irreducible water phase saturation	$[-]$	0.2	0.2	0.2
Residual oil phase saturation	$[-]$	0.2	0.2	0.2
Water phase endpoint relative permeability	$[-]$	0.3	0.3	0.3
Oil phase endpoint relative permeability	$[-]$	0.8	0.8	0.8
Water/oil phase Corey exponent	$[-]$	2	2	2

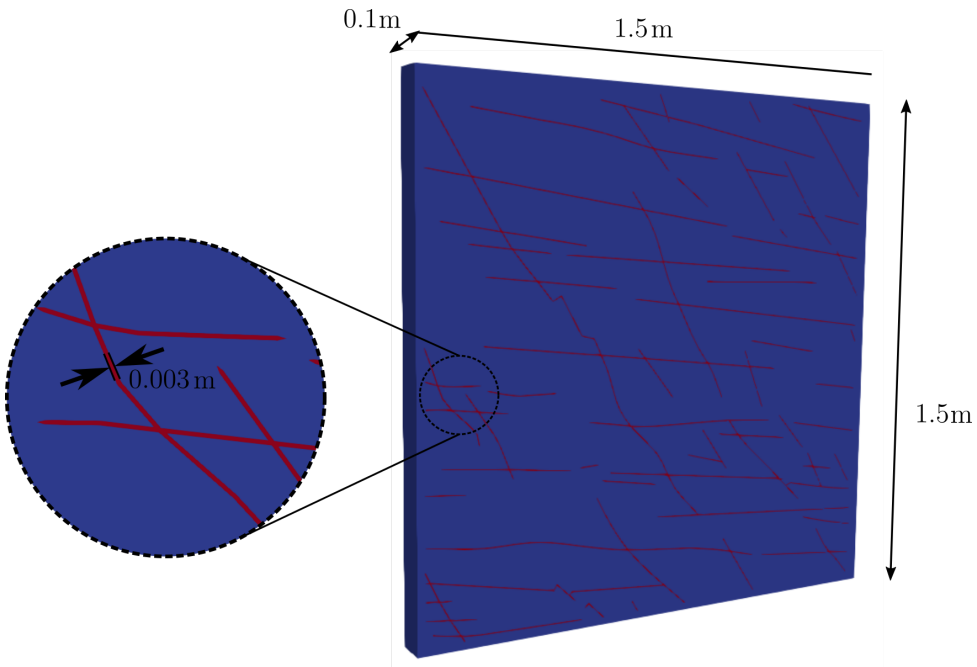
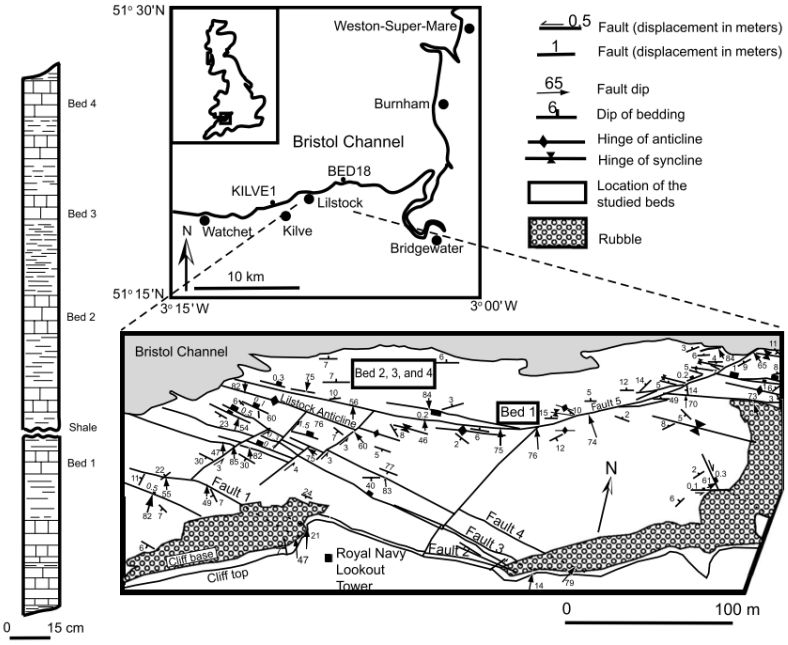


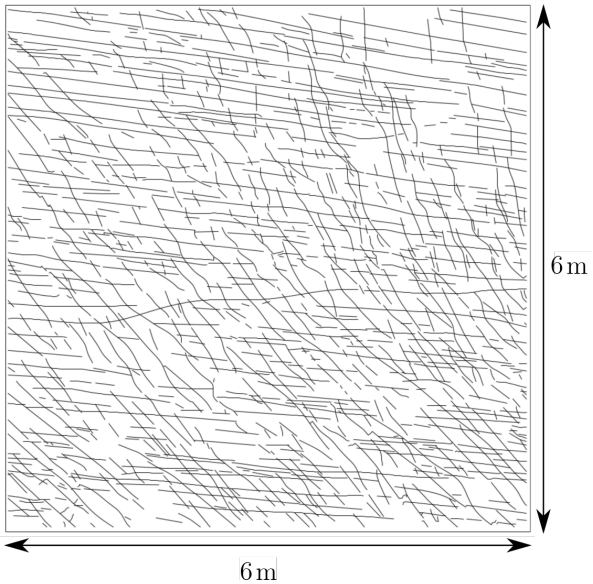
FIGURE 5.8: 1.5×1.5m sample of the Kilve model (Figure 5.9c) extruded 0.1 m . Fracture width are uniform at 3 mm.



(A)



(B)



(C)

FIGURE 5.9: (A) Structural map of Lilstock on the southern margin of the Bristol Channel coast, showing the Lilstock anticline and regional map showing the location of the Kilve model; (B) The gently folded alternating limestone and shale beds of the Kilve anticline. Early joints were formed parallel to the fold axis around the hinge zone of the anticline; (C) Kilve sketch, Area = 6×6m. From Belayneh et al. (2006).

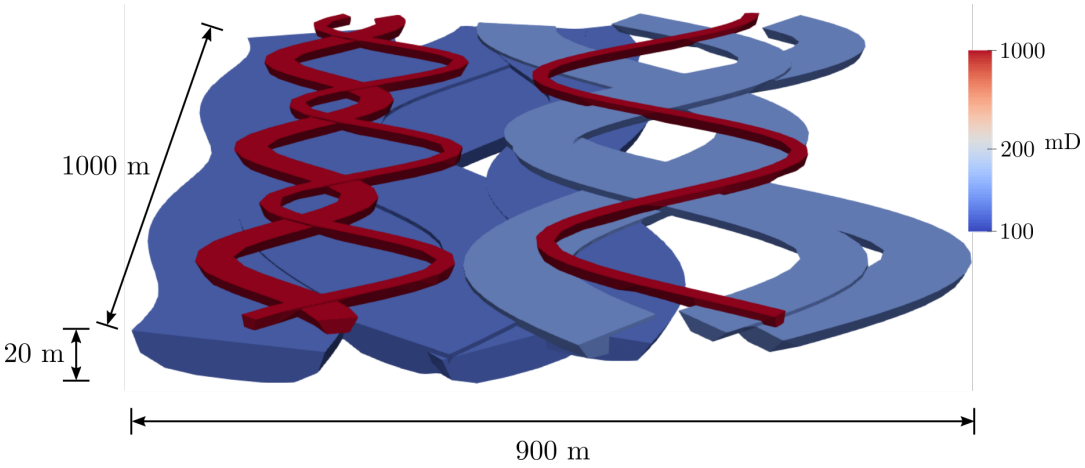


FIGURE 5.10: SBM 2. Channelised sandstone reservoir with three channel groups; 1,000 mD (Domain 1), 200 md (Domain 2) and 100 mD (Domain 3). Non-reservoir mudstone is not modelled. Vertical exaggeration 4×.

the high permeability small channels are resolved and can act as thief zones, whereas at lower resolutions these channels are bypassed as they are no longer connected.

The surface-based modelling (SBM) approach is able to preserve the original geometry without the need for stair-stepping. Figure 5.12 shows the mesh D1 with approximately 8,000 elements and a finer mesh (mesh D2) with around 13,000 elements. Note that around an order of magnitude fewer elements were needed to capture the geometry of the channels compared with the models in Figure 5.11.

For flow simulations we discretised this model using unstructured tetrahedral elements; non-reservoir volumes are not meshed as they do not contribute to flow (Figure 5.10). We use this model to highlight the importance of preserving complex geometric architectures during mesh adaptivity.

Adaptive mesh simulations adapt to reduce the error of the saturation only with a tolerance of 1% only and applying the non-linear adaptivity routine.

Fault model (SBM 3)

Finally SBM 3 (Table 5.4), is of a layered reservoir offset by conjugate normal faults. Structurally complex reservoirs can be difficult to represent using conventional approaches. Faults that are not aligned with the principle axis or that are vertically intersecting can require modifications, simplifications or removal from the model (see Chapter 2).

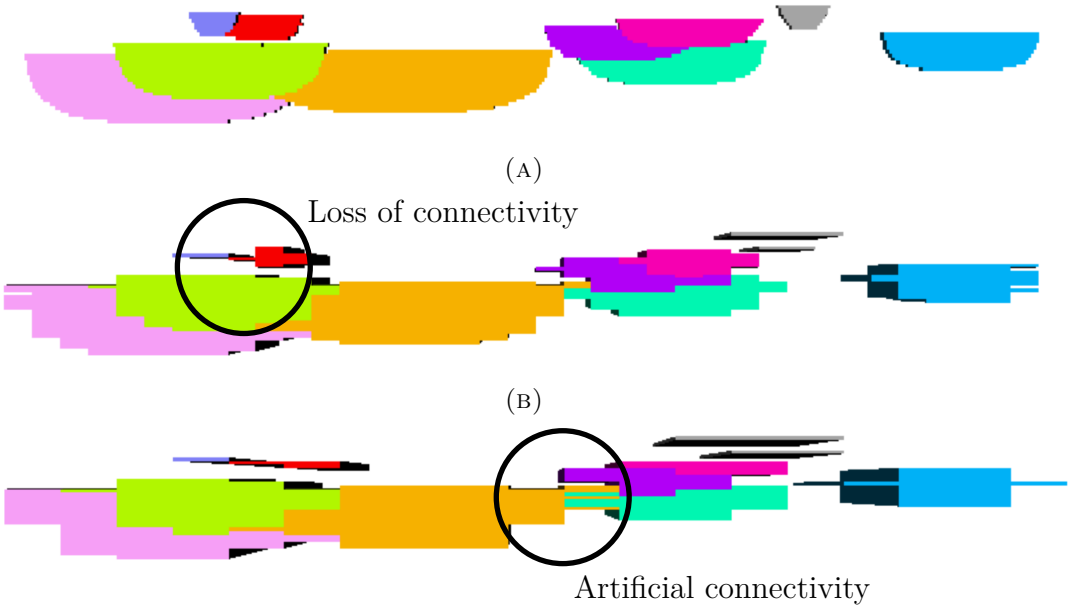
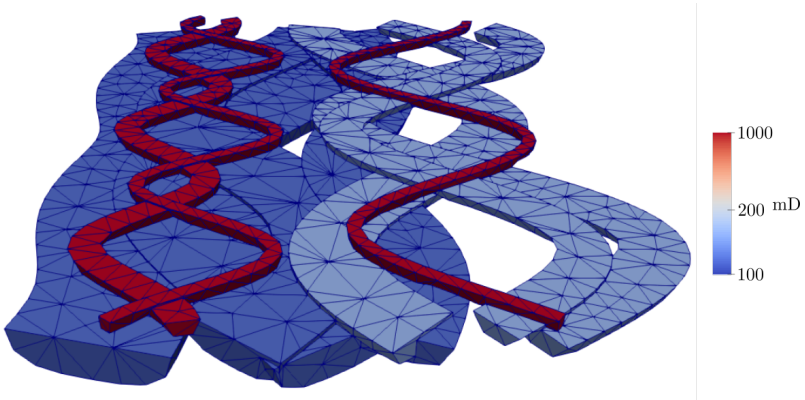
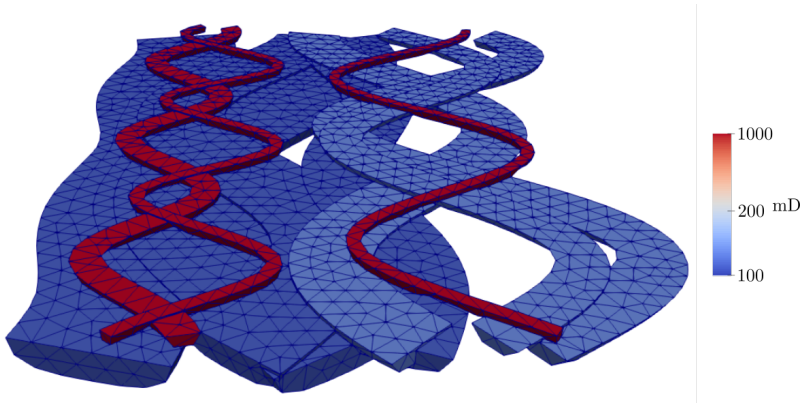


FIGURE 5.11: Cross section of SBM 2, discretised using Cartesian grids at decreasing resolution (vertical exaggeration 5×). (A) model made up of 400,000 cells (109,585 active cells); (B) model made up of 100,000 cells (26,735 active cells); (C) model made up of 25,000 cells (6,477 active cells). The connectivity of the smallest channels is lost as the mesh is coarsened. We also encounter some artificial connectivity.

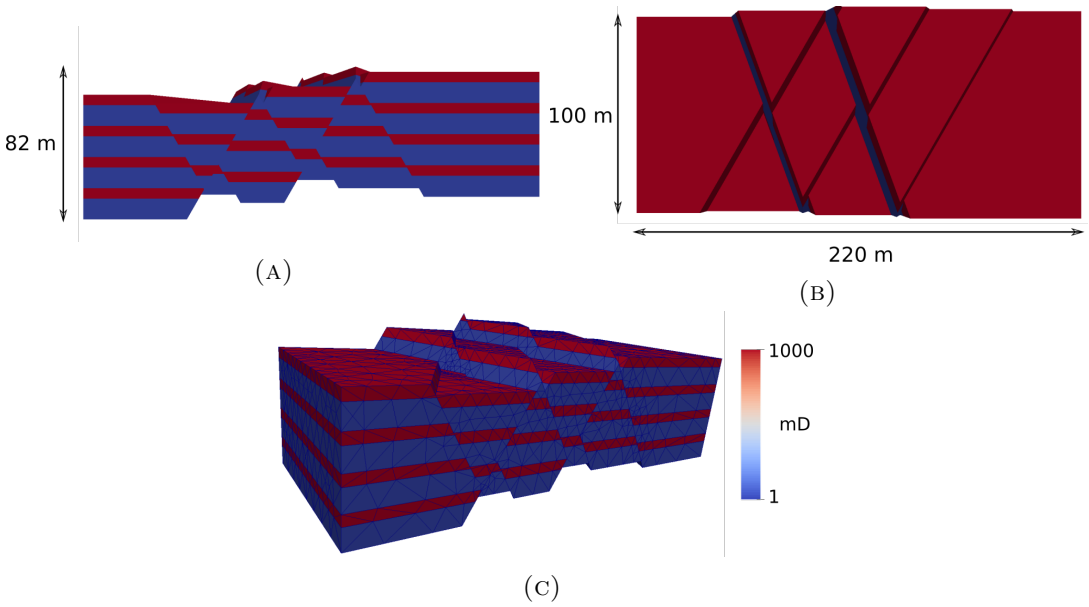


(A)



(B)

FIGURE 5.12: Surface-based channel model (SBM 2) made up (A) approximately 8,000 elements (mesh D1); (B) mesh D2, 13,000 elements



(A) (B) (C)

FIGURE 5.13: SBM 3. Conjugate normal faults offsetting stratigraphic layers of contrasting permeability; 1,000 mD (Domain 1) and 1 mD (Domain 2); (A) side view; (B) top view; (C) example of unstructured tetrahedral mesh.

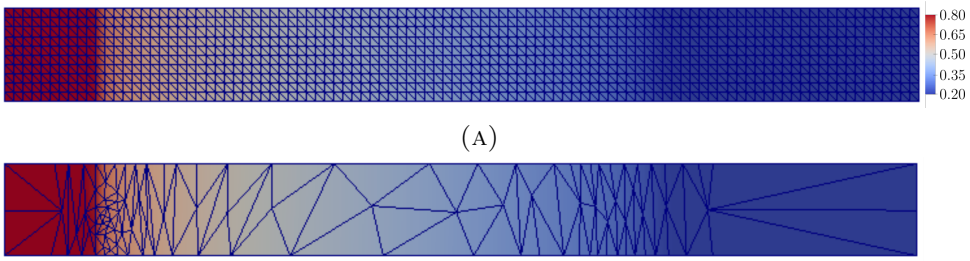
Figure 5.13 shows the model dimensions and initial unstructured mesh (mesh E1). Initially saturated with oil and irreducible water, the injection of water through the right-hand boundary is simulated, displacing oil towards the right-hand boundary ignoring gravitational and capillary forces. All other boundaries are closed to flow. With this model we show how DAMO can be used to significantly improve simulation accuracy and speed.

For the adaptive mesh simulation, the mesh is adapted using the non-linear algorithm to minimise both the saturation (1% tolerance) and pressure (10% tolerance). In addition to saturation, adapting to pressure ensures that before the shock front reaches the outlet, higher resolution is maintained at the outlet face. This was seen to improve the flux calculations across the outlet face, especially where the outlet face is made up of heterogeneous layers.

5.4 Results

5.4.1 Spontaneous imbibition

We first validated the DCVFEM and DAMO algorithm by comparing the SI simulation against the analytical solution. Figure 5.14 shows the saturation snap shot on a fixed and adapted mesh after 10,000 seconds. The mesh resolution is concentrated on regions with large saturation changes. Here the mesh resolution



(A)

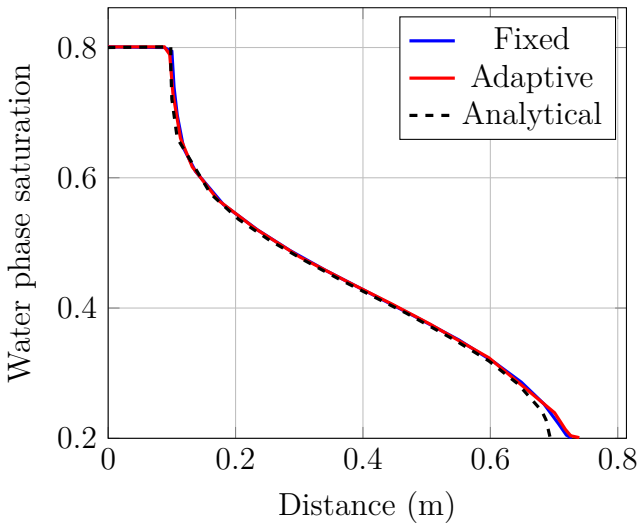
(B)

FIGURE 5.14: Saturation snap shots after 10,000 seconds. (A) with a fixed mesh (mesh A3, 8,000 elements); (B) adapted mesh AA3 with < 100 elements.

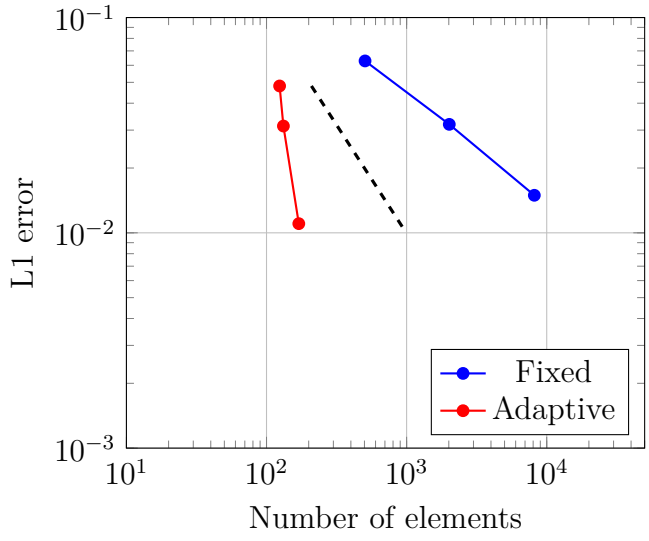
is highest at the imbibition front and also at the interface of the two regions, but low elsewhere. We observe similar profiles for adaptive and fixed mesh simulations (Figure 5.15b). In the DAMO simulation the mesh adaptively refines at the imbibition front. Smaller elements at the front reduce numerical dispersion and larger elements ahead of and behind the front. This leads to more accurate solutions with significantly fewer elements than a fixed mesh simulation, with nearly two orders of magnitude fewer elements (Figure **??**). The fixed mesh simulations display roughly linear convergence, while adaptive mesh simulations show improved convergence. This is likely due to the dynamically optimised mesh to reduce the interpolation error. This results in a much greater reduction in L1 error with far fewer elements than are needed with a fixed mesh simulation. Dynamic optimisation of the mesh comes at an increased computational cost. However, as we show later in Section 5.5, this cost is minimal.

5.4.2 DNAPL infiltration

We now compare the simulation of DNAPL infiltration using fixed and adaptive meshes. Figure 5.16 shows DNAPL-saturation levels after 2,360 seconds, for a set of fixed meshes and an adaptive meshes. As the DNAPL-saturation front reaches the fine sand the DNAPL should not penetrate due to the difference in capillary entry pressure (Figure 5.16f). However, similar to all traditional CVFEMs, the CV of the DCVFEM spans element boundaries which leads to smearing across the upper horizontal interface between coarse and fine sands. This non-physical penetration into the fine sand is reduced as the mesh is refined. The adaptive mesh allows for a more accurate description of the saturation discontinuity with far fewer elements. This can be quantified by the normalised error (Equation 5.8). Figure 5.17 shows the normalised error as a function of the number of elements for the fixed and DAMO simulations. With the DAMO simulation



(A)



(B)

FIGURE 5.15: (A) Comparison of numerical results for counter-current spontaneous imbibition against the analytical solution for fixed mesh simulations. The dashed line denotes the analytical solution; (B) The L1 error norm of the fixed and adaptive mesh solutions after 10,000 seconds; the dashed line denotes linear convergence. The adaptive mesh simulations yields similar solution quality to the fixed mesh results using approximately two orders of magnitude fewer elements when comparing the highest resolution adaptive and fixed models.

an error of the same size is achieved with more than an order of magnitude fewer elements than the fixed mesh, which still show significant non-physical infiltration of DNAPL.

5.4.3 Fracture model (SBM 1)

We now examine the first surface-based model, SBM 1, with explicitly resolved fractures. Figure 5.18 shows the saturation snap shot after 0.1 pore volumes injected. With the fixed mesh, C1 (Figure 5.18b), there is no sharp saturation interface between the high permeability fracture and low permeability matrix. Instead, saturation is smeared around the fractures into the matrix. With increasing resolution, this smearing is reduced and the saturation interface sharpens (Figure 5.18d). On a fixed mesh, C2, this requires close to $500,000$ elements. This leads to an earlier water breakthrough (time to first production of water; Figure 5.19b).

On the other hand, the DAMO simulation, with fewer than $60,000$ elements, is able to produce quantitatively similar results (Figure 5.18f). The water breakthrough is even earlier as the mesh better captures the fracture/matrix interface.

Although the DAMO simulation was able to improve the representation of the fracture/matrix interface, saturation smearing is still not eliminated due to CVs spanning element boundaries. This issue is addressed later in Chapter 6 with a new discretisation model termed the discontinuous DCVFEM.

5.4.4 Channel model (SBM 2)

A vital part of the DAMO algorithm employed here is that the original geometry is preserved by adapting only within domains. Figure 5.20 shows an example of a DAMO simulation adapting to the saturation solution. The mesh resolution is refined around the water front and coarsened elsewhere, while ensuring channel connectivity is maintained. Figure 5.21 shows the production of oil and water breakthrough as a function of pore volumes injected. For clarity we show only the coarsest and finest fixed meshes (D1 and D2) as well as the adaptive DA1 simulation.

Here we see that the production of fluids is very similar at all levels of refinement tested, within 1%. However, a closer look at the production and water breakthrough plots shows that the DAMO simulations are closest to the finest mesh solutions (Figures 5.21b and 5.21d). While this example does not seem to

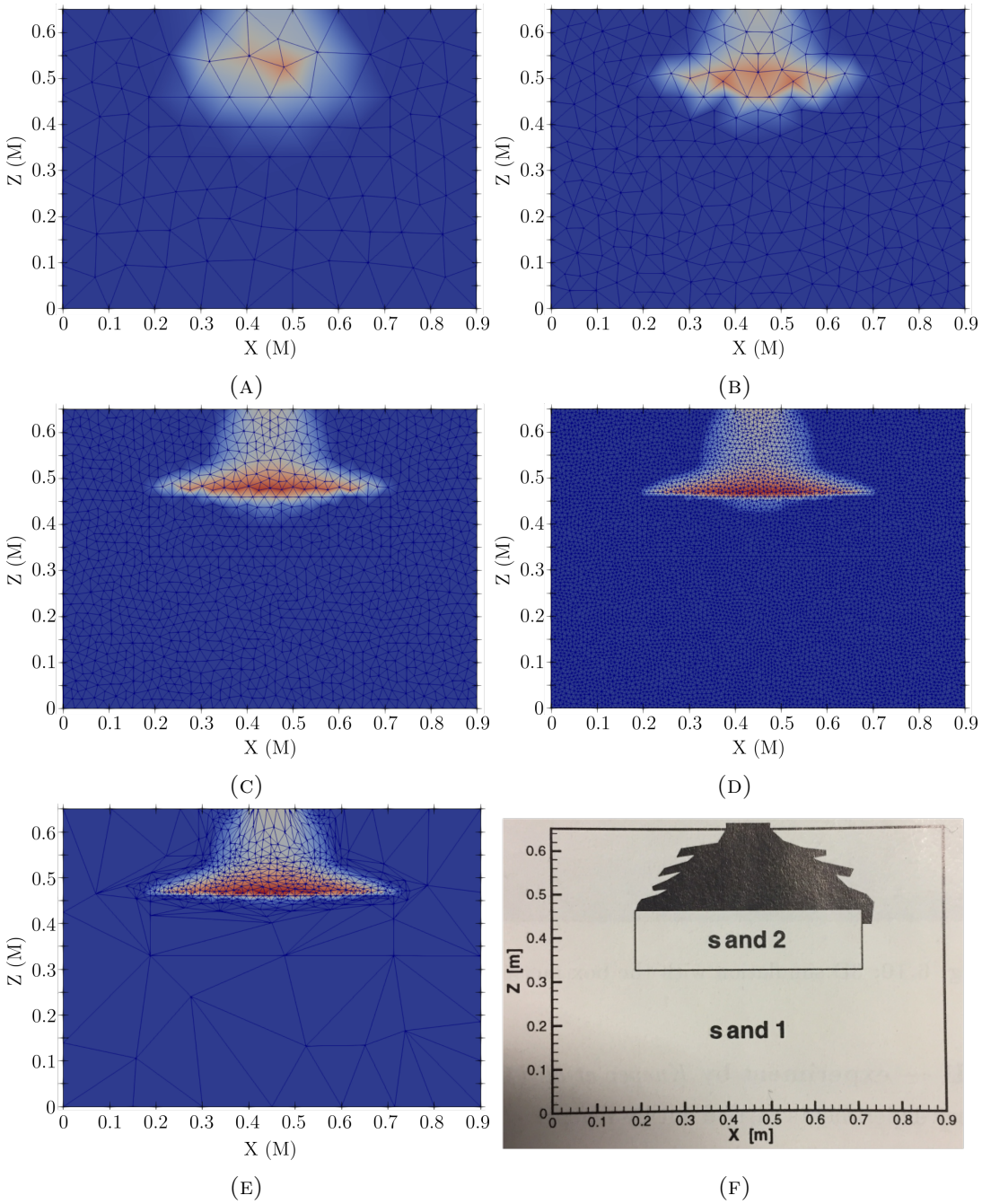


FIGURE 5.16: Infiltration results after 2,360 seconds. (A) Fixed mesh B1 (202 elements) simulation; (B) fixed mesh B2 (666 elements) simulation; (C) fixed mesh B3 (2,604 elements); (D) fixed mesh B4 (17,082) (B) DAMO simulation with an average of 1380 elements (mesh BA3); (C) experimental results (Helmig and Huber, 1998).

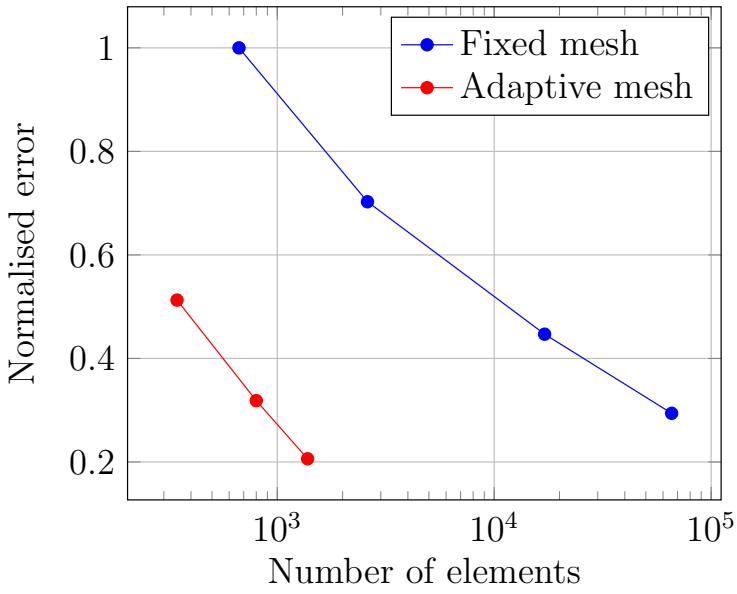


FIGURE 5.17: Normalised mass leakage into the capillary barrier corresponding to the time step in Figure 5.16

show a big advantage to adaptivity, it does show that the DAMO algorithm is able to preserve the important architectures during adaptivity. Further, it shows that the SBM approach allows us to capture these architectural elements, in this case channel bodes, with a small number of elements and achieve accurate flow predictions. Therefore in this example, surprisingly, the mesh resolution required to capture the channel architecture was also sufficient to capture flow. This is most likely due to the fact that the non-reservoir mudstone was removed from the model where control volume smearing would have necessitated further mesh refinement.

5.4.5 Fault model (SBM 3)

Finally, we compare fixed and DAMO simulations of the fault model. Figure 5.22 shows the oil recovery and water breakthrough as a function of pore volumes injected with different mesh resolutions. It is clear that the results depend on the mesh resolution: water breakthrough occurs earlier as the mesh is refined. This is due to a reduction in saturation smearing across the material boundary between the high and low permeability layers and a reduction in numerical dispersion. As the mesh is refined this material interface is better resolved leading to reduced saturation smearing, to the surrounding low permeability mudstone. Fixed mesh E1 shows severe smearing (Figure 5.23a) which is significantly reduced with fixed mesh E4 (Figure 5.23b). However, the use of a fixed mesh with (almost) isotropic elements leads to a large number of elements in areas where there is

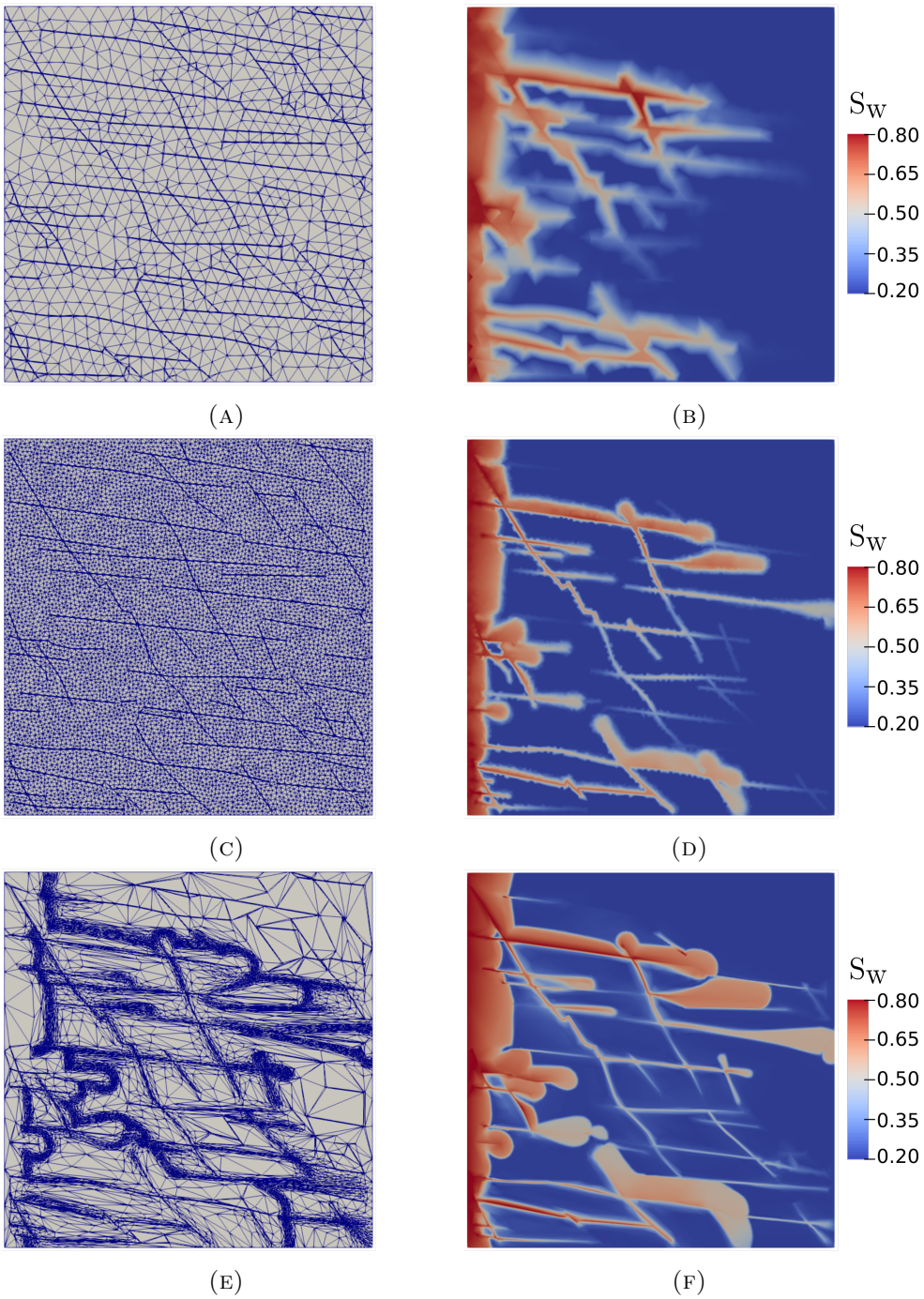
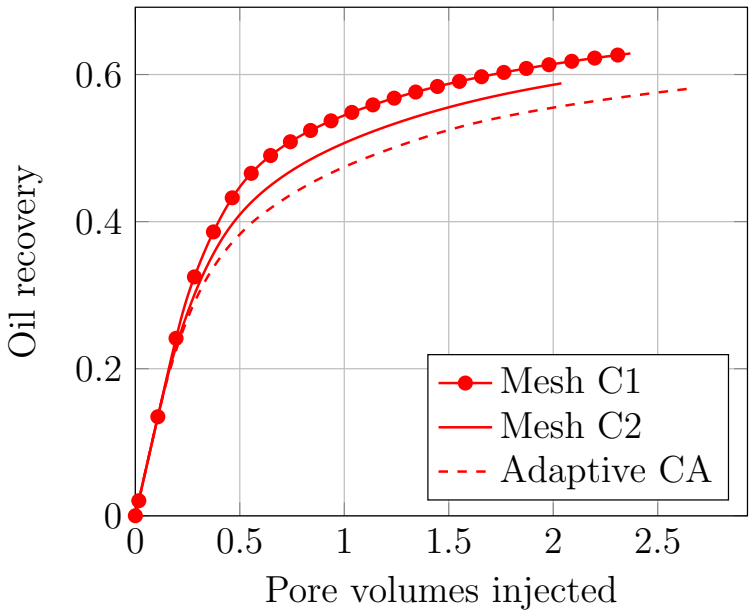
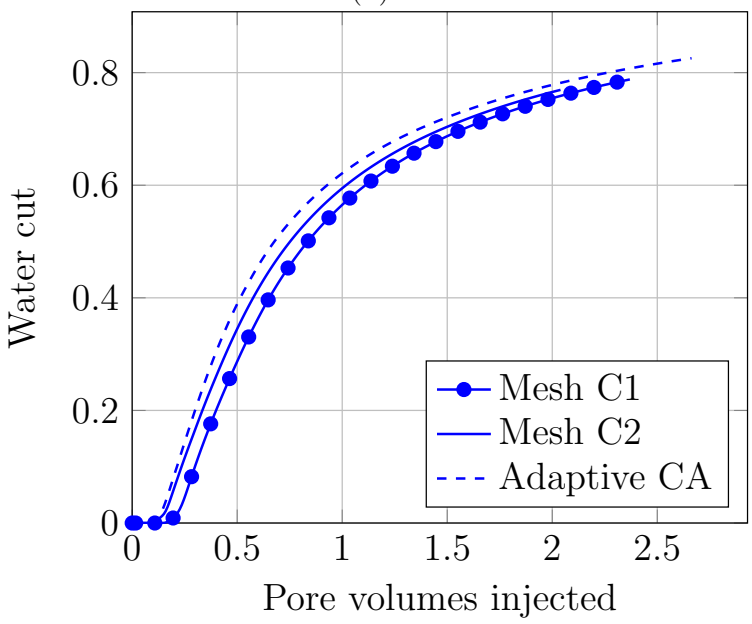


FIGURE 5.18: Water saturation after approximately 0.1 pore volumes injected. (A) fixed mesh C1, with 33,606 elements; (B) fixed mesh C2, with 477,759 elements; (C) DAMO simulation an average of 41,653 elements (mesh CA1).



(A)



(B)

FIGURE 5.19: Oil recovery and water cut plots as a function of the pore volume injected (dimensionless time), (A) Oil recovery as a proportion of the volume originally in place; (B) watercut (ratio of produced water to total volume produced)

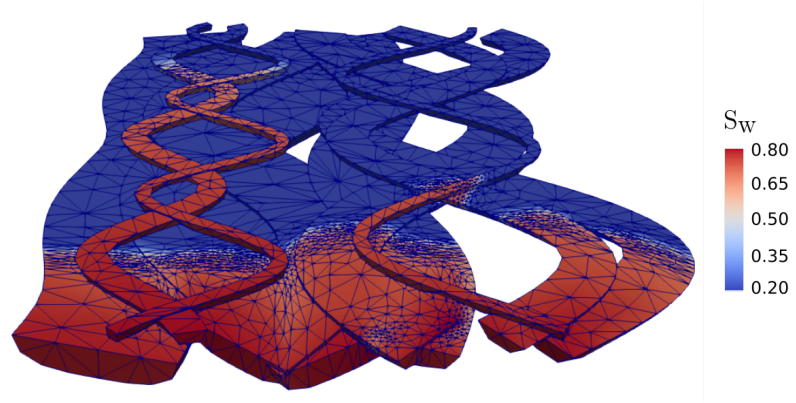


FIGURE 5.20: The geometry of SBM 2 is maintained at all levels of refinement. This ensures that the connectivity of the channels are preserved during DAMO.

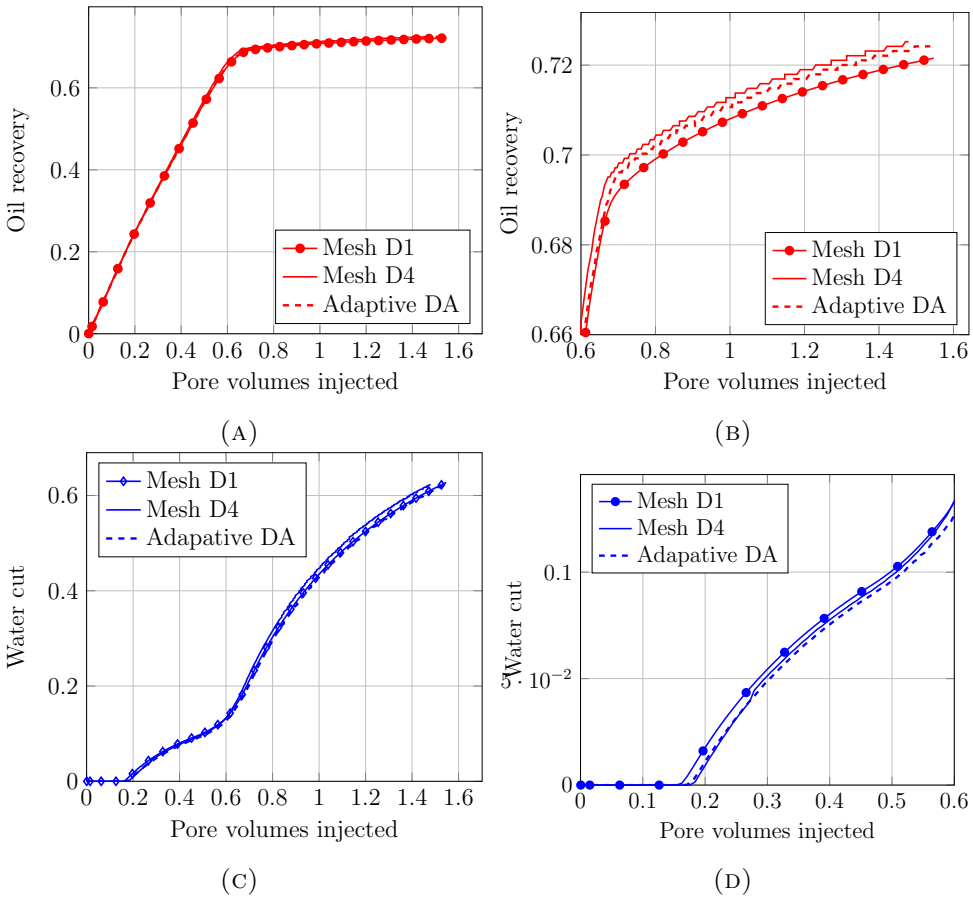


FIGURE 5.21: Oil recovery and water cut plots as a function of the pore volume injected (dimensionless time), (A) Oil recovery as a proportion of the volume originally in place; (B) zoomed in section of oil recovery; (C) watercut (ratio of produced water to total volume produced); (D) zoomed in section of watercut

no significant change in saturation, which is an inefficient use of computational resources.

The DAMO simulation shows improved representation of the inclined fault boundaries and the interface between high/low permeability layers. Moreover, at the top of the model elements are long and thin, capturing the water front with the fewest number of elements (Figure 5.23c). This ensures that we achieve similar oil recovery and water breakthrough results to that of the finest fixed mesh (E4) with fewer than 10% of the elements required with a fixed mesh (Figure 5.22).

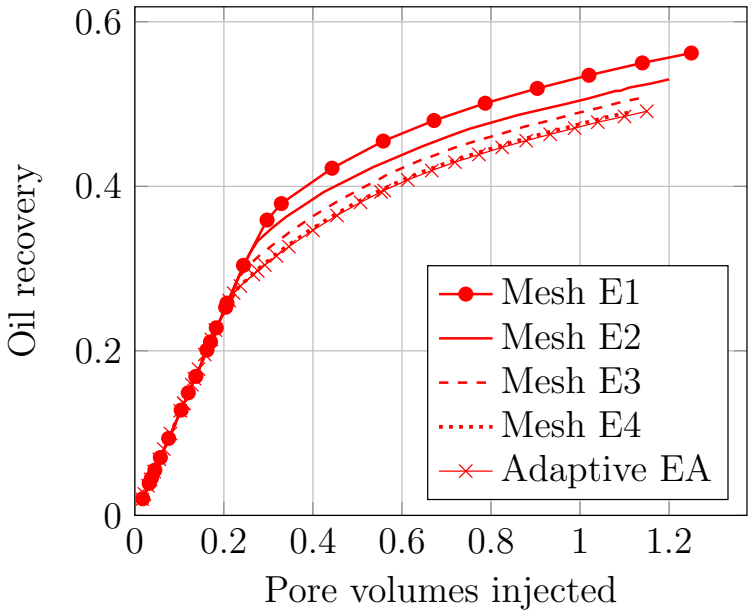
5.5 Cost of adaptivity

In the examples shown above we have taken the number of elements as a gauge of the computational demand of each simulation. This is normally sufficient for simulations using fixed meshes. However, for DAMO simulations it is important to account for the computational overhead associated with adapting the mesh and interpolating the solution fields. In order to assess the cost of adaptivity we use the SI and SBM 3 simulations as described above. Similar results were obtained for the other cases.

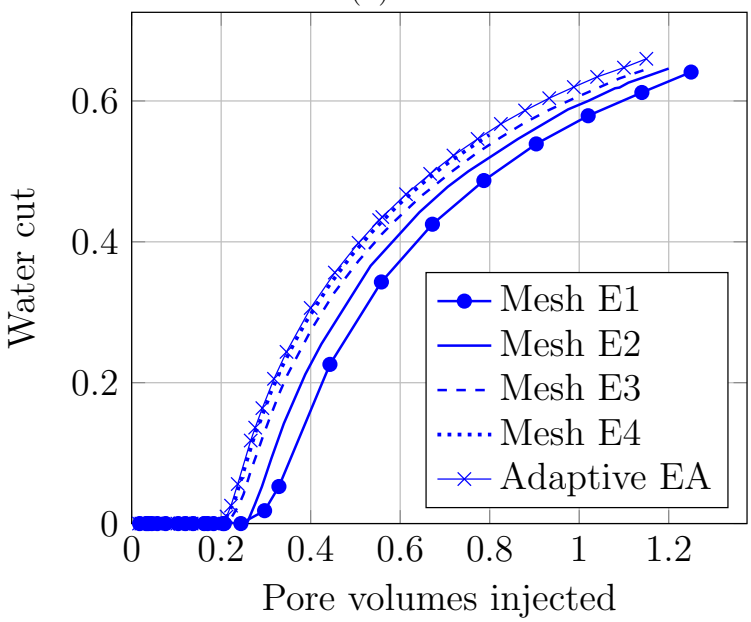
The first set of simulations were run for one time step on each mesh. Another set included one time step followed by one run of the adaptivity routine. This ensures that the incremental cost of adaptivity can be calculated accurately. Each simulation was run three times and the CPU time averaged. The averaged CPU time was then normalised to the time taken by the coarsest mesh.

Figure 5.24a shows the results for the 2D SI model. The difference arrows indicate that the time spent during the adaptivity routine is on average 11.4% of one time step. Similar results were seen with the 3D SBM 3 model (Figure 5.24b) where the adaptivity routine averaged at 12.6% of one time step. These results are in line with those previously reported (Piggott et al., 2009; Hiester et al., 2011).

Figure 5.25 shows the CPU time of the full SBM 3 simulation runs normalised to the CPU time of the coarsest mesh (E1). The adaptive mesh simulation (EA) yields a similar solution to the finest resolution mesh, E4 (Figure 5.22) at a fraction of the total cost.

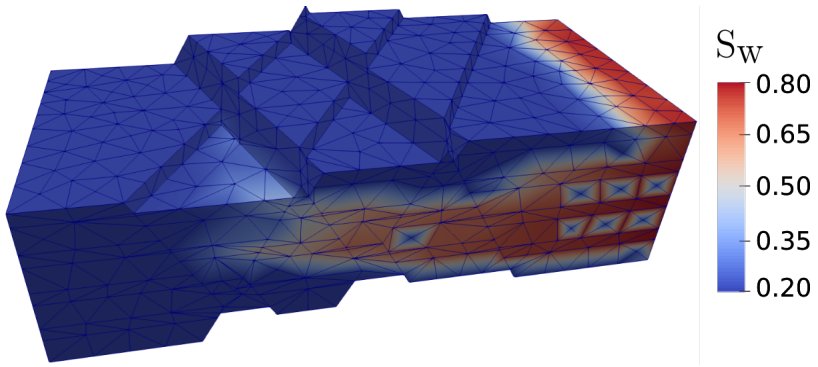


(A)

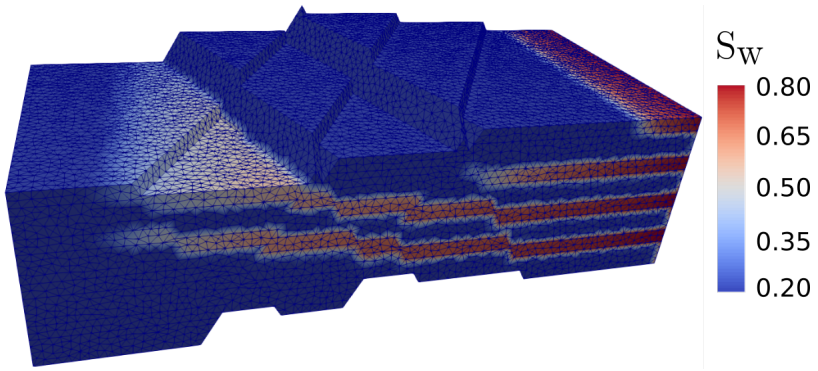


(B)

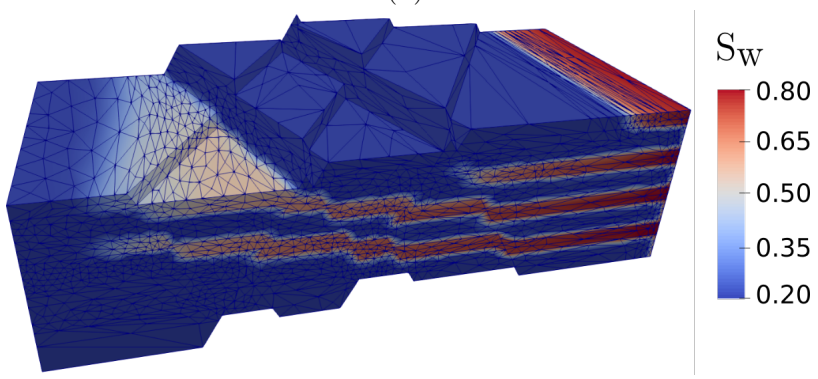
FIGURE 5.22: Production plots as a function of time for simulations of the fault model. (A) oil recovery; (B) water cut.



(A)

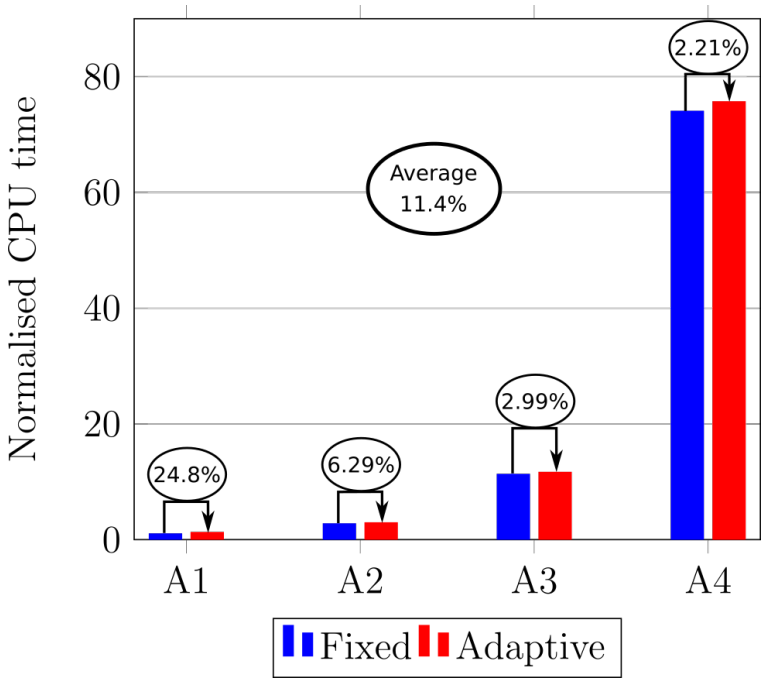


(B)

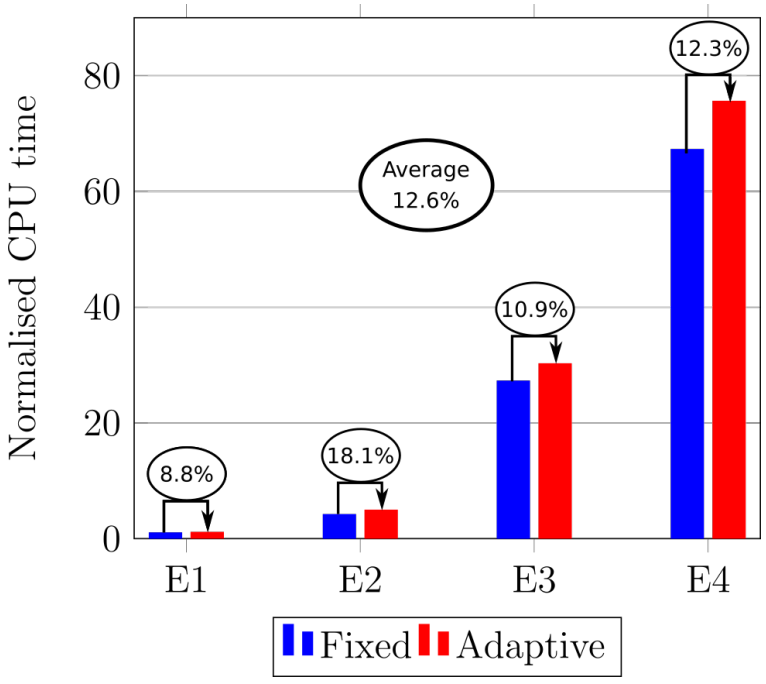


(C)

FIGURE 5.23: Water saturation after 0.2 pore volumes injected. (A) Mesh A; (B) Mesh D; (C) DAMO simulation.



(A)



(B)

FIGURE 5.24: Comparison of CPU times (normalised to the coarsest fixed mesh time) between one time step without adaptivity (blue bars) and one time step followed by one adaptive step (red bar). (A) SI model; (B) Fault model (SBM 3).

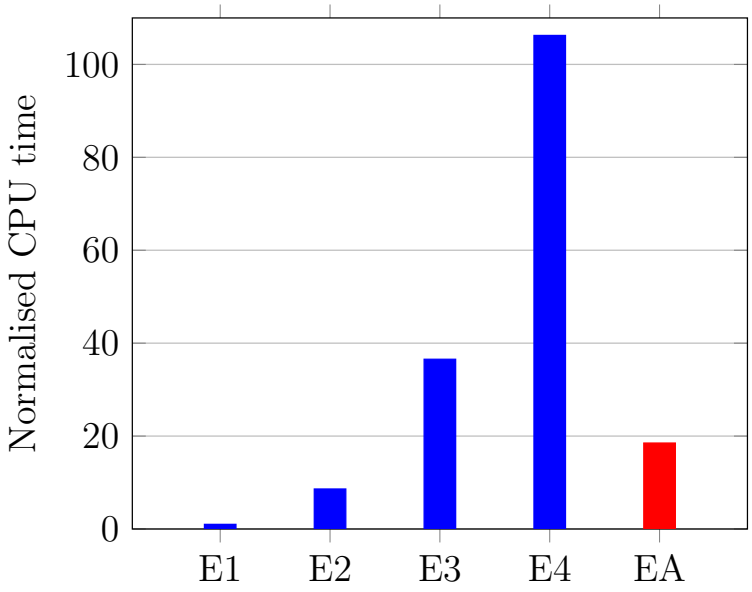


FIGURE 5.25: Total CPU time for the Fault model (SBM 3) normalised to CPU time for mesh E1. Blue bars denote fixed meshes, red bar denotes the DAMO simulation.

5.6 Discussion

There are significant benefits from DAMO in surface-based reservoir modelling and simulation. First, numerical dispersion can be reduced significantly, as the mesh is refined near more rapidly changing solution variables. We demonstrated this with the SI simulation. Due to capillary pressure, the saturation front is not sharp but more smooth. However, we have shown that the DAMO is able to track the front leading to more accurate solutions with orders of magnitude fewer elements compared to the fixed mesh solution.

Second, we demonstrated that DAMO simulations can reduce the effect of saturation smearing with the DNAPL infiltration test case. This is a well known issue with the CVFEM where CVs span element boundaries. This causes CV-wise solution variables such as saturation to be smeared across element boundaries which can represent material boundaries. The non-physical penetration is significantly reduced as the resolution is concentrated at the coarse/fine sand interface.

Third, multi-scale features can be better resolved in a computational efficient manner. The DAMO combined with the SBM approach adopted here allows adaptive meshing to be used without the need for re-scaling every time a mesh is changed. Petrophysical properties are modelled as constant within geologically defined domains and the meshes are coarsened or refined only within these

domains.

Re-scaling properties has been one of the main obstacles to mesh adaptivity in reservoir simulations. The re-scaling of spatially varying material properties such as permeability to develop effective properties is non-trivial. Effective properties are generally process dependent and depend heavily on the flow conditions or underlying grid used to derive them. The computational costs associated with developing new effective properties after each mesh change is therefore prohibitive.

The DAMO algorithm used here ensures that the complex reservoir geometries are preserved during the simulation. This was demonstrated with Models 2 and 3. In SBM 2, we showed how channelised reservoir geometries can be easily modelled using SBMs and meshed with 10× fewer elements than conventional Cartesian grid blocks. Moreover, we showed how maintaining architectural integrity of these channelised models is difficult using conventional modelling techniques. Unless a high resolution is used, channel connectivity may be lost and or artificially created. However, even when the geometries are preserved, with a large number of grid blocks, simulation results will be highly dependent on the grid orientation (due to non-k-orthogonality).

We demonstrated DAMO on a faulted reservoir in SBM 3. During the simulation the DAMO algorithm was shown to resolve both geological interfaces, between high and low permeable facies, as well as the sharp fluid interfaces. This lead to an order of magnitude fewer elements in the DAMO simulation to reproduce the highest resolution fixed mesh results. The DAMO algorithm was also shown to be very efficient, requiring approximately 10% of the cost of one time step.

While explicitly resolving fractures should be considered when modelling transient flow through fractures and geo-mechanical activation and propagation of fractures, it is less useful for viscous dominated flows (Heße et al., 2013) like the one simulated in SBM 1. The DAMO algorithm maintains the master nodes of the initial coarse mesh, which is vital for preserving the geological architectures. However, in SBM 1, a large proportion of the nodes are master nodes. This reduces the flexibility of the algorithm, as few nodes are free to move or be deleted. A commonly used simplification is to represent the fractures (and other high aspect ratio structures) as lower-dimensional features (Ahmed et al., 2015; Monteagudo and Firoozabadi, 2004) and was shown to be justified for many typical conditions (Heße et al., 2013). This is not yet available in IC-FERST. The addition of lower-dimensional structures could significantly increase the efficiency of the DAMO simulations of fracture models.

5.7 Conclusions

In conventional finite-difference-finite-volume method (FDFVM), two-point-flux approximation (TPFA) simulators, one of the main factors affecting accurate simulation of multi-phase flow in reservoir models is the grid size and orientation. Typically, this results in the need for very fine-scale models and simplified geological interpretations to reduce the number of non-k-orthogonal grids. High performance computing has made it possible to routinely run models with millions grid cells. However, the storage, manipulations and simulation of high-resolution geological models remains a great challenge.

One way of reducing the size of the over all system while still being able to resolve small-scale features is to use mesh adaptivity. This tool has revolutionised many areas of engineering science, especially aeronautical engineering (Alauzet and Loseille, 2016). Mesh adaptive techniques are generally divided into three main stages: metric formation, where a suitable metric is formed to guide the mesh adapt; mesh optimisation, where the mesh is locally modified; and mesh interpolation where solution fields are interpolated from the donor to the target mesh.

In this chapter we presented a DAMO algorithm tailored to the unique challenges of reservoir models. To take advantage of mesh adaptivity in a computationally efficient way, while preserving geological architecture, meshes are adapted only within surface bounded geological domains. This removes the need for up-, cross- or down-scaling petrophysical properties every time a mesh is coarsened or refined. The re-scaling of these properties, in particular permeability, is non-trivial and computationally expensive.

We have demonstrated the capabilities of our CVFEM method combined with a DAMO approach by use of a series of models of complex geology, from a channelised fluvial system to a normal faulted layered reservoir; geological heterogeneity that are difficult or impossible to capture on conventional k-orthogonal grids, without a very large number of grid cells. By adapting the mesh within geological domains our approach captures important multi-scale flow features while simultaneously preserving the original geological architecture.

The use of SBM and DAMO have shown great potential, a powerful alternative to the current grid-based modelling and simulations workflows ubiquitous in the petroleum industry. The computational cost of the DAMO routine (metric construction, mesh optimisation and interpolation) was found to be less than one time-step iteration for the problems assessed ($< 13\%$). Considering the

reduction in the number of elements required and the insignificant cost of DAMO, the results presented here demonstrate the advantages of mesh adaptivity for geological models.

Further developments of the CVFEM numerical method are needed to enable lower-dimensional structures such fractures to be modelled and simulated efficiently. Complementing this development, the DAMO algorithm needs to ensure these lower-dimensional structures are preserved during simulation, which is currently not possible.

Chapter 6

Modelling material and property discontinuities

In the previous chapters we highlighted the need for flexible numerical methods to accurately model heterogeneous material and fluid interfaces. In Chapter 3 we introduced the continuous DCVFEM. In this chapter we present a new discretisation that overcomes the major limitation of the continuous DCVFEM, namely its inability to accurately capture the sharp discontinuities in saturation between domains with large material property contrasts i.e. permeability or capillary pressure. The new method, called the discontinuous DCVFEM drastically decreases the non-physical smearing of saturation across material boundaries observed with the continuous DCVFEM. The method uses discontinuous piecewise linear functions enriched with bubble functions for velocity and discontinuous piecewise linear functions for pressure evaluated on CV. LBB stability is maintained with a very efficient velocity:pressure degrees of freedom ratio of 1.25 on tetrahedral meshes. Classical CVFEM on the other hand may reach a ratio of 5. The method does not require CVs to span element boundaries and as a result is able to accurately preserve saturation discontinuities across material boundaries. The method is able to maintain the significant stability improvement on high aspect ratio meshes we have seen with the continuous DCVFEM.

Contents

6.1 Introduction 132

6.2 Stability 133

6.3 Discretisation with bubble functions 136

6.3.1 Force-balance equation 136

6.3.2 Global and local continuity equation 138

6.3.3 Inter-element fluxes 138

6.3.4 Special considerations for the mass matrix 139

6.3.5 Solution mechanism 140
6.4 Numerical Experiments 140
6.5 Results 143
6.5.1 Model 1 143
6.5.2 Model 2 143
6.5.3 Model 3 147
6.6 Conclusions 149

6.1 Introduction

Geological porous media typically comprise numerous domains with contrasting material properties, high aspect ratio geometries (often of order 1000:1 in length:height), and non-parallel, non-orthogonal boundaries across which changes in material properties are effectively discontinuous, occurring over a few tens or hundreds of pores (Nick and Matthäi, 2011; Graham et al., 2015a). Differences in material properties can also induce discontinuities in dependent variables such as fluid saturation and composition (Debbabi et al., 2017a; Debbabi et al., 2017b).

Although control-volume-finite-element method (CVFEM) schemes can handle complex geometries, they fail to accurately capture discontinuities in saturation and other dependent variables across geological domain boundaries, because control-volumes (CVs) span these boundaries (Edwards, 2006; Nick and Matthäi, 2011; Abushaikha et al., 2015; Salinas et al., 2018a). The CV-based solutions artificially 'leak' across the domain boundaries (Abushaikha et al., 2015; Nick and Matthäi, 2011; Edwards, 2006; Salinas et al., 2018a).

Methods to reduce or remove the effect of CVs spanning geological domain boundaries have been proposed by Nick and Matthäi (2011), Bazrafkan and Matthäi (2011), Abushaikha et al. (2015), and Salinas et al. (2018a). Nick and Matthäi (2011) separated the CVs at element boundaries that correspond to material boundaries; however, this approach is inconsistent across element boundaries, so does not guarantee local mass conservation, and was tested only for single-phase flow in 2D. Bazrafkan and Matthäi (2011) used finite-elements (FEs) as CVs and enforced local mass conservation in a post-processing step to calculate fluxes between CVs. However, this approach is inconsistent and was tested only on 2D problems where the local mass conservation equations are radially constructed, which is not the case with 3D elements. Abushaikha et al.

(2015) suggested a new scheme termed the interface control-volume-finite-element method (ICVFEM). In this scheme, pressure is calculated at element interfaces, rather than at element vertices (Figure 6.1b). CVs are constructed around element interfaces, so CVs are shared by, at most, two elements. However, CVs still span material boundaries. Salinas et al. (2018a) presented a new mass conservative CVFEM in 3D that did not require CVs to span material boundaries (Figure 6.1c). The authors demonstrated that their method was able to accurately preserve sharp saturation changes associated with large material property contrasts across geological domain boundaries. However, the method cannot handle elements with large internal angles, which are typically required to discretise high aspect ratio domains such as geological reservoirs.

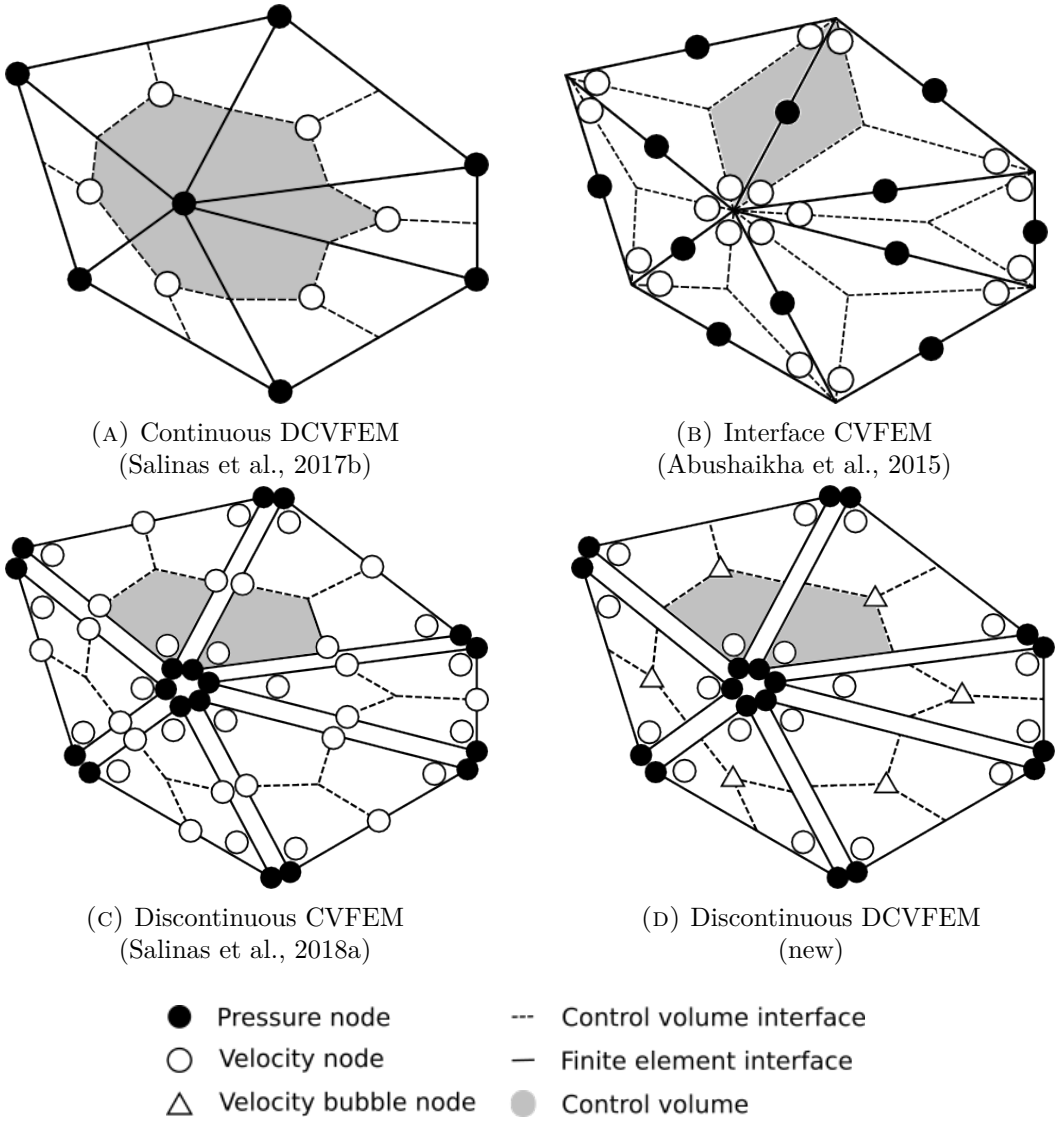
In this chapter, we introduce a new numerical scheme that both removes non-physical leakage across geological boundaries and improves the robustness of classical CVFEM. The new scheme is based on the double control-volume-finite-element method (DCVFEM) (Salinas et al., 2017b) but we introduce discontinuous CVs by allowing the pressure to be discontinuous between FEs. The new finite element pair comprises equal-order finite element pairs (discontinuous linear elements for both the pressure and velocity fields i.e. $P1_{DG} - P1_{DG}$). LBB stability issues are overcome by the use of bubble functions, as explained below.

We demonstrate the capabilities of the new method and compare them to alternative formulations that deal separately with non-physical leakage and stability of high aspect ratio meshes. Currently dynamic adaptive-mesh optimisation (DAMO) is not compatible with discontinuous control volumes, an area for future work. Numerical experiments will therefore be run on static meshes.

6.2 Stability

Stability is an essential property of any numerical discretisation scheme and refers to the relationship between the exact solutions to the discrete problem, and the computed solutions that include round-off/iteration errors (Kuzmin, 2010). Unstable discretisations can lead to the contamination of the numerical solution with numerical artefacts or worse, a solution not being found at all. The stability issue is particularly important for incompressible and near-incompressible flows (Zienkiewicz et al., 2013), leading to highly oscillatory results.

The choice of shape functions in the FE discretisation can have a profound effect on the stability of the projection matrix ($\mathbf{C}^T\mathbf{M}^{-1}\mathbf{C}$; Equation 3.24, Chapter 3).



(A) Continuous DCVFEM (Salinas et al., 2017b)

(B) Interface CVFEM (Abushaikha et al., 2015)

(C) Discontinuous CVFEM (Salinas et al., 2018a)

(D) Discontinuous DCVFEM (new)

FIGURE 6.1: Four CVFEM schemes in their lowest order variants (A) *Continuous DCVFEM*, where CVs span multiple elements. Sharp saturation/component interfaces can not be preserved without significant grid refinement. (B) ICVFEM from Abushaikha et al. (2015), where pressure nodes are placed on the element-element interfaces. CVs are therefore shared by, at most, two elements. CV smearing is reduced but not eliminated. (C) *Discontinuous CVFEM* from Salinas et al. (2018a), where pressure nodes are allowed to be discontinuous between elements. CVs are therefore discontinuous and sharp saturation/component interfaces can be honoured. However this discretisation is based on a $P2_{DG} - P1_{DG}$ element pair making it an expensive method in terms of the DOFs needed and is not robust on distorted meshes. (D) The new *discontinuous DCVFEM* uses a linear element pair $P1_{DG} - P1_{DG}$ with a bubble function augmented velocity space i.e. $P1_{BLDG} - P1_{DG}$.

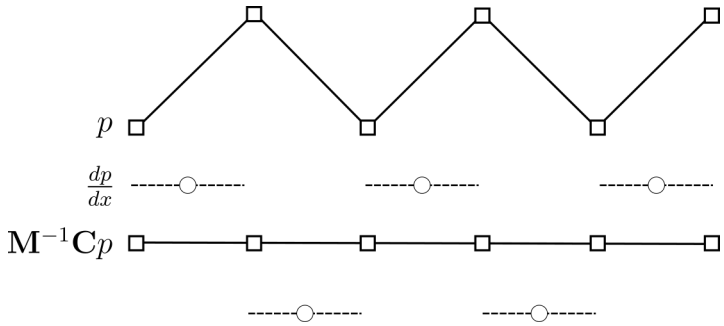


FIGURE 6.2: 1D illustration of an unstable equal order discretisation. The pressure field is piecewise linear; the pressure gradient is therefore piecewise constant. The discrete gradient operator $\mathbf{M}^{-1}\mathbf{C}p$ evaluates the gradient onto the velocity nodes, in this case at the same locations as it is equal order. This results in the gradient being evaluated as zero everywhere. Adapted from Wilson (2009).

The analysis of the stability properties of the projection matrix was performed by Ladyzhenskaya (1969), Babuska (1971), and Brezzi (1974) resulting in the concept of the LBB stability condition. For a discretisation to be LBB stable the discretised representation of the pressure gradient, evaluated in the velocity space must be bounded and not zero for any non-constant pressure function i.e. the element pair must be free from eigenvalues which tend to zero as the discretisation is refined. This condition is not satisfied if equal order element pairs are used, i.e. if equal order interpolation functions are used for both velocity and pressure. This is illustrated in Figure 6.2. In essence the projection matrix is a discrete Laplace operator (i.e. taking the gradient then the divergence) on the pressure field. If a P1P1 element is used, the pressure is a piecewise linear continuous function, so the gradient will therefore exist on each element as a piecewise constant. However, the discrete gradient operator $\mathbf{M}^{-1}\mathbf{C}p$ maps the pressure gradient onto the velocity space; on equal order elements these are the same as the pressure nodes. This results in a zero gradient everywhere. This expansion of the null space means that P1P1 elements are always LBB unstable.

One way to overcome this issue is to have more velocity degrees of freedom than pressure (Elman et al., 2006; Cotter et al., 2009). We achieve this here by the use of interior velocity *bubble* functions. This allows us to admit linear discontinuous pressure functions (thereby achieving discontinuous CVs) while keeping linear discontinuous velocity functions.

6.3 Discretisation with bubble functions

In the formulation presented here velocity, permeability and porosity are represented FE-wise; while pressure, saturation, relative permeability and fluid properties such as viscosity and density are represented CV-wise. This is based on the DCVFEM formulation presented in Chapter 3.

The computational domain (Ω) is discretised into a family of non-overlapping triangular or tetrahedral elements (Ω_E) with a constrained conforming Delaunay triangulation (Shewchuck, 2002).

6.3.1 Force-balance equation

We consider an enriched finite element space $\mathcal{V}$; a linear combination of linear Lagrangian polynomial functions (N_i) and volume bubble functions restricted to each finite element (Arnold et al., 1984).

The bubble functions, $N_E^b \subset \mathcal{V}$ vanish at the element boundaries and have a maximum value at the barycentre of the element

$$\begin{aligned} &N_E^b(\mathbf{x}) > 0 \quad \forall \mathbf{x} \in \Omega_E \\ &N_E^b(\mathbf{x}) = 0 \quad \forall \mathbf{x} \in \Gamma_E \\ &N_E^b(\mathbf{x}) = \text{maximum at barycentre of element E} \end{aligned} \tag{6.1}$$

and are evaluated as a product of the linear Lagrangian basis functions (Zienkiewicz et al., 2013)

$$N_E^b(\mathbf{x}) = \beta \prod_{i=1}^{d+1} N_i(\mathbf{x}) \quad \mathbf{x} \in \Omega_E \tag{6.2}$$

where d is the number of physical dimensions. β is the scaling parameter: setting $\beta = 27$ for 2D elements and $\beta = 256$ for 3D elements returns a value of 1 at the barycentre, which is well known in the literature. However, as we show later, scaling the bubble functions with smaller values of β provides more accurate results.

Any function $\omega \in \mathcal{V}$ can be written as

$$\omega(\mathbf{x}) = \sum_j \omega(\mathbf{x_j}) N_j + \sum_E \omega(\mathbf{x_b}) N_E^b \tag{6.3}$$

where $\mathbf{x_j}, \mathbf{x_b}$ are the coordinate vectors of the element vertex nodes and element barycentres, respectively.

In its weak form, the force balance equation (ignoring source terms) is given by

$$\int_\Omega N_i \left(\boldsymbol{\nu}_\alpha + \nabla p_\alpha\right) dV = \mathbf{0} \tag{6.4}$$

for all basis functions N_i. Applying integration by parts to the pressure gradient term we obtain

$$\int_\Omega N_i \cdot \boldsymbol{\nu}_\alpha dV + \int_\Omega \nabla N_i \cdot p_\alpha dV - \int_{\Gamma_\Omega} p_\alpha \cdot N_i \cdot \mathbf{n} ds = \mathbf{0} \tag{6.5}$$

where Γ_Ω is the domain boundary and $\mathbf{n}$ the outward pointing normal on Γ_Ω. Applying integration by parts to the second term, we obtain

$$\int_\Omega N_i \cdot \boldsymbol{\nu}_\alpha dV + \int_\Omega \nabla p_\alpha \cdot N_i dV - \int_{\Gamma_\Omega} p_\alpha \cdot N_i \cdot \mathbf{n} ds + \int_{\Gamma_\Omega} p^*_\alpha \cdot N_i \cdot \mathbf{n} ds = \mathbf{0} \tag{6.6}$$

where for a continuous pressure formulation $p = p^*$ and therefore would return to Equation 6.4. However, to account for possible jumps in pressure, two pressure solution functions p, p_{ne} are collocated at the same spatial coordinates, and we set p^* as the arithmetic mean of the collocated pressures i.e. $p^* = 0.5(p + p_{ne})$

$$\int_\Omega N_i \cdot \boldsymbol{\nu}_\alpha dV + \int_\Omega \nabla p_\alpha \cdot N_i dV - 0.5 \int_{\Gamma_\Omega} (p_\alpha - p_{\alpha,ne}) \cdot N_i \cdot \mathbf{n} ds = \mathbf{0} \tag{6.7}$$

We now approximate the solution fields $\boldsymbol{\nu}_\alpha$ and p by trial functions expressed in terms of the FE (N_j) and CV basis functions (M_j)

$$\boldsymbol{\nu}_\alpha(\mathbf{x}, t) \approx \sum_j \boldsymbol{\nu}_\alpha(\mathbf{x_j}, t)^T N_j + \sum_E \boldsymbol{\nu}_\alpha(\mathbf{x_b}, t)^T N_E^b \tag{6.8}$$

$$p_\alpha(\mathbf{x}, t) \approx \sum_j p_\alpha(\mathbf{x_j}, t) M_j \tag{6.9}$$

Substituting these trial functions into Equation 6.7 generates the following linear algebraic system

$$\sum_E \int_{\Omega_E} N_i N_j \boldsymbol{\nu}_{\alpha,j} dV + \sum_E \int_{\Omega_E} N_i N_E^b \boldsymbol{\nu}_{\alpha,b} dV + \sum_{CV} \int_{\Gamma_{CV_j}} N_i p_{\alpha,j} \cdot \mathbf{n} ds - 0.5 \sum_E \int_{\Gamma_E} N_i M_j \left(p_{\alpha,j} - p_{\alpha,j,ne}\right) \cdot \mathbf{n} ds + \int_{\Gamma_\Omega} N_i M_j \left(p_{\alpha,j} - p_{\alpha,bc}\right) \cdot \mathbf{n} ds = \mathbf{0} \tag{6.10}$$

where Ω_E, Γ_E are the volume and boundary of the FE, Γ_{CV} is the boundary of the CV. The last term in Equation 6.10 is used to weakly enforce any pressure boundary condition, $p_{\alpha,bc}$ on the domain boundary (Γ_Ω).

6.3.2 Global and local continuity equation

The mass continuity equation is discretised in the standard way by testing with CV basis functions M_j and with the θ-method in time for each phase α (Gomes et al., 2017), as in Chapter 3.

6.3.3 Inter-element fluxes

The implementation of discontinuous pressures requires additional flux calculations for CVs that are between neighbouring elements (Figure 6.3). However, due to the elliptic nature of the pressure equation, information must propagate in all directions across the domain. Hence, a first order upwinding scheme, which can be performed for fluxes within the element, cannot be used here. Instead we use a volume-weighted harmonic mean to calculate the interface flux between two neighbouring CVs i and j, with volumes V_i and V_j, respectively

$$\overline{\mathbf{u}}_\alpha = \left(V_j \boldsymbol{\sigma}_{\alpha,j} \mathbf{u}_{\alpha,i} + V_i \boldsymbol{\sigma}_{\alpha,i} \mathbf{u}_{\alpha,j}\right) \left(V_i \boldsymbol{\sigma}_{\alpha,i} + V_j \boldsymbol{\sigma}_{\alpha,j}\right)^{-1} \tag{6.11}$$

In matrix notation Equation 6.10 can be written as

$$\mathbf{M}\underline{\boldsymbol{\nu}} = -\mathbf{C}\underline{\mathbf{p}} + \underline{\mathbf{R}} \tag{6.12}$$

where $\underline{\mathbf{v}}$ and $\underline{\mathbf{p}}$ are respectively, the force density and pressure solution vectors. The mass matrix $\mathbf{M}$, gradient matrix $\mathbf{C}$ and right hand side vector $\underline{\mathbf{R}}$ are assembled by the usual method from element submatrices

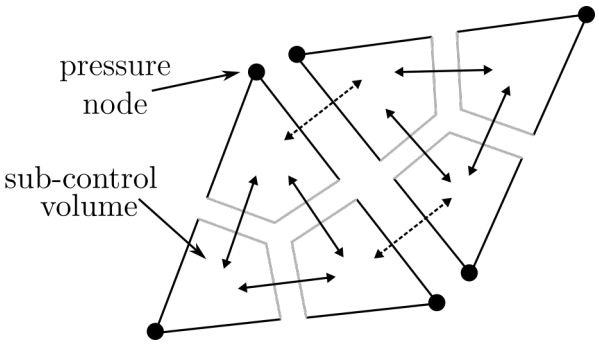


FIGURE 6.3: Intra-element fluxes (sold lines) between sub-control volumes inside the element are calculated for both the continuous and discontinuous formulations. With the discontinuous formulation, sub-control volumes are discontinuous between elements as well, where inter-element flux (dashed lines) are calculated.

$$\begin{aligned}
\mathbf{m}_{i,j} &= \int_{\Omega_E} N_i N_j dV, \\
\mathbf{c}_{i,j} &= \sum_{CV \ni E} \int_{\Gamma_{CV}} N_i M_j \cdot \mathbf{n} ds + \int_{\Gamma_E} N_i M_j \cdot \mathbf{n}^{E,j} ds \int_{\Gamma_E \ni \Gamma_D} N_i M_j \cdot \mathbf{n} ds \\
\boldsymbol{r} &= - \int_{\Gamma_E \ni \Gamma_D} N_i M_j p_{\alpha,bc} \cdot \mathbf{n} ds,
\end{aligned} \tag{6.13}$$

where i and j are the degrees of freedom of element E, $\mathbf{n} = (n_1, n_2, n_3)^T$ are the outward-pointing normal vector of the domain Ω and $\mathbf{n}^{E,j}$ is the normal to the boundary of element E and is outward-pointing if p_j takes support on E, and inward-pointing otherwise.

6.3.4 Special considerations for the mass matrix

The consistent form of the mass matrix above, creates a symmetric, non-diagonal matrix on each finite element. Diagonalisation of the mass matrix, referred to as 'mass lumping' is a common practice and has been shown to be essential to guarantee smooth, non-oscillatory solutions for simulations of unsaturated flow (Celia et al., 1990). While for linear elements (use of linear Lagrangian polynomial functions) lumping procedures are physically obvious, no such procedures exist for hierarchical shape functions such as bubble functions (Zienkiewicz et al., 2013). We tested several approaches and found that the row-sum approach, with scaled bubble functions, gave the best results where

$$M^{\mathrm{L}}_{i,i} = \sum_j M_{i,j} \tag{6.14}$$

We examined the scaling parameter β (Equation 6.2) on the solution of multi-phase flow using the Buckley-Leverett test case in 2D and 3D with pressure boundary conditions. The displacement front was compared with the analytical solution. Figure 6.4a plots the evolution of the error using the row-sum method as a function of the scaling parameter β. It is observed that solution errors are reduced as β decreases, independently of the mesh resolution. Similar results were seen in 3D (Figure 6.4b). However, as β tends to zero the stabilisation effect of the bubble element diminishes, tending (in the end member) to the equal order $P1_{DG} - P1_{DG}$ formulation, which is unstable. As a result we have decided to use $\beta = 1$ for 2D elements and $\beta = 100$ for 3D elements, balancing stability and accuracy.

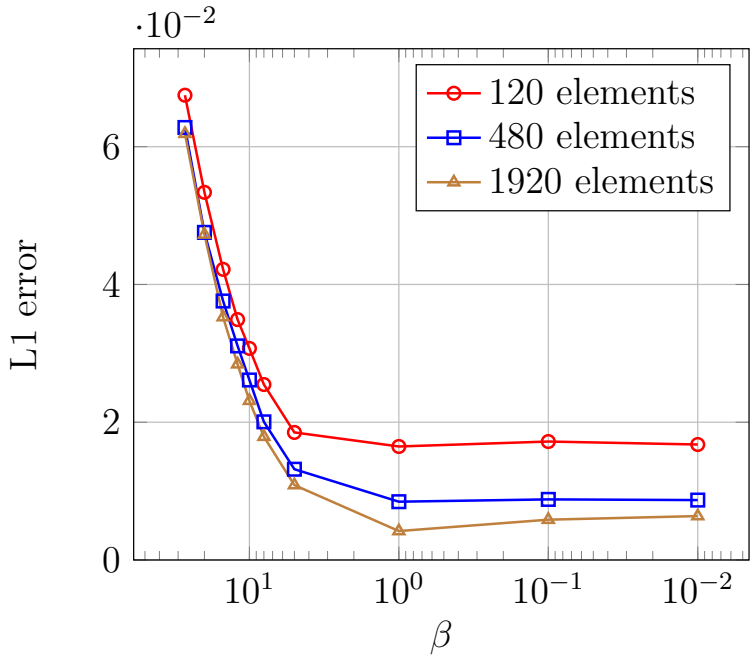
6.3.5 Solution mechanism

The system of equations are solved using the same method as described in Chapter 3. However, the introduction of discontinuous pressure in this formulation can significantly deteriorate the convergence behaviour in the case of non-smooth solutions (Gross and Reusken, 2007; Ausas et al., 2010). In order to stabilise the system we make use of a vanishing artificial diffusion (VAD) method presented by Salinas et al. (2018c). VAD helps to smooth out the pressure solution and improves the convergence rate of the non-linear solver by controlling the non-linearity of the equations in a mass conservative manner (see Salinas et al., 2018c for details).

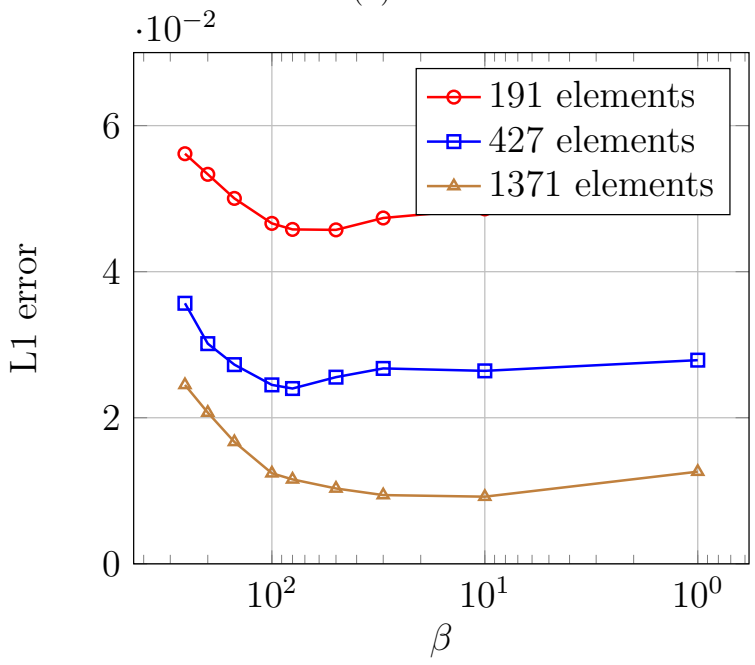
The pressure equation is solved by use of the generalised minimal residual (GMRES) method Krylov subspace solver (Saad and Schultz, 1986) with a multi-grid preconditioner of the PETSc framework (Balay et al., 1997). For the test cases that follow, a GMRES solver with 30 restart iterations and the geometric agglomerated algebraic multi-grid (GAMG) preconditioner were used with default PETSc configurations.

6.4 Numerical Experiments

To test the performance of our formulation, we present two and three-dimensional models (2D and 3D) with a broad range of material properties and boundary conditions, (Table 6.1). First, we benchmark the convergence of the discontinuous DCVFEM against the 2D Buckley-Leverett analytical solution (Model 1). The Buckley-Leverett solution describes the one-dimensional flow of two incompressible, immiscible fluids in a porous media. Water is injected into an



(A)



(B)

FIGURE 6.4: Numerical experiments to obtain the optimal β scaling parameters in 2D and 3D. Error evolution for the 2D Buckley Leverett a) and 3D b) solution as a function of β.

initially oil saturated rectangular domain. The 2D domain is discretised with uniform and isotropic triangular FEs (e.g. Figure 6.5a).

Second, we investigate the formulation's reduction of non-physical fluid smearing using the 3D model of a high permeability fracture embedded in a low permeability domain presented by Abushaikha et al. (2015) (Model 2). This represents a ubiquitous example of geological heterogeneity. Intermediate permeability domains are added to the left and right edges of the model to remove boundary effects (Figure 6.8a). Initially saturated with oil, water is injected at a constant rate at the left boundary. All other boundaries are closed except the right boundary where oil and water are produced at constant pressure.

Finally, we show the stability of the method against a 3D model with highly distorted meshes, representing a common subsurface reservoir type (Model 3).

All the models tested simulate two-phase flow with relative permeabilities given by the Brooks-Corey model

$$\begin{aligned} k_{rw}(S_w) &= k_{rw}^{max}\left(\frac{S_w - S_{wr}}{1 - S_{wr} - S_{nr}}\right)^{n_w} \\ k_{rn}(S_n) &= k_{rn}^{max}\left(\frac{S_n - S_{nwr}}{1 - S_{wr} - S_{nr}}\right)^{n_n} \end{aligned} \tag{6.15}$$

where $k_{rw}(S_w)$ and $k_{rn}(S_n)$ are, respectively, the wetting and non-wetting relative permeabilities, $k_{rw}^{max}(S_w)$ and $k_{rn}^{max}(S_n)$, are the wetting and non-wetting end-point relative permeabilities, S_{wr} and S_{nr} are the irreducible wetting and non-wetting phase saturations, and n_w and n_n are the exponents for the wetting and non-wetting phases. The influence of capillary and gravitational forces are assumed to be negligible.

The reduction in non-physical fluid smearing in the embedded fracture test case is quantified using a normalised measure of the mass leakage into the low permeability domain (Abushaikha et al., 2015; Salinas et al., 2018a). Similar to Salinas et al. (2018a), the mass leakage at time t is defined as the pore-volume-weighted average change in water saturation (S_w) in the low permeability domain

$$\eta(t) = \frac{\sum_i^{n_{CV}^{k_{low}}} \left(S_{i,w}^{t} - S_{i,w}^{t_0}\right) V_i \phi_i}{\sum_i^{n_{CV}^{k_{low}}} V_i \phi_i} \tag{6.16}$$

TABLE 6.1: Model set up.

Property	Model 1	Model 2	Model 3
Domain 1 permeability	1[-]	0.01 [-]	1000 [mD]
Domain 2 permeability	N/A	1 [-]	200 [mD]
Domain 3 permeability	N/A	100 [-]	100 [mD]
Water viscosity	1 [-]	1 [-]	0.001 [Pa.s]
Porosity	0.2 [-]	0.2 [-]	0.2 [-]
Oil viscosity	1 [-]	1 [-]	0.004 [Pa.s]
Water/oil phase endpoint relative permeability	1 [-]	1 [-]	1 [-]
Water/oil phase Corey exponent	2 [-]	2 [-]	2 [-]

where $n_{CV}^{k_{low}}$ is the number of control volumes within the low permeability domain. The mass leakage is normalised against the largest value at a particular time step.

6.5 Results

6.5.1 Model 1

Figure 6.5b shows the saturation maps at two time steps as water displaces oil. As the mesh is refined the numerical solution of the new method converges to the analytical solution (Figure 6.6). The L_1 error norms of the new discretisation, discontinuous DCVFEM shows close to linear convergence (Figure 6.7a). However, for such a simple case, with homogeneous permeability the continuous DCVFEM is much more computationally efficient as far fewer degrees of freedom are required to obtain the same quality solution (Figure 6.7b).

6.5.2 Model 2

With the continuous DCVFEM in which CVs span the boundaries between high and low permeability domains, significant non-physical smearing is introduced across this boundary. While the geometry of the embedded fracture is accurately captured (Figure 6.8b), the CV mesh, where saturation and saturation related fields are calculated, does not conform to the boundaries of the fracture. Figure 6.9a shows the CV mesh that is constructed for the continuous CVFEM on the same tetrahedral mesh shown in Figure 6.8b. The CVs (highlighted in green) span the fracture boundary depicted by the red rectangle, while using

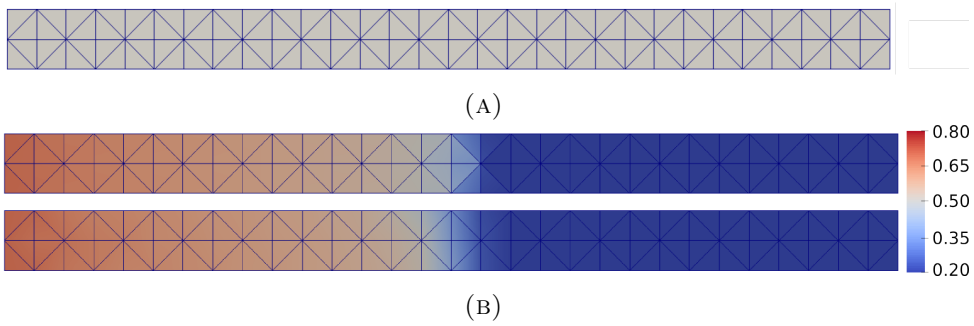


FIGURE 6.5: (A) The coarsest 2D mesh used in the Buckley-Leverett model, (B) saturation maps of the water phase after 0.6 pore volumes injected (PVI) with the continuous DCVFEM and the new discontinuous DCVFEM, respectively. Water is injected at the left-hand boundary displacing oil of equal viscosity in a homogeneous domain.

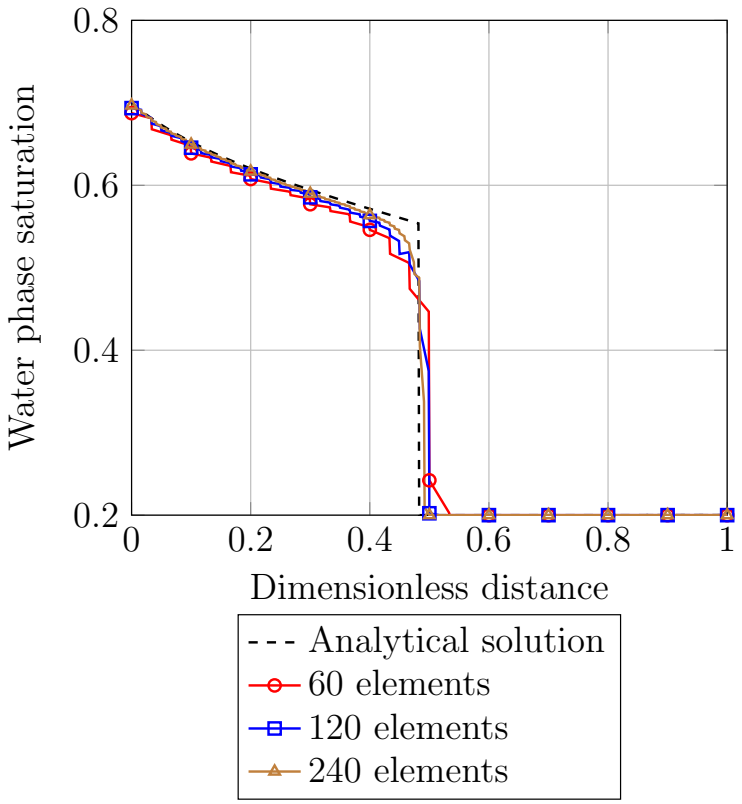
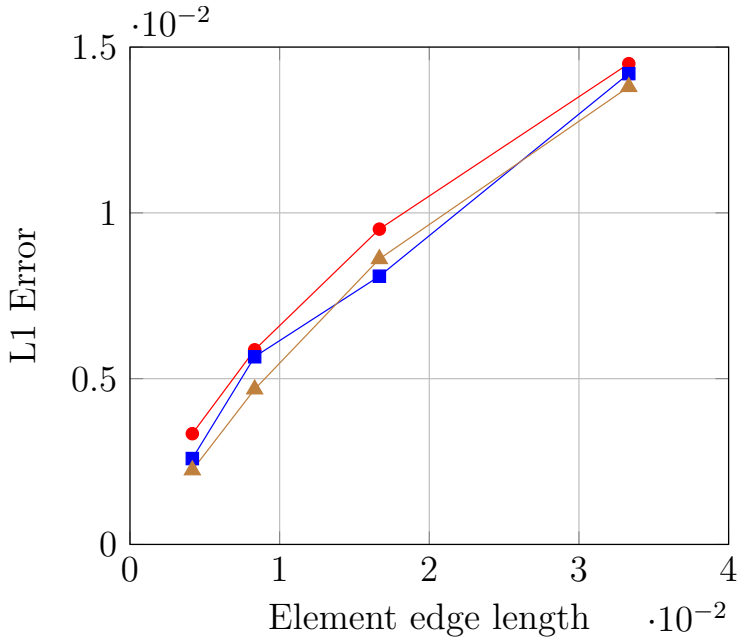
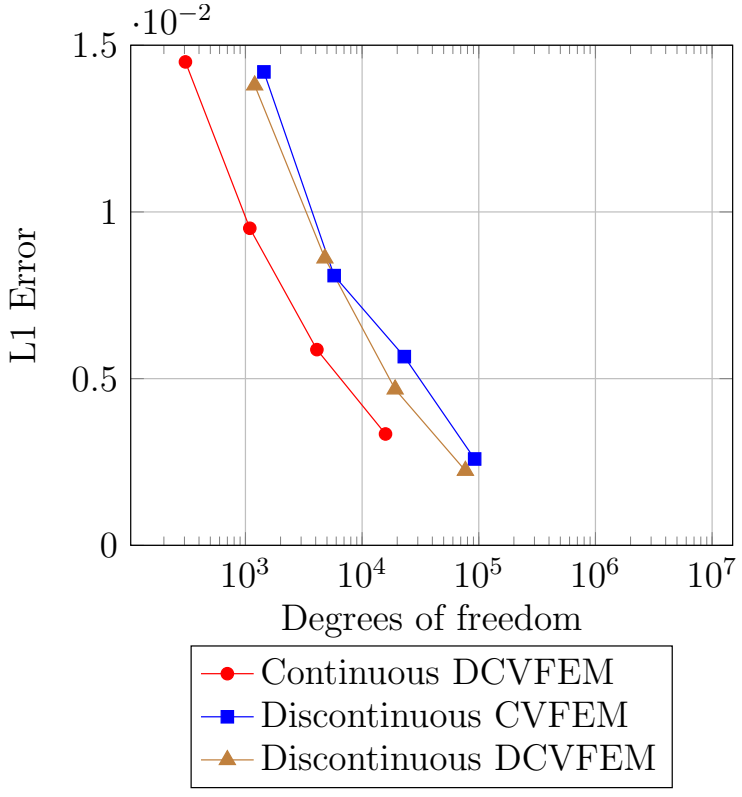


FIGURE 6.6: Comparison of the analytical Bucklet-Leverett solution at distance 0.5 dimensionless units from the inlet boundary to the numerical solution of the new method (discontinuous DCVFEM) using three meshes. Number of elements are in the flow direction, meshes are refined by edge splitting.

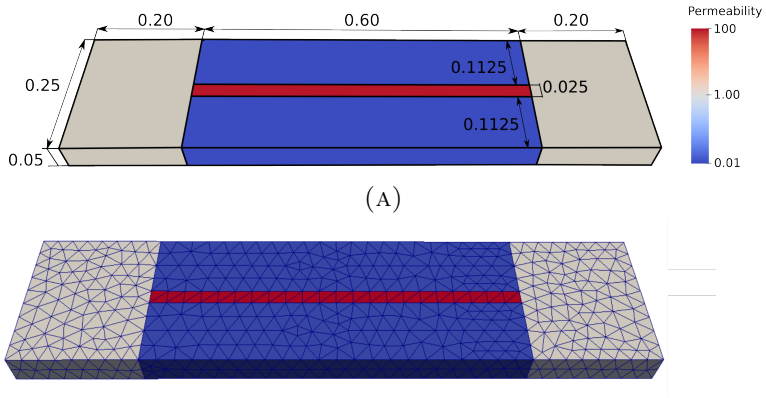


(A)



(B)

FIGURE 6.7: a) Convergence of the L_1 error of the water saturation as a function of the mesh element length for the numerical solution of the Buckley-Leverett problem using the continuous DCVFEM, the discontinuous DCVFEM and the new element pair reported discontinuous DCVFEM; b) Convergence of the L_1 error as a function of number of degrees of freedom.



(A)

(B)

FIGURE 6.8: (A) Permeability map and dimensions (dimensionless units) of the embedded fracture model (Salinas et al., 2018a). Permeability contrast of 1×10^4 between the high permeability fracture and surrounding low permeability domain, (B) an example of the unstructured tetrahedral mesh used.

the new formulation (discontinuous DCVFEM) CVs do not span the fracture boundary (Figure 6.9b). The CV mesh in Figure 6.9b is constructed from a coarser tetrahedral mesh but contains approximately the same number of degrees of freedom as the continuous DCVFEM discretisation in order to perform a fair comparison.

The discontinuous DCVFEM results in a significant reduction in non-physical smearing (Figures 6.9c - 6.9d), quantified by mass leakage into the low permeability domain (Figure 6.10a, solid lines). With less artificial smearing, the water is able to penetrate further into the domain, leading to an earlier water breakthrough. As time progresses the front is slowed down by the intermediate permeability domain at the outlet end. This leads to cross flow into the low permeability domain which is a physically realistic solution (Figure 6.9f).

The reduction in artificial smearing can be as much as an order of magnitude. As the mesh is refined the amount of mass leakage decreases, however, even with an order of magnitude more degrees of freedom the continuous CVFEM is unable to achieve the same reduction in non-physical mass leakage as the discontinuous methods. Moreover, the efficiency of discontinuous DCVFEM can also be seen with the ratio of velocity to pressure nodes (Figure 6.10a, dashed lines). While the solution is equally accurate for the two discontinuous formulations, the discontinuous DCVFEM is able to achieve this with half as many velocity nodes to pressure nodes compared to the discontinuous CVFEM (Figure 6.10a).

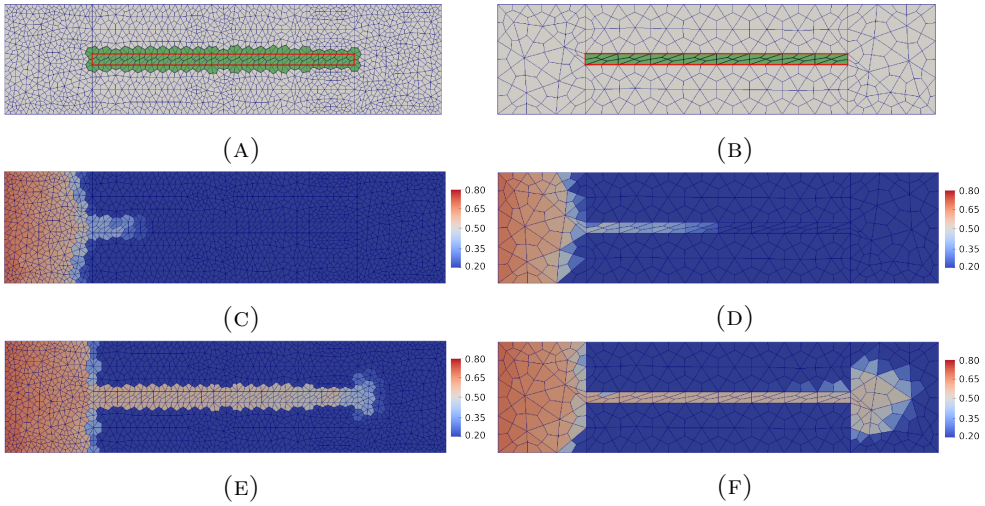
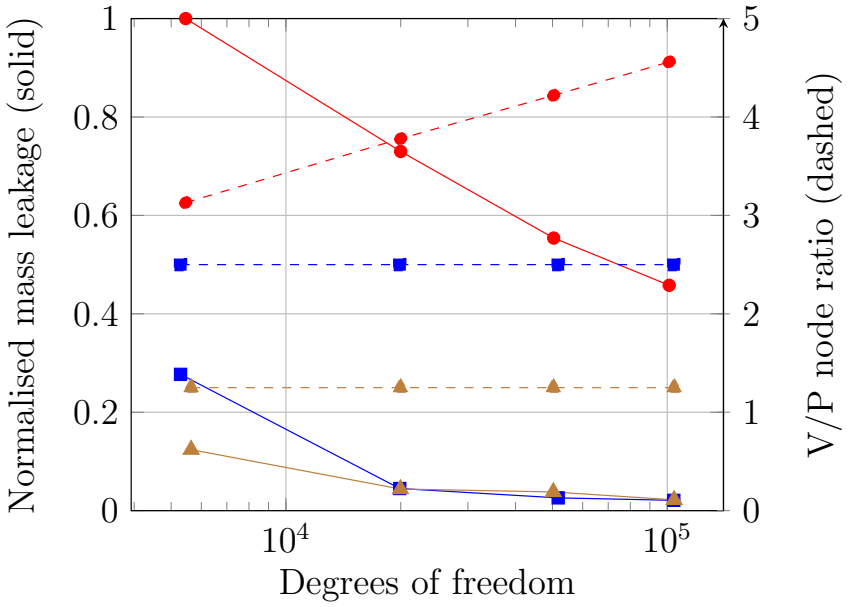


FIGURE 6.9: 2D slice of the embedded fracture model using the classical CVFEM (left) and the new formulation (right). (A),(B) The control volume dual mesh for each method. The embedded fracture is depicted by the red rectangle. The CVs around the fracture are highlighted in green. In the classical CVFEM discretisation they span the fracture boundary while in the new formulation the sharp interface is retained. Both meshes have the same number of degrees of freedom. (C),(B) saturation maps of the water phase after 0.08 PVI and (E),(F) saturation maps of the water phase after 0.15 PVI.

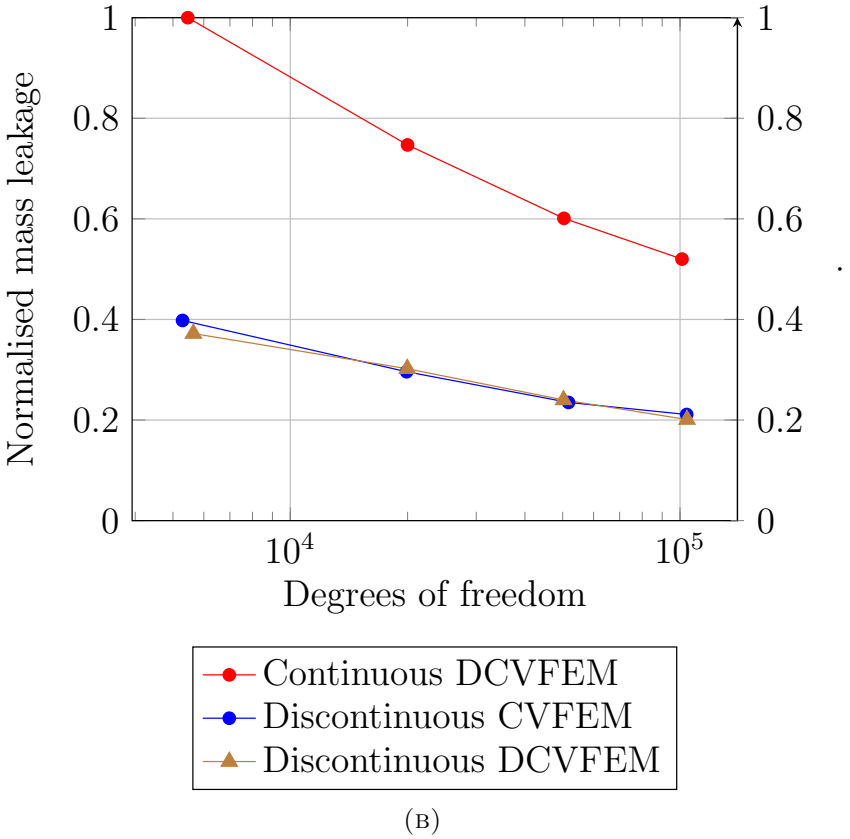
6.5.3 Model 3

In this final numerical example we use the channelised sandstone reservoir model (SBM 2), from Chapter 5. The complex architecture of the channelised sandbodies are honoured with an efficient number of elements. However, the resulting mesh is highly distorted. Not only is the aspect ratio of the model very large, the intersection between individual channels creates features with even higher aspect ratios (see highlighted elements in Figure 6.11). The majority of elements on this mesh have angles greater than 120° and a significant number of elements have angles greater than 170°. Although these high aspect ratio features could be meshed with high quality elements, it would require a very large number of (small) elements, which would be computationally expensive.

We investigate the efficiency of the proposed method using three different meshes of the channel model with increasing resolution. Mesh A consists of $12,854$ elements. The refined meshes B and C are created via a 'refine-by-splitting' approach to retain the same mesh quality in all three meshes, with respectively, $102,832$ and $824,464$ elements. Initially saturated with oil and residual water, we simulate the displacement of oil with water injected from the right hand boundary with production from the left hand boundary, with all other boundaries



(A)



(B)

FIGURE 6.10: Normalised mass leakage into the low permeability domain in the embedded fracture model at (A) after 0.08 PVI; (B) after 0.15 PVI. The ratio of velocity:pressure nodes is shown in (A) for the three discretisations.

closed. Figure 6.13 shows water saturation maps of the model at various time steps for both the continuous DCVFEM and discontinuous DCVFEM. The reduction in smearing means that the water front propagates faster across the model with an earlier breakthrough through the small high permeability channels. Through the larger, low permeability channels the sharp front is preserved with the discontinuous DCVFEM while the continuous DCVFEM is more dispersive. This effect would be even more pronounced if non-reservoir volumes were included in the model (Figure 6.9).

Figure 6.12 shows the reduction in residual error as a function of the number of iterations using GMRES and 30 restart iterations together with the GAMG. For the multi-grid solver we consider as stopping criterion a 10 order reduction of the maximum residual (typically used in literature; Salinas et al. (2006)) The continuous DCVFEM shows extremely stable performance independent of the mesh resolution, requiring less than 30 iterations to reduce the residual error 10 orders of magnitude. The discontinuous CVFEM also shows mesh independent behaviour but requires an order of magnitude more iterations to achieve the same reduction in residual error. However, we note that although the discontinuous CVFEM was able to solve for pressure (albeit slowly) on this distorted mesh, the subsequent velocity calculations were incorrect. As previously discussed, the discontinuous CVFEM requires the computation of shape function derivatives which can be very inaccurate on highly distorted meshes. The new discontinuous DCVFEM makes use of the CV pressure discretisation which in turn removes the need for these derivatives. This was seen to greatly improve the quality of the pressure matrix which leads to fewer iterations of the linear solver (Figure 6.12) and accurate flux calculations. The discontinuous DCVFEM shows similar behaviour on Mesh A and B needing around twice the number of iterations as the continuous DCVFEM. The highest resolution mesh needed around 90 iterations. However, considering the poor quality of the mesh the discontinuous DCVFEM method shows very good results.

6.6 Conclusions

We presented a new CVFEM which improves the modelling of multi-phase flow in high aspect ratio, heterogeneous models. The method uses discontinuous linear elements for both pressure and velocity fields and addresses the loss of LBB stability through the use of a scaled bubble function for the velocity field. Moreover, the pressure field is discretised using CV shape functions, the element pair is therefore $P1_{BLDG} - P1_{DG}$.

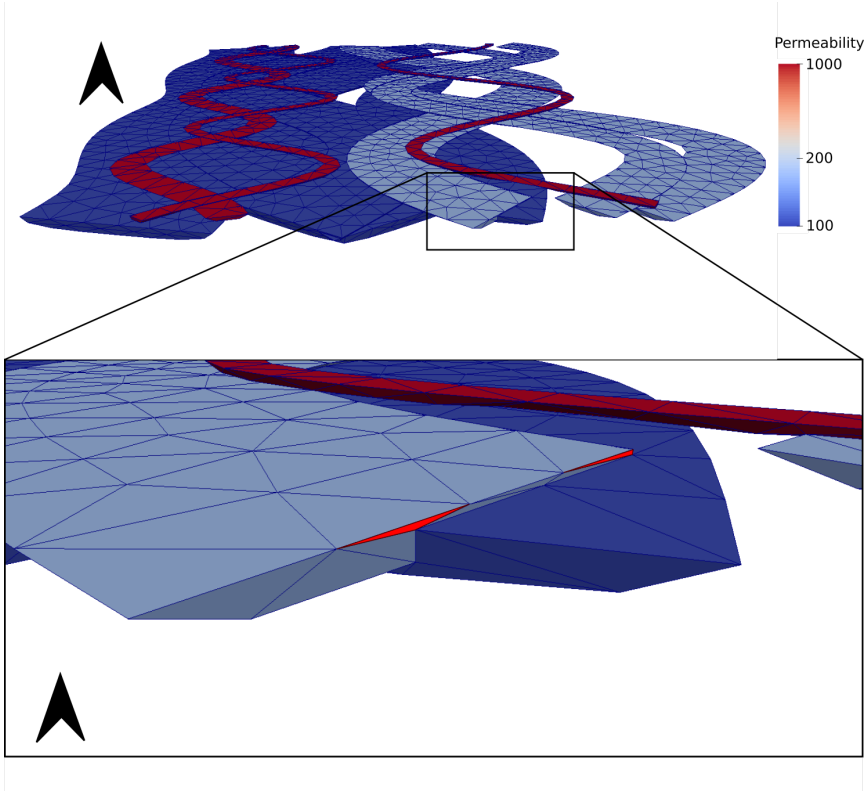


FIGURE 6.11: Channel model meshed using unstructured tetrahedral elements. Three groups of channels are shown with large contrast in permeability (top). High aspect ratio elements are needed to capture the geometry. Examples of distorted elements are highlighted in red (bottom).

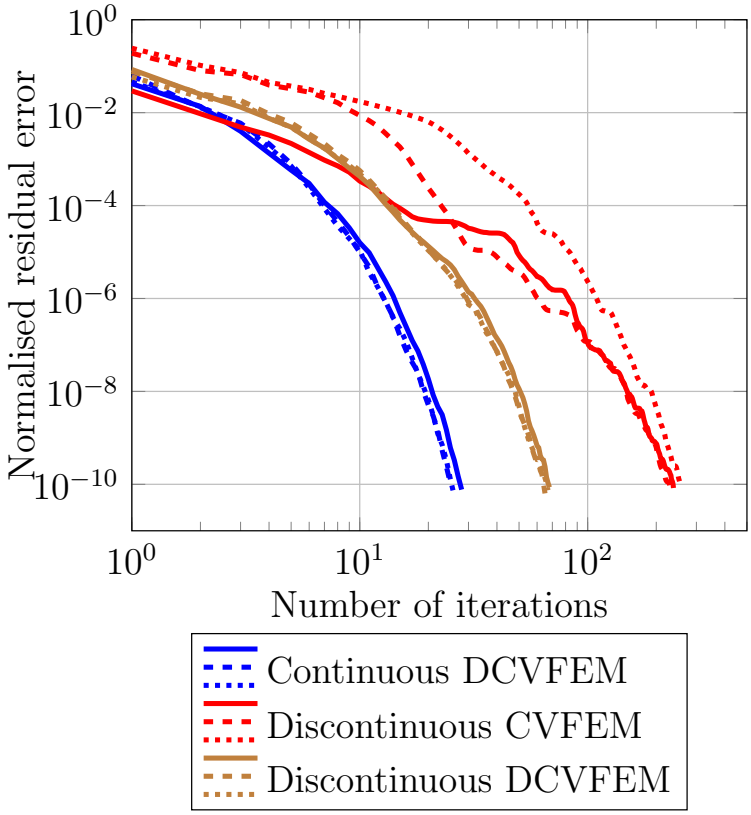


FIGURE 6.12: Reduction in residual error as a function of the number of iterations for the initial time-step. Solid lines, dashed lines and dotted lines are, respectively, the results on Mesh A, B and C.

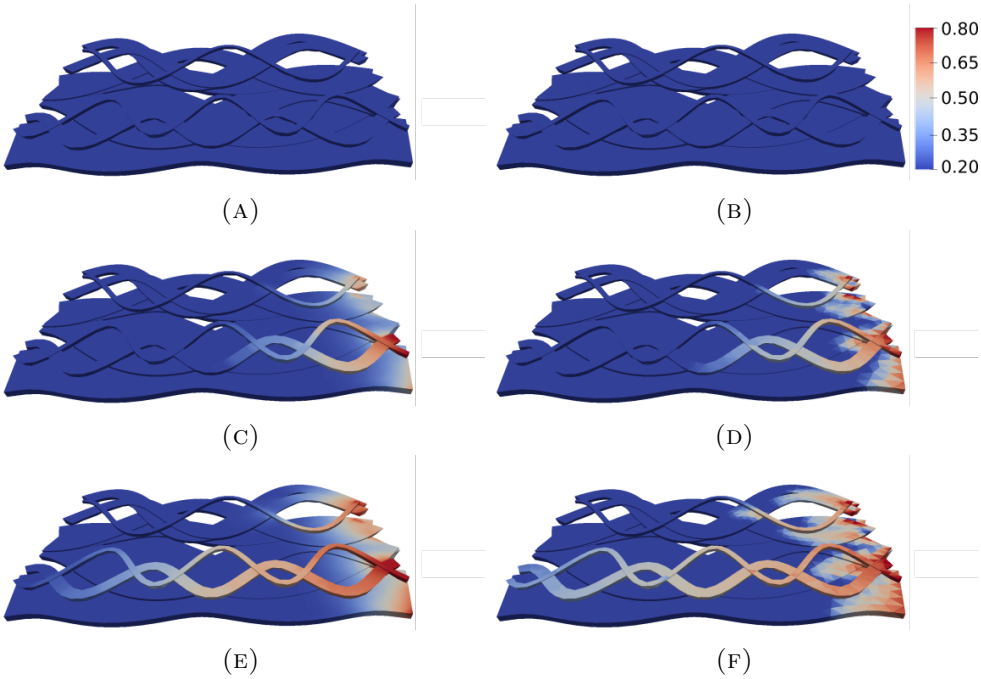


FIGURE 6.13: Water saturation distribution at various time steps of the channel model using the continuous DCVFEM (left) and the discontinuous DCVFEM (right); vertical exaggeration ×4. Water injection is at the right boundary, production at the left boundary.

We demonstrate that the new method produces accurate solutions with first-order convergence when tested against the analytical solution of the Buckley-Leverett benchmark problem.

The discontinuous pressure allows the implementation of CVs that do not span domain boundaries. We demonstrate that this approach is able to accurately preserve sharp saturation changes across material property boundaries. The reduction in non-physical smearing of the saturation can be as large as an order of magnitude when compared to the continuous DCVFEM. The results are almost identical to the discontinuous CVFEM method, however, the new method has half the number of velocity nodes (on 3D meshes). This makes the new method computationally far more efficient.

This formulation also provides significantly better pressure matrices in highly heterogeneous and distorted models. We verify this on a high aspect ratio model of a channelised reservoir. The complex geometries of this model and their high aspect features produce mesh elements with very large angles which can only be avoided if very high resolution meshes are used which would be computationally prohibitive on large models. Results have shown that the new method performs significantly better than the discontinuous CVFEM method which struggles to

converge on the highly distorted meshes.

The applications of the method above seem promising. We demonstrate that at reasonable computational costs the discontinuous DCVFEM is able to accurately model multi-phase flow through three-dimensional models of highly heterogeneous, high aspect ratio porous media.

In the future we also plan to develop a hybrid scheme that makes use of this new formulation at material boundaries with the lower order scheme (continuous DCVFEM) in homogeneous regions. Another area of development needed is the DAMO algorithm which is as of yet not compatible with this new formulation.

Chapter 7

Conclusions and Future Work

7.1 Conclusions

The modelling and simulation of multi-phase flow and transport in subsurface reservoirs will continue to be of major interest. This is largely driven by the need to securely store CO_2 and nuclear waste underground as well as improving recovery from geothermal and hydrocarbon reservoirs. Significant progress has been made in the development of more advanced geological modelling and numerical discretisation methods. In this thesis we explored a new workflow that replaces the conventional grid-based approach to modelling and simulation. The approach combines surface-based modelling (SBM), a new CVFEM (called DCVFEM) and DAMO to preserve key flow features associated with multi-scale geological heterogeneity.

Conventional grid-based reservoir models typically contain a large number of petrophysical property values that vary on a cell-to-cell basis. In Chapter 4 we show that these property values can be collapsed into a much smaller number of larger and internally homogeneous but more geometrically complex geological domains. This was found to be irrespective of the reservoir geology, fluid properties or well configurations. In fact, we argue that cell-to-cell scale variability is not necessary in reservoir models to capture multi-phase flow.

In our SBM approach, geologically defined rock volumes are modelled with homogeneous petrophysical properties. This allows adaptive meshing to be used in reservoir simulation without the need for up-, cross or down-scaling petrophysical properties after each mesh adapt. For free flow problems, DAMO is well known to generate significant computational savings and/or higher resolution models. However, the computational cost of re-scaling petrophysical properties, especially permeability, has held back DAMO for porous media flows. In Chapter 5 we demonstrate the use of DAMO to capture complex flow features in SBMs of

realistic geological heterogeneity. Crucially, the surfaces that define the geological domains are preserved during mesh adapts, so geological model heterogeneity is not lost.

The cost of DAMO was found to be insignificant, less than 13% of one time-step iteration. In conjunction with the reduction of the number of elements, the computational cost of a DAMO simulations was found to be far lower than that of running a high resolution model, to obtain the same solution accuracy. Indeed the resolution required to obtain such high quality results with conventional grid-based models would be unrealistic in practical applications.

Although CVFEM with DAMO can provide accurate solutions to multi-phase flow problems in subsurface models, their use is not widespread. In Chapter 5 we tackle the two main challenges of standard CVFEMs with a new discretisation, i.e. the failure to represent saturation discontinuities and robustness on high aspect ratio elements. The new method uses discontinuous linear elements for both pressure and velocity fields and addresses the loss of LBB stability through the use of a scaled bubble function for the velocity field. Moreover, the pressure field is discretised using CV shape functions. CVs do not span domain boundaries and can therefore accurately represent sharp saturation changes near material discontinuities. The new formulation was also found to provide significantly better pressure matrices in highly heterogeneous and distorted meshes.

7.2 Future Work

The workflow described in this thesis is being actively developed. Applications shown in this work have been promising. However, in order to make Imperial College Finite Element Reservoir SimulaTor (IC-FERST) a day-to-day reservoir management tool significant developments are needed in both practical and research relevant areas.

Practical improvements such as computational efficiency and incorporating more complex phase flow physics, well modelling, coupling with surface facility and improved nonlinear solvers are important to make IC-FERST more attractive for industrial applications. An industrial partner has been found and progress is being made to commercialise IC-FERST.

As well as these practical improvements, further research work is being pursued to advance the capabilities of IC-FERST.

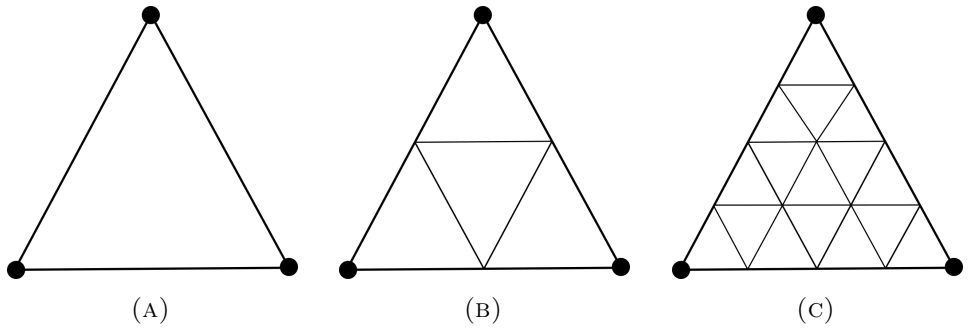


FIGURE 7.1: Semi-structured meshing. Starting from a coarse mesh represented by a single element in (A), a hierarchy of meshes can be obtained by refine-by-splitting (B) and (C).

The following are a few examples of proposed projects to improve the capabilities and robustness of the methodology.

The drawbacks of grid-based methods that rely on k-orthogonal grids and two-point-flux approximation (TPFA) simulators are well known (Chapter 2). However, conventional modelling and simulation workflows using structured meshes, have had one major advantage over the next generation alternatives, that is of speed. Unstructured meshes, used in IC-FERST, are flexible enough to represent the complex geological geometries found in subsurface reservoirs but if non-neighbouring connections are needed this can add a large computational overhead to store elements, nodes and connectivity tables. While DAMO was shown to increase computational efficiency over fixed meshes, greater improvements are needed. One way is to use semi-structured meshes. With semi-structured meshes, an initial unstructured coarse mesh is created to honour the geological architecture. Then a logically nested set of meshes can be created via refine-by-splitting within each of the coarse mesh elements (Figure 7.1). This creates a set of structured meshes with logical node connectivity, which can lead to a significant speed up of the method.

Although it has been demonstrated here and elsewhere that surface-based models can accurately represent very complex geological heterogeneities, they are more difficult to constrain to different types of data (Bertoncello et al., 2013; Zhang and Pyrcz, 2006). This also makes sensitivities and history matching simulations more complex to perform, although not impossible (Trani and Graham, 2016). Further work is therefore needed to develop robust workflows to condition and history match surface-based models.

High aspect ratio features such as fractures are often conceptualised as lower-dimensional structures embedded into the surrounding matrix. This simplification is typically made with numerical simulations as well as demonstrated by various authors (Monteagudo and Firoozabadi, 2004; Ahmed et al., 2015; Reichenberger et al., 2006). This simplification is valid for viscous dominated flow and can lead to significant reductions in computational costs (Heße et al., 2013)

In Chapter 6 we introduced a new discretisation, the discontinuous DCVFEM, that tackles the issue of saturation smearing across sharp material property boundaries, due to CVs spanning material boundaries. In future, the new formulation will be tested using the wide range of test cases presented in Chapter 5 which form a more challenging set of test cases. However, the increased computational cost of this method is not justified in homogeneous areas or where material boundaries are smooth. A hybrid implementation which utilises the discontinuous DCVFEM only where necessary and the continuous DCVFEM elsewhere is therefore needed.

Further developments in the DAMO algorithm are also needed. Currently DAMO does not 'recognise' lower-dimensional volumes as structures to honour. Therefore 1D fractures in 2D models or 2D fractures in 3D models are not preserved through the DAMO routine. Another area for future work is to ensure that the adaptivity algorithm is compatible with the new finite element formulation presented in Chapter 6. As yet the adaptivity algorithm is not compatible with discontinuous control volumes.

Accurate modelling of near-well flows are important in reservoir simulation but are typically poorly represented. Conventional simulation techniques connect perforated grid cells to the solution by indices that often do not represent complex well trajectories (Fung et al., 2014). Local grid refinement is also often needed to resolve the flow dynamics, which can contribute to numerical errors due to strong grid orientation effects. The use of unstructured, non-k-orthogonal meshes can better represent near-well effects. Although a simple well-model currently exists in IC-FERST further development is needed to make it more robust and efficient.

Bibliography

Aarnes, J. E., V. Kippe, and K. A. Lie (2005). "Mixed multiscale finite elements and streamline methods for reservoir simulation of large geomodels". In: *Advances in Water Resources* 28, pp. 257–271. ISSN: 03091708. DOI: 10.1016/j.advwatres.2004.10.007.

Aarnes, J. E., S. Krogstad, and K. A. Lie (2006). "A hierarchical multiscale method for two-phase based upon mixed finite elements and nonuniform coarse grids". In: *SIAM* 5.2, pp. 337–363. ISSN: 1755-3245; 0008-6363. DOI: 10.1093/cvr/cvp175.

– (2008). "Multiscale mixed/mimetic methods on corner-point grids". In: *Computational Geosciences* 12.3, pp. 297–315. ISSN: 14200597. DOI: 10.1007/s10596-007-9072-8.

Aavatsmark, I (2002). "An introduction to multipoint flux approximations for quadrilateral grids". In: *Computational Geosciences* 6.3-4, pp. 405–432. ISSN: 14200597. DOI: 10.1023/A:1021291114475.

Aavatsmark, I., T. Barkve, Ø. Bøe, and T. Mannseth (1994). "Discretization on non-orthogonal curvilinear grids for multi-phase flow". In: *Proceedings of 4th European Conference on the Mathematics of Oil Recovery*, pp. 1–17.

Aavatsmark, I., G. T. Eigestad, B. T. Mallison, and J. M. Nordbotten (2008). "A Compact Multipoint Flux Approximation Method with Improved Robustness". In: *Numerical Methods for Partial Differential Equasion*. DOI: 10.1002/num.

Abushaikha, A. S., M. J. Blunt, O. R. Gosselin, C. C. Pain, and M. D. Jackson (2015). "Interface control volume finite element method for modelling multi-phase fluid flow in highly heterogeneous and fractured reservoirs". In: *Journal of Computational Physics* 298, pp. 41–61. ISSN: 10902716. DOI: 10.1016/j.jcp.2015.05.024. URL: http://dx.doi.org/10.1016/j.jcp.2015.05.024.

Aghaei, A and M Piri (2015). "Direct pore-to-core up-scaling of displacement processes: Dynamic pore network modeling and experimentation". In: *Journal of Hydrology* 522, pp. 488–509. ISSN: 00221694. DOI: 10.1016/j.jhydrol.2015.01.004. URL: http://dx.doi.org/10.1016/j.jhydrol.2015.01.004.

Ahmed, R, M G Edwards, S Lamine, and B A H Huisman (2015). "Control-Volume Distributed Multi-Point Flux Approximation Coupled with a Lower-Dimensional Fracture Model". In: *SPE Reservoir Simulation Symposium*.

Alauzet, F., P. J. Frey, P. L. George, and B. Mohammadi (2007). "3D transient fixed point mesh adaptation for time-dependent problems: Application to CFD simulations". In: *Journal of Computational Physics* 222.2, pp. 592–623. ISSN: 00219991. DOI: 10.1016/j.jcp.2006.08.012.

Alauzet, Frédéric and Adrien Loseille (2016). "A decade of progress on anisotropic mesh adaptation for computational fluid dynamics". In: *CAD Computer Aided Design* 72, pp. 13–39. ISSN: 00104485. DOI: 10.1016/j.cad.2015.09.005.

Allard, D., R. Froidevaus, and P. Biver (2004). "Accounting for non-stationarity and interactions in object simulation for reservoir heterogeneity characterization". In: *Geostatistics Banff*. Springer, pp. 155–164.

Anderson, D. G. (1965). "Iterative Procedures for Nonlinear Integral Equations". In: *Journal of the ACM* 12.4, pp. 547–560. ISSN: 00045411. DOI: 10.1145/321296.321305. URL: http://portal.acm.org/citation.cfm?doid=321296.321305.

Arnold, D. N. and F. Brezzi (1985). "Mixed and nonconforming finite element methods: implementation, postprocessing and error estimates". In: *Mathematical Modelling and Numerical Analysis* 19.1, pp. 7–32.

Arnold, D N, F Brezzi, and M Fortin (1984). "A stable finite element for the stokes equations". In: *Calcolo* 21.4, pp. 337–344. ISSN: 00080624. DOI: 10.1007/BF02576171.

Ausas, R. F., F. S. Sousa, and G. C. Buscaglia (2010). "An improved finite element space for discontinuous pressures". In: *Computer Methods in Applied Mechanics and Engineering* 199.17-20, pp. 1019–1031. ISSN: 00457825. DOI: 10.1016/j.cma.2009.11.011. URL: http://dx.doi.org/10.1016/j.cma.2009.11.011.

Aziz, K. (1993). "Reservoir Simulation Grids: Opportunities and Problems". In: *Journal of Petroleum Technology* 45.July. ISSN: 0149-2136. DOI: 10.2118/25233-PA.

Aziz, K. and A. Settari (1979). *Petroleum reservoir simulation*. Applied Science Publishers. ISBN: 0853347875. URL: http://books.google.co.uk/books/about/Petroleum{_}reservoir{_}simulation.html?id=GJ5TAAAAMAAJ{\&}pgis=1.

Babuska, I. (1971). "Error-bounds for finite element methods". In: *Numerical Math* 16, pp. 322–33.

Babuska, I. and M. Suri (1994). "The P and H-P Versions of the Finite Element Method, Basic Principles and Properties". In: *SIAM Journal on Scientific and Statistical Computing* 36.4, pp. 578–632.

Bagheri, M. and a. Settari (2007). "Methods for modelling full tensor permeability in reservoir simulators". In: *Journal of Canadian Petroleum Technology* 46.2, pp. 31–38. ISSN: 00219487. DOI: 10.2118/07-03-02.

Baillie, J., T. Coombes, and S. Rae (1996). "Dunbar Reservoir Model, A Multidisciplinary Approach to Update Brent Reservoir Description and Modelling". In: *Euopean 3-D Reservoir Modelling Conference*. Stavanger, Norway: SPE 35528. ISBN: 0121495264. DOI: doi:10.2118/35528-MS.

Balay, S., W. D. Gropp, L. C. McInnes, and B. F. Smith (1997). *Efficient Management of Parallelism in Object-Oriented Numerical Software Libraries*, pp. 163–202.

Baliga, B. R. and S. V. Patankar (1980). "a New Finite-Element Formulation for Convection-Diffusion Problems". In: *Numerical Heat Transfer* 3, pp. 393–409. ISSN: 0149-5720. DOI: 10.1080/01495728008961767. URL: http://www.tandfonline.com/doi/abs/10.1080/01495728008961767.

Barczewski, B. and H.P. Koschitzky (1996). *Groundwater and Subsurface Remediation, The VEGAS Research Facility: Technical Equipment and Research Projects*. Ed. by H. Kobus, B. Barczewski, and H.P. Koschitzky. Springer Berlin Heidelberg, pp. 129–157.

Bastian, P. and R. Helmig (1999). "Efficient fully-coupled solution techniques for two-phase flow in porous media". In: *Advances in Water Resources* 23, pp. 199–216. ISSN: 03091708. DOI: 10.1016/S0309-1708(99)00014-7.

Batdorf, M., L. A. Freitag, and C. Ollivier-Gooch (1997). "Computational Study of the Effect of Unstructured Mesh Quality on Solution Efficiency". In: *Convergence*.

Batenburg, D. V. and M. Bosch (2011). "Application of Dynamic Gridding Techniques to IOR / EOR-Processes". In: *SPE Reservoir Simulation Symposium held in The Woodlands, Texas*, pp. 1–16. URL: http://www.onepetro.org/mslib/servlet/onepetropreview?id=SPE-141711-MS.

Bazilevs, Y and T J R Hughes (2007). "Weak imposition of Dirichlet boundary conditions in fluid mechanics". In: *Computers and Fluids* 36.1, pp. 12–26. ISSN: 00457930. DOI: 10.1016/j.compfluid.2005.07.012.

Bazrafkan, S. and S. K. Matthäi (2011). "A new hybrid simulation method for multiphase flow on unstructured grids with discrete representations of material interfaces". In: *IAMG conference*.

Bear, J. (1972). *Dynamics of Fluids in Porous Media*. New York: Elsevier, p. 764. ISBN: 0-486-65675-6.

Belayneh, M W, S Geiger, and S K Matthäi (2006). "Numerical simulation of water injection into layered fractured carbonate reservoir analogs". In: *AAPG Bulletin* 90, pp. 1473–1493. ISSN: 0149-1423. DOI: 10.1306/05090605153.

Belayneh, M. W., S. K. Matthäi, M. J. Blunt, and S. F. Rogers (2009). "Comparison of deterministic with stochastic fracture models in water-flooding numerical simulations". In: *AAPG Bulletin* 93.11, pp. 1633–1648. ISSN: 01491423. DOI: 10.1306/07220909031.

Bentley, M. and P. Ringrose (2017). "Future directions in reservoir modelling: new tools and fit-for-purpose workflows". In: *Geological Society, London, Petroleum Geology Conference series*. ISSN: 2047-9921. DOI: 10.1144/PGC8.40. URL: http://pgc.lyellcollection.org/lookup/doi/10.1144/PGC8.40.

Berge, R. L., O. S. Klemetsdal, and K. A. Lie (2019). "Unstructured Voronoi grids conforming to lower dimensional objects". In: *Computational Geosciences* 23.1, pp. 169–188. ISSN: 15731499. DOI: 10.1007/s10596-018-9790-0.

Berger, M. J. and P. Colella (1989). "Local adaptive mesh refinement for shock hydrodynamics". In: *Journal of Computational Physics* 82.1, pp. 64–84. ISSN: 00219991. DOI: 10.1016/0021-9991(89)90035-1. URL: http://www.sciencedirect.com/science/article/pii/0021999189900351.

Berger, M. J. and J. Oliger (1984). "Adaptive mesh refinement for hyperbolic partial differential equations". In: *Journal of Computational Physics* 53.3, pp. 484–512. ISSN: 00219991. DOI: 10.1016/0021-9991(84)90073-1. URL: http://dx.doi.org/10.1016/0021-9991(84)90073-1.

Bertoncello, A., T. Sun, H. Li, G. Mariethoz, and J. Caers (2013). "Conditioning Surface-Based Geological Models to Well and Thickness Data". In: *Mathematical Geosciences* 45.7, pp. 873–893. ISSN: 18748961. DOI: 10.1007/s11004-013-9455-4.

Bianchi, M and C Zheng (2016). "A lithofacies approach for modeling non-Fickian solute transport in a heterogeneous alluvial aquifer". In: *Water Resources Research*, pp. 1–24. ISSN: 00431397. DOI: 10.1002/2015WR018186.

Blunt, M. J. (2017). *Multiphase Flow in Permeable Media: A Pore-Scale Perspective*. Cambridge, United Kingdom: Cambridge University Press. ISBN: 9781316145098. DOI: 10.1017/9781316145098. URL: http://ebooks.cambridge.org/ref/id/CBO9781316145098.

Blunt, M. J. and B. Rubin (1992). "Implicit flux limiting schemes for petroleum reservoir simulation". In: *Journal of Computational Physics* 102.1, pp. 194–210. ISSN: 00219991. DOI: 10.1016/S0021-9991(05)80015-4.

Blunt, M. J., K. Liu, and M. R. Thiele (1996). "A generalized streamline method to predict reservoir flow". In: *Petroleum Geoscience* 2, pp. 259–269. ISSN: 1354-0793. DOI: 10.1144/petgeo.2.3.259.

Brezzi, F (1974). "On the existence, uniqueness and approximation of saddle point problems arising from Lagrangian multiplier". In: *Analyse numérique* 8, pp. 129–151.

Bryant, I. D. and S. S. Flint (1993). "Quantitative Clastic Reservoir Geological Modelling: Problems and Perspectives". In: *The Geological Modelling of Hydrocarbon Reservoirs and Outcrop Analogues*. Chap. 1, pp. 1–20.

Buckley, S E and M C Leverett (1942). "Mechanism of Fluid Displacement in Sands". In: *Transactions of the AIME* 146.01, pp. 107–116. ISSN: 0081-1696. DOI: 10.2118/942107-G. arXiv: SPE-942107-G. URL: http://www.onepetro.org/doi/10.2118/942107-G.

Budd, C J, W Huang, and R D Russell (2009). "Adaptivity with moving grids". In: *Acta Numerica* 18.May 2009, pp. 111–241. ISSN: 0962-4929. DOI: 10.1017/S0962492906400015. URL: http://dx.doi.org/10.1017/S0962492906400015.

Burman, E., S. Claus, P. Hansbo, M. G. Larson, and A. Massing (2015). "CutFEM: Discretizing geometry and partial differential equations". In: *International Journal for Numerical Method in Engineering*. ISSN: 0743-1619. DOI: 10.1002/nme. arXiv: 1010.1724.

Carlson, M. R. (2003). *Practical Reservoir Simulation: Using, Assessing, and Developing Results*.

Caumon, G., P. Collon-Drouaillet, C. Le Carlier De Veslud, S. Viseur, and J. Sausse (2009). "Surface-based 3D modeling of geological structures". In: *Mathematical Geosciences* 41.8, pp. 927–945. ISSN: 18748961. DOI: 10.1007/s11004-009-9244-2.

Celia, M. A., E. T. Bouloutas, and R. L. Zarba (1990). "A General Mass-Conservative Numerical-Solution for the Unsaturated Flow Equation". In: *Water Resources Research* 26.7, pp. 1483–1496. DOI: 10.1029/90wr00196.

Chen, Q, J Wan, Y Yang, and R T Mifflin (2007). "A New Multipoint Flux Approximation for Reservoir Simulation". In: *SPE Reservoir Simulation Symposium*.

Chen, Y, L J Durlofsky, M Gerritsen, and X H Wen (2003). "A coupled local-global upscaling approach for simulating flow in highly heterogeneous formations". In: *Advances in Water Resources* 26.10, pp. 1041–1060. ISSN: 03091708. DOI: 10.1016/S0309-1708(03)00101-5.

Chen, Z and T Y Hou (2002). "A Mixed Multiscale Finite Element Method for Elliptic Problems With Oscillating Coefficients". In: *Mathematics of Computation* 72.242, pp. 541–576. ISSN: 0025-5718. DOI: 10.1090/S0025-5718-99-01077-7.

Chen, Z-X. (1988). "Some Invariant Solutions to Two-Phase Fluid Displacement Problems Including Capillary Effect". In: *SPE reservoir engineering* 3.02, pp. 691–700. ISSN: 0885-9248. DOI: 10.2118/14874-PA.

Christie, M A and M J Blunt (2001). "Tenth SPE Comparative Solution Project: A Comparison of Upscaling Techniques". In: *SPE Reservoir Evaluation & Engineering* 4.4, pp. 308–317. ISSN: 1094-6470. DOI: 10.2118/72469-PA.

Coats, K. H., W. D. George, C. Chu, and B. E. Marcum (1974). "Three-Dimensional Simulation of Steamflooding". In: *Society of Petroleum Engineers Journal* 14.6, pp. 573–592. DOI: 10.2118/4500-PA.

Cotter, C J, D A Ham, C C Pain, and S Reich (2009). "LBB stability of a mixed Galerkin finite element pair for fluid flow simulations". In: *Journal of Computational Physics* 228.2, pp. 336–348. ISSN: 00219991. DOI: 10.1016/j.jcp.2008.09.014. URL: http://dx.doi.org/10.1016/j.jcp.2008.09.014.

Courant, R., K. Friedrichs, and H. Lewy (1967). "On the partial difference equations of mathematical physics". In: *IBM Journal of Research and Development* 11.2, pp. 215–234.

Dagan, G, A Fiori, and I Janković (2013). "Upscaling of flow in heterogeneous porous formations: Critical examination and issues of principle". In: *Advances in Water Resources* 51, pp. 67–85. ISSN: 03091708. DOI: 10.1016/j.advwatres.2011.12.017. URL: http://dx.doi.org/10.1016/j.advwatres.2011.12.017.

Dahle, H. K., M. S. Espedal, R. E. Ewing, and O. Saevereid (1990). "Characteristic adaptive subdomain methods for reservoir flow problems". In: *Numerical Methods for Partial Differential Equations* 6.4, pp. 279–309. ISSN: 1098-2426. DOI: 10.1002/num.1690060402. URL: http://dx.doi.org/10.1002/num.1690060402.

Dahle, H. K., M. S. Espedal, and O. Saevereid (1992). "Characteristic, local grid refinement techniques for reservoir flow problems". In: *International Journal for Numerical Methods in Engineering* 34.3, pp. 1051–1069. ISSN: 1097-0207. DOI: 10.1002/nme.1620340324. URL: http://dx.doi.org/10.1002/nme.1620340324.

Dalen, V. (1979). "Simplified Finite-Element Models for Reservoir Flow Problems". In: *Society of Petroleum Engineers Journal* 19.October. ISSN: 00379999. DOI: 10.2118/7196-PA.

Damsleth, E., C. B. Tjolsen, and H. H. Haldorsen (1992). "A Two-Stage Stochastic Model Applied to a North Sea Reservoir". In: *SPE Annual Technical Conference and Exhibition held in New Orleans* April, pp. 402–486.

Darwish, M S and F H Moukalled (1994). "Normalized variable and space formulation methodology for high-resolution schemes". In: *Numerical Heat Transfer, Part B: Fundamentals* 26.1, pp. 79–96. ISSN: 15210626. DOI: 10.1080/10407799408914918.

Davies, D. R., C. R. Wilson, and S. C. Kramer (2011). "Fluidity: A fully unstructured anisotropic adaptive mesh computational modeling framework for geodynamics". In: *Geochemistry, Geophysics, Geosystems* 12.6. ISSN: 15252027. DOI: 10.1029/2011GC003551.

Dawe, R. A., M. R. Wheat, and M. S. Bidner (1992). "Experimental investigation of capillary pressure effects on immiscible displacement in lensed and layered porous media". In: *Transport in Porous Media* 7.1, pp. 83–101. ISSN: 01693913. DOI: 10.1007/BF00617318.

Debbabi, Y, M D Jackson, G J Hampson, and P Salinas (2017a). "Capillary Heterogeneity Trapping and Crossflow in Layered Porous Media". In: *Transport in Porous Media* 120.1, pp. 183–206. ISSN: 1573-1634. DOI: 10.1007/s11242-017-0915-z. URL: https://doi.org/10.1007/s11242-017-0915-z.

Debbabi, Y, M D Jackson, G J Hampson, P J R Fitch, and P Salinas (2017b). "Viscous Crossflow in Layered Porous Media". In: *Transport in Porous Media* 117.2, pp. 281–309. ISSN: 15731634. DOI: 10.1007/s11242-017-0834-z.

Denver, L. E. and D.C. Phillips (1990). "Stratigraphic geocellular modelling". In: *Geobyte* 5.1, pp. 45–47.

Deutsch, C. V. and A. G. Journel (1998). *GSLIB. Geostatistical Software Library and User's Guide*. 2nd. Oxford University Press, New York, p. 369.

Deutsch, C V and L Wang (1996). "Hierarchical object-based stochastic modeling of fluvial reservoirs". In: *Mathematical Geology* 28.7, pp. 857–880. ISSN: 0882-8121. DOI: 10.1007/BF02066005.

Deveugle, P. E. K., M. D. Jackson, G. J. Hampson, J. Stewart, M. D. Clough, T. Ehighebolo, M. E. Farrell, C. S. Calvert, and J. K. Miller (2014). "A comparative study of reservoir modeling techniques and their impact on predicted performance of fluvial-dominated deltaic reservoirs". In: *AAPG Bulletin* 98.4, pp. 729–763. ISSN: 01491423. DOI: 10.1306/08281313035.

Dogru, A. H., H. A. Sunaidi, L. S. K. Fung, W. A. Habiballah, N. Al-Zamel, and K. G. Li (2002). "A parallel reservoir simulator for large-scale reservoir simulation". In: *SPE Reservoir Evaluation & Engineering* 5.1, pp. 11–23. ISSN: 1094-6470. DOI: 10.2118/75805-PA.

Dogru, A. H., L. S. K. Fung, U. Middya, T. Al-Shaalan, and J. A. Pita (2009). "A Next-Generation Parallel Reservoir Simulator for Giant Reservoirs". In: *SPE Reservoir Simulation Symposium*, pp. 1–29. DOI: 10.2118/119272-MS. URL: http://www.onepetro.org/doi/10.2118/119272-MS.

Dokken, T., T. Lyche, and K. F. Pettersen (2013). "Polynomial splines over locally refined box-partitions". In: *Computer Aided Geometric Design* 30.3, pp. 331–356. ISSN: 01678396. DOI: 10.1016/j.cagd.2012.12.005. URL: http://dx.doi.org/10.1016/j.cagd.2012.12.005.

Donea, J and A Huerta (2003). *Finite Element Methods for Flow Problems*. John Wiley & Sons, Inc. ISBN: 0471496669. DOI: 10.1002/0470013826.

Durlofsky, L. J. and M. C. H. Chien (1993). "Development of a Mixed Finite-Element-Based Compositional Reservoir Simulator". In: *Proceedings of SPE Symposium on Reservoir Simulation*. ISBN: 9781555634933. DOI: 10.2118/25253-MS. URL: http://www.onepetro.org/mslib/servlet/onepetropreview?id=00025253{\&}soc=SPE.

Durlofsky, L J, R C Jones, and W J Milliken (1997). "A nonuniform coarsening approach for the scale-up of displacement processes in heterogeneous porous media". In: *Advances in Water Resources* 20.5-6, pp. 335–347. ISSN: 03091708. DOI: 10.1016/S0309-1708(96)00053-X. URL: http://www.sciencedirect.com/science/article/pii/S030917089600053X.

Durlofsky, Louis J. (1994). "Accuracy of mixed and control volume finite element approximations to Darcy velocity and related quantities". In: *Water Resources Research* 30.4, pp. 965–973. ISSN: 00431397. DOI: 10.1029/94WR00061. URL: http://doi.wiley.com/10.1029/94WR00061.

Edwards, M. G. (2002). "Unstructured, control-volume distributed, full-tensor finite-volume schemes with flow based grids". In: *Computational Geosciences* 3, pp. 433–452.

Edwards, M G (2006). "Higher-resolution hyperbolic-coupled-elliptic flux-continuous CVD schemes on structured and unstructured grids in 2-D". In: *International Journal for Numerical Methods in Fluids*, pp. 1059–1077. ISSN: 02712091. DOI: 10.1002/fld.

Edwards, M. G. and C. F. Rogers (1998). "Finite volume discretization with imposed flux continuity for the general tensor pressure equation". In: *Computational Geosciences* 2.4, pp. 259–290. ISSN: 14200597. DOI: 10.1023/A:1011510505406.

Eigestad, G. T., I. Aavatsmark, and M. S. Espedal (2002). "Symmetry and M-matrix issues for the O-method on an unstructured grid". In: *Computational Geosciences* 6.3-4, pp. 381–404. ISSN: 14200597. DOI: 10.1023/A:1021239130404.

Elman, H., D. Silvester, and A. Wathen (2006). *Finite Elements and Fast Iterative Solvers*. ISBN: 9780198528678.

Enge, H D and J A Howell (2010). "Impact of deltaic clinothems on reservoir performance: Dynamic studies of reservoir analogs from the Ferron Sandstone Member and Panther Tongue, Utah". In: *AAPG Bulletin* 94.2, pp. 139–161. ISSN: 01491423. DOI: 10.1306/07060908112.

Erten, H. and A. Ungor (2009). "Computing Triangulations without Small and Large Angles". In: *Sixth International Symposium on Voronoi Diagrams*. Copenhagen, pp. 192–201. DOI: 10.1109/ISVD.2009.32.

Erten, Hale and Alper Üngör (2009). "Quality Triangulations with Locally Optimal Steiner Points". In: *SIAM Journal on Scientific Computing* 31.3, pp. 2103–2130. ISSN: 1064-8275. DOI: 10.1137/080716748. URL: http://epubs.siam.org/doi/10.1137/080716748.

Ewing, R. E., B. A. Boyett, D. K. Babu, and R. F. Heinemann (1989). "Efficient Use of Locally Refined Grids for Multiphase Reservoir Simulation". In: *SPE Symposium on Reservoir Simulation in Houston*, pp. 55–69.

Farhloul, M. and M. Fortin (2002). "Review and complements on mixed-hybrid finite element methods for fluid flows". In: *Journal of Computational and Applied Mathematics* 140.1-2, pp. 301–313. ISSN: 03770427. DOI: 10.1016/S0377-0427(01)00520-9.

Farin, G. E. (2002). *Curves and surfaces for CAGD: a practical guide*. Morgan Kaufmann.

Farmer, C. L. (2005). "Geological modelling and reservoir simulation". In: *Mathematical Methods and Modelling in Hydrocarbon Exploration and Production*. Ed. by Armin Iske and Trygve Randen, pp. 119–212.

Farrell, P E and J R Maddison (2011). "Conservative interpolation between volume meshes by local Galerkin projection". In: *Computer Methods in Applied Mechanics and Engineering* 200.1-4, pp. 89–100. ISSN: 00457825. DOI: 10.1016/j.cma.2010.07.015. URL: http://dx.doi.org/10.1016/j.cma.2010.07.015.

Farthing, M. W., C. E. Kees, and C. T. Miller (2003). "Mixed finite element methods and higher order temporal approximations for variably saturated groundwater flow". In: *Advances in Water Resources* 26, pp. 373–394. DOI: 10.1016/S0309-1708(02)00187-2.

Ferziger, J. H. and M. Perić (2002). *Computational Methods for Fluid Dynamics*. 3rd ed. Springer-Verlag, pp. 21–37. ISBN: 3-540-42074-6.

Feyen, L and J Caers (2006). "Quantifying geological uncertainty for flow and transport modeling in multi-modal heterogeneous formations". In: *Advances in Water Resources* 29.6, pp. 912–929. ISSN: 03091708. DOI: 10.1016/j.advwatres.2005.08.002.

Firoozabadi, Abbas and Hussein Hoteit (2015). "Numerical Simulation of Complex Reservoir Problems and the Need for a Different Line of Attack". In: *The Way Ahead* 03.03, pp. 17–19. ISSN: 2224-4522. DOI: 10.2118/0307-017-twa.

Fisher, W L (1991). "Future supply potential of US oil and natural gas". In: *The Leading Edge* 10.Table 2, p. 15. ISSN: 1070485X. DOI: 10.1190/1.1436797.

Fokas, A S and Y C Yortsos (1982). "On the exactly solvable equation S, = [(13S+t)-Sl + (13S +)-S occuring in two-phase flow in porous media". In: *SIAM Journal on Applied Mathematics* 42.2, pp. 318–332.

Forsyth, P A (1991). "A Control Volume Finite Element Approach to NAPL Groundwater Contamination". In: *SIAM Journal on Scientific and Statistical Computing* 12, pp. 1029–1057. ISSN: 0196-5204. DOI: 10.1137/0912055.

Fried, I (1972). "Condition of finite element matrices generated from nonuniform meshes." In: *AIAA Journal* 10.2, pp. 219–221. ISSN: 0001-1452. DOI: 10.2514/3.6561. URL: http://arc.aiaa.org/doi/10.2514/3.6561.

Friis, H A and M G Edwards (2011). "A family of MPFA finite-volume schemes with full pressure support for the general tensor pressure equation on cell-centered triangular grids". In: *Journal of Computational Physics* 230.1, pp. 205–231. ISSN: 00219991. DOI: 10.1016/j.jcp.2010.09.012.

Fung, L. S. K., A. D. Hiebert, and L. X. Nghiem (1992). "Reservoir Simulation With a Control-Volume Finite-Element Method". In: *SPE Reservoir Engineering* 7. ISSN: 0885-9248. DOI: 10.2118/21224-PA.

Fung, L. S. K., X. Y. Ding, and A. H. Dogru (2014). "Unconstrained Voronoi Grids for Densely Spaced Complex Wells in Full-Field Reservoir Simulation". In: *SPE Journal* October, pp. 803–815.

Gander, M. J. and L. Halpern (2013). "Techniques for Locally Adaptive Time Stepping Developed over the Last Two Decades". In: *Domain Decomposition Methods in Science and Engineering XX*. Ed. by Randolph Bank, Michael

Holst, Olof Widlund, and Jinchao Xu. Berlin, Heidelberg: Springer Berlin Heidelberg, pp. 377–385. ISBN: 978-3-642-35275-1.

Geiger, S., S. G. Roberts, S. K. Matthäi, C. Zoppou, and A. Burri (2004). "Combining finite element and finite volume methods for efficient multiphase flow simulations in highly heterogeneous and structurally complex geologic media". In: *Geofluids* 4, pp. 284–299. ISSN: 14688115. DOI: 10.1111/j.1468-8123.2004.00093.x.

Geiger, S., K. S. Schmid, and Y. Zaretskiy (2012). "Mathematical analysis and numerical simulation of multi-phase multi-component flow in heterogeneous porous media". In: *Current Opinion in Colloid & Interface Science* 17, pp. 147–155. ISSN: 13590294. DOI: 10.1016/j.cocis.2012.01.003.

Gerritsen, M. G. and L. J. Durlofsky (2005). "Modeling Fluid Flow in Oil Reservoirs". In: *Annual Review of Fluid Mechanics*. Vol. 37, pp. 211–238. DOI: 10.1146/annurev.fluid.37.061903.175748.

Gomes, J. L M A, C. C. Pain, M. D. Eaton, A. J H Goddard, M. D. Piggott, A. K. Ziver, C. R E de Oliveira, and Y. Yamane (2008). "Investigation of nuclear criticality within a powder using coupled neutronics and thermofluids". In: *Annals of Nuclear Energy* 35.11, pp. 2073–2092. ISSN: 03064549. DOI: 10.1016/j.anucene.2008.05.012.

Gomes, J L M A, D Pavlidis, P Salinas, Z Xie, J R Percival, Y Melnikova, C C Pain, and M D Jackson (2017). "A force-balanced control volume finite element method for multi-phase porous media flow modelling". In: *International Journal for Numerical Methods in Fluids*, pp. 431–445. ISSN: 10970363 02712091. DOI: 10.1002/fld.4275. arXiv: fld.1 [DOI: 10.1002].

Gorman, G. J., J. Southern, P. E. Farrell, M. D. Piggott, G. Rokos, and P. H. J. Kelly (2012). "Hybrid OpenMP/MPI anisotropic mesh smoothing". In: *Procedia Computer Science* 9, pp. 1513–1522. ISSN: 18770509. DOI: 10.1016/j.procs.2012.04.166. URL: http://dx.doi.org/10.1016/j.procs.2012.04.166.

Graham, G. H., M. D. Jackson, and G. J. Hampson (2015a). "Three-dimensional modeling of clinoforms in shallow-marine reservoirs : Part 1 . Concepts and application". In: *AAPG Bulletin* 6.6, pp. 1013–1047. DOI: 10.1306/01191513190.

Graham, G H, M D Jackson, and G J Hampson (2015b). "Three-dimensional modeling of clinoforms in shallow-marine reservoirs : Part 2 . Impact on fluid flow and hydrocarbon recovery in fluvial-dominated deltaic reservoirs". In: *AAPG Bulletin* 6.6, pp. 1049–1080. DOI: 10.1306/01191513191.

Gringarten, E., A. Haouesse, B. Arpat, and L. Nghiem (2009). "Advantages of Using Vertical Stair Step Faults in Reservoir Grids for Flow Simulation". In: *Reservoir Simulation Symposium in The Woodlands, Texas*.

Gross, S. and A. Reusken (2007). "An extended pressure finite element space for two-phase incompressible flows with surface tension". In: *Journal of Computational Physics*, pp. 40–58. ISSN: 14329360. DOI: 10.1007/s00791-008-0099-8.

Guion, A. N., B. Skaflestad, K. A. Lie, and X. H. Wu (2019). "Validation of a Non-Uniform Coarsening and Upscaling Framework". In: *SPE Reservoir Simulation Conference*. DOI: 10.2118/193891-ms.

Haldorsen, H and L W Lake (1984). "A New Approach to Shale Management in Field-Scale Models". In: *Society of Petroleum Engineers Journal* 24.4. ISSN: 0197-7520. DOI: 10.2118/10976-PA.

Haldorsen, H. H. and E. Damsleth (1990). "Stochastic Modeling". In: *Journal of Petroleum Technology* April, pp. 404–412.

Hassanpour, M. M., M. J. Pyrcz, and C. V. Deutsch (2013). "Improved geostatistical models of inclined heterolithic strata for McMurray Formation, Alberta, Canada". In: *AAPG Bulletin* 97.7, pp. 1209–1224. ISSN: 01491423. DOI: 10.1306/01021312054.

Heinemann, Z E and G Von Hantelmann (1983). "Using Local Grid Refinement in a Multiple-Application Reservoir Simulator". In: *SPE Reservoir Simulation Symposium*. SPE 12255, pp. 205–215.

Heinemann, Z. E., C. W. Brand, M. Munka, and Y. M. Chen (1991). "Modeling Reservoir Geometry With Irregular Grids". In: *Society of Petroleum Engineers*, pp. 225–232. DOI: 10.2118/18412-PA. URL: http://www.onepetro.org/mslib/servlet/onepetropreview?id=00021228{\&}soc=SPE.

Helmig, R. (1997). *Multiphase flow and transport processes in the subsurface: a contribution to the modeling of hydrosystems*. Springer-Verlag.

Helmig, R. and R. Huber (1998). "Comparison of Galerkin-type discretization techniques for two-phase flow in heterogeneous porous media". In: *Advances in Water Resources* 21.8, pp. 697–711. ISSN: 03091708. DOI: 10.1016/S0309-1708(97)00023-7.

Helmig, R., J. Niessner, and H. Class (2006). "Recent advances in finite element methods for multi-phase flow processes in porous media". In: *International Journal of Computational Fluid Dynamics* 20.February 2015, pp. 245–252. ISSN: 1061-8562. DOI: 10.1080/00036810600792154.

Heße, F., V. Prykhodko, and S. Attinger (2013). "Assessing the validity of a lower-dimensional representation of fractures for numerical and analytical

investigations". In: *Advances in Water Resources* 56, pp. 35–48. ISSN: 03091708. DOI: 10.1016/j.advwatres.2013.03.003.

Hiester, H R, M D Piggott, and P A Allison (2011). "The impact of mesh adaptivity on the gravity current front speed in a two-dimensional lock-exchange". In: *Ocean Modelling* 38.1-2, pp. 1–21. ISSN: 14635003. DOI: 10.1016/j.ocemod.2011.01.003. URL: http://dx.doi.org/10.1016/j.ocemod.2011.01.003.

Hoang, H. and J Kleppe (2006). "A parallel adaptive finite difference algorithm for reservoir simulation". In: *SPE Europec/EAGE Annual Conference and Exhibition*. URL: http://www.onepetro.org/mslib/servlet/onepetropreview?id=SPE-99572-MS{\&}soc=SPE.

Hofstee, C., C. Gutiérrez Ziegler, O. Trötschler, and J. Braun (2003). "Removal of DNAPL contamination from the saturated zone by the combined effect of vertical upward flushing and density reduction". In: *Journal of Contaminant Hydrology* 67.1-4, pp. 61–78. ISSN: 01697722. DOI: 10.1016/S0169-7722(03)00088-3.

Hoteit, H. and A. Firoozabadi (2006). "Compositional Modeling of Discrete-Fractured Media Without Transfer Functions by the Discontinuous Galerkin and Mixed Methods". In: *SPE Journal* 11.October 2004, pp. 26–29. ISSN: 1086-055X. DOI: 10.2118/90277-PA.

Hou, T Y and X H Wu (1997). "A Multiscale Finite Element Method for Elliptic Problems in Composite Materials and Porous Media". In: *Journal of Computational Physics* 134.1, pp. 169–189. ISSN: 00219991. DOI: 10.1006/jcph.1997.5682. URL: http://www.sciencedirect.com/science/article/pii/S0021999197956825.

Hu, L., P. Joseph, and O. Dubrule (1994). "Random Genetic Simulation of the Internal Geometry of Deltaic Sandstone Bodies". In: *SPE Formation Evaluation* 9.4. ISSN: 0885-923X. DOI: 10.2118/24714-PA.

Hu, L. Y. and T. Chugunova (2008). "Multiple-point geostatistics for modeling subsurface heterogeneity: A comprehensive review". In: *Water Resources Research* 44.11, pp. 1–14. ISSN: 00431397. DOI: 10.1029/2008WR006993.

Huber, R. and R. Helmig (1999). "Multiphase flow in heterogeneous porous media: A classical finite element method versus an implicit pressure-explicit saturation-based mixed finite element-finite volume approach". In: *International Journal for Numerical Methods in Fluids* 29, pp. 899–920. ISSN: 02712091. DOI: 10.1002/(SICI)1097-0363(19990430)29:8<899::AID-FLD715>3.0.CO;2-W.

Hurtado, F S V, C R Maliska, and A F C Silva (2007). "On the Factors Influencing the Grid Orientation Effect in Reservoir Simulation". In: *19th International Congress of mechanical Engineering (COBEM)* 1989.

Huyakorn, P S and G F Pinder (1978). "A new finite element technique for the solution of two-phase flow through porous media". In: *Advances in Water Resources* 1.5, pp. 285–298. ISSN: 03091708. DOI: 10.1016/0309-1708(78)90042-8.

Ingram, D. M., D. M. Causon, and C. G. Mingham (2003). "Developments in Cartesian cut cell methods". In: *Mathematics and Computers in Simulation* 61.3-6, pp. 561–572. ISSN: 03784754. DOI: 10.1016/S0378-4754(02)00107-6.

Jackson, M D and A H Muggeridge (2000). "Effect of discontinuous shales on reservoir performance during horizontal waterflooding". In: *SPE Journal* 5.4, pp. 446–455. ISSN: 1086055X.

Jackson, M. D., A. H. Muggeridge, S. Yoshida, and H. D. Johnson (2003). "Upscaling permeability measurements within complex heterolithic tidal sandstones". In: *Mathematical Geology* 35.5, pp. 499–520.

Jackson, M. D., S. Yoshida, A. H. Muggeridge, and H. D. Johnson (2005). "Three-dimensional reservoir characterization and flow simulation of heterolithic tidal sandstones". In: *AAPG Bulletin* 89.4, pp. 507–528. ISSN: 0149-1423. DOI: 10.1306/11230404036.

Jackson, M. D., G. J. Hampson, and R. P. Sech (2009). "Three-dimensional modeling of a shoreface-shelf parasequence reservoir analog: Part 2. Geologic controls on fluid flow and hydrocarbon recovery". In: *AAPG Bulletin* 93.9, pp. 1183–1208. ISSN: 0149-1423. DOI: 10.1306/05110908145.

Jackson, M D, G J Hampson, J H Saunders, A El-Sheikh, G H Graham, and B Y G Massart (2013). "Surface-based reservoir modelling for flow simulation". In: *Geological Society of London Special Publications*. ISSN: 0305-8719. DOI: 10.1144/SP387.2. URL: http://sp.lyellcollection.org/cgi/doi/10.1144/SP387.2.

Jackson, M. D., J. R. Percival, P. Mostaghimi, B. S. Tollit, D. Pavlidis, C. C. Pain, J. L. M. A. Gomes, M. J. Blunt, P. Salinas, and A. H. Muggeridge (2015). "Reservoir Modeling for Flow Simulation by Use of Surfaces, Adaptive Unstructured Meshes, and an Overlapping-Control- Volume Finite-Element Method". In: *SPE Reservoir Evaluation & Engineering*, pp. 1–20. DOI: 10.2118/163633-PA.

Jacquemyn, C., M. D. Jackson, and G. J. Hampson (2018). "Surface-Based Geological Reservoir Modelling Using Grid-Free NURBS Curves and Surfaces".

In: *Mathematical Geosciences*. ISSN: 1874-8953. DOI: 10.1007/s11004-018-9764-8. URL: https://doi.org/10.1007/s11004-018-9764-8.

Janssen, G. M. C. M., J. R. Valstar, and S. E. A. T. M. Van Der Zee (2006). "Inverse modeling of multimodal conductivity distributions". In: *Water Resources Research* 42.3, pp. 1–13. ISSN: 00431397. DOI: 10.1029/2005WR004356.

Jasak, H., H. G. Weller, and A. D. Gosman (1999). "High Resolution Nvd Differencing Scheme for Arbitrarily Unstructured Meshes". In: *International Journal for Numerical Method in Fluids* 449.July 1998, pp. 431–449.

Jenny, P., S. H. Lee, and H. A. Tchelepi (2006). "Adaptive fully implicit multi-scale finite-volume method for multi-phase flow and transport in heterogeneous porous media". In: *Journal of Computational Physics* 217.2, pp. 627–641. ISSN: 10902716. DOI: 10.1016/j.jcp.2006.01.028.

Jenny, P., H. A. Tchelepi, and S. H. Lee (2009). "Unconditionally convergent nonlinear solver for hyperbolic conservation laws with S-shaped flux functions". In: *Journal of Computational Physics* 228.20, pp. 7497–7512. ISSN: 00219991. DOI: 10.1016/j.jcp.2009.06.032. URL: http://dx.doi.org/10.1016/j.jcp.2009.06.032.

Jia, A, D He, and C Jia (2012). "Advances and Challenges of Reservoir Characterization: A Review of the Current State-of-the-Art". In: *Earth Sciences*, pp. 205–224. DOI: 10.5772/26404. URL: http://cdn.intechopen.com/pdfs/27593/InTech-Advances{_}and{_}challenges{_}of{_}reservoir{_}characterization{_}a{_}review{_}of{_}the{_}current{_}state{_}of{_}the{_}art.pdf.

Jiang, J. and H. A. Tchelepi (2019). "Nonlinear acceleration of sequential fully implicit (SFI) method for coupled flow and transport in porous media". In: *Computer Methods in Applied Mechanics and Engineering* 352, pp. 246–275. ISSN: 00457825. DOI: 10.1016/j.cma.2019.04.030. URL: https://doi.org/10.1016/j.cma.2019.04.030.

Johannessen, K. A. (2014). "Isogeometric Analysis Using Locally Refined B-splines". PhD thesis. ISBN: 9788232606689.

Jones, J. E., Z. Cai, S. F. McCormick, and T. F. Russell (1997). "Control-Volume Mixed Finite Element Methods". In: *Computational Geosciences* 1, pp. 289–315.

Journel, A. G and C. J. Huijbregts (1978). *Mining geostatistics*. Academic press London.

Juanes, R, J Kim, S F Matringe, U Stanford, and L K Thomas (2005). "Implementation and Application of a Hybrid Multipoint Flux Approximation

for Reservoir Simulation on Corner-Point Grids". In: *SPE Annual Technical Conference and Exhibition*.

Julio, C, G Caumon, and M Ford (2015). "Impact of the en echelon fault connectivity on reservoir flow simulations". In: *Interpretation* 3.4, SAC23–SAC34. ISSN: 2324-8858. DOI: 10.1190/INT-2015-0060.1. URL: http://library.seg.org/doi/10.1190/INT-2015-0060.1.

Kashchiev, D. and A. Firoozabadi (2002). "Analytical Solutions for 1D Countercurrent Imbibition in Water-Wet Media". In: *SPE Journal*. ISSN: 1086-055X. DOI: doi:10.2118/75166-MS.

Kippe, V., J. E. Aarnes, and K. A. Lie (2008). "A comparison of multiscale methods for elliptic problems in porous media flow". In: *Computational Geosciences* 12.3, pp. 377–398. ISSN: 1420-0597. DOI: 10.1007/s10596-007-9074-6.

Klemetsdal, O. S., R. L. Berge, K. A. Lie, H. M. Nilsen, and O. Møyner (2017). "Unstructured Gridding and Consistent Discretizations for Reservoirs with Faults and Complex Wells". In: *SPE Reservoir Simulation Conference in Montgomery*. DOI: 10.2118/182666-ms.

Klemetsdal, O. S., O. Moyner, and K. A. Lie (2018). "Use Of Dynamically Adapted Basis Functions To Accelerate Multiscale Simulation Of Complex Geomodels". In: *16th European Conference on the Mathematics of Oil Recovery (ECMOR XVI)* September 2018.

Klemetsdal, O. S., O. Møyner, and K. A. Lie (2019). "Accelerating multiscale simulation of complex geomodels by use of dynamically adapted basis functions". In: *Computational Geosciences*. ISSN: 1420-0597. DOI: 10.1007/s10596-019-9827-z.

Ko, S C M and A D K Au (1979). "A weighted nine-point finite-difference scheme for eliminating the grid orientation effect in numerical reservoir simulation". In: *SPE Annual Technical Conference and Exhibition*. URL: http://www.onepetro.org/mslib/servlet/onepetropreview?id=00008248.

Kuzmin, Dmitri (2010). "A Guide to Numerical Methods for Transport Equations". In: *Friedrich-Alexander-Universitat Erlangen-Nurnberg*, pp. 5–8. ISSN: 00219991. DOI: 10.1007/978-3-642-11640-7_3. URL: http://www.mathematik.uni-dortmund.de/{\%}7B{~}{\%}7Dkuzmin/Transport.pdf.

Ladyzhenskaya, O A (1969). *The Mathematical Theory of Viscous Incompressible Flow*. Gordon and Breach.

Li, B., Z. Chen, and G. Huan (2003). "Control volume function approximation methods and their applications to modeling porous media flow". In: *Advances in Water Resources* 26, pp. 435–444. ISSN: 03091708. DOI: 10.1016/S0309-1708(02)00161-6.

Lie, K. A., S. Krogstad, I. S. Ligaarden, J. R. Natvig, H. M. Nilsen, and B. Skaflestad (2012). "Open-source MATLAB implementation of consistent discretisations on complex grids". In: *Computational Geosciences* 16.2, pp. 297–322. ISSN: 14200597. DOI: 10.1007/s10596-011-9244-4.

Lie, K. A., O. Moyner, J. R. Natvig, A. Kozlova, K. Bratvedt, S. Watanabe, and Z. Li (2017a). "Successful application of multiscale methods in a real reservoir simulator environment". In: *Computational Geosciences* 21.5-6, pp. 981–998. ISSN: 15731499. DOI: 10.1007/s10596-017-9627-2.

Lie, K. A., O. Møyner, and J. R. Natvig (2017b). "Use of Multiple Multiscale Operators To Accelerate Simulation of Complex Geomodels". In: *SPE Journal* March, pp. 20–22.

Lie, K. A., T. S. Mykkeltvedt, and O. Moyner (2018). "Fully Implicit WENO Schemes On Stratigraphic And Fully Unstructured Grids". In: *16th European Conference on the Mathematics of Oil Recovery (ECMOR XV)*. September 2018. ISBN: 9789462822603. DOI: 10.5277/msc152212.

Lohner, R., K. Morgan, and O. C. Zienkiewicz (1985). "An Adaptive Finite Element Procedure for Compressible High Speed Flows". In: *Computer Methods in Applied Mechanics and Engineering* 51, pp. 441–465.

Lohrenz, J, B Bray, and C Clark (1964). "Calculating Viscosities of Reservoir Fluids From Their Compositions". In: *Journal of Petroleum Technology* 16.10, pp. 1171–1176. ISSN: 0149-2136. DOI: 10.2118/915-PA. URL: http://www.onepetro.org/doi/10.2118/915-PA.

Lunati, I. and P. Jenny (2006). "Multiscale finite-volume method for compressible multiphase flow in porous media". In: *Journal of Computational Physics* 216.2, pp. 616–636. ISSN: 00219991. DOI: 10.1016/j.jcp.2006.01.001.

MacDonald, A. C., L. M. Falt, and A. L. Hektoen (1998). "Stochastic modeling of incised valley geometries". In: *AAPG BULLETIN* 82.6, pp. 1156–1172.

Maliska, C. R., J. Cordazzo, and A. F. C. Silva (2007). "Petroleum reservoir simulation using EbFVM: the nagative transmissbility issue". In: *4th International Conference on Computational Methods in Multiphase Flow*. WIT Press, pp. 133–142.

Mallison, B., C. Sword, T. Viard, W. Milliken, and A. Cheng (2014). "Unstructured Cut-Cell Grids for Modeling Complex Reservoirs". In: *SPE Journal* April.

Manchuk, J G and C V Deutsch (2009). *The structure of unstructured training*. Tech. rep. DOI: 10.1108/eb017264.

Manzoor, S., M. G. Edwards, A. Dogru, and T. M. Al-shaalan (2018). *Interior boundary-aligned unstructured grid generation and cell-centered versus vertex-centered CVD-MPFA performance*. Computational Geosciences, pp. 195–230. ISBN: 1059601796.

Martinez, P.A. and J.W. Harbaugh (1993). "Simulating Near-shore Environments". In: 265pp.

Massart, B. Y. G., M. D. Jackson, G. J. Hampson, H. D. Johnson, B. Legler, and C. A. L. Jackson (2016). "Effective flow properties of heterolithic, cross-bedded tidal sandstones: Part 1. Surface-based modeling". In: *AAPG Bulletin* 100.May, pp. 697–721.

Matthäi, S. K., A. A. Mezentsev, C. C. Pain, and M. D. Eaton (2005a). "A high-order TVD transport method for hybrid meshes on complex geological geometry". In: *International Journal for Numerical Methods in Fluids* 47.10-11, pp. 1181–1187. ISSN: 02712091. DOI: 10.1002/fld.901.

Matthäi, S. K., A. Mezentsev, and M. Belayneh (2005b). "Control-volume finite-element two-phase flow experiments with fractured rock represented by unstructured 3D hybrid meshes". In: *SPE Reservoir Simulation ...* DOI: 10.2118/93341-MS. URL: https://www.onepetro.org/conference-paper/SPE-93341-MS.

Matthäi, S. K., S. Geiger, S. G. Roberts, A. Paluszny, M. W. Belayneh, A. Burri, A. Mezentsev, H. Lu, D. Coumou, T. Driesner, and C. A. Heinrich (2007). "Numerical simulation of multi-phase fluid flow in structurally complex reservoirs". In: *Geological Society, London, Special Publications* 292, pp. 405–429. ISSN: 0305-8719. DOI: 10.1144/SP292.22.

McCarthy, J F (1995). "Comparison of fast algorithms for estimating large-scale permeabilities of heterogeneous media". In: *Transport in Porous Media* 19.2, pp. 123–137. ISSN: 01693913. DOI: 10.1007/BF00626662.

McWhorter, D B and D K Sunada (1990). "Exact integral solutions for two-phase flow". In: *Water Resources Research* 26.3, pp. 399–413. ISSN: 19447973. DOI: 10.1029/WR026i003p00399.

Melnikova, Y., C. Jacquemyn, H. Osman, P. Salinas, G. Gorman, G. J. Hampson, and M. D. Jackson (2016). "Reservoir Modelling Using Parametric Surfaces and Dynamically Adaptive Fully Unstructured Grids". In: *ECMOR XV - 15th European Conference on the Mathematics of Oil Recovery*. DOI: 10.3997/2214-4609.201601887.

Merland, R., G. Caumon, L. Bruno, and P. Collon-Drouaillet (2014). "Voronoi grids conforming to 3D structural features". In: *Compuational Geosciences*, pp. 373–383. DOI: 10.1007/s10596-014-9408-0.

Michael, H. A., H. Li, A. Boucher, T. Sun, J. Caers, and S. M. Gorelick (2010). "Combining geologic-process models and geostatistics for conditional simulation of 3-D subsurface heterogeneity". In: *Water Resources Research* 46.5, pp. 1–20. ISSN: 0043-1397. DOI: 10.1029/2009WR008414.

Miller, C T, G Christakos, P T Imhoff, J F Mcbride, and J A Pedit (1998). "Multiphase flow and transport modeling in heterogeneous porous media: challenges and approaches". In: *Advances in Water Resources* 21.2, pp. 77–120. ISSN: 0309-1708. DOI: 10.1016/S0309-1708(96)00036-X.

Mitchener, B. C., D. A. Lawrence, M. A. Partington, M. B. J. Bowman, and J. Gluyas (1992). "Brent Group: sequence stratigraphy and regional implications". In: *Geology of the Brent Group* 61.61, pp. 45–80. ISSN: 0305-8719. DOI: 10.1144/GSL.SP.1992.061.01.05.

Mlacnik, M. J. and Z. E. Heinemann (2001). "Using Well Windows in Full Field Reservoir Simulation". In: *SPE*.

Mlacnik, M. J., L. J. Durlofsky, and Z. E. Heinemann (2006). "Sequentially adapted flow-based PEBI grids for reservoir simulation". In: *SPE Journal* 11.3, pp. 317–327. ISSN: 1086055X.

Monteagudo, J E P and A Firoozabadi (2004). "Control-volume method for numerical simulation of two-phase immiscible flow in two- and three-dimensional discrete-fractured media". In: *Water Resources Research* 40.7, pp. 1–20. ISSN: 0043-1397. DOI: 10.1029/2003WR002996.

Moortgat, J and A Firoozabadi (2010). "Higher-order compositional modeling with Fickian diffusion in unstructured and anisotropic media". In: *Advances in Water Resources* 33.9, pp. 951–968. ISSN: 03091708. DOI: 10.1016/j.advwatres.2010.04.012. URL: http://dx.doi.org/10.1016/j.advwatres.2010.04.012.

– (2016). "Mixed-hybrid and vertex-discontinuous-Galerkin finite element modeling of multiphase compositional flow on 3D unstructured grids". In: *Journal of Computational Physics* 315, pp. 476–500. ISSN: 10902716. DOI: 10.1016/j.jcp.2016.03.054. URL: http://dx.doi.org/10.1016/j.jcp.2016.03.054.

Mosser, L., O. Dubrule, and M. J. Blunt (2017). "Reconstruction of three-dimensional porous media using generative adversarial neural networks". In: *Physical Review E* 96.4. ISSN: 24700053. DOI: 10.1103/PhysRevE.96.043309. arXiv: 1704.03225.

– (2018). "Stochastic Reconstruction of an Oolitic Limestone by Generative Adversarial Networks". In: *Transport in Porous Media* 125.1, pp. 81–103. ISSN: 15731634. DOI: 10.1007/s11242-018-1039-9. arXiv: 1712.02854. URL: https://doi.org/10.1007/s11242-018-1039-9.

Mostaghimi, P., J. R. Percival, D. Pavlidis, R. J. Ferrier, J. L. M. A. Gomes, G. J. Gorman, M. D. Jackson, S. J. Neethling, and C. C. Pain (2015). "Anisotropic Mesh Adaptivity and Control Volume Finite Element Methods for Numerical Simulation of Multiphase Flow in Porous Media". In: *Mathematical Geosciences*. ISSN: 1874-8961. DOI: 10.1007/s11004-014-9579-1. URL: http://link.springer.com/10.1007/s11004-014-9579-1.

Moyner, O. and K. A. Lie (2016). "A multiscale restriction-smoothed basis method for high contrast porous media represented on unstructured grids". In: *Journal of Computational Physics* 304, pp. 46–71. ISSN: 10902716. DOI: 10.1016/j.jcp.2015.10.010. URL: http://dx.doi.org/10.1016/j.jcp.2015.10.010.

Muskat, M. (1949). *Physical Principles of Oil Production*. London: McGraw-Hill.

Nelson, P H (2009). "Pore-throat sizes in sandstones, tight sandstones, and shales". In: *AAPG Bulletin* 93.3, pp. 329–340. ISSN: 01491423. DOI: 10.1306/10240808059.

Nick, H M and S K Matthäi (2011). "A Hybrid Finite-Element Finite-Volume Method with Embedded Discontinuities for Solute Transport in Heterogeneous Media". In: *Vadose Zone Journal* 10.1, p. 299. ISSN: 1539-1663. DOI: 10.2136/vzj2010.0015. URL: https://www.soils.org/publications/vzj/abstracts/10/1/299.

Njifenjou, A and I M Nguena (2008). "A new MPFA formulation for subsurface flow problems on unstructured grids: derivation of the discrete problem". In: *Mathematical Modeling, Simulation, Visualization and e-Learning*. Springer, pp. 75–89. ISBN: 9783540743385.

Nooruddin, H. A. and M. J. Blunt (2016). "Analytical and numerical investigations of spontaneous imbibition in porous media". In: *Water Resources Research* 52.9, pp. 7284–7310. ISSN: 19447973. DOI: 10.1002/2015WR018451.

Nordahl, K and P S Ringrose (2008). "Identifying the representative elementary volume for permeability in heterolithic deposits using numerical rock models". In: *Mathematical Geosciences* 40.7, pp. 753–771. ISSN: 18748961. DOI: 10.1007/s11004-008-9182-4.

Nourdeen, H. A (2018). "Upscaling Immiscible Capillary-Controlled Two-Phase Flow in Porous Media". PhD thesis. Imperial College London.

Nutting, P. G. (1930). "Physical analysis of oil sands". In: *AAPG Bulletin*, pp. 1337–1349.

Osman, H., P. Salinas, C.C. Pain, and M. D. Jackson. "An efficient control volume finite element method for multi-phase flow in heterogeneous porous media on challenging meshes". In: *To be submitted* ().

Osman, H., G. H. Graham, A. Moncorge, and C. Jacquemyn. "Is cell-to-cell scale variability necessary in reservoir models". In: *submitted* ().

Osman, H., G. H. Graham, A. Moncorge, and M. D. Jackson (2018). "Impact Of Cell-To-Cell Scale Variability On Flow In Reservoir Models". In: *15th European Conference on the Mathematics of Oil Recovery (ECMOR XV)* September 2018.

Pain, C. C., A. P. Umpleby, C. R. E. De Oliveira, and A. J. H. Goddard (2001). "Tetrahedral mesh optimisation and adaptivity for steady-state and transient finite element calculations". In: *Computer Methods in Applied Mechanics and Engineering* 190, pp. 3771–3796. ISSN: 00457825. DOI: 10.1016/S0045-7825(00)00294-2.

Paluszny, A., S. K. Matthäi, and M. Hohmeyer (2007). "Hybrid finite element-finite volume discretization of complex geologic structures and a new simulation workflow demonstrated on fractured rocks". In: *Geofluids* 7.2, pp. 186–208. ISSN: 14688115. DOI: 10.1111/j.1468-8123.2007.00180.x.

Pau, G. S. H., J. B. Bell, A. S. Almgren, K. M. Fagnan, and M. J. Lijewski (2012). "An adaptive mesh refinement algorithm for compressible two-phase flow in porous media". In: *Computational Geosciences* 16.3, pp. 577–592. ISSN: 14200597. DOI: 10.1007/s10596-011-9270-2.

Pavlidis, D., J. L. M. A. Gomes, Z. Xie, J. R. Percival, C. C. Pain, and O. K. Matar (2015). "Compressive adevection and multi-component methods for interface-capturing". In: *International Journal for Numerical Methods in Fluids* 80, pp. 256–282. ISSN: 02712091. DOI: 10.1002/fld.4078.

Peng, Ding Yu and Donald B Robinson (1976). "A New Two-Constant Equation of State". In: *Industrial and Engineering Chemistry Fundamentals* 15.1, pp. 59–64. ISSN: 01964313. DOI: 10.1021/i160057a011.

Piggott, M. D., G. J. Gorman, C. C. Pain, P. A. Allison, A. S. Candy, B. T. Martin, and M. R. Wells (2008). "A new computational framework for multi-scale ocean modelling based on adapting unstructured meshes". In: *International Journal for Numerical Methods in Fluids* 56, pp. 1003–1015. ISSN: 09727302. DOI: 10.1002/fld.

Piggott, M. D., P. E. Farrell, C. R. Wilson, G. J. Gorman, and C. C. Pain (2009). "Anisotropic mesh adaptivity for multi-scale ocean modelling". In: *Philosophical Transactions of the Royal Society A: Mathematical, Physical and Engineering Sciences* 367.1907, pp. 4591–4611. ISSN: 1364503X. DOI: 10.1098/rsta.2009.0155. arXiv: 9905084 [math.CO].

Ponting, D. K. (1992). "Corner Point Geometry in Reservoir Simulation". In: *The Mathematics of Oil Recovery, Institute of Mathematics and its Applications,* ed. by P.R. King, pp. 45–65. DOI: 10.3997/2214-4609.201411305.

Potempa, T (1985). "Mobility Weighting in Numerical Reservoir Simulation". In: *Society of Petroleum Engineers Journal* 25.4, pp. 565–572. ISSN: 01977520. DOI: 10.2118/12566-PA.

Prakash, C. (1987). "Examination of the upwind (donor-cell) formulation in control volume finite-element methods for fluid flow and heat transfer". In: *Numerical Heat Transfer* 11, pp. 401–416.

Pruess, K and F S Bodvarsson (1983). "A Seven-Point Finite Difference Method for Improved Grid Orientation Performance in Pattern Steamfloods". In: *SPE Reservoir Simulation Symposium*. SPE 12252. ISBN: 978-1-55563-649-4. DOI: 10.2118/12252-MS. URL: https://www.onepetro.org/conference-paper/SPE-12252-MS.

Pyrcz, M. J. and C. V. Deutsch (2014). *Geostatistical Reservoir Modeling*. Second. Oxford University Press, New York.

Pyrcz, M J, O Catuneanu, and C V Deutsch (2005). "Stochastic surface-based modeling of turbidite lobes". In: *AAPG Bulletin* 89.2, pp. 177–191. ISSN: 0149-1423. DOI: 10.1306/09220403112.

Pyrcz, M. J., R. P. Sech, J. A. Covault, B. J. Willis, Z. Sylvester, and T. Sun (2015). "Stratigraphic rule-based reservoir modeling". In: *Bulletin of Canadian Petroleum Geology* 63.4, pp. 287–303. ISSN: 00074802. DOI: 10.2113/gscpgbull.63.4.287.

Quandalle, P. and P. Besset (1985). "Reduction of Grid Effects Due to Local Sub-Gridding in Simulations Using a Composite Grid". In: *SPE Reservoir Simulation Symposium*, pp. 295–305.

Reichenberger, V., H. Jakobs, P. Bastian, and R. Helmig (2006). "A mixed-dimensional finite volume method for two-phase flow in fractured porous media". In: *Advances in Water Resources* 29.7, pp. 1020–1036. ISSN: 03091708. DOI: 10.1016/j.advwatres.2005.09.001.

Renard, Ph. and G. De Marsily (1997). "Calculating equivalent permeability: a review". In: *Advances in Water Resources* 20.5-6, pp. 253–278. ISSN: 03091708. DOI: 10.1016/S0309-1708(96)00050-4.

Reza, Z. A., M. J. Pranter, and P. Weimer (2006). "ModDRE: A program to model deepwater-reservoir elements using geomorphic and stratigraphic constraints". In: *Computers and Geosciences* 32.8, pp. 1205–1220. ISSN: 00983004. DOI: 10.1016/j.cageo.2005.11.004.

Ringrose, P. S. and M. Bentley (2015). *Reservoir Model Design*. New York: Springer.

Ringrose, P S, A W Martinius, and J Alvestad (2008). "Multiscale geological reservoir modelling in practice". In: *Geological Society, London, Special Publications* 309.1, pp. 123–134. ISSN: 0305-8719. DOI: 10.1144/SP309.9.

Ritchie, J. S. (2003). "The Dunbar, Ellon and Grant Fields (Alwyn South Area), Blocks 3/8a, 3/9b, 3/13a, 3/14, 3/15, UK North Sea". In: *Geological Society, London, Memoirs* 20.1, pp. 265–281. DOI: 10.1144/GSL.MEM.2003.020.01.23. URL: http://mem.lyellcollection.org/content/20/1/265.abstract.

Ruiu, J., G. Caumon, and S. Viseur (2016). "Modeling Channel Forms and Related Sedimentary Objects Using a Boundary Representation Based on Non-uniform Rational B-Splines". In: *Mathematical Geosciences* 48.3, pp. 259–284. ISSN: 18748953. DOI: 10.1007/s11004-015-9629-3.

Saad, Y. and M. H. Schultz (1986). "GMRES: A Generalized Minimal Residual Algorithm for Solving Nonsymmetric Linear Systems". In: *SIAM Journal on Scientific and Statistical Computing* 7.3, pp. 856–869. ISSN: 0196-5204. DOI: 10.1137/0907058. URL: http://epubs.siam.org/doi/10.1137/0907058.

Salinas, P., C. Rodrigo, F. J. Gaspar, and F. J. Lisbona (2006). "Multi-scale modelling of two-phase–two-component processes in heterogeneous porous media". In: *Numerical Linear Algebra with Applications* m.July, pp. 699–715. DOI: 10.1002/nla. URL: http://onlinelibrary.wiley.com/doi/10.1002/nla.497/abstract.

Salinas, P., J. R. Percival, D. Pavlidis, Z. Xie, J. L. M. A. Gomes, C. C. Pain, and M. D. Jackson (2015). "A Discontinuous Overlapping Control Volume Finite Element Method for Multi-Phase Porous Media Flow Using Dynamic Unstructured Mesh Optimization". In: *SPE Reservoir Simulation Symposium*. SPE 173279.

Salinas, P., D. Pavlidis, Z. Xie, A. Adam, C. C. Pain, and M. D. Jackson (2017a). "Improving the convergence behaviour of a fixed-point-iteration solver for multiphase flow in porous media". In: *International Journal for Numerical Methods in Fluids* 84.8, pp. 466–476. ISSN: 10970363. DOI: 10.1002/fld.4357.

Salinas, P., D. Pavlidis, Z. Xie, C. Jacquemyn, Y. Melnikova, M. D. Jackson, and C. C. Pain (2017b). "Improving the robustness of the control volume finite element method with application to multiphase porous media flow". In: *International Journal for Numerical Methods in Fluids* January, pp. 235–246. ISSN: 10970363. DOI: 10.1002/fld.4381.

Salinas, P., D. Pavlidis, Z. Xie, H. Osman, C. C. Pain, and M. D. Jackson (2018a). "A discontinuous control volume finite element method for multi-phase flow

in heterogeneous porous media". In: *Journal of Computational Physics* 352, pp. 602–614. ISSN: 00219991. DOI: 10.1016/j.jcp.2017.09.058.

Salinas, P, D Pavlidis, Z Xie, H Osman, C C Pain, and M D Jackson (2018b). "A robust mesh optimisation method for multiphase porous media flows". In: *Computational Geosciences*. ISSN: 1420-0597. DOI: 10.1007/s10596-018-9759-z.

Salinas, P., C. C. Pain, H. Osman, C. Heaney, D. Pavlidis, and M. D. Jackson (2018c). "Vanishing Artificial Capillary Pressure For Improved Real-Size Reservoir Simulations". In: *ECMOR XVI-16th European Conference on the Mathematics of Oil Recovery.*

Salinas, P., C. C. Pain, H. Osman, Z. Xie, and M. D. Jackson (2019). "Vanishing artificial diffusion as a mechanism to accelerate convergence for multiphase porous media flow". In: *Computer Methods in Applied Mechanics and Engineering.*

Schmid, K S and S Geiger (2012). "Universal scaling of spontaneous imbibition for water-wet systems". In: *Water Resources Research* 48.3. DOI: doi:10.1029/2011WR011566..

Schmid, K S, S Geiger, and K S Sorbie (2011). "Semianalytical solutions for cocurrent and countercurrent imbibition and dispersion of solutes in immiscible two-phase flow". In: *Water Resources Research* 47.2, pp. 1–16. ISSN: 00431397. DOI: 10.1029/2010WR009686.

Schmid, K. S., S. Geiger, and K. S. Sorbie (2013). "Higher order FE-FV method on unstructured grids for transport and two-phase flow with variable viscosity in heterogeneous porous media". In: *Journal of Computational Physics* 241, pp. 416–444. ISSN: 00219991. DOI: 10.1016/j.jcp.2012.12.017. URL: http://dx.doi.org/10.1016/j.jcp.2012.12.017.

Schmidt, G. H. and F. J. Jacobs (1988). "Adaptive local grid refinement and multi-grid in numerical reservoir simulation". In: *Journal of Computational Physics* 77.1, pp. 140–165. ISSN: 0021-9991.

Schneider, M., B. Flemisch, R. Helmig, K. Terekhov, and H. A. Tchelepi (2018). "Monotone nonlinear finite-volume method for challenging grids". In: *Computational Geosciences* 22.2, pp. 565–586. ISSN: 15731499. DOI: 10.1007/s10596-017-9710-8.

Sech, R P, M D Jackson, and G J Hampson (2009). "Three-dimensional modeling of a shoreface-shelf parasequence reservoir analog: Part 1. surface-based modeling to capture high-resolution fades architecture". In: *AAPG Bulletin* 93, pp. 1155–1181. ISSN: 01491423. DOI: 10.1306/05110908144.

Sederberg, T. W., G. T. Finnigan, X. Li, H. Lirp, and H. Ipson (2008). "Watertight trimmed NURBS". In: *ACM Trans. Graph* 27.3. DOI: 10.1145/1360612.1360678.

Seifert, D. and J. L. Jensen (2000). "Object and pixel-based reservoir modeling of a braided fluvial reservoir". In: *Mathematical Geology* 32.5, pp. 581–603. ISSN: 08828121. DOI: 10.1023/A:1007562221431.

Shewchuck, J. R. (2002). "Delaunay refinement algorithms for triangular mesh generation." In: *Computational Geometry* 22, pp. 21–74. ISSN: 09257721. DOI: doi:10.1016/S0925-7721(01)00047-5.

Shewchuk, J. R. (1996). "Triangle: Engineering a 2D quality mesh generator and Delaunay triangulator". In: *Workshop on Applied Computational Geometry*, pp. 203–222.

Shmaryan, L. E. and C. V. Deutsch (1999). "Object-Based Modeling of Fluvial / Deepwater Reservoirs with Fast Data\nConditioning: Methodology and Case Studies". In: *Proceedings of SPE Annual Technical Conference and Exhibition* 1, pp. 1–10. DOI: 10.2523/56821-MS. URL: http://www.spe.org/elibrary/servlet/spepreview?id=00056821.

Spivak, A., H. S. Price, and A. Settari (1975). "Solution of the Equations for Multidimensional , Two- Phase , Immiscible Flow by Variational Methods". In: *SPE Symposium on Numerical Simulation of Reservoir Performance*, pp. 27–41.

Stoyan, D., W. S. Kendall, and J. Mecke (1987). *Stochastic Geometry and its Applications*. John Wiley & Sons.

Strebelle, S. B. (2002). "Conditional simulation of complex geological structures using multiple-point statistics". In: *Mathematical Geology*. Vol. 34. 1, pp. 1–21. ISBN: 0882-8121. DOI: 10.1023/A:1014009426274.

Sylvester, Z., A. Cantelli, and C. Pirmez (2015). "Stratigraphic evolution of intraslope minibasins: Insights from surface-based model". In: *AAPG Bulletin* 99.6, pp. 1099–1129. ISSN: 01491423. DOI: 10.1306/01081514082.

Tchelepi, H. A., P. Jenny, S. H. Lee, and C. Wolfsteiner (2007). "Adaptive Multiscale Finite-Volume Framework for Reservoir Simulation". In: *SPE Journal* 12.02, pp. 188–195. ISSN: 1086-055X. DOI: 10.2118/93395-PA. URL: http://www.onepetro.org/doi/10.2118/93395-PA.

Tetzlaff, D. M. and J. W. Harbaugh (1989). "Simulating Clastic Sedimentation". In: *Computer Methods in the Geosciences*, p. 196.

Thomas, S., S. Du, G. Dufour, B. Mallison, P. Muron, and A. Rey (2019). "Recent Developments in Unstructured Aggregation-Based Upscaling for Simulation Workflows and Applications". In: *SPE Reservoir Simulation Conference*.

Thompson, C.M. and L. Shure (1995). *Image Processing Toolbox: For Use with MATLAB; [user's Guide]*. MathWorks.

Todd, M R, P M O'Dell, and G J Hirasaki (1972). "Methods for Increased Accuracy in Numerical Reservoir Simulators". In: *Society of Petroleum Engineers Journal* 12. ISSN: 0197-7520. DOI: 10.2118/3516-PA.

Trangenstein, J A (2002). "Multi-scale iterative techniques and adaptive mesh refinement for flow in porous media". In: *Advances in Water Resources* 25.8-12, pp. 1175–1213. ISSN: 03091708. DOI: 10.1016/S0309-1708(02)00053-2.

Trani, Mario and G. H. Graham (2016). "History-matching surface-based property models using the ensemble Kalman filter". In: *Petroleum Geoscience* 23, pp. 210–222. ISSN: 1354-0793. DOI: 10.1144/petgeo2016-045.

Verma, S. and K. Aziz (1997). "A Control Volume Scheme for Flexible Grids in Reservoir Simulation". In: *Society of Petroleum Engineers Reservoir Simulation Symposium*. ISBN: 9781555634032. DOI: 10.2118/37999-MS.

Wang, Y., H. Hajibeygi, and H. A. Tchelepi (2014). "Algebraic multiscale solver for flow in heterogeneous porous media". In: *Journal of Computational Physics* 259, pp. 284–303. ISSN: 00219991. DOI: 10.1016/j.jcp.2013.11.024. URL: http://dx.doi.org/10.1016/j.jcp.2013.11.024.

Wang, Y, C H Arns, S S Rahman, and J Y Arns (2018). "Porous Structure Reconstruction Using Convolutional Neural Networks". In: *Mathematical Geosciences* 50.7, pp. 1–19. ISSN: 18748953. DOI: 10.1007/s11004-018-9743-0. arXiv: arXiv:1609.01000v1. URL: https://doi.org/10.1007/s11004-018-9743-0.

Watts, J. W. (1986). "A Compositional Formulation of the Pressure and Saturation Equations". In: *SPE Reservoir Engineering*. ISSN: 0885-9248. DOI: 10.2118/12244-pa.

Wheeler, M. F. and I. Yotov (2006). "A Multipoint Flux Mixed Finite Element Method". In: *SIAM Journal on Scientific and Statistical Computing* 44.5, pp. 2082–2106.

White, C D and M D Barton (1999). "Translating Outcrop Data to Flow Models, With Applications to the Ferron Sandstone". In: *SPE Reservoir Evaluation & Engineering* 2.4, pp. 5–8. ISSN: 1094-6470. DOI: 10.2118/57482-PA.

White, C D, B J Willis, S P Dutton, J P Bhattacharya, and K Narayanan (2004). "Sedimentology, statistics, and flow behavior for a tide-influenced deltaic sandstone, Frontier Formation, Wyoming, United States". In: *AAPG Memoir* 80, pp. 129–152. ISSN: 02718529.

Willis, B. J. and C. D. White (2000). "Quantitative Outcrop Data for Flow Simulation". In: *Journal of Sedimentary Research* 70.4, pp. 788–802. ISSN:

1527-1404. DOI: 10.1306/2DC40938-0E47-11D7-8643000102C1865D. URL: http://jsedres.sepmonline.org/cgi/doi/10.1306/2DC40938-0E47-11D7-8643000102C1865D.

Wilson, C R (2009). "Modelling multiple-material flows on adaptive unstructured meshes". PhD thesis.

Wolff, M., B. Flemisch, and R. Helmig (2013). "An adaptive multiscale approach for modeling two-phase flow in porous media including capillary pressure". In: *Water Resources Research* 49.12, pp. 8139–8159. ISSN: 00431397. DOI: 10.1002/2013WR013800.

Wu, X H and R Parashkevov (2009). "Effect of Grid Deviation on Flow Solutions". In: *SPE Journal* 14.1, pp. 67–77. ISSN: 1086-055X. DOI: 10.2118/92868-PA.

Wyckoff, R. D., H. G. Botset, M. Muskat, and D. W. Reed (1933). "The Measurement of the Permeability of Porous Media for Homogeneous Fluids". In: *Review of Scientific Instruments* 4.7, pp. 394–405.

Xiao, D., P. Yang, F. Fang, J. Xiang, C. C. Pain, I. M. Navon, and M. Chen (2017). "A non-intrusive reduced-order model for compressible fluid and fractured solid coupling and its application to blasting". In: *Journal of Computational Physics* 330, pp. 221–244. ISSN: 10902716. DOI: 10.1016/j.jcp.2016.10.068. URL: http://dx.doi.org/10.1016/j.jcp.2016.10.068.

Xie, Y., A. S. Cullick, and C. V. Deutsch (2001). "Surface-Geometry and Trend Modeling for Integration of Stratigraphic Data in Reservoir Models". In: *SPE Western Regional Meeting Proceedings* SPE 68817, pp. 1–5. ISSN: <null>. DOI: 10.2118/68817-MS. URL: papers2://publication/uuid/14CE2F30-8FC5-48AC-84FB-F0AECA456A13.

Xie, Z, D Pavlidis, P Salinas, J R Percival, C C Pain, and O K Matar (2016). "A balanced-force control volume finite element method for interfacial flows with surface tension using adaptive anisotropic unstructured meshes". In: *Computers and Fluids* 138, pp. 38–50. ISSN: 00457930. DOI: 10.1016/j.compfluid.2016.08.005. URL: http://dx.doi.org/10.1016/j.compfluid.2016.08.005.

Yang, P., J. Xiang, F. Fang, D. Pavlidis, and C. C. Pain (2019). "Modelling of fluid-structure interaction for moderate reynolds number flows using an immersed-body method". In: *Computers and Fluids* 179, pp. 613–631. ISSN: 00457930. DOI: 10.1016/j.compfluid.2018.11.030. URL: https://doi.org/10.1016/j.compfluid.2018.11.030.

Yanosik, J L and T A McCracken (1979). "A Nine-Point, Finite-Difference Reservoir Simulator for Realistic Prediction of Adverse Mobility Ratio Displacements". In: *Society of Petroleum Engineers Journal* 19. ISSN: 0197-7520. DOI: 10.2118/5734-PA.

Yortsos, Y C and A S Fokas (1983). "An Analytical Solution for Linear Waterflood Including the Effects of Capillary Pressure". In: *Society of Petroleum Engineers Journal* February. ISSN: 0197-7520. DOI: 10.2118/9407-PA.

Zhang, X and M J Pyrcz (2006). *Advances in Stochastic Surface Modeling : Conditioning , Facies and Non Stationarity*. Tech. rep. CCG Report University of Alberta, pp. 204–227. DOI: http://www.ccgalberta.com/ccgresources/report08/2006-204-stochastic_surface_modeling.pdf.

Zhang, X, M J Pyrcz, and C V Deutsch (2009). "Stochastic surface modeling of deepwater depositional systems for improved reservoir models". In: *Journal of Petroleum Science and Engineering* 68.1-2, pp. 118–134. ISSN: 09204105. DOI: 10.1016/j.petrol.2009.06.019. URL: http://dx.doi.org/10.1016/j.petrol.2009.06.019.

Zienkiewicz, O C, R L Taylor, and J Z Zhu (2013). *The Finite Element Method: its Basis and Fundamentals*, pp. 493–543. ISBN: 9781856176330. DOI: 10.1016/B978-1-85617-633-0.00015-0. URL: http://www.sciencedirect.com/science/article/pii/B9781856176330000150.

Appendix A

Analytical solution for Spontaneous Imbibition

A.1 Analytical solution for Spontaneous Imbibition

Spontaneous imbibition displacement is controlled entirely by capillary forces. Here we derive the analytical solution of counter-current imbibition using the fractional flow concept first proposed by McWhorter and Sunada (1990) which is seen as the analogue to the viscous-dominated Buckley-Leverett solution (Buckley and Leverett, 1942).

We start with the continuity equation (Equation 2.3) written for one-dimensional flow in terms of the wetting phase with no sources

$$\phi \frac{\partial S_w}{\partial t} + \frac{\partial q_w}{\partial x} = 0 \tag{A.1}$$

where q_w is the wetting phase Darcy velocity, S_w is the wetting phase saturation and ϕ is the porosity of the porous medium.

The wetting phase Darcy velocity can be written as (Bear, 1972)

$$q_w = q_t f_w - D \frac{\partial S_w}{\partial t} \tag{A.2}$$

where $q_t = q_w + q_n$ is the total volume flux of the wetting and non-wetting phases.

For counter-current flow, $q_t = 0$ therefore Equation A.2 reduces to

$$q_w = -D\frac{\partial S_w}{\partial t} \tag{A.3}$$

The fractional flow function, f_w and capillary diffusion function, D are saturation-dependent functions given by

$$f_w(S_w) = \frac{1}{1 + \frac{\mu_w k_{r,n}}{\mu_o k_{r,w}}} \tag{A.4}$$

$$D(S_w) = -\frac{K k_{r,n}}{\mu_o} f_w \frac{dp_c}{dS_w} \tag{A.5}$$

where μ_w, μ_n are the wetting and non-wetting phase viscosities, respectively, $k_{r,w}, k_{r,o}$ are the wetting and non-wetting phase relatively permeabilities, p_c is the capillary pressure and K is the absolute permeability.

the governing equations are subject to the following initial and boundary conditions

$$\begin{aligned} S_w(x, t = 0) &= S_{wi} \\ S_w(x = 0, t) &= S_0 \\ S_w(x = \infty, t) &= S_{wi} \end{aligned} \tag{A.6}$$

where $S_0, S_{wi}$are the initial and inlet wetting phase saturations

The recovery as a function of time during spontaneous imbibition has a characteristic behaviour that has been studied by many authors (e.g. Yortsos and Fokas, 1983; Kashchiev and Firoozabadi, 2002; Chen, 1988; Fokas and Yortsos, 1982). McWhorter and Sunada (1990) presented a solution based on the assumption that the imbibition rate (for both co- and counter-current flow) is inversely proportional to the square-root of time. However, it was not until the work by Schmid et al., 2011 that this boundary condition was shown to be an inherent physical characteristic and therefore generally applicable for spontaneous imbibition.

The key idea behind the solution by McWhorter and Sunada, 1990 is to define an another fractional flow function F_w for the case of capillary dominated flow, where the wetting phase flux is normalised to the inlet wetting phase flux rather than the total flux,

$$F_w(S_w) = \frac{q_w(x,t)}{q_w(0,t)} \tag{A.7}$$

We now introduce the following similarity variable

$$\kappa = \frac{x}{\sqrt{t}} \tag{A.8}$$

Substituting Equation A.7 into Equation A.1 and using the variable transformation in Equation A.8 we can write

$$\begin{aligned} \phi\frac{dS_w}{d\kappa}\frac{d\kappa}{dt} + q_w(0,t)\frac{dF}{dS_w}\frac{dS_w}{d\kappa}\frac{d\kappa}{dx} = 0 \\ \phi\frac{dS_w}{d\kappa}\frac{-\kappa}{2t} + q_w(0,t)\frac{dF}{dS_w}\frac{dS_w}{d\kappa}\frac{1}{\sqrt{t}} = 0 \end{aligned} \tag{A.9}$$

The wetting phase flux at the inlet face, $q_w(0,t)$, is assumed to be inversely proportional to square-root of time

$$q_w(0,t) = \frac{A}{\sqrt{t}} \tag{A.10}$$

where A is the imbibition rate parameter.

We can now write Equation A.9 as

$$\phi\frac{dS_w}{d\kappa}\frac{\kappa}{2} = A\frac{dF_w}{dS_w}\frac{dS_w}{d\kappa} \tag{A.11}$$

then

$$\kappa = \frac{2A}{\phi}\frac{dF_w}{dS_w} \tag{A.12}$$

the saturation profile can therefore be written as

$$x = \frac{2A}{\phi}\frac{dF_w}{dS_w}\sqrt{t} \tag{A.13}$$

which is subject to

$$F_w(S_w = S_0, t) = 1 \tag{A.14}$$

$$F_w(S_w = S_{wi}, t) = 0 \tag{A.15}$$

To solve for x requires the determination of both F'_w and A. Taking the derivative of Equation A.12 with respect to S_w and substituting into Equation A.3 we obtain

$$\frac{d^2F}{dS_w^2} = -\frac{\phi}{2A^2}\frac{D}{F_w} \tag{A.16}$$

The solution can be found simply by direct integration of Equation A.16 to find F_w (McWhorter and Sunada, 1990; Schmid et al., 2011; Nooruddin and Blunt, 2016)

$$F_w = 1 - \left(\int_{S_w}^{S_0} \frac{(\tau - S_w)D(\tau)}{F_w(\tau)}d\tau\right)\left(\int_{S_{wi}}^{S_0} \frac{(\tau - S_w)D(\tau)}{F_w(\tau)}d\tau\right)^{-1} \tag{A.17}$$

hence

$$F'_w = \left(\int_{S_w}^{S_0} \frac{D(\tau)}{F_w(\tau)}d\tau\right)\left(\int_{S_{wi}}^{S_0} \frac{(\tau - S_w)D(\tau)}{F_w(\tau)}d\tau\right)^{-1} \tag{A.18}$$

$$A = \left(\frac{\phi}{2}\int_{S_{wi}}^{S_0} \frac{(\tau - S_{wi})D(\tau)}{F_w(\tau)}d\tau\right)^{1/2} \tag{A.19}$$

This completes the analytical solution. The saturation profile, $x(S_w, t)$ is obtained by the following procedure

1. Solve for F_w using Equation A.17
2. Compute F'_w and A using Equations A.18 and A.19
3. Solve for x using Equation A.13

Due to the implicit integral solution, an iterative scheme is required. First, we assume $F_w(S_w) = 1, \forall S_w$. The updated F_w from Equation A.17 is then used in the next iteration until a prescribed error tolerance is reached.